INTERPOLATING PERTURBATION SCHEME FOR CORRELATED ELECTRON SYSTEMS

BY HENRIK KAJUETER

A dissertation submitted to the

Graduate School—New Brunswick

Rutgers, The State University of New Jersey

in partial fulfillment of the requirements

for the degree of

Doctor of Philosophy

Graduate Program in Physics and Astronomy

Written under the direction of

G. Kotliar

and approved by

New Brunswick, New Jersey

October, 1996

ABSTRACT OF THE DISSERTATION

Interpolating Perturbation Scheme for Correlated Electron Systems

by Henrik Kajueter

Dissertation Director: G. Kotliar

We introduce a new iterative perturbation scheme for correlated fermion systems in infinite dimensions. The approach makes use of an interpolating expression for the self energy which becomes exact in various limits. The results are in good agreement with those obtained from exact diagonalization. For single band models the scheme presents an extension of iterative perturbation theory to arbitrary filling. The approach is generalized to multiband problems with fillings less than (or close to) one, the case relevant for systems like $La_{1-x}Sr_xTiO_3$. We apply the scheme to the one and the two band Hubbard model and study the influence of orbital degeneracy on the Mott transition in infinite dimensions. In addition, we compare the optical conductivity of the two band model with measurements in $La_{1-x}Sr_xTiO_3$ and $La_{2-x}Sr_xCuO_4$. As an application to real materials, we establish a new paradigm for the description of photoemission spectra of doped transition metal oxides by taking inhomogeneities at some length scale into account.

Finally, we propose and study a new scaling for next neighbor interactions in infinite dimensions.

Acknowledgements

My deepest gratitude goes to Gabriel Kotliar for directing this work. I very much appreciated our countless discussions and am particularly grateful for all the advice I received.

Special thanks to Vlad Dobrosavljević, Goetz Moeller, and Marcelo Rozenberg for several useful discussions.

Thank you also to all the people of the condensed matter theory group at Rutgers, in particular to Marc Horbach and Andrew Schofield as well as my officemates Stanko Barle and Andrew Getter.

Moreover, I thank Harold Baranger, Torgny Gustafsson, Lev Ioffe, and Claud Lovelace for acting as members of my Ph. D. committee.

This work has been supported by a Fulbright scholarship and, subsequently, a graduate assistantship of the Department of Physics, Rutgers University.

The time in the United States has been great. I will always remember it as a rewarding life experience. Thanks to all who made my stay here so enjoyable.

Dedication

For Shang-Chun, Yi-Ju, and Yu-Ching.

Table of Contents

List of Tables

List of Figures

List of Abbreviations

DOS Density of states.

IPT Iterative perturbation theory – more precisely, the perturbation scheme developed in this thesis (in contrast to *ordinary* IPT).

CPA Coherent potential approximation.

Chapter 1

Introduction

Stimulated by the discovery of high temperature superconductivity in 1986 [1] and new areas like heavy fermions [2], there has been a revived interest in strongly correlated electron systems during recent years.

Unfortunately, these systems are quite difficult to tackle theoretically. Most of the interesting phenomena like, for example, the correlation induced metal insulator transition, appear in a regime where the kinetic energy and the potential energy are of the same order. In this case there seems to be no natural small parameter which allows an expansion around a solvable limit.

However, Metzner and Vollhardt [3] realized that on a lattice with coordination number z (i. e. on a lattice where each site has z next neighbors) the reciprocal value $\frac{1}{z}$ can serve as such a parameter. This idea, which had been well known in the context of the Ising model [4], led to the limit of infinite (spatial) dimensions. It allows to construct a controlled approximation which treats the kinetic and the potential energy on the same footing.

Following this pioneering work there has been a lot of subsequent research. Particularly important are the contributions of Georges and Kotliar [6] who showed that the large d limit of the lattice problem can be mapped onto an impurity model together with a self consistency condition. This observation made this limit accessible to techniques which were already known from the impurity problem [26].

Afterwards, there has been much effort to develop the numerical tools necessary to finally solve the rather simple Hubbard model in large dimensions [20, 25, 21, 24]. Although the results provide a qualitative explanation for some experiments [19, 5], it is clear that a more detailed study has to take into account more refined models.

Right now, it is a rewarding challenge to improve the applicability of the infinite d limit to *real systems* like transition metal oxides. In this context the scope of this thesis is twofold: We develop a new perturbation scheme which allows to treat the large d limit of more complicated lattice models and present some work aiming at improving the limit itself.

So far several approaches have been used to treat the large d limit: qualitative analysis of the mean field equations [6], quantum Monte Carlo methods [7, 8, 27], iterative perturbation theory (IPT) [6, 13], exact diagonalization methods [14], and the projective self-consistent method, a renormalization technique [15]. However, each of these methods has its shortfalls. While quantum Monte Carlo calculations are not applicable in the zero temperature limit, the exact diagonalization methods and the projective self consistent method yield only a discrete number of poles for the density of states. Moreover, the computational requirements of the exact diagonalization and the quantum Monte Carlo methods are such that they can only be implemented for the simplest Hamiltonian. To carry out realistic calculations it is necessary to have an accurate but fast algorithm for solving the impurity model. In this context iterative perturbation theory has turned out to be a useful and reliable tool for the case of half filling [20, 19]. However, for finite doping the naive extension of the IPT scheme is known to give unphysical results. There is still no method which can be applied away from half filling and which at the same time is powerful enough to treat more complicated models involving several bands. The main part of this thesis is therefore devoted to the development of an iterative perturbation scheme which is applicable at arbitrary filling and can be extended to several bands. The basic idea is to construct a self energy expression which interpolates between various correct limits. This scheme is not only applicable to models which were not accessible by other methods, it also provides a much better resolution in many situations which have been treated in other ways before. We illustrate the scheme by applying it to topics like the description of photoemission data of doped transition metal oxides. Particularly interesting is the application to multiband models.

Although in many cases the large d limit provides a reasonable qualitative description of experiments [5], it displays some features which are unphysical with respect to finite dimensions. A well known artifact is the k independence of the self energy which signals the relationship to an underlying impurity model. Another shortfall is the negligence of density fluctuations between next neighbor sites. We study the influence of these fluctuations by introducing a new scaling for the spinless fermion model. The results yield a somewhat more realistic description for the phase transition into a staggered phase at half filling. However, the k-independence of the self energy cannot be removed by this approach.

The thesis is organized as follows: In chapter 2 we give a short introduction to the the limit of infinite dimensions as well as iterative perturbation theory at half filling. Chapter 3 can be viewed as the heart of the present work. Here, the new approximation scheme is derived for the single band case at zero temperature. We discuss its accuracy as well as several limits. Afterwards (chapters 4 - 5) the scheme is illustrated by several applications: First we apply it to the frustrated Hubbard model (chapter 4). In chapter 5 we present a new theoretical approach for the description of photoemission spectra in transition metal oxides. Then (chapter 6) the scheme is generalized to the multiband case. As an example, we study the frustrated two band Hubbard model. Chapter 7 concludes the treatment of the perturbation scheme with a discussion of a generalization to finite temperatures. Afterwards, we turn to the second part of this thesis exploring a new scaling for spinless fermions in infinite dimensions (chapter 8). We conclude in chapter 9 with a summary of the dissertation.

Some further results are contained in four appendices: Appendix A describes how iterative perturbation theory can be implemented on the real axis using the Keldysh formalism. Some results for the half filled Hubbard model at finite temperatures are presented. Appendix B is devoted to the effects of orbital degeneracy on the magnetic properties of $LaTiO_3$. It is shown that multiband effects lead to magnetic frustration. Afterwards (appendix C) we discuss whether our approach can also be applied to construct an interpolating perturbation scheme for finite dimensions. Finally, we present in appendix D some results for the half filled Hubbard model with binary site randomness. The comparison with analytic results might serve as an additional check for the validity of our scheme.

Chapter 2

The Limit of Infinite Dimensions

As outlined in the introduction we will almost always deal with the limit of large spatial dimensions (also referred to as large d limit). It is therefore useful to give a short summary on this topic establishing the basic notation for succeeding chapters.

The equations are derived for the case of the (single band) Hubbard model, which is given by[1]

$$H = \tilde{t} \sum_{<ij>,\sigma} c_{i\sigma}^{+} c_{j\sigma} \;+\; U \sum_{i} n_{i\uparrow} n_{i\downarrow} \tag{2.1}$$

This Hamiltonian, which was first introduced in the sixties [9, 10, 11, 12], describes lattice electrons with next neighbor hopping (first term) and on site interaction (second term). Although the model seems to be rather simple, it cannot be solved exactly. The complications arise since the interaction is diagonal in real space while the kinetic energy is diagonal in reciprocal (i. e. momentum) space. During recent years some progress in the study of the Hubbard model has been made by treating it in the limit of infinite dimensions or, respectively, coordination number [26].

For simplicity, we consider a Bethe lattice with coordination number z. To obtain a well defined and non trivial limit for $z \to \infty$ one has to scale the model parameters such that the relevant energy scales remain finite. For the Hubbard model the scaling

$$\tilde{t} = \frac{t}{\sqrt{z}} \tag{2.2}$$

is used. It ensures that the kinetic and the potential energy are treated on equal footing. In contrast to, e. g., the hypercubic lattice, the Bethe lattice has the advantage of a

---

[1] $\sum_{<ij>}$ denotes the sum over all next neighbor sites i and j of the lattice such that each pair (i,j) is included twice.

bounded bare (i. e. noninteracting) density of states:

$$\rho_0(\omega) = \frac{2}{\pi}\sqrt{1 - \left(\frac{\omega}{D}\right)^2} \tag{2.3}$$

where $D := 2t$. In the remaining parts of this thesis we set $D = 1$. All energies are then given in units of D.

In section 2.1 we outline how the lattice model is mapped onto an impurity problem. At half filling one possible way to solve the resulting self consistent set of equations is the application of iterative perturbation theory (IPT). We give a short introduction on this subject in section 2.2.

2.1 Mapping onto an impurity problem

The success of the large d limit is based on the mapping onto an impurity problem, which allows to apply techniques known from the investigation of such models.

Starting with the general action of (2.1)

$$\begin{aligned} S(\psi_{1,\sigma_1}, \psi^\dagger_{1,\sigma_1}, \psi_{2,\sigma_2}, \psi^\dagger_{2,\sigma_2}, \ldots) = &- \int_0^\beta d\tau \int_0^\beta d\tau' \sum_{i,\sigma} \psi_{i,\sigma}(\tau) \left(\frac{\partial}{\partial \tau'} - \mu\right) \psi^\dagger_{i,\sigma}(\tau') \\ &- \int_0^\beta d\tau \left(\tilde{t} \sum_{\langle ij \rangle, \sigma} \psi_{i,\sigma}(\tau)\psi^\dagger_{j,\sigma}(\tau) + U \sum_i \psi^\dagger_{i,\uparrow}(\tau)\psi_{i,\uparrow}(\tau)\psi^\dagger_{i,\downarrow}(\tau)\psi_{i,\downarrow}(\tau) \right) \end{aligned} \tag{2.4}$$

one can choose a particular lattice site i and integrate out all but this lattice site. This results in an effective action which for the Bethe lattice is given by [22, 21]

$$\begin{aligned} S(\psi_\sigma, \psi^\dagger_\sigma) \quad = \quad &- \int_0^\beta d\tau \int_0^\beta d\tau' \sum_\sigma \psi_\sigma(\tau) G_0^{-1}(\tau - \tau')\psi^\dagger_\sigma(\tau') \\ &- \int_0^\beta d\tau\, U \;\psi^\dagger_\uparrow(\tau)\psi_\uparrow(\tau)\psi^\dagger_\downarrow(\tau)\psi_\downarrow(\tau) \end{aligned} \tag{2.5}$$

Here, $G_0^{-1}(i\omega_n) := i\omega_n + \mu - t^2 G(i\omega_n)$ corresponds to the Weiss field in statistical mechanics. Unlike there it depends on frequency which is due to the itinerant nature of the model.

The important observation is that (2.5) is a purely *local* problem. This leads to the idea to look for an impurity problem which has an action of the same form. For the

Hubbard model the Anderson impurity model satisfies this condition:

$$\begin{aligned} H_{imp} &= \epsilon_f \sum_\sigma f_\sigma^+ f_\sigma + \sum_{k,\sigma} \epsilon_{k,\sigma}\, c_{k\sigma}^+ c_{k\sigma} \\ &+ \sum_{k,\sigma} V_k \left(c_{k\sigma}^+ f_\sigma + f_\sigma^+ c_{k\sigma} \right) + U f_\downarrow^+ f_\downarrow\, f_\uparrow^+ f_\uparrow \end{aligned} \tag{2.6}$$

It describes an impurity f coupled to a bath of conduction electrons $c_{k\sigma}$. After integrating out the bath one is left with an effective action for the impurity:

$$\begin{aligned} S_{eff}(\psi_{f\sigma}, \psi_{f\sigma}^\dagger) &= -\int_0^\beta d\tau \int_0^\beta d\tau' \sum_\sigma \psi_{f\sigma}(\tau) G_{f0}^{-1}(\tau - \tau') \psi_{f\sigma}^\dagger(\tau') \\ &\quad - \int_0^\beta d\tau\, U\, \psi_{f\uparrow}^\dagger(\tau)\psi_{f\uparrow}(\tau)\psi_{f\downarrow}^\dagger(\tau)\psi_{f\downarrow}(\tau) \end{aligned} \tag{2.7}$$

where $G_{f0}^{-1}(i\omega_n) := i\omega_n - \epsilon_f - \Delta(i\omega_n)$ with $\Delta(i\omega_n) := \sum_k \frac{V_k^2}{i\omega_n - \epsilon_k}$. Now, the expressions (2.5) and (2.7) are equivalent if one requires

$$G(i\omega_n) = t^{-2}\Delta(i\omega_n) = t^{-2} \sum_k \frac{V_k^2}{i\omega_n - \epsilon_k} \tag{2.8}$$

and

$$\mu = -\epsilon_f \tag{2.9}$$

The last two equations are the self consistency conditions which establish the mapping between the large d limit of the original lattice model and the impurity problem. Once an algorithm for the solution of the impurity model is known the lattice problem can be solved by iteration (see figure 2.1): Starting with a guess for the Green function G, parameters V_k and ϵ_k are determined such that (2.8) is fulfilled. Afterwards the corresponding impurity model (with $\epsilon_f = -\mu$) is solved yielding an impurity Green function G_f. The mapping requires $G = G_f$ so that the self consistency is closed. Among the methods currently available for solving the impurity problem are Monte Carlo calculations [7, 8, 27], exact diagonalization [14], the projective self consistent method [15], and, at half filling, iterative perturbation theory (IPT) [6, 13]. As has already been mentioned in the introduction (chapter 1) all these methods have serious limitations when more complicated models are to be treated. Because the main part of this thesis will focus on a generalization of the IPT scheme we will explain this approach in more detail below.

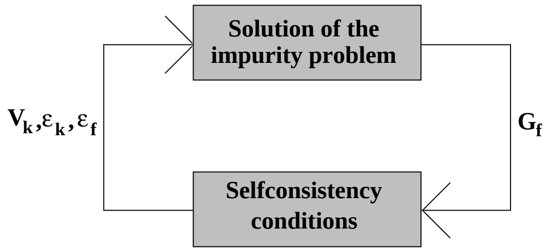

Figure 2.1: Iterative solution of the lattice problem.

2.2 Iterative perturbation theory at half filling

Iterative perturbation theory as a perturbation scheme for the half filled Hubbard model was originally proposed by Georges and Kotliar [6]. It is based on approximating the self energy of the impurity problem by its second order contribution in U. For the Bethe lattice (at half filling) the algorithm proceeds as follows. Using a guess for the Green function $G(i\omega_n)$ one determines

$$G_0(i\omega_n) := \frac{1}{i\omega_n - t^2\, G(i\omega_n)} \tag{2.10}$$

Now, the second order contribution of the self energy is calculated

$$\tilde{\Sigma}^{(2)}(\tau) = -U^2\ (G_0(\tau))^2\, G_0(-\tau) \tag{2.11}$$

From the Dyson equation one obtains a new Green function

$$G(i\omega_n) = \frac{1}{G_0^{-1}(i\omega_n) - \tilde{\Sigma}^{(2)}(i\omega_n)} \tag{2.12}$$

so that the next iteration can be started.

In appendix A we describe how this algorithm can be implemented on the real axis using the Keldysh formalism. Some results for the half filled Hubbard model at finite temperature can be found in section A.3.

Iterative perturbation theory at half filling has some remarkable features which make it a promising starting point for a generalization to more complicated problems. First of all the algorithm is extremely efficient as it uses only Fourier transforms which can be performed numerically without hassle. On the imaginary axis a solution is found within a few iterations so that the computation time is several orders of magnitude smaller than with the exact diagonalization or the quantum Monte Carlo calculations.

Moreover, the scheme yields quite reliable results at half filling as can be verified by comparing the outcome with other methods (see section A.4 of appendix A). It has been shown that that the approximation is not only exact to order U^2 in the weak coupling limit but also to order V^2 in the atomic limit [8]. Furthermore, it has the right behavior for small and large frequencies so that one deals with an interpolation scheme between exact limits.

The success of the method is however limited to half filling. The naive extension to finite doping displays unphysical results like negative compressiblities.

The major part of the following chapters will be devoted to show how these difficulties can be overcome. We will thereby derive a perturbation scheme which is generally applicable, very efficient, and also reliable.

Chapter 3

Iterative Perturbation Scheme for Arbitrary Filling (T=0)

3.1 Introduction

In recent years there has been an ongoing interest in doped transition metal oxides like $La_{1-x}Ti_xO_3$. These materials exhibit interesting phenenoma like the correlation induced metal insulator transition. Although there are several experimental data available now [28, 29, 33] it is still quite difficult to treat these substances theoretically. The most promising way towards a theoretical description, perhaps, is the limit of large spatial dimensions [3] as it was outlined in the last chapter. However, applying this limit to real systems requires a numerical tool which is powerful enough to deal with more complicated models and finite doping. Among the methods which are currently available (Monte Carlo calculations [7, 8, 27], exact diagonalization [14], the projective self consistent method [15], and iterative perturbation theory (IPT) [6, 13]) only IPT requires little computation time. In addition it produces quite accurate results at half filling. However, for finite doping the naive extension of the ordinary IPT scheme is known to give unphysical results like negative compressibilities. The success of the approach at half filling can be understood by that it becomes exact in various limits, namely for weak and strong coupling as well as for low and high frequencies [20]. The basic idea of this chapter is to construct an extension which keeps these features at finite doping. Thus, we obtain a scheme which interpolates between exact limits. The accuracy of this new method is discussed by comparing it with results obtained for an exactly solvable toy model as well as from exact diagonalization of the Hubbard model.

For simplicity, we will limit us to the fully frustrated single band case at zero temperature. An extension to $T \neq 0$ will be discussed in chapter 7 while chapter 6 is devoted to multiband models.

In the large d limit lattice models are mapped onto an impurity problem together with a self consistency condition. Therefore we will start deriving the perturbation scheme for the impurity model (section 3.2). Since the Luttinger theorem and the Friedel sum rule respectively play an important role in this approach, a derivation of these relations is presented in section 3.3. Afterwards various limits are discussed (section 3.4) and the accuracy of the method is tested by benchmarking it against the exact solution of a two site (toy) model (section 3.5). The solution of the lattice problem is illustrated for the Hubbard model (section 3.6). In section 3.7 we show how the Mott transition as a function of μ appears. In addition the insulator is treated. We conclude by summarizing the most important results (section 3.8).

3.2 Derivation of the approximation scheme for the impurity model

In the following we derive the approximation scheme which, given the hybridization function $\Delta(\omega) := \sum_k \frac{V_k^2}{\omega - \epsilon_k}$ and the impurity level ϵ_f, provides a solution of the (asymmetric) Anderson impurity model

$$
\begin{aligned}
H_{imp} &= \epsilon_f \sum_\sigma f_\sigma^+ f_\sigma + \sum_{k,\sigma} \epsilon_k \, c_{k\sigma}^+ c_{k\sigma} \\
&+ \sum_{k,\sigma} V_k \left(c_{k\sigma}^+ f_\sigma + f_\sigma^+ c_{k\sigma} \right) + U f_\downarrow^+ f_\downarrow f_\uparrow^+ f_\uparrow
\end{aligned} \tag{3.1}
$$

At this point we only treat a metallic hybridization function $\Delta(\omega)$. The insulating case will be discussed in section 3.7.

The procedure is an extension of the ordinary IPT scheme to finite doping. As indicated above, the idea of our approach is to construct a self energy expression which at arbitrary doping is exact in the weak coupling ($U \to 0$), the atomic ($V_k \to 0$), the low frequency ($\omega \to 0$), and finally the high frequency limit ($\omega \to \infty$). Moreover, at half filling our result should reduce to the ordinary IPT approximation which approximates the self energy by its second order contribution: $\Sigma(\omega) \approx Un + \tilde{\Sigma}_0^{(2)}(\omega)$ where

$$
\begin{aligned}
\tilde{\Sigma}_0^{(2)}(\omega) &:= U^2 \int_{-\infty}^{E_F=0} d\epsilon_1 \int_{E_F=0}^{\infty} d\epsilon_2 d\epsilon_3 \, \frac{\rho^{(0)}(\epsilon_1)\, \rho^{(0)}(\epsilon_2)\, \rho^{(0)}(\epsilon_3)}{\omega + \epsilon_1 - \epsilon_2 - \epsilon_3 - i\eta} \\
&+ U^2 \int_{E_F=0}^{\infty} d\epsilon_1 \int_{-\infty}^{E_F=0} d\epsilon_2 d\epsilon_3 \, \frac{\rho^{(0)}(\epsilon_1)\, \rho^{(0)}(\epsilon_2)\, \rho^{(0)}(\epsilon_3)}{\omega + \epsilon_1 - \epsilon_2 - \epsilon_3 - i\eta}
\end{aligned} \tag{3.2}
$$

with $\rho^{(0)} = \frac{1}{\pi}\mathrm{Im}G_0$. Here, the (advanced) Green function $G_0(\omega)$ is defined by

$$G_0(\omega) := \frac{1}{\omega + \tilde{\mu}_0 - \Delta(\omega)} \tag{3.3}$$

The parameter $\tilde{\mu}_0$ is given by $-\epsilon_f - Un$. In particular it vanishes at half filling. The full Green function follows from

$$G_f(\omega) = \frac{1}{G_0^{-1} - \tilde{\mu}_0 - \epsilon_f - \Sigma(\omega)} \tag{3.4}$$

To ensure the correctness of this approximation scheme in different limits, we modify the self energy functional as well as the definition of the parameter $\tilde{\mu}_0$.

We start with an ansatz for the self energy:

$$\Sigma_{int}(\omega) = Un + \frac{A\,\tilde{\Sigma}_0^{(2)}(\omega)}{1 - B\,\tilde{\Sigma}_0^{(2)}(\omega)} \tag{3.5}$$

Here, $\tilde{\Sigma}_0^{(2)}(\omega)$ is the normal second order contribution defined in equation (3.2). We determine the parameter A from the condition that the self energy has the exact behavior at high frequencies. Afterwards, B is determined from the atomic limit.

The leading behavior for large ω can be obtained by expanding the Green function into a continuous fraction [34]: $G_f(\omega) = 1/(\omega - \mu_1 - \frac{\mu_2 - \mu_1^2}{\omega + \ldots})$. Here, μ_i marks the ith order moment of the density of states. One can compute these quantities by evaluating a commutator (see [35]). We obtain for our model $G_f(\omega) = 1/(\omega - \epsilon_f - Un - \frac{\sum_k V_k^2 + U^2\,n(1-n)}{\omega + \ldots})$. The leading term of the self energy is therefore given by

$$\Sigma(\omega) = Un + U^2\,n(1-n)\,\frac{1}{\omega} + O\left(\left(\frac{1}{\omega}\right)^2\right) \tag{3.6}$$

Here, n is the physical particle number defined by $n = \int_{-\infty}^{0} d\omega\,\mathrm{Im}G_f(\omega)$. (3.6) has to be compared with the large frequency limit of (3.2):

$$\tilde{\Sigma}_0^{(2)}(\omega) = U^2\,n_0(1-n_0)\,\frac{1}{\omega} + O\left(\left(\frac{1}{\omega}\right)^2\right) \tag{3.7}$$

where n_0 is a fictitious particle number determined from G_0 (i. e. $n_0 = \int_{-\infty}^{0} d\omega\,\mathrm{Im}G_0(\omega)$). From (3.5), (3.6), and (3.7) we conclude

$$A = \frac{n(1-n)}{n_0(1-n_0)} \tag{3.8}$$

Choosing A in this way guarantees that our self energy is correct to order $\frac{1}{\omega}$. It should be noted from the continuous fraction considered above that consequently the moments of the density of states up to second order are reproduced exactly.

Next, we have to fix B. The exact impurity Green function for $V_k \to 0$ is given by [36]

$$G_f(\omega) = \frac{n}{\omega - \epsilon_f - U - i\eta} + \frac{1-n}{\omega - \epsilon_f - i\eta} \tag{3.9}$$

This can be written as $G_f(\omega) = 1/(\omega - \epsilon_f - \Sigma_{atomic}(\omega))$ where

$$\Sigma_{atomic}(\omega) = Un + \frac{n(1-n)\,U^2}{\omega - \epsilon_f - (1-n)U - i\eta} \tag{3.10}$$

This expression is to be compared with the atomic limit of our ansatz (3.5). Since[1] $\tilde{\Sigma}_0^{(2)}(\omega) \to \frac{U^2\, n_0(1-n_0)}{\omega + \tilde{\mu}_0 - i\eta}$, we obtain

$$B = \frac{(1-n)\,U + \epsilon_f + \tilde{\mu}_0}{n_0(1-n_0)\,U^2} \tag{3.11}$$

Thus, the final result for our interpolating self energy is

$$\Sigma_{int}(\omega) = Un + \frac{\frac{n\,(1-n)}{n_0\,(1-n_0)}\,\tilde{\Sigma}_0^{(2)}(\omega)}{1 - \frac{(1-n)\,U + \epsilon_f + \tilde{\mu}_0}{n_0\,(1-n_0)\,U^2}\,\tilde{\Sigma}_0^{(2)}(\omega)} \tag{3.12}$$

Yet, $\tilde{\mu}_0$ is still a free parameter. We fix it imposing the Luttinger theorem

$$\int_{-i\infty}^{+i\infty} \frac{d\omega}{2\pi i} G_f(\omega) \frac{\partial \Sigma_{int}(\omega)}{\partial \omega} = 0 \tag{3.13}$$

or, equivalently, the Friedel sum rule [40]

$$\begin{aligned} n &= \frac{1}{2} - \frac{1}{\pi}\mathrm{arctg}\left(\frac{\epsilon_f + \mathrm{Re}\Sigma_{int}(0) + \mathrm{Re}\Delta(0)}{\mathrm{Im}\Delta(0)}\right) \\ &\quad + \int_{-i\infty}^{+i\infty} \frac{d\omega}{2\pi i}\, G_f(\omega) \frac{\partial \Delta(\omega)}{\partial \omega} \end{aligned} \tag{3.14}$$

Both statements will be derived in the next section. They should be viewed as a condition on the zero frequency value of the self energy to obtain the correct low energy behavior. The use of the Friedel sum rule (or the Luttinger theorem) is the main difference to a earlier approximation schemes [37, 38, 39] and is essential to obtain a good agreement with the exact diagonalization method.

[1] This is only true if $\tilde{\mu}_0$ vanishes for $V \to 0$. We will show in section 3.4 that this is indeed the case.

So far, we considered three different limits: strong coupling, zero frequency and large frequency. It remains to check the weak coupling limit. Taking into account that $n = n_0$ and $\tilde{\mu}_0 = -\epsilon_f$ for $U \to 0$, it follows that (3.12) is indeed exact to order U^2.

The actual solution of the impurity model is determined by a pair ($\tilde{\mu}_0$, n) which satisfies equations (3.2), (3.3), (3.4), (3.12), and (3.14). For the numerical implementation Broyden's method [43], a generalization of Newton's method, has turned out to be very powerful. Defining two functions $f_1(n, \tilde{\mu}_0) := n - \frac{1}{\pi}\int_{-\infty}^{0} d\omega \mathrm{Im} G_f[n, \tilde{\mu}_0](\omega)$ and $f_2(n, \tilde{\mu}_0) := n - n_{Friedel}[n, \tilde{\mu}_0]$ the impurity problem can be solved by searching for the zeros of f_1 and f_2 ($n_{Friedel}$ is the particle number determined from the Friedel sum rule). The algorithm is very efficient as in most cases a solution is found within 4 to 10 iterations.

3.3 Derivation of the Luttinger theorem and the Friedel sum rule

The Luttinger theorem or, equivalently, the Friedel sum rule play an important role in our perturbation scheme. Therefore, we find it useful to give a derivation of these relations here.

For this purpose, we use the Green functions $G(i\omega)$ which are the zero temperature equivalent of the Matsubara Green functions.

There is a functional $\Phi[G]$ which can be represented by a set of diagrams containing only (exact) G lines [65]. The functional derivative of Φ with respect to G yields the self energy:

$$\Sigma(i\omega) = \frac{\delta\Phi}{\delta G(i\omega)} \tag{3.15}$$

The functional is invariant under a frequency shift in $G(i\omega)$:

$$G(i\omega) \to G'(i\omega) := G(i\omega + i\lambda) = G(i\omega) + i\lambda \frac{\partial G(i\omega)}{\partial i\omega} + O(\lambda^2) \tag{3.16}$$

This implies (to first order in λ)

$$0 = \int_{-i\infty}^{+i\infty} \frac{d\omega}{2\pi i} \frac{\delta\Phi}{\delta G(\omega)} \frac{\partial G(\omega)}{\partial\omega} = \int_{-i\infty}^{+i\infty} \frac{d\omega}{2\pi i} \Sigma(\omega) \frac{\partial G(\omega)}{\partial\omega} \tag{3.17}$$

Integrating (3.17) by parts yields the *Luttinger theorem*

$$0 = \int_{-i\infty}^{+i\infty} \frac{d\omega}{2\pi i} \frac{\partial\Sigma(\omega)}{\partial\omega} G(\omega) \tag{3.18}$$

which can also be written as

$$0 = \mathrm{Im} \int_{-\infty}^{0} \frac{d\omega}{\pi} \frac{\partial \Sigma_{adv}(\omega)}{\partial \omega} G_{adv}(\omega) \tag{3.19}$$

For an impurity model with a hybridization function $\Delta(\omega)$ this expression can be transformed into an equivalent statement on the particle number n:[2]

$$\begin{aligned} n &= \int_{-\infty}^{0} \frac{d\omega}{\pi} \mathrm{Im} G_{adv}(\omega) \\ &= -\int_{-\infty}^{0} \frac{d\omega}{\pi} \frac{\partial}{\partial \omega} \mathrm{Im} \log G_{adv}(\omega) + \mathrm{Im} \int_{-\infty}^{0} \frac{d\omega}{\pi} G_{adv}(\omega) \frac{\partial \Delta_{adv}(\omega)}{\partial \omega} \\ &\quad + \mathrm{Im} \int_{-\infty}^{0} \frac{d\omega}{\pi} G_{adv}(\omega) \frac{\partial \Sigma_{adv}(\omega)}{\partial \omega} \end{aligned} \tag{3.20}$$

Due to the Luttinger theorem (3.19) the last term in (3.20) vanishes. Moreover, we obtain for the first integral

$$\begin{aligned} \int_{-\infty}^{0} \frac{d\omega}{\pi} \frac{\partial}{\partial \omega} \mathrm{Im} \log G_{adv}(\omega) &= \frac{1}{\pi} \mathrm{Im} \log \left(\frac{G_{adv}(\omega)}{G^{\star}_{adv}(\omega)} \right) \Bigg|_{-\infty}^{0} \\ &= \frac{1}{\pi} \left(\phi(0) - \phi(-\infty) \right) \end{aligned} \tag{3.21}$$

Where $\phi(\omega)$ is defined as argument of the complex number $G_{adv}(\omega)$,[3] i. e.

$$\phi(\omega) = \mathrm{arctg} \left(\frac{\mathrm{Im} G_{adv}(\omega)}{\mathrm{Re} G_{adv}(\omega)} \right) \tag{3.22}$$

For $\omega \to -\infty$ the real part of the Green function behaves like $-\frac{1}{|\omega|}$ while the imaginary part is positive and decays exponentially. Thus

$$\phi(-\infty) = \pi \tag{3.23}$$

Moreover, we obtain

$$\begin{aligned} \phi(0) &= \mathrm{arctg} \left(\frac{\mathrm{Re} G_{adv}(0)}{\mathrm{Im} G_{adv}(0)} \right) \\ &= \frac{\pi}{2} + \mathrm{arctg} \left(-\frac{\mathrm{Re} G_{adv}(0)}{\mathrm{Im} G_{adv}(0)} \right) \\ &= \frac{\pi}{2} + \mathrm{arctg} \left(\frac{\mathrm{Re} \Sigma_{adv}(0) + \mathrm{Re} \Delta_{adv}(0) + \epsilon_f}{\mathrm{Im} \Delta_{adv}(0)} \right) \end{aligned} \tag{3.24}$$

---

[2] Here, we put the branch cut of the complex logarithm on the negative imaginary axis.

[3] We made use of the relation $\log(z) = \log|z| + i\arg(z)$, which is valid for an arbitrary complex number z.

Here we used $\mathrm{Im}\Sigma_{adv}(0) = 0$.

Substituting (3.24) together with (3.23) into (3.21) and afterwards (3.21) and (3.19) into (3.20) yields the *Friedel sum rule*:

$$\begin{aligned} n &= \frac{1}{2} - \frac{1}{\pi}\mathrm{arctg}\left(\frac{\mathrm{Re}\Sigma_{adv}(0) + \mathrm{Re}\Delta_{adv}(0) + \epsilon_f}{\mathrm{Im}\Delta_{adv}(0)}\right) \\ &\quad + \mathrm{Im}\int_{-\infty}^{0} \frac{d\omega}{\pi} G_{adv}(\omega) \frac{\partial \Delta_{adv}(\omega)}{\partial \omega} \end{aligned} \tag{3.25}$$

Here the last integral can be rewritten in the form

$$\mathrm{Im}\int_{-\infty}^{0} \frac{d\omega}{\pi} G_{adv}(\omega) \frac{\partial \Delta_{adv}(\omega)}{\partial \omega} = i \int_{-\infty}^{+\infty} \frac{d\omega}{2\pi i} G(\omega) \frac{\partial \Delta(\omega)}{\partial \omega} \tag{3.26}$$

which gives the Friedel sum rule in the form (3.14)

In contrast to most treatments in the literature, we derived a more general form of the Friedel sum rule keeping the full frequency dependence of the hybridization function $\Delta(\omega)$. This yields an additional term depending on $\frac{\partial \Delta(\omega)}{\partial \omega}$. For the numerical implementation both, the Luttinger theorem and the Friedel sum rule are equally suitable.

3.4 Discussion of various limits

To obtain a deeper understanding of the perturbation scheme introduced above we study its behavior in different limits of the parameters U and V_k. In particular, we are interested in the limits $U \to 0$, $U \to \infty$, $V_k \to 0$, and $V_k \to \infty$.

In the last section, we already saw that the scheme is exact to order U^2 in the weak coupling limit ($U \to 0$). In addition, it is easily seen that for large V_k the self energy contribution $\tilde{\Sigma}_0^{(2)}$ vanishes. Therefore $V_k \to \infty$ essentially corresponds to the weak coupling limit.

The atomic limit ($V_k \to 0$) and the strong coupling limit ($U \to \infty$) are more interesting. Let us first consider the perturbation scheme for small V. There are two questions which we would like to address: First of all the behavior of $\tilde{\mu}_0$ in the atomic limit and secondly the question whether the scheme is exact to order V^2 in the atomic limit.

To illustrate the first point, let us consider a constant hybridization $\Delta(\omega) = i\,\rho\,V^2 =: i\Gamma$, so that

$$\rho_0(\epsilon) = \frac{1}{\pi}\frac{\Gamma}{(\omega+\tilde{\mu}_0)^2+\Gamma^2} \tag{3.27}$$

which is used to evaluate the second order diagram (3.2). After a change of integration variables substituting $\tilde{\epsilon}_i := \frac{\epsilon_i+\tilde{\mu}_0}{\Gamma}$ we obtain

$$\begin{aligned}\tilde{\Sigma}_0^{(2)}(\omega) &= \frac{U^2}{\Gamma}\int_{-\infty}^{\frac{\tilde{\mu}_0}{\Gamma}} d\tilde{\epsilon}_1 \int_{\frac{\tilde{\mu}_0}{\Gamma}}^{\infty} d\tilde{\epsilon}_2 d\tilde{\epsilon}_3 \frac{\frac{1}{\tilde{\epsilon}_1^2+1}\frac{1}{\tilde{\epsilon}_2^2+1}\frac{1}{\tilde{\epsilon}_3^2+1}}{\frac{\omega+\tilde{\mu}_0}{\Gamma}+\tilde{\epsilon}_1-\tilde{\epsilon}_2-\tilde{\epsilon}_3-i\eta}\\ &+ \frac{U^2}{\Gamma}\int_{\frac{\tilde{\mu}_0}{\Gamma}}^{\infty} d\tilde{\epsilon}_1 \int_{-\infty}^{\frac{\tilde{\mu}_0}{\Gamma}} d\tilde{\epsilon}_2 d\tilde{\epsilon}_3 \frac{\frac{1}{\tilde{\epsilon}_1^2+1}\frac{1}{\tilde{\epsilon}_2^2+1}\frac{1}{\tilde{\epsilon}_3^2+1}}{\frac{\omega+\tilde{\mu}_0}{\Gamma}+\tilde{\epsilon}_1-\tilde{\epsilon}_2-\tilde{\epsilon}_3-i\eta}\end{aligned} \tag{3.28}$$

Now, we show that the following ansatz for $\tilde{\mu}_0$ is consistent with the Luttinger theorem:

$$\tilde{\mu}_0 = \Gamma\,\alpha(\Gamma) \quad \text{with} \quad \alpha(0) = 0 \tag{3.29}$$

Here, $\alpha(\Gamma)$ is a function which will be determined later.

With (3.29) $\tilde{\Sigma}_0^{(2)}(\omega = 0)$ can be expressed as

$$\tilde{\Sigma}_0^{(2)}(0) = \frac{U^2}{\Gamma} I\left(\alpha(\Gamma)\right) \tag{3.30}$$

with

$$\begin{aligned}I(\alpha) &= \int_{-\infty}^{\alpha} d\tilde{\epsilon}_1 \int_{\alpha}^{\infty} d\tilde{\epsilon}_2 d\tilde{\epsilon}_3 \frac{\frac{1}{\tilde{\epsilon}_1^2+1}\frac{1}{\tilde{\epsilon}_2^2+1}\frac{1}{\tilde{\epsilon}_3^2+1}}{\alpha+\tilde{\epsilon}_1-\tilde{\epsilon}_2-\tilde{\epsilon}_3-i\eta}\\ &+ \int_{\alpha}^{\infty} d\tilde{\epsilon}_1 \int_{-\infty}^{\alpha} d\tilde{\epsilon}_2 d\tilde{\epsilon}_3 \frac{\frac{1}{\tilde{\epsilon}_1^2+1}\frac{1}{\tilde{\epsilon}_2^2+1}\frac{1}{\tilde{\epsilon}_3^2+1}}{\alpha+\tilde{\epsilon}_1-\tilde{\epsilon}_2-\tilde{\epsilon}_3-i\eta}\end{aligned} \tag{3.31}$$

From symmetry arguments we see that $I(0) = 0$. Moreover, I is a continuous function of α. For an arbitrary but fixed β we can therefore *define* a function $\alpha(\Gamma)$ implicitly by

$$I(\alpha(\Gamma)) = \beta\Gamma \tag{3.32}$$

Substitution into (3.30) yields

$$\tilde{\Sigma}_0^{(2)}(0) = U^2\,\beta \tag{3.33}$$

The parameter β is now chosen such that the Friedel sum rule is fulfilled. For small Γ we have $n \approx \frac{1}{2}$ as well as $n_0 \approx \frac{1}{2}$, so that (3.14) becomes

$$\begin{aligned}0 &\approx \epsilon_f + \mathrm{Re}\Sigma_{int}(0) &(3.34)\\ &\approx \epsilon_f + \frac{U}{2} + \frac{U^2\,\beta}{1-4\,(\frac{U}{2}+\epsilon_f)\beta} &(3.35)\end{aligned}$$

which means[4]

$$\beta = \frac{\epsilon_f + \frac{U}{2}}{4\,(\epsilon_f + \frac{U}{2})^2 - U^2} \tag{3.36}$$

We thereby showed that our ansatz (3.29) is consistent with the Friedel sum rule. Thus $\tilde{\mu}_0$ goes in the atomic limit faster to zero than V^2 (or Γ).

The way we built the atomic limit into our perturbation scheme was to consider only the zeroth order in V. It is therefore not clear whether our method is also exact to higher order in V. This issue can be explored by expanding the interpolating self energy to order V^2:

$$\begin{aligned}\Sigma_{int}(\omega) \;&=\; Un + \frac{U^2\,n(1-n)}{\omega - \epsilon_f - (1-n)U - i\eta}\left[1 + 3\,\frac{\Delta(0)}{\omega - \tilde{\mu}_0}\left(1 - \frac{(1-n)U + \epsilon_f + \tilde{\mu}_0}{\omega - \epsilon_f - (1-n)U - i\eta}\right)\right] \\ &\quad + O(V^4)\end{aligned} \tag{3.37}$$

This should be compared with the work of Brenig and Schönhammer [36] or Bell and Madhukar [44] who obtained the exact result to order V^2 using the equations of motion:

$$\Sigma_{exact}(\omega) = Un + \frac{U^2\,n(1-n)}{\omega - \epsilon_f - (1-n)U - i\eta}\left(1 + \frac{(\frac{1}{2}\Delta(\omega) + \tilde{\Delta})/n(1-n)}{\omega - \epsilon_f - (1-n)\,U - i\eta}\right) \;+\; O(V^4) \tag{3.38}$$

where

$$\tilde{\Delta} := \sum_k V_k^2\,\left((1-n)\,\frac{\theta(\epsilon_f) - \theta(\epsilon_k)}{\epsilon_f - \epsilon_k} \;-\; n\,\frac{\theta(\epsilon_f + U) - \theta(\epsilon_k)}{\epsilon_f + U - \epsilon_k}\right)$$

We conclude from (3.37) and (3.38) that our scheme is *not* exact to order V^2. For large ω equations (3.37) and (3.38) show deviations in order $\frac{1}{\omega^2}$. Consequently, the spectral moments of higher than second order are not reproduced exactly. This can be seen by expanding the exact self energy into a continuous fraction [34]:

$$\Sigma(\omega) = Un + \cfrac{\alpha_2\alpha_3}{\omega + \alpha_3 + \alpha_4 - \cfrac{\alpha_4\alpha_5}{\omega + \alpha_5 + \alpha_6 - \cfrac{\alpha_6\alpha_7}{\ddots}}} \tag{3.39}$$

[4] Note that $\epsilon_f = -\frac{U}{2}$ yields $\beta = 0$ which implies $\alpha(\Gamma) = 0$ and thus $\tilde{\mu}_0 = 0$, the exact result for the particle hole symmetric case.

where each α_i depends on the spectral moments $\mu_1, \ldots, \mu_{i-1}$[5]

The complications which arise as V becomes finite can be illustrated if the Green function is split into four different contributions

$$\begin{aligned} G_{f\uparrow}(t,t') &= \left\langle T\left(n_\downarrow(t)\,\psi_{f\uparrow}(t)\;\psi^+_{f\uparrow}(t')\,n_\downarrow(t')\right)\right\rangle \\ &+ \left\langle T\left((1-n_\downarrow(t))\,\psi_{f\uparrow}(t)\;\psi^+_{f\uparrow}(t')\,(1-n_\downarrow(t'))\right)\right\rangle \\ &+ \left\langle T\left((1-n_\downarrow(t))\,\psi_{f\uparrow}(t)\;\psi^+_{f\uparrow}(t')\,n_\downarrow(t')\right)\right\rangle \\ &+ \left\langle T\left(n_\downarrow(t)\,\psi_{f\uparrow}(t)\;\psi^+_{f\uparrow}(t')\,(1-n_\downarrow(t'))\right)\right\rangle \end{aligned} \tag{3.40}$$

The last two terms describe transition amplitudes between different down spin configurations. In the atomic limit these terms vanish and we are left with the first two expressions which correspond to the sum in (3.9). However, as soon as V is finite, there are additional contributions from the "off diagonal" terms. Our perturbation scheme fails to capture them properly.

Our construction of the interpolating self energy does not make use of the large U limit. Therefore, it is important to answer the question whether the scheme has a well defined limit for $U \to \infty$. At the level of the impurity model we address this question by expanding the self energy Σ_{int} in powers of $\frac{1}{U}$. Assuming that $\tilde{\mu}_0$, n_0, and n become constant in the limit considered[6] we obtain (for $U = \infty$):

$$\Sigma_{int}(\omega) = \frac{n}{1-n}\left(\epsilon_f + \tilde{\mu}_0 - \frac{U^2\, n_0(1-n_0)}{\tilde{\Sigma}_0^{(2)}(\omega)}\right) \tag{3.41}$$

where $\tilde{\Sigma}_0(\omega)$ is of order U^2. Thus $\Sigma_{int}(\omega)$ remains *finite.*

In addition it is important to see that in the large U limit there is still a Kondo peak at small frequencies. I. e. we have to show that the effective mass diverges for $V \to 0$. The effective mass $m^\star$ can be obtained from the quasiparticle residue

$$Z = \frac{m}{m^\star} = \frac{1}{1 - \left.\frac{\partial \mathrm{Re}\,\Sigma(\omega)}{\partial\omega}\right|_{\omega=0}} \tag{3.42}$$

---

[5]See (6.10) for the first expressions.

[6]We checked that this assumption is fulfilled for the toy model treated in section 3.5.

From 3.41 we obtain (using $n_0 \approx \frac{1}{2}$)

$$\left.\frac{\partial\Sigma(\omega)}{\partial\omega}\right|_{\omega=0} = \frac{U^2}{4}\,\frac{\frac{\partial}{\partial\omega}\tilde{\Sigma}_0^{(2)}(0)}{\left(\tilde{\Sigma}_0^{(2)}(0)\right)^2} \tag{3.43}$$

Let us consider again a constant hybridization $\Delta(\omega) = i\Gamma$. In the limit $U \to \infty$ equation (3.36) yields $\beta = \frac{1}{8\epsilon_f}$ so that (3.33) becomes

$$\tilde{\Sigma}_0^{(2)}(0) = \frac{U^2}{8\epsilon_f} \tag{3.44}$$

Moreover, we have

$$\frac{\partial}{\partial\omega}\tilde{\Sigma}_0^{(2)}(0) = -\frac{U^2}{\Gamma^2}\,\tilde{I}\left(\alpha(\Gamma)\right) \tag{3.45}$$

where

$$\begin{aligned} \tilde{I}\left(\alpha\right) \;&:=\; \int_{-\infty}^{\alpha} d\tilde{\epsilon}_1 \int_{\alpha}^{\infty} d\tilde{\epsilon}_2 d\tilde{\epsilon}_3 \,\frac{\frac{1}{\tilde{\epsilon}_1^2+1}\,\frac{1}{\tilde{\epsilon}_2^2+1}\,\frac{1}{\tilde{\epsilon}_3^2+1}}{\left(\alpha+\tilde{\epsilon}_1-\tilde{\epsilon}_2-\tilde{\epsilon}_3-i\eta\right)^2} \\ &+\; \int_{\alpha}^{\infty} d\tilde{\epsilon}_1 \int_{-\infty}^{\alpha} d\tilde{\epsilon}_2 d\tilde{\epsilon}_3 \,\frac{\frac{1}{\tilde{\epsilon}_1^2+1}\,\frac{1}{\tilde{\epsilon}_2^2+1}\,\frac{1}{\tilde{\epsilon}_3^2+1}}{\left(\alpha+\tilde{\epsilon}_1-\tilde{\epsilon}_2-\tilde{\epsilon}_3-i\eta\right)^2} \end{aligned} \tag{3.46}$$

Now, $\tilde{I}(\alpha)$ remains positive and finite for $\alpha \to 0$:

$$\lim_{\alpha\to 0}\tilde{I}(\alpha) = c > 0 \tag{3.47}$$

Thus combining equations (3.43) to (3.46) yields for small V:

$$\left.\frac{\partial\Sigma(\omega)}{\partial\omega}\right|_{\omega=0} \approx -\frac{16c\epsilon_f^2}{\Gamma^2} \tag{3.48}$$

which diverges in the atomic limit so that according to (3.42) $Z \to 0$ and $m^\star \to \infty$ respectively. So the scheme presented here does not break down in the large U limit.

The large frequency behavior of (3.41) follows from $\tilde{\Sigma}_0^{(2)}(\omega) \simeq \frac{U^2 n_0(1-n_0)}{\omega}$. I. e.

$$\Sigma_{int} \simeq \frac{n}{1-n}\;\omega \tag{3.49}$$

or

$$G(\omega) \simeq \frac{1-n}{\omega} \tag{3.50}$$

I. e. the total weight of the Green function is decreased by that of the upper Hubbard band which disappears for $U \to \infty$. The remaining spectral weight obeys an exact sum rule (see [23]).

Above we saw that our perturbation scheme is not correct to order V^2. This remains true for $U \to \infty$ where the perturbation scheme yields

$$G_{int}(\omega) = \frac{1-n}{\omega - \epsilon_f} + \frac{1-n}{(\omega-\epsilon_f)^2} \; ((1-n)\Delta(\omega) - 3n\,\Delta(0)) + O(V^4) \tag{3.51}$$

while the expansion of the exact Green function in V is given by

$$G_{exact}(\omega) = \frac{1-n}{\omega - \epsilon_f} + \frac{1-n}{(\omega-\epsilon_f)^2} \left(\Delta(\omega) + \frac{\frac{1}{2}\Delta(\omega) + \tilde{\Delta}}{1-n} \right) + O(V^4) \tag{3.52}$$

We will come back to the large U limit in context with the lattice model (see section 3.7).

3.5 Benchmark against an exactly solvable toy model

To check the accuracy of the interpolation scheme it should be tested against some exact results. For this purpose, we consider the case where the bandwidth of the conduction electrons vanishes:

$$H_{imp} = \epsilon_f \sum_\sigma f^+_\sigma f_\sigma \; + \sum_\sigma V \left(c^+_\sigma f_\sigma + f^+_\sigma c_\sigma \right) \; + \; U f^+_\downarrow f_\downarrow \, f^+_\uparrow f_\uparrow \tag{3.53}$$

I. e. we are left with an effective two site model which can be diagonalized exactly yielding the exact eigenstates $|n\rangle$ with energies E_n $(n = 1 \ldots 16)$. The groundstate $|gs\rangle$ is always a singlet with two particles:

$$|gs\rangle = \alpha_1 \, f^+_\sigma f^+_{-\sigma}|0\rangle + \alpha_2 \, f^+_\sigma c^+_{-\sigma}|0\rangle + \alpha_3 \, f^+_{-\sigma} c^+_\sigma |0\rangle + \alpha_4 \, c^+_{-\sigma} c^+_\sigma |0\rangle \tag{3.54}$$

where the coefficients α_i depend on the model parameters. The Green function of the f site follows from

$$G_{f\sigma}(\omega) = \sum_n \left(\frac{|\langle n| f^+_\sigma |gs\rangle|^2}{\omega - (E_n - E_{gs}) - i\eta} + \frac{|\langle n| f_\sigma |gs\rangle|^2}{\omega + (E_n - E_{gs}) - i\eta} \right) \tag{3.55}$$

Only four poles in this representation have a finite weight. For $U >> V$, two of them appear at the upper an lower Hubbard bands (i.e. at $\approx \epsilon_f$ and $\approx U + \epsilon_f$) while the remaining poles represent the low frequency feature around zero, which corresponds to the Kondo peak in the case of a finite conduction electron bandwidth. Typical examples for the spectral function are plotted in figure 3.1 (full line) for different parameters.

a)

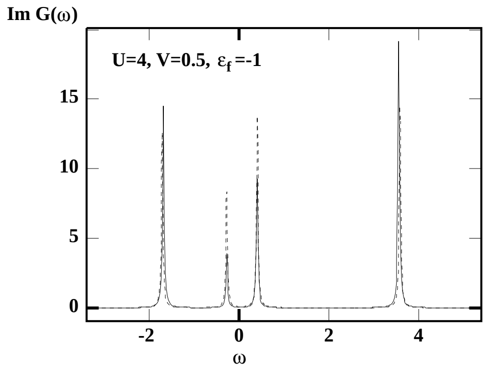

b)

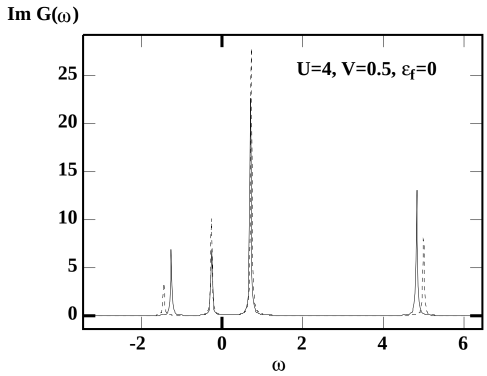

c)

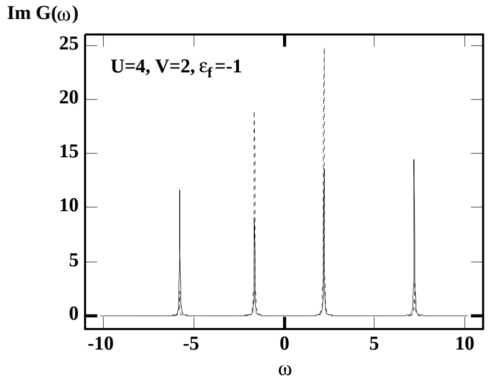

Figure 3.1: Comparison of the perturbation scheme (dashed line) vs exact diagonalization (full line) for different parameters. The poles have been broadened ($\eta = 0.02$) to make them visible.

Also the perturbation scheme yields a four pole structure for the density of states. This can be seen as follows: The model (3.53) implies $\Delta(\omega) = \frac{1}{\omega - i\eta}$. Thus

$$G_0(\omega) = \frac{1}{\omega + \tilde{\mu}_0 - \frac{V^2}{\omega - i\eta}} = \frac{\omega}{\epsilon_1 - \epsilon_2}\left(\frac{1}{\omega - \epsilon_1} - \frac{1}{\omega - \epsilon_2}\right) \tag{3.56}$$

where $\epsilon_{1,2} = -\frac{\tilde{\mu}_0}{2} \pm \sqrt{\frac{\tilde{\mu}_0^2}{4} + V^2}$. Without loss of generality we can assume $\epsilon_1 < 0$ and $\epsilon_2 > 0$. Then we obtain from (3.56) $n_0 = \frac{\epsilon_1}{\epsilon_1 - \epsilon_2}$. Evaluating the second order diagram for the self energy according to (3.2) yields

$$\tilde{\Sigma}_0^{(2)}(\omega) = U^2 n_0(1 - n_0)\left(\frac{1 - n_0}{\omega + \epsilon_2 - 2\epsilon_1 - i\eta} + \frac{n_0}{\omega + \epsilon_1 - 2\epsilon_2 - i\eta}\right) \tag{3.57}$$

I. e. there are two poles in $\tilde{\Sigma}_0^{(2)}$. Inserting (3.57) into (3.12) gives two poles for the interpolating self energy Σ_{int}. Now, since $G_f(\omega) = 1/(\omega - \epsilon_f - \Sigma_{int}(\omega) - \frac{V^2}{\omega})$ it follows that there are four poles in the Green function G_f.

For comparison, the numerical results of the perturbation scheme are included into figure 3.1 (dashed line). Apparently, there is a good agreement with the exact diagonalization. Only for large doping (figure 3.1 b) we see slight differences in the positions of the poles indicating the Hubbard bands.

A more quantitative evaluation has to consider the weights w_i and the position p_i of the poles ($i = 1 \ldots 4$). The data are given in tables 3.1 - 3.4 for various parameters.

Table 3.1 contains data for the particle hole symmetric case ($\epsilon_f = -\frac{U}{2}$) and various U (a) and V (b). We find that the position of the poles agrees over several digits in both cases. It should be noted that in the perturbation scheme the weights were determined by integration and have some numerical error ($\delta w \approx 0.005$). Within this error range both methods are in good agreement. Thus, we conclude that the perturbation scheme is almost exact at half filling, where it reduces to the ordinary IPT scheme.

Let us now turn to the case of finite doping. In table 3.2 we give results for $U = 4$, $V = 0.5$, and increasing hole doping. We find for all dopings a good agreement between the weights w_i, the positions of the low frequency poles (p_2 and p_3), and the particle number n_σ. Only p_1 and p_4 deviate a bit for extremely large doping. However, in this limit their weights become small so that this should not be a matter of concern.

a)

$V = 0.5$, $\epsilon_f = -\frac{U}{2}$ and increasing U

	p_1	p_2	p_3	p_4	w_1	w_2	w_3	w_4
$U = 1$								
pt	-1.589792	-0.4717593	0.4717593	1.589792	0.0638	0.4335	0.4335	0.0638
ed	-1.589793	-0.4717594	0.4717594	1.589793	0.0602	0.4398	0.4398	0.0602
$U = 2$								
pt	-1.825141	-0.4109268	0.4109268	1.825141	0.1713	0.3259	0.3259	0.1713
ed	-1.825141	-0.4109272	0.4109272	1.825141	0.1709	0.3291	0.3291	0.1709
$U = 4$								
pt	-2.532248	-0.2961789	0.2961789	2.532248	0.3259	0.1703	0.1703	0.3259
ed	-2.532248	-0.2961796	0.2961796	2.532248	0.3291	0.1709	0.1709	0.3291
$U = 8$								
pt	-4.297621	-0.1745114	0.1745114	4.297621	0.4344	0.0599	0.0599	0.4344
ed	-4.297621	-0.1745152	0.1745152	4.297621	0.4398	0.0602	0.0602	0.4398

b)

$U = 4$, $\epsilon_f = -2$ and increasing V

	p_1	p_2	p_3	p_4	w_1	w_2	w_3	w_4
$V = 0.1$								
pt	-2.024791	-1.0864563E-02	1.0864563E-02	2.024791	0.4833	0.0129	0.0129	0.4833
ed	-2.024791	-1.4816341E-02	1.4816341E-02	2.024791	0.4891	0.0110	0.0110	0.4891
$V = 1$								
pt	-3.650281	-0.8218542	0.8218542	3.650281	0.1696	0.3266	0.3266	0.1696
ed	-3.650281	-0.8218544	0.8218544	3.650281	0.1709	0.3291	0.3291	0.1709
$V = 4$								
pt	-12.18536	-3.939152	3.939152	12.18536	0.0168	0.4771	0.4771	0.0168
ed	-12.18536	-3.939152	3.939152	12.18536	0.0169	0.4831	0.4831	0.0169

Table 3.1: Perturbation scheme vs exact diagonalization at half filling: a) $V = 0.5$, $\epsilon_f = -\frac{U}{2}$ and increasing U b) $U = 4$, $\epsilon_f = -2$ and increasing V.

The comparison as a function of U (table 3.3) and V displays again a reasonable agreement. Small deviations occur in the large U and the small V limits. This is probably since the perturbation scheme in the atomic limit is only exact to zeroth order in V so that the agreement is worse than in the weak coupling case where the scheme is exact to order U^2.

3.6 Solution of the lattice model

Once a solution of the impurity problem is known for arbitrary parameters a large number of lattice models can be solved by iteration. Thus the interpolation scheme introduced above turns into an *iterative* perturbation scheme. In the remaining parts of this thesis we refer to our method as IPT (in contrast to *ordinary* IPT which means the naive extension of the classical IPT to finite doping).

The most popular example for a lattice model is perhaps the Hubbard Hamiltonian:

$$H = -\frac{t}{\sqrt{z}} \sum_{\langle ij \rangle, \sigma} c_{i\sigma}^{+} c_{j\sigma} \; + \; U \sum_i n_{i\uparrow} n_{i\downarrow} \tag{3.58}$$

$U = 4$, $V = 0.5$, increasing doping

	n_σ	p_1	p_2	p_3	p_4	w_1	w_2	w_3	w_4
$\epsilon_f = -2$									
pt	0.500	-2.532248	-0.2961787	0.2961787	2.532248	0.3259	0.1703	0.1703	0.3259
ed	0.500	-2.532248	-0.2961796	0.2961796	2.532248	0.3291	0.1709	0.1709	0.3291
$\epsilon_f = -1$									
pt	0.425	-1.715805	-0.2783394	0.4057437	3.588402	0.2517	0.1721	0.2725	0.2955
ed	0.426	-1.688301	-0.2740875	0.4000555	3.562333	0.2610	0.1655	0.2692	0.3044
$\epsilon_f = 0$									
pt	0.271	-1.446742	-0.2652427	0.7231318	4.988853	0.0700	0.2036	0.5544	0.1645
ed	0.277	-1.261557	-0.2615572	0.7000044	4.823110	0.0828	0.1943	0.5392	0.1837
$\epsilon_f = 1$									
pt	0.114	-2.004058	-0.1752505	1.353975	6.825336	0.0066	0.1119	0.8222	0.0520
ed	0.116	-1.590292	-0.1760779	1.333675	6.432694	0.0064	0.1096	0.8224	0.0616

Table 3.2: Perturbation scheme vs exact diagonalization for $U = 4$, $V = 0.5$, and increasing doping

$V = 0.5$, $\epsilon_f = 0$, increasing U

	n_σ	p_1	p_2	p_3	p_4	w_1	w_2	w_3	w_4
$U = 1$									
pt	0.352	-1.379343	-0.3549682	0.6486699	2.085642	0.0316	0.3216	0.5781	0.0634
ed	0.353	-1.354638	-0.3546377	0.6475309	2.061744	0.0290	0.3237	0.5854	0.0619
$U = 2$									
pt	0.305	-1.384460	-0.3035000	0.6915517	2.996410	0.0532	0.2530	0.5679	0.1199
ed	0.306	-1.301938	-0.3019377	0.6839038	2.919972	0.0562	0.2500	0.5658	0.1281
$U = 4$									
pt	0.271	-1.446742	-0.2652427	0.7231318	4.988853	0.0700	0.2036	0.5544	0.1645
ed	0.277	-1.261557	-0.2615572	0.7000044	4.823110	0.0828	0.1943	0.5392	0.1837
$U = 8$									
pt	0.250	-1.545173	-0.2416182	0.7482847	9.038507	0.0774	0.1749	0.5490	0.1901
ed	0.263	-1.236302	-0.2363018	0.7051730	8.767430	0.1016	0.1610	0.5210	0.2164

Table 3.3: Perturbation scheme vs exact diagonalization for large doping ($\epsilon_f = 0$), $V = 0.5$, and increasing U

$U = 4$, $\epsilon_f = 0$, increasing V

	n_σ	p_1	p_2	p_3	p_4	w_1	w_2	w_3	w_4
$V = 0.1$									
pt	0.234	-0.3344748	-4.4973146E-02	0.1545822	4.224951	0.0894	0.1646	0.5291	0.2066
ed	0.255	-0.2438551	-4.3855157E-02	0.1413567	4.146354	0.1151	0.1396	0.5087	0.2366
$V = 0.5$									
pt	0.271	-1.446742	-0.2652429	0.7231317	4.988853	0.0696	0.2036	0.5544	0.1645
ed	0.277	-1.261557	-0.2615572	0.7000044	4.823110	0.0828	0.1943	0.5392	0.1837
$V = 1$									
pt	0.304	-2.768941	-0.6070215	1.383075	5.992888	0.0514	0.2533	0.5700	0.1183
ed	0.306	-2.603875	-0.6038755	1.367808	5.839943	0.0562	0.2500	0.5658	0.1281
$V = 4$									
pt	0.404	-11.29466	-3.254666	4.782888	13.76644	0.0111	0.3884	0.5687	0.0194
ed	0.404	-11.25443	-3.254426	4.782290	13.72656	0.0112	0.3933	0.5758	0.0197

Table 3.4: Perturbation scheme vs exact diagonalization for large doping ($\epsilon_f = 0$), $U = 4$, and increasing V

which can actually serve as an effective Hamiltonian for the description of doped transition metal oxides [5]. On a Bethe lattice with infinite coordination number z the Hubbard model is connected to the impurity model by the following self consistency condition:

$$\Delta(\omega) = t^2 \, G(\omega) \tag{3.59}$$

and $\epsilon_f = -\mu$. The mapping requires that the propagator of the lattice problem is given by the impurity Green function ($G = G_f$). Below we set (as always) $D := 2t = 1$.

Starting with a guess for $\Delta(\omega)$ one can solve the impurity model using the scheme described above. This yields a propagator $G_f = G$, which can be used to determine a new hybridization function $\Delta(\omega)$ according to (3.59). The iteration is continued until convergence is attained. It is most accurate to perform the calculation first on the imaginary axis. Once the constants A and B in the interpolating self energy are determined in this way, they can be used to perform the iteration on the real axis.

In the case of the Hubbard model, the Luttinger theorem takes the simple form [42]

$$\mu_0 = \mu - \Sigma_{int}(\omega = 0), \quad \mu_0 := \mu|_{U=0} \tag{3.60}$$

This can be used to simplify the self consistency procedure if $\tilde{\mu}_0$ rather than μ is fixed. Starting with a guess for G and μ, one can compute G_0, n, and n_0. Afterwards (3.12) yields $\Sigma_{int}(\omega)$ and a new μ is obtained from (3.60).

To illustrate the accuracy of our method we compare it with results obtained using the exact diagonalization algorithm of Caffarel and Krauth [14]. On the imaginary axis, both methods are in close agreement as far as the imaginary part of the Green function is concerned (figure 3.2) . Only the real part displays a visible deviation at low frequencies (figure 3.3). This can be interpretated in the following way. It is known that IPT yields (at half filling) a critical U_c for the Mott transition which is about $0.5D$ higher than the result obtained with exact diagonalization [20, 24, 21]. For interactions which are not too far away from U_c this suggests that the IPT results correspond to an effective interaction which is somewhat smaller than the bare value U. Thus $U = 4$ in the exact diagonalization code should be compared to $U = 4.5$ in IPT. As displayed in figure 3.4, this yields a better agreement for the real part of $G(i\omega)$ at small frequencies,

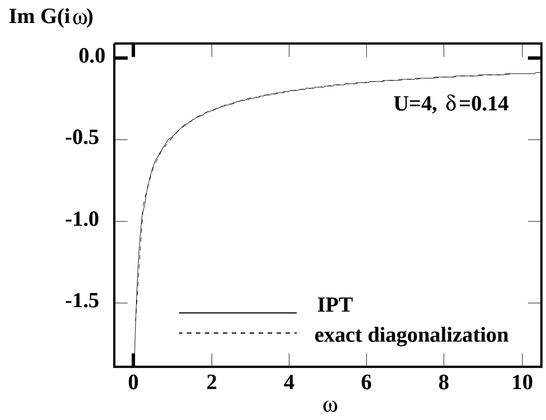

Figure 3.2: Im$G(i\omega)$ at $T = 0$ for $U = 4D$ and hole doping $\delta = 0.14$: iterative perturbation scheme (full line) vs. exact diagonalization (dashed line)

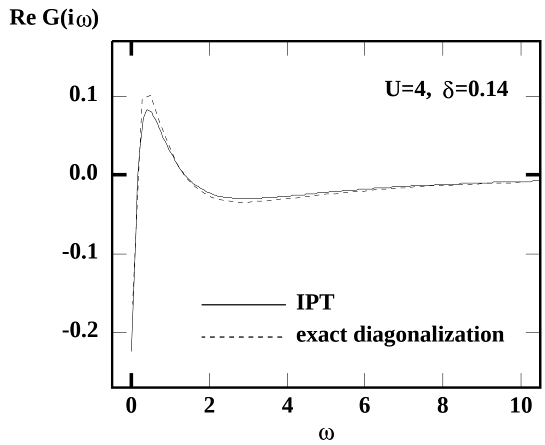

Figure 3.3: Re$G(i\omega)$ at $T = 0$ for $U = 4D$ and hole doping $\delta = 0.14$: iterative perturbation scheme (full line) vs. exact diagonalization (dashed line)

while the imaginary part changes only slightly.

The real advantage of our perturbation scheme compared to the exact diagonalization is disclosed when we display the spectral functions obtained by these two methods on the real axis (figure 3.5).

It is clear that the exact diagonalization is doing its best in producing the correct spectral distribution. But it is unable to give a smooth density of states. Instead several sharp structures occur as a consequence of treating only a finite number of orbitals in the Anderson model. Compared to the exact diagonalization the IPT scheme allows to compute many features of the Hubbard model with a much higher resolution. We will come back to this in chapter 4 where we study some selected applications to the

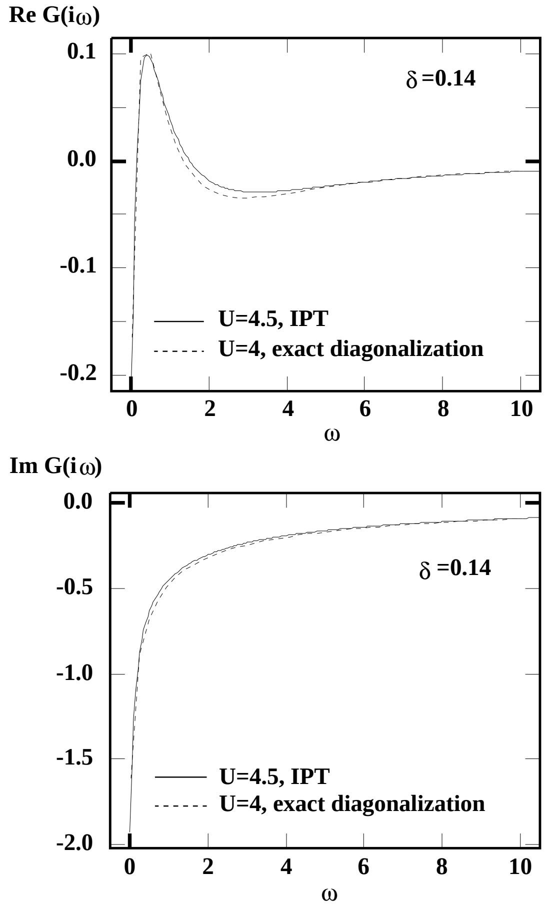

Figure 3.4: Comparison of $G(i\omega)$: IPT at $U = 4.5$ vs exact diagonalization at $U = 4$.

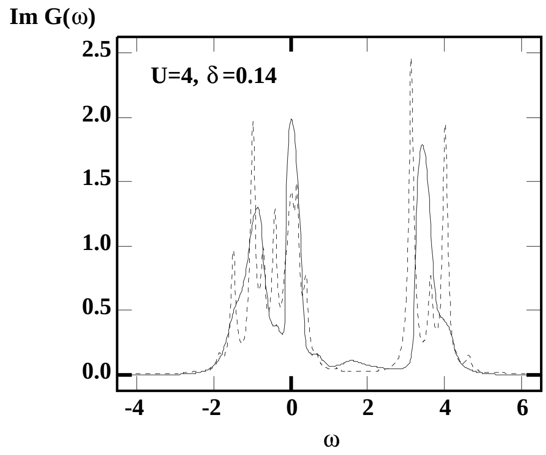

Figure 3.5: Im$G(\omega)$ at $T = 0$ for $U = 4D$ and hole doping $\delta = 0.14$: iterative perturbation scheme (full line) vs. exact diagonalization (dashed line).

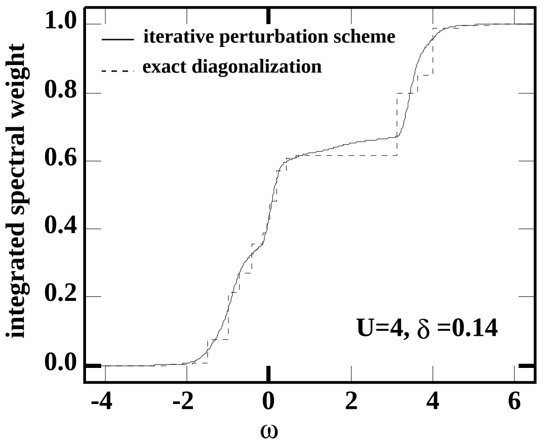

Figure 3.6: Integrated spectral weight $F(\omega) := \frac{1}{\pi}\int_{-\infty}^{\omega} d\tilde{\omega}\mathrm{Im}\,G(\tilde{\omega})$ for $U = 4D$ and hole doping $\delta = 0.14$: iterative perturbation scheme (full line) vs. exact diagonalization (dashed line).

Hubbard model at finite doping.

To obtain a quantitative comparison on the real axis we plotted in figure 3.6 the integrated spectral weight $F(\omega) := \frac{1}{\pi}\int_{-\infty}^{\omega} d\tilde{\omega}\mathrm{Im}\,G(\tilde{\omega})$ as obtained from both methods. It is seen that the spectral distribution agrees fairly well.

With regard to the shortfalls of the ordinary IPT scheme away from particle hole symmetry it is important to stress that our method gives positive compressibilities. As an example, the n vs μ curve is plotted in figure 3.7 for $U = 4$. At large doping the IPT-data (full line) are in close agreement with the exact diagonalization (dashed line), while at small doping IPT yields for given μ a slightly smaller particle number compared to exact diagonalization.[7] It should be noted that the direction of the deviation is consistent with the results obtained for the toy model in section 3.4. Also in that case our perturbation scheme shows a tendency to produce a slightly smaller particle number than the exact solution (see tables 3.2-3.4).

In the end we would like to point out that at finite doping the effective mass $m^\star$ remains finite for large U (see figure 3.8). This too is in agreement with results from exact diagonalization [5]. The doping dependence of $m^\star$ will be discussed in chapter 4.

[7] This deviation does not disappear if we compare the exact diagonalization data for $U = 4$ with the IPT data for $U = 4.5$.

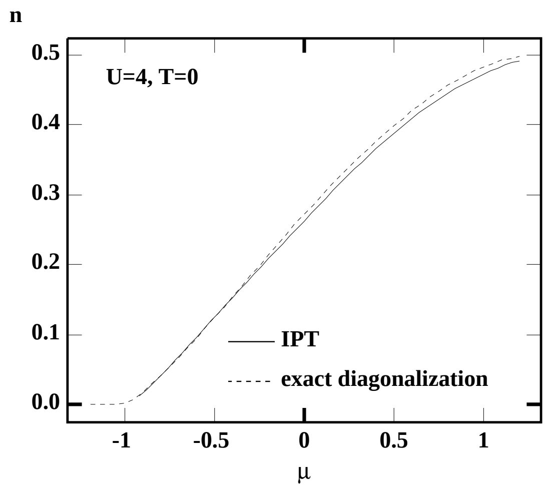

Figure 3.7: Particle density n versus chemical potential μ as obtained from IPT (full line) and exact diagonalization (dashed line).

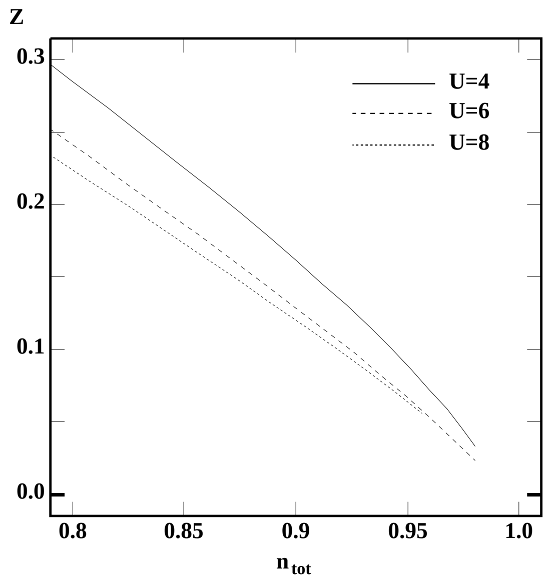

Figure 3.8: Quasiparticle residue $Z = \frac{m}{m^\star}$ for large U as a function of filling n_{tot}. The data were obtained from the imaginary axis with effective temperature $T_{eff} = 0.003$.

3.7 Discussion of the Mott transition and the insulator

So far we only dealt with the metallic problem. From other treatments of the Hubbard model we know however that the metallic solution breaks down at a critical value of the chemical potential (μ_c) provided U is large enough. One then observes a phase transition to a Mott insulator. In the following, we illustrate how this mechanism occurs in our perturbation scheme for $U = \infty$. We treat again the frustrated Hubbard model with self consistency condition $\Delta(\omega) = t^2\, G(\omega)$.

Let 2Γ be the width of the resonance peak. For frequencies which are larger than Γ but smaller than the the energy range of the Hubbard bands one can parameterize the Green function by

$$t^2\, G(\omega) = \frac{\Gamma \tilde{D}}{\omega + \epsilon\Gamma - i\Gamma} + c_0 + c_1\, \omega + O(\omega^2) \tag{3.61}$$

The shift $\epsilon\Gamma$ of the resonance peak and the parameter $\tilde{D}$ have to be determined from the Luttinger theorem, i. e $G(0) = \frac{2}{D^2}\left(iD + \mu_0(n) + O(\mu_0(n)^2)\right)$. Here, $\mu_0(n)$ is the chemical potential of the noninteracting system at given particle number n. For small doping one has $|\mu_0(n)| << D$. We obtain in this way

$$\epsilon = \frac{1}{D}\left(\mu_0(n) - 2c_0\right) \tag{3.62}$$

and

$$\tilde{D} = \frac{1}{2D}\left(1 + \epsilon^2\right) \tag{3.63}$$

A rough estimate for $c_0 = \mathrm{Re}\Delta(0)$ and c_1 can be obtained from the atomic limit:

$$c_0 \approx \frac{t^2}{\mu}\,(1-n) \approx \frac{t^2}{2\mu} \tag{3.64}$$

and

$$c_1 \approx -\frac{t^2}{\mu^2}\,(1-n) \approx -\frac{t^2}{2\mu^2} \tag{3.65}$$

As the Mott transition is approached the difference $\tilde{\mu}_0 - c_0$ decays linearly in Γ:

$$\tilde{\mu}_0 - c_0 \simeq \alpha\,\Gamma \tag{3.66}$$

where α depends on μ_c. For the propagator G_0 we get from (3.61)

$$G_0^{-1}(\omega) = \omega(1 - c_1) + \tilde{\mu}_0 - c_0 - \frac{\Gamma \tilde{D}}{\omega + \epsilon\Gamma - i\Gamma} + O(\omega^2) \tag{3.67}$$

For small Γ the corresponding "density of states" $\rho_0(\omega) = \frac{1}{\pi} G_0(\omega)$ is peaked around two poles at

$$\omega_p = -\bar{\omega} \pm \Delta\omega \tag{3.68}$$

where

$$\bar{\omega} := \frac{\tilde{\alpha}}{2(1-c_1)}\Gamma \tag{3.69}$$

with $\tilde{\alpha} := \epsilon(1-c_1) - \alpha$ and

$$\Delta\omega := \sqrt{\frac{\Gamma\tilde{D}}{1-c_1}} \tag{3.70}$$

The corresponding weight is $\frac{1}{2(1-c_1)}$. Now, evaluating $\tilde{\Sigma}_0^{(2)}(\omega)$ yields

$$\tilde{\Sigma}_0^{(2)}(\omega) = U^2\, S_0\, \left(1 - \frac{\omega}{\bar{\omega}}\right) + O(\omega^2) \tag{3.71}$$

where $S_0 := \frac{-\tilde{\alpha}}{72(1-c_1)^3\tilde{D}}$. For the interpolating self energy (3.41) this implies

$$\Sigma_{int}(\omega) = \frac{n}{1-n}\left(-\mu + \tilde{\mu}_0 - \frac{n_0(1-n_0)}{S_0}\left(1 + \frac{\omega}{\bar{\omega}} + O(\omega^2)\right)\right) + O(\omega^2) \tag{3.72}$$

The parameter $\tilde{\alpha}$ (or S_0 respectively) is fixed by the Luttinger theorem $-\Sigma_{int}(\omega+0) + \mu = \mu_0(n) \approx 0$ for $n \approx \frac{1}{2}$. Using $n_0 \approx \frac{1}{2}$ near half filling, we obtain

$$\tilde{\alpha} \approx \frac{18(1-c_1)^3\,\tilde{D}}{2\mu - \frac{t^2}{2\mu}} \tag{3.73}$$

Substituting into (3.72) gives for the interpolating self energy

$$\Sigma_{int}(\omega) = \mu - \frac{A}{\Gamma}\omega + O(\omega^2) \tag{3.74}$$

where

$$A \approx -\frac{8}{9}\frac{\mu\left(1 - \frac{t^2}{4\mu^2}\right)}{\left(1 + \frac{t^2}{2\mu^2}\right)^2\left(1 + \left(\frac{t^2}{\mu D}\right)^2\right)} \approx -\frac{8}{9}\mu\,\left(1 - \frac{13}{32}\frac{D^2}{\mu^2}\right) \tag{3.75}$$

The last approximation is valid for $\mu \geq D$ (as expected near half filling). The expression (3.74) has to be compared with the relation optained by substituting G and G_0 according to (3.61) and (3.67) into $\Sigma_{int}(\omega) = G_0^{-1}(\omega) - G^{-1}(\omega) + \mu - \tilde{\mu}_0$:

$$\Sigma_{int}(\omega) = \mu + \left(B + \frac{C}{\Gamma}\right)\omega + O(\omega^2) \tag{3.76}$$

where

$$\begin{aligned} B &= 1 - 2c_1 \\ C &= -D\left(1 - \frac{2\epsilon^2}{1+\epsilon^2} - \frac{2\epsilon}{1+\epsilon^2}\,\frac{\mu_0(n)}{D}\right) \end{aligned} \tag{3.77}$$

Equating the coefficients of the terms linear in ω in (3.74) and (3.76), we obtain

$$\Gamma = \frac{A - C}{B} \tag{3.78}$$

The critical chemical potential at which the metallic solution disappears follows from $A = C$, the numerical evalution of which yields $\mu_c \approx 1.35D$. For $\mu < \mu_c$, there is a metallic solution (i. e. $\Gamma > 0$). Above μ_c, in contrast, no such solution exists. Near μ_c, B and C vary only slightly as a function of the chemical potential, so that the broadening of the resonance with decreasing μ is mainly determined by the μ dependence of A which in turn is fixed by the Luttinger theorem. At this point the important role of the Luttinger theorem for describing the Mott transition becomes apparent.

When treating the Mott insulator (at arbitrary U) one cannot use the Luttinger theorem and the Friedel sum rule respectively since these theorems do not hold for a doublet groundstate. From relation (3.65) which is valid for all U we learn how to fix the parameter $\tilde{\mu}_0$ instead:

$$\tilde{\mu}_0 = \mathrm{Re}\Delta(\omega = 0) \tag{3.79}$$

This choice for $\tilde{\mu}_0$ implies that the propagator $G_0 = \frac{1}{\omega+\mu-\Delta(\omega)}$ has a pole at zero frequency allowing for a degenerate groundstate.

The exact solution for the Mott insulator depends on ω and μ only via the sum $\omega + \mu$:

$$G(\omega, \mu) = G(\omega + \mu) \tag{3.80}$$

This means that the solution is simply shifted as the chemical potential is varied. In particular, the particle number is constant as a function of μ. In figure 3.9, we show the numerical solution for the Mott insulator at $U = 4$ (Hubbard model) for the particle hole symmetric case ($\mu = 2$) and away from particle hole symmetry ($\mu = 1.5$). Obviously, our approach does not satisfy relation (3.80). However, the scheme tries to shift the

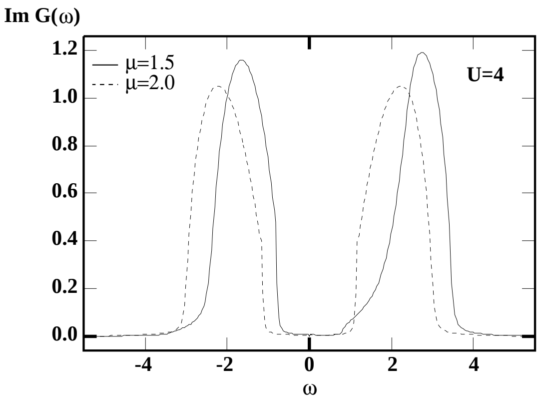

Figure 3.9: Spectral function of the Mott insulator for $U = 4$ at and away from particle hole symmetry.

bands as much as possible so that it comes close to the exact solution. In addition, we obtain the correct total particle density $n_{tot} = 1$ independent of μ.

Finally, let us summarize how the impurity in an insulating bath $\Delta(\omega)$ must be treated by our scheme. In general one has to proceed as follows: First, it is checked whether there are solutions for a singlet groundstate by fixing $\tilde{\mu}_0$ by the Friedel sum rule. Afterwards, one looks for triplets using relation (3.79). It might happen that there are more than one solution. In this case the one which is lowest in energy has to be chosen.

3.8 Conclusions

In this chapter we introduced a new interpolating perturbation scheme for impurity and lattice models at arbitrary filling. The basic idea is to construct an expression for the self energy which interpolates between correct limits, namely the weak coupling and the atomic as well as the small and high frequency limits. The proper low frequency behavior is ensured by the Friedel sum rule (or, equivalently, the Luttinger theorem). This is important to obtain the right low energy features in the spectral density. The overall distribution of the density of states on the other hand is determined by the spectral moments, which are reproduced exactly up to second order by satisfying the proper large frequency behavior. In the light of these features it might not be too astonishing that our method yields reasonable results. The comparison with an exactly solvable model displays an excellent agreement at half filling and the small U and large V limits. Away from particle hole symmetry the agreement is still reasonable with the tendency to become worse for large U and small V. These findings can be understood by the behavior of the scheme in different limits. In the weak coupling case the perturbation scheme is exact to order U^2, while in the atomic limit the scheme is at finite doping only exact to zeroth order in V. However, it is exact to order V^2 at half filling where it reduces to the ordinary IPT. For $U \to \infty$ the self energy remains finite and the scheme yields a diverging effective mass for small doping so that the basic features of the impurity model are also captured in this limit.

We illustrated the solution of the lattice problem for the case of the Hubbard model. On the imaginary axis there is a good agreement with the exact diagonalization data as far as the imaginary part of the Green function ($\mathrm{Im}G(i\omega)$) is concerned. But the corresponding real part (i.e. $\mathrm{Re}G(i\omega)$) turns out to be somewhat more susceptible and shows visible deviations to the exact diagonalization data for the same U. This can be explained if the difference in the critical U_c is taken into account. Unlike the ordinary IPT scheme our approach does not suffer from negative compressibilities.

We explained in detail how the Mott transition as a function of U appears in the perturbation scheme for $U = \infty$.

When treating an impurity model in an insulating hybridization function $\Delta(\omega)$ one has to distinguish between the singlet and the triplet groundstate. In the former case the Luttinger theorem (and the Friedel sum rule respectively) is valid and used to fix $\tilde{\mu}_0$. However the degenerate triplet groundstate requires putting the pole of $G_0(\omega)$ at zero frequency which is achieved by choosing $\tilde{\mu}_0 = \mathrm{Re}\Delta(0)$.

For a Mott insulator the exact solution is simply shifted as the chemical potential is varied. This symmetry property is not described correctly by our scheme. Nevertheless, the approximate solutions try to imitate the band shifting.

The practical relevance of our method concerns mainly the large d limit. In appendix C some thoughts on finite dimensions can be found.

An advantage of the IPT compared to the exact diagonalization is that on the real axis it provides continuous curves instead of a finite number of poles. This allows to obtain many results with a much higher resolution. Moreover, the relatively low numerical effort which is necessary to perform the iteration allows the application to more complicated problems. Some examples will be treated in the following chapters.

Chapter 4

Some Selected Applications to the Frustrated Hubbard Model

4.1 Introduction

The Hubbard model [9, 10, 11, 12] plays an important role in the investigation of correlated fermion systems. In contrast to real materials, which contain several bands, the Hubbard Hamiltonian is restricted to the single band case. However, it is believed that it might serve as an effective Hamiltonian able to describe more complicated systems like $La_xSr_{1-x}TiO_3$ at least qualitatively [5]. For this purpose the effects of orbital degeneracy have to be taken into account. It is shown in appendix B that the multiband problem is rather frustrated. Therefore, the single band model has to be considered on a frustrated lattice in order to yield a reasonable description of realistic systems.

In this section we will thus treat the fully frustrated Hubbard model. Although there are several results available, which were obtained from Monte Carlo calculations [7, 8, 27] and exact diagonalization [14], we find it useful to apply our perturbation scheme to this case. With little numerical effort we obtain zero temperature results which are not accessible by Monte Carlo and have a *much* higher resolution than those obtained by exact diagonlization. The comparison allows a further check of our method.

The iterative procedure for the solution of the lattice problem has already been described in section 3.6. We do not have to repeat it here but merely present some results obtained from the perturbation scheme. Section 4.2 discusses the spectral functions and the optical conductivity. Like almost always in this thesis the calculations are done for the Bethe lattice. More realistic lattices are discussed in section 4.3.

4.2 Results for the frustrated Hubbard model (Bethe lattice)

Figures 4.1 and 4.2 show the evolution of the spectral density with increasing hole doping δ for the doped metal ($U = 2$) and the doped Mott insulator ($U = 4$). The qualitative features are those expected from the spectra of the single impurity [14] and are in agreement with the quantum Monte Carlo calculations [17]. For small doping, there is a clear resonance peak at the Fermi level. As δ is increased, the peak broadens and is shifted through the lower Hubbard band. At the same time the weight of the upper band decreases.

In the doped Mott insulator (figure 4.2) the position of the resonance as a function of doping can be related to the different physical regimes of the corresponding Anderson impurity model [70, 21, 5] . For small doping the lattice sites are predominantly single occupied. There are virtually no charge fluctuations and the system is in the *local moment regime* dominated by quantum fluctuations between the $|\uparrow>$ and the $|\downarrow>$ states. In this case the resonance is well separated from the lower Hubbard band.

With increasing doping charge fluctuations between single occupied and empty states become important *(mixed valence regime)*. The resonance merges into the lower Hubbard band.

Once the particle density gets so small that the lattice sites are predominantly empty, the *empty orbital regime* is reached. At this point the characteristic resonance peak looses its identity and the spectral function resembles that of the noninteracting system.

The most striking feature of the evolution of the density of states as a function of doping is the finite shift of the Kondo resonance from the insulating band edge as the doping goes to zero. It was demonstrated analytically that this is a genuine property of the exact solution of the Hubbard model in infinite dimensions using the projective self consistent method [18] and is one of the most striking properties of the Hubbard model in large dimensions. This feature did not appear in the earlier studies of the Hubbard model in large dimensions using Monte Carlo techniques [17] at higher temperatures, and is also not easily seen in exact diagonalization algorithms [21].

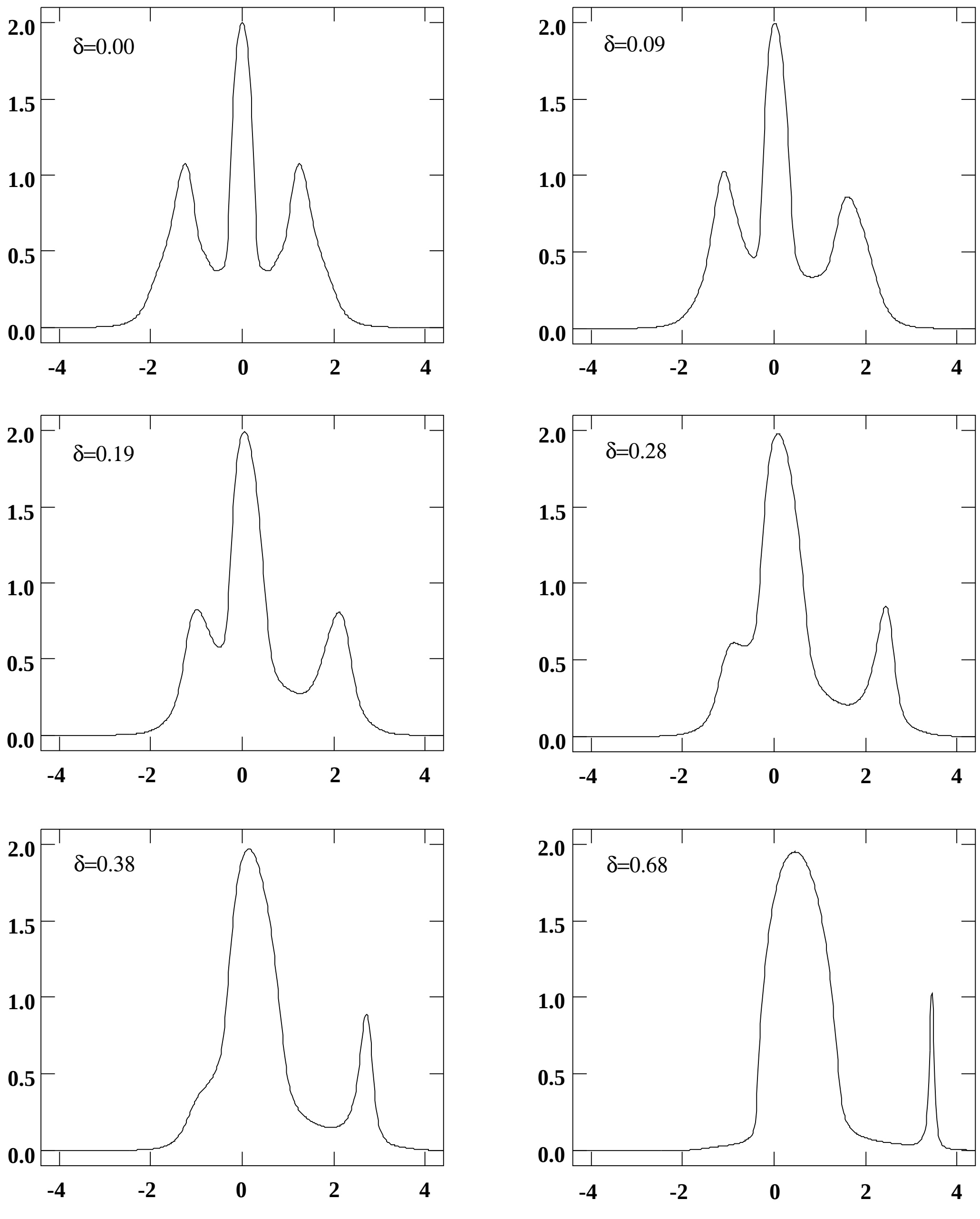

Figure 4.1: Evolution of the spectral function for $U = 2$ and $T = 0$ with increasing hole doping δ

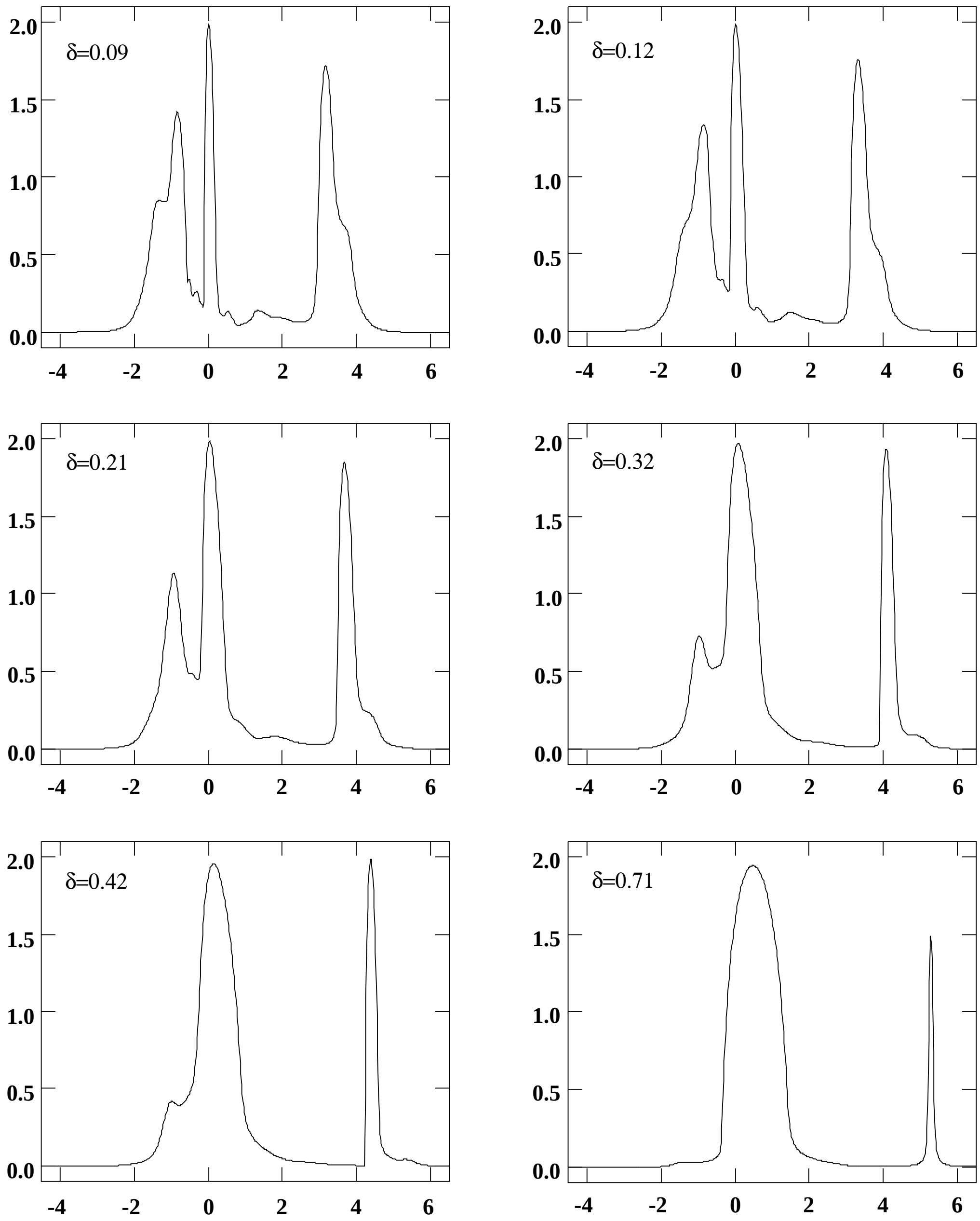

Figure 4.2: Evolution of the spectral function for $U = 4$ and $T = 0$ with increasing hole doping δ

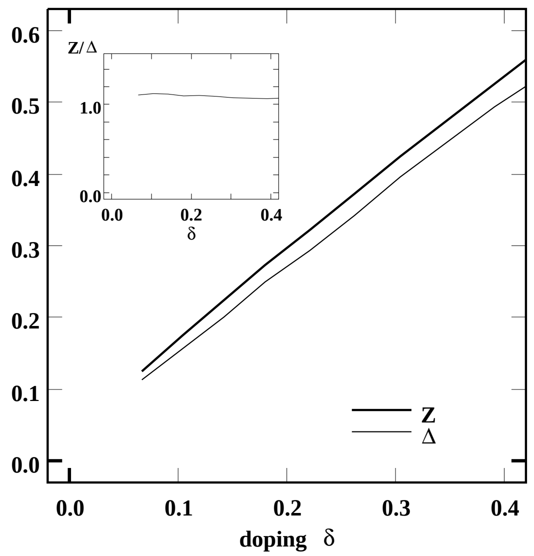

Figure 4.3: Comparison between the quasiparticle residue Z and the width of the resonance peak 2Δ ($U = 4$, $D = 1$)

In the case of the doped Mott insulator, the width 2Δ of the resonance peak is approximately given by twice the quasiparticle residue $Z = 1/(1 - \frac{\partial \Sigma'(\omega)}{\partial \omega}|_{\omega=0})$: $Z \approx \frac{\Delta}{D}$ (see figure 4.3). As the doping is reduced, Z scales to zero, which implies a divergence of the effective mass ($Z = \frac{m}{m^\star}$), so that the renormalized Fermi energy $\epsilon_f = ZD$ vanishes.

In infinite dimensions, the optical conductivity can be calculated from the single particle Green function by a simple convolution [66]:

$$\sigma(\omega) = \sigma_o \frac{D^2}{\omega} \int_{-\infty}^{+\infty} d\epsilon\, \rho_o(\epsilon) \int_{-\infty}^{+\infty} \frac{d\omega'}{2\pi} A_\epsilon(\omega')\, A_\epsilon(\omega' + \omega)(n_f(\omega') - n_f(\omega' + \omega)) \;, \quad (4.1)$$

where $\sigma_o = \frac{e^2 a^2}{4\nu\hbar}$ and $A_{\epsilon_k}(\omega) = -2\,\mathrm{Im}\, G_k(\omega) = -2\,\mathrm{Im} \frac{1}{\omega + \mu - \epsilon_k - \Sigma_{int}(\omega)}$. The result for $U = 4$ and $\delta = 0.07$ is plotted in figure 4.4. Apart from the Drude peak at zero frequency, the conductivity displays several features which are related to the structures of the spectral function (see inset of figure 4.4). There is a peak (P_1) at $\omega \approx 0.8$ which

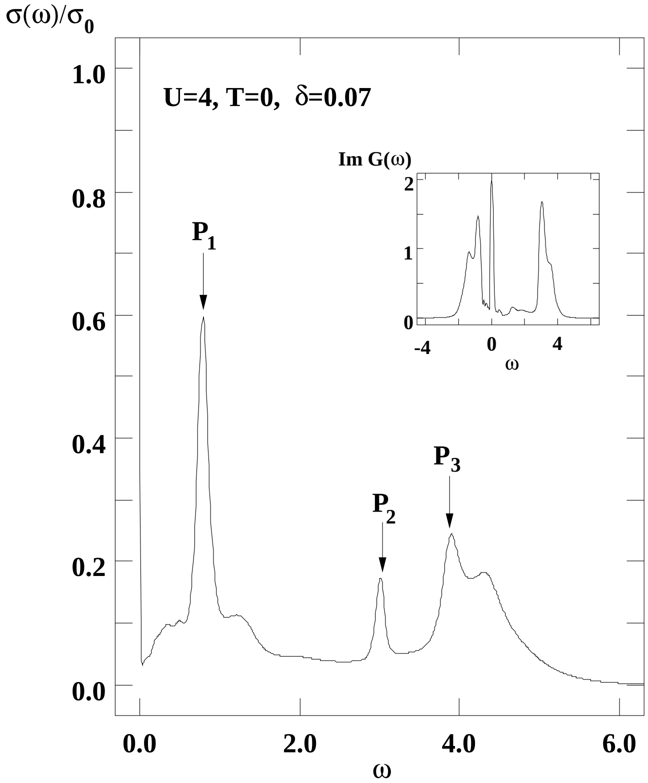

Figure 4.4: Optical conductivity for $U = 4$, $T = 0$ and $\delta = 0.07$. Inset: corresponding spectral function

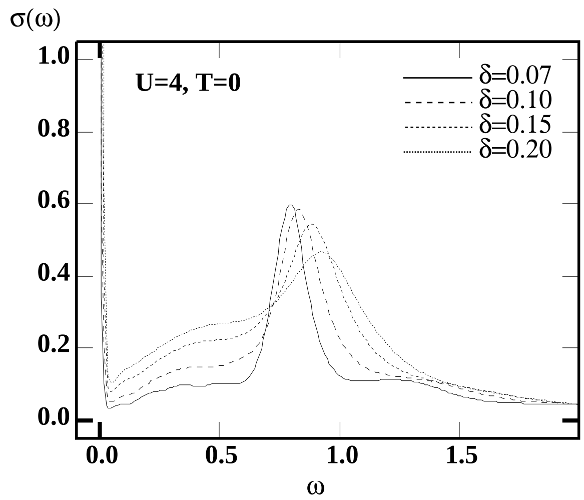

Figure 4.5: Small frequency behavior of the optical conductivity for $U = 4$, $T = 0$ and different dopings δ.

corresponds to transitions between the lower Hubbard band and the resonance peak. In analogy, $\sigma(\omega)$ has a maximum (P_2) at $U \approx 3.2$ resulting from excitations between the resonance peak and the upper Hubbard band. Finally, there is a broad feature (P_3) around $U = 4$ which is related to transitions between the lower and the upper Hubbard band. P_1 as well as P_3 have a small side maximum which is caused by the second peak in the lower Hubbard band of the spectral function.

In comparison with Monte Carlo studies [69], which are done at finite temperature, our zero temperature calculation displays much sharper structures in the optical conductivity. In particular, the maxima P_1 and P_2 which are related to the resonance peak are much more pronounced at $T = 0$. However, we expect a strong temperature dependence of these peaks (see section 7.3).

In figure 4.5 we compare the small frequency behavior of $\sigma(\omega)$ for different dopings δ. Since the resonance peak in the density of states broadens with increasing δ, we observe the same behavior for the corresponding maximum in $\sigma(\omega)$. Moreover, it should be realized that near $\omega = 0$ the optical conductivity decreases considerably as $\delta \to 0$. This is due to the divergence of the effective electron mass in this limit. Such a behavior of $\sigma(\omega)$ has actually been measured (at finite temperature) in systems like $La_xSr_{1-x}TiO_3$ [76].

4.3 Realistic lattices

So far, all calculations were done for the Bethe lattice. In this case G and G_0 are related by a simple condition ($G_0(\omega) = 1/(\omega + \tilde{\mu}_0 - t^2 G(\omega))$), which simplifies the numerical implementation.

With respect to real physics, it is important to consider a bare lattice density of states (DOS) which displays the basic features of *finite* dimensional lattices. In this context, the Bethe lattice has the advantage of having a bounded (bare) DOS in contrast to, for example, the hyper cubic lattice. In two dimensions, however, van Hove singularities play an important role. The presence of such sharp features can actually be used to explain several features of the normal state of high T_c superconductors (see e. g. [67, 68] and references therein).

In this section, we show how more realistic lattices can be treated within our approach. As an example, we choose as bare lattice DOS

$$\rho_{0,log}(\epsilon) = \frac{1}{4}\left(1 - \log\frac{|\epsilon|}{D}\right) \quad , \tag{4.2}$$

which is similar to that of a two dimensional square lattice and has a logarithmic singularity at $\epsilon = 0$ (see thin curve in figure 4.6). For comparison, calculations are also done for a constant DOS:

$$\rho_{0,const} = \begin{cases} \frac{1}{2D} & \text{if } |\epsilon| \leq D \\ 0 & \text{if } |\epsilon| > D \end{cases} \tag{4.3}$$

In the general case, the numerical algorithm has to be slightly modified. For fixed $\tilde{\mu}_0$ we proceed as follows: Starting with a guess for the interpolating self energy Σ_{int} and the particle density n, we determine μ from the Luttinger theorem

$$\mu = \mu_0(n) + \Sigma_{int}(\omega = 0) \quad . \tag{4.4}$$

where $\mu_0(n) = \mu(n)|_{U=0}$. Then the full Green function G is given by a Hilbert transform:

$$\begin{aligned} G(\omega) &= \int_{-\infty}^{+\infty} \frac{\rho_0(\epsilon)}{\omega - i\eta + \mu - \epsilon - \Sigma_{int}(\omega)}\, d\epsilon \\ &= \Phi(\omega - i\eta + \mu - U\,n - \tilde{\Sigma}^{(2)}(\omega)) \end{aligned} \tag{4.5}$$

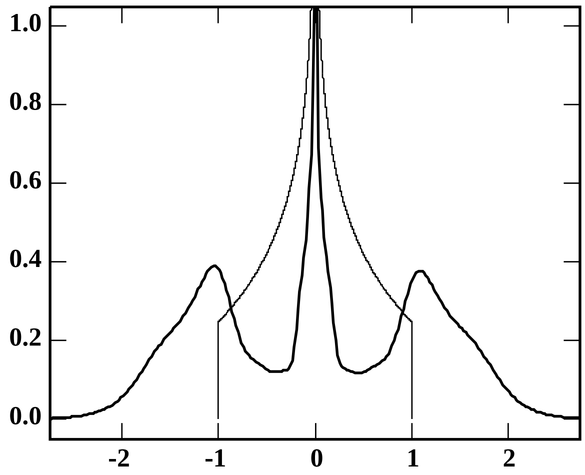

Figure 4.6: Correlation effects on the DOS: interacting electrons for $U = 2$ and $\delta = 0.01$ (thick line) versus logarithmic bare lattice DOS (thin line)

The Green function G can be used to obtain a new value for the particle density ($n = \frac{1}{\pi}\int_{-\infty}^{+\infty} d\omega \mathrm{Im} G(\omega)$). Then the bare Green function G_0 follows from

$$G_0^{-1}(\omega) = G^{-1}(\omega) - \mu + \tilde{\mu}_0 + \Sigma_{int}(\omega) \tag{4.6}$$

Now, n_0 is determined by G_0 and a new interpolating self energy $\Sigma int(\omega)$ can be obtained from (3.12). Afterwards one returns to (4.4) and iterates these steps. From a practical point of view, it is useful to tabulate and spline the Hilbert transform needed in (4.5).

In figure 4.6, we compare the DOS of interacting electrons near half filling with the bare lattice DOS. We see that the van Hove singularity becomes considerably sharper due to correlations. The spectral functions for various dopings (figures 4.7 and 4.8) are similar to those obtained for the Bethe lattice. The main difference occurs in the shape of the coherence peak, which is much sharper due to the van Hove singularity. From the pinning of the density of states at zero frequency we actually know that at half filling the singularity survives in the presence of correlations.

For comparison, figures 4.9 and 4.10 contain results obtained for the constant lattice DOS (4.3). Here again, the resonance peak displays a shape which is characteristic for the underlying lattice. Obviously, an arbitrary lattice can be treated in this way by inserting the appropriate ρ_0 in (4.5).

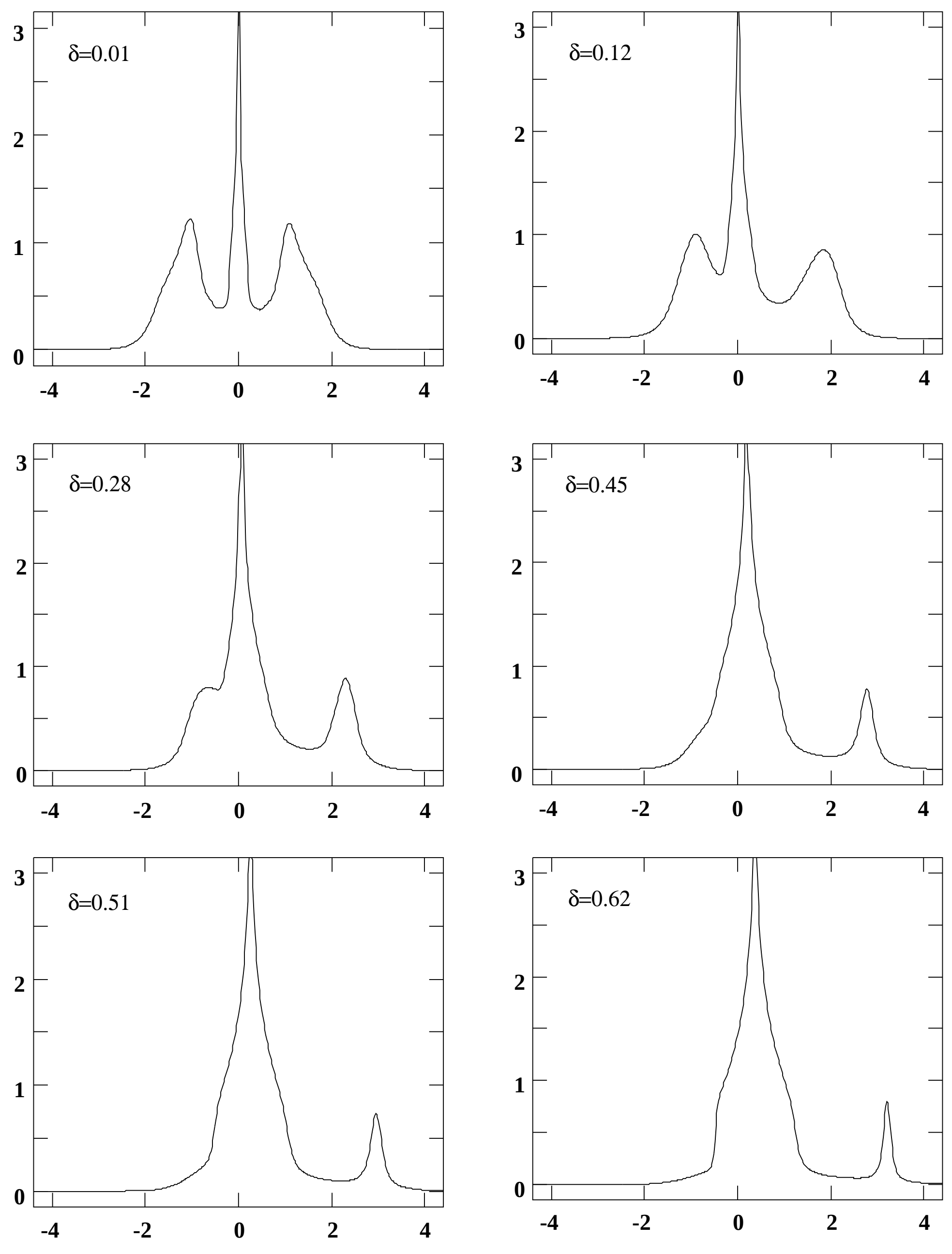

Figure 4.7: Development of the spectral function with increasing doping for a logarithmic lattice DOS ($U = 2$).

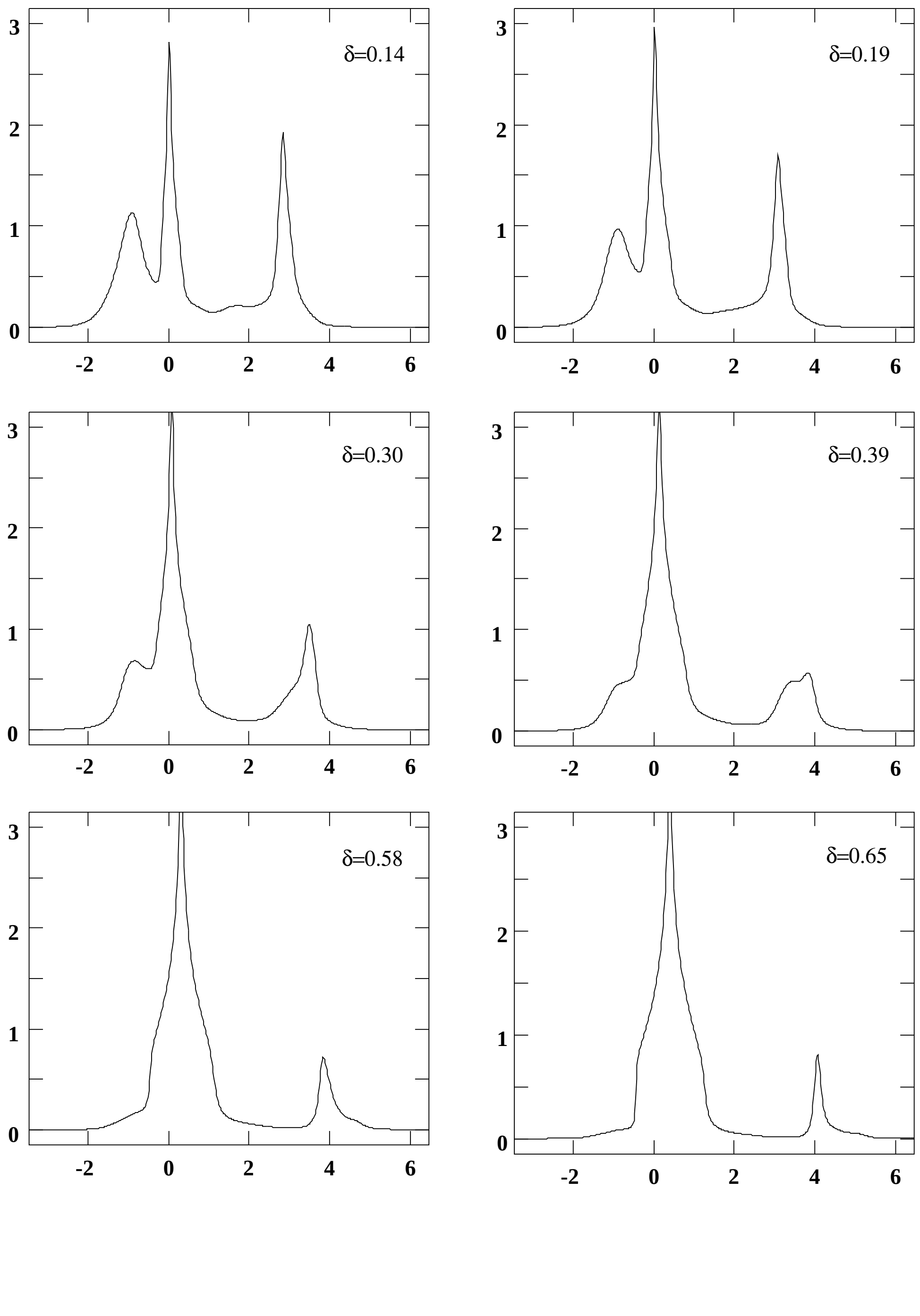

Figure 4.8: Development of the spectral function with increasing doping for a logarithmic lattice DOS ($U = 3$).

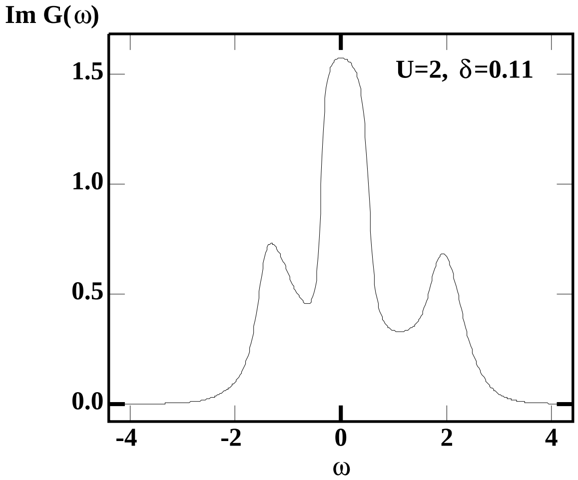

Figure 4.9: Spectral function ($U = 2$ and $\delta = 0.11$) for the case of a constant lattice DOS.

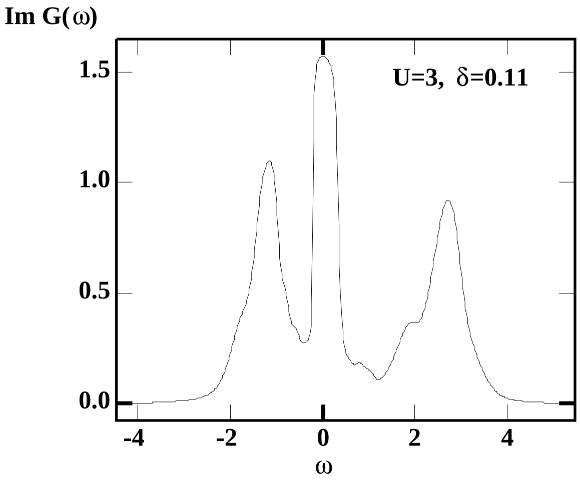

Figure 4.10: Spectral function ($U = 3$ and $\delta = 0.11$) for the case of a constant lattice DOS.

4.4 Conclusions

Our perturbation scheme provides an efficient algorithm for solving the (frustrated) Hubbard model in infinite dimensions. The results for the doped Mott insulator display all characteristic features which are known from other methods. Furthermore, the spectral functions can be obtained with a much higher resolution compared to exact diagonalization. These findings confirm that our perturbation scheme is not only numerically efficient but also reliable.

A first step towards a more realistic description of real systems can be done by introducing an appropriate lattice density of states $\rho_0(\epsilon)$ into the self consistent set of equations. Another step, namely the inclusion of orbital degeneracy, will be addressed in chapter 6.

Chapter 5

Spectral Functions in Doped Transition Metal Oxides

5.1 Introduction

Following the discovery of high T_c oxides [1], there has been a resurgence of interest in the electronic structure of doped transition metal oxides. Recent investigations have revealed some very unusual physics in these systems [28, 32, 52, 53]. $La_xSr_{1-x}TiO_3$ [28] is a system containing d electrons where the carrier concentration can be varied in a controlled fashion. At one end, $LaTiO_3$ is a Mott-Hubbard insulator with a d^1 configuration, while at the other end of the solid solution, $SrTiO_3$ is a band insulator with a d^0 configuration. Thus, varying x tunes the electron configuration continuously between 1 and 0. For large values of x, the transport and magnetic properties [28] as well as the experimentally observed spectral weights behave as a correlated doped Mott insulator. For small values of x (≈ 0), the system represents a small amount of electron doping in a d^0 configuration, and thus, it should behave as a *doped band insulator* and is expected to show little correlation effects. This expectation is also consistent with transport and magnetic properties of such compounds [28, 54] which exhibit an essentially free-electron like behavior.

Interestingly however, ultra-violet photoemission spectra (UPS) of $La_xSr_{1-x}TiO_3$ with small x ($= 0.1$ and 0.2) exhibit two features: a coherent low energy feature and a very prominent incoherent feature which is in fact found to be *more intense* than the coherent feature [53]. The observation of a large fraction of incoherent to coherent spectral weight suggests the presence of very strong correlation effects, in contrast to transport and magnetic properties, as well as to the theoretical expectations of an uncorrelated behavior close to the d^0 configuration. Coherent features at low energies and incoherent features at around 1.4 eV are also seen in systems with one d electron per unit cell [52]. The evolution of the redistribution of spectral weight as a function of interaction strength in the half filled system can be accounted for by zero temperature large d calculations based on the Hubbard model [8, 26]. The doping dependence of these features, however, have not been accounted within this framework.

In order to clarify these important issues, the electronic structure of lightly doped d^0 systems should be reinvestigated both experimentally and theoretically. In this context Sarma and Barman [51] supplemented the already existing UPS of $La_xSr_{1-x}TiO_3$ with those of $SrTiO_{3-\delta}$, where the oxygen deficiency δ introduces electrons into the stoichiometric d^0 system. They also carried out inverse photoemission experiments in these systems. Since it is expected that the strength of the incoherent features is more visible in the unoccupied part of the spectrum of systems which have a small number of d electrons, this technique is ideal for settling the importance of correlations here. The experimental results conclusively establish that the observed spectral function is inconsistent with the *homogeneous* Hubbard model which is normally used in the interpretation of this kind of experiments. We present a new theoretical treatment of inhomogeneity (arising from disorder in the real system) within a Hubbard-like model to establish qualitatively new descriptions for the evolution of spectral functions in real systems which is in very good agreement with the experimental results. Whereas a very large number of substituted compounds have been investigated in the past, the role of disorder has almost always been neglected. Thus, our findings have important implications for a very large number of compounds that have been vigorously investigated in recent times.

5.2 Experimental results

In this section, we quote the experimental results obtained by Sarma and Barman [51].

Figure 5.1 displays the experimental He I UPS of $SrTiO_{3-\delta}$ for δ = 0.0, 0.08 and 0.28 near the Fermi energy (E_F) region. The inset shows a typical spectrum over a wider energy range, being very similar for all the compositions with the intense doublet feature at about 7 eV binding energy arising from primarily oxygen $2p$ derived states.

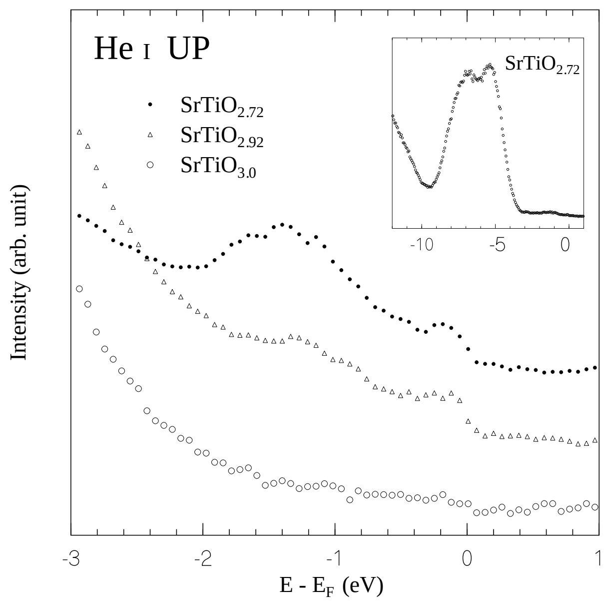

Figure 5.1: He I photoemission of $SrTiO_{3-\delta}$ for three values of δ.

The overall spectral shape of $SrTiO_3$ is reasonably well described by band calculations [55]. Expectedly, the wide band gap material, $SrTiO_3$ shows no intensity at E_F. On introducing oxygen vacancies ($\delta > 0$), thereby doping electrons in the system, it is clear that two spectral features emerge in the near E_F region, one appearing at E_F and another at a higher binding energy of about 1.3 eV, in striking similarity to those of $La_xSr_{1-x}TiO_3$ [53]. While the feature at E_F is due to electron doping and the consequent movement of the Fermi energy into the conduction band as confirmed by band structure results on $SrTiO_{3-\delta}$, the calculations do not have any counterpart of the experimentally observed 1.3 eV feature (see later in the text). Furthermore, this higher binding energy feature in figure 5.1 (and also in $La_xSr_{1-x}TiO_3$ [53]) is similar in shape and energy position to the incoherent feature observed in $LaTiO_3$ [52] which is an end member of the solid solution $La_xSr_{1-x}TiO_3$. These observations along with the absence of this feature in single-particle calculations, would strongly suggest correlation effects being responsible for the origin of this peak in these lightly doped electron systems.

In figure 5.2 we show the Bremsstrahlung isochromat (BI) spectra of $SrTiO_3$ and $SrTiO_{2.72}$ compared to the theoretically calculated BI spectrum of $SrTiO_3$ obtained from band structure calculations and calculated matrix elements [56]. The calculated

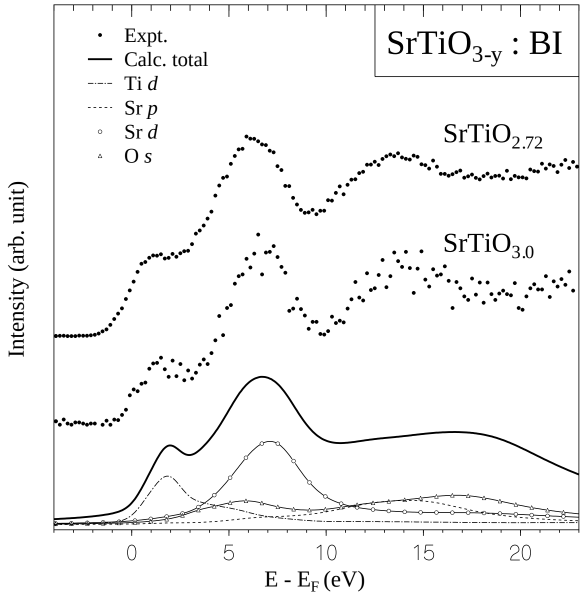

Figure 5.2: Bremsstrahlung isochromat spectra of $SrTiO_3$ and $SrTiO_{2.72}$.

spectrum provides a good description of the experimentally observed one for $SrTiO_3$ within the first 10 eV of E_F; the mismatch at higher energies arises from the well-known limitation of linearized band structure methods. This agreement is consistent with the fact that $SrTiO_3$ with a d^0 configuration is primarily a band insulator with correlation effects playing no major role. However it is interesting to note that the BI spectrum of $SrTiO_{2.72}$ is almost identical to that of $SrTiO_3$, except for a small shift ($\approx$ 0.5 eV) of the peaks and some overall broadening of the spectral features. The shift is consistent with the electron doping of the system and thus, is explainable within a rigid shift of E_F with respect to the one-electron results for $SrTiO_3$ with no perceptible signature of any correlation induced features in contrast to the occupied spectral features (figure 5.1). One, however, cannot rule out the presence of weak intensity features corresponding to the upper Hubbard band which may be considerably broadened if it coexists in the region of 4-9 eV with extended O and Sr states which have a much larger intensity.

The above results of the presence of correlation induced feature in the occupied parts and a simultaneous absence of any such feature in the unoccupied parts, are very surprising in view of the small occupancy of the *d* band. It is well known that for few electrons in the band (such as Ce [57] and U [58] containing systems) correlation induced features appear most prominently in the unoccupied spectral function, whereas in Ni based systems with few holes in the band the correlation effects are prominent only in the occupied parts. Sarma and Barman [51] demonstrated explicitly that the evolution of photoemission and inverse photoemission spectra as a function of doping cannot be accounted by a homogeneous one band or multiband model by incorporating self-energy corrections to the calculated Ti d density of states (DOS) in $SrTiO_{3-\delta}$ (δ = 0.125) within a second order perturbative treatment of correlation [59]. The results for $U = 0eV$ and $U = 4.6eV$ are shown in figure 5.3. It is clear from this figure that a correlation induced satellite appears outside the one-electron ($U/W = 0$) bandwidth in the unoccupied parts with increasing U and no such distinct feature can be seen in the occupied parts. Similar results are also found within exact diagonalization studies of the Hubbard model and in the solution of the Hubbard model in infinite dimensions, while *exactly the opposite trend* is observed in the experimental results in figures 5.1 and 5.2. Thus, it is clear that the evolution of the photoemission and inverse photoemission spectra as a function of doping cannot be accounted by the simple Hubbard model, or an extended Hubbard model, establishing the need to go *beyond the standard models.*

5.3 Theoretical description

In order to understand this surprising result, we first note that the Hubbard model represents a homogeneous system, whereas in real systems electron (or hole) doping is brought about by chemical substitution; *this invariably introduces disorder or inhomogeneity at some length scale.* We propose that it is essential to develop a spatially *inhomogeneous* picture to model these systems. The basic idea is that in these systems the electrons experience different local environments. The angular integrated photoemission spectrum, as a local probe, captures a suitable average of the Green function over the local environment. In principle the degree of inhomogeneity can vary between two limits. If the system is disordered on a microscopic scale, but homogeneous on a macroscopic scale, i.e. the impurities do not form clusters, a model of uncorrelated disorder is appropriate. If there is a tendency of the defects to form clusters, this may reinforce the natural tendency of strongly correlated systems to phase separate [98] and

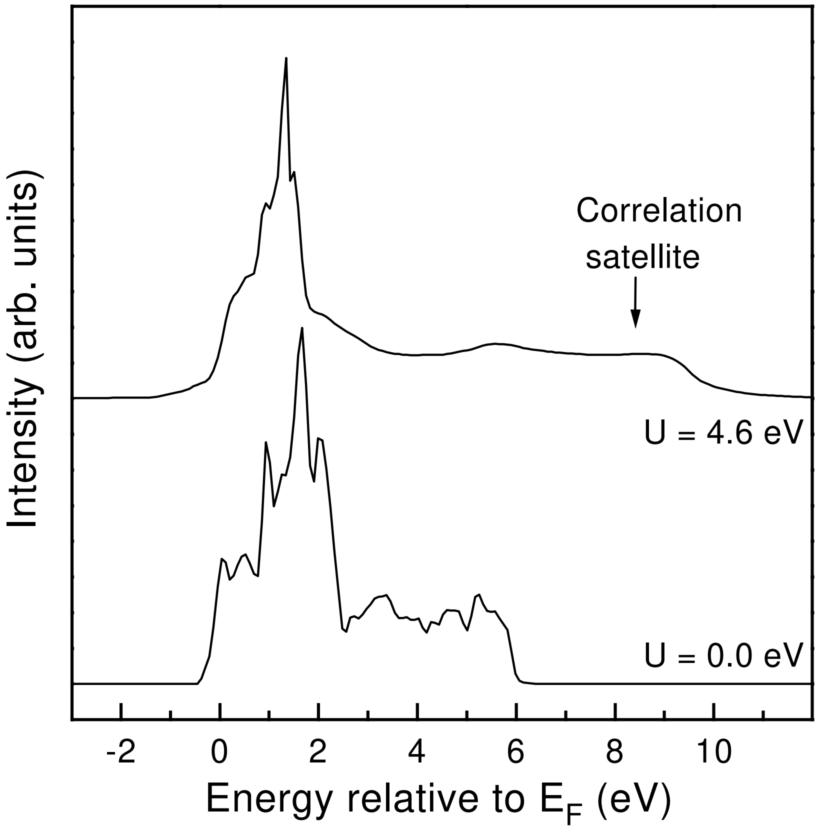

Figure 5.3: Second order perturbation theory applied to the density of states obtained from the linearized muffin-tin orbital method within the atomic sphere approximation.

a model of macroscopic inhomogeneities is more suitable. The application of our IPT scheme to the infinite dimensional Hubbard model with binary randomness allows us to make these ideas more quantitative. We study the evolution of photoemission spectra in these two well defined limits. We expect that the physical situation is somewhere in between. We stress that in both limits we find the photoemission spectrum as a function of x to be very different from the predictions of the Hubbard model and very similar to what is observed experimentally.

In the microscopically inhomogeneous situation we describe $La_xSr_{1-x}TiO_3$ or $SrTiO_{3-\delta}$ using a Hubbard model with diagonal disorder. The Hamiltonian is given by:

$$H = -\sum_{\langle ij \rangle} t_{ij} C^{+}_{i\sigma} C_{j\sigma} + \sum_{i} (\epsilon_i - \mu) C^{+}_{i\sigma} C_{i\sigma} + \sum_{i} n_{i\uparrow} n_{i\downarrow} U_i$$

To get a bounded density of states and a well defined limit as the lattice coordination gets large, we take the hopping matrix elements t_{ij} to be defined on a Bethe lattice and scale them as $\frac{t}{\sqrt{d}}$. The full bandwidth $2D = 4t$ is estimated from band structure calculations. The ϵ_i are random variables which take the values ϵ_A with probability P_A and ϵ_B with probability P_B. P_A and P_B are given by the composition, as 2δ and $(1-2\delta)$ in $SrTiO_{3-\delta}$ and x and $(1-x)$ in $La_xSr_{1-x}TiO_3$ respectively. Band structure calculations suggest that the band-width $2D = 2.5$ eV is appropriate. Supercell calculations for $SrTiO_{2.875}$ and $SrTiO_{2.75}$ showed that several bands are pulled down compared to $SrTiO_3$ due to the presence of vacancies by about 1.5 - 3.0 eV which provides an estimate for $(\epsilon_B - \epsilon_A)$. We use $(\epsilon_B - \epsilon_A) \sim 2.4$ eV; however, the qualitative features of the calculations do not depend on this exact value. $U_A = U_B = 4.6$ eV was estimated from earlier spectroscopic analysis. The chemical potential μ is chosen so that the number of d electrons is equal to x in $La_xSr_{1-x}TiO_3$ or 2δ in $SrTiO_{3-\delta}$.

The mean field theory which is exact in the $d \to \infty$ limit determines the local Green functions at the A and B sites as the local f electron Green function of an Anderson impurity model

$$H = \sum_{k} \epsilon_k a^{+}_{k\sigma} a_{k\sigma} + U f^{+}{}_{\uparrow} f_{\uparrow} f^{+}{}_{\downarrow} f_{\downarrow} + \sum_{k} V_k (a^{+}_{k\sigma} f_{\sigma} + f^{+}_{\sigma} a_{ko}) + \epsilon_f f^{+}{}_{\sigma} f_{\sigma} \qquad (5.1)$$

Here the f level position ϵ_f is given by $E_A - \mu$ or $\epsilon_f = E_B - \mu$ respectively. The hybridization function $\Delta(i\omega_n)$

$$\Delta(i\omega_n) = \sum_k \frac{V_k^2}{(i\omega_n - \epsilon_k)} \tag{5.2}$$

has to be determined self consistently from the local Green functions via the equation:[1]

$$\Delta(i\omega_n) = t^2\ G_{av}(i\omega_n) := t^2\ (P_A\ G_A(i\omega_n) + P_B\ G_B(i\omega_n))$$

It is to be noticed that the A and B sites are connected by the same hybridization function which depends on the local physics at both sites. Thus we have a coupled system of equations. To solve the mean field equations we use the IPT scheme developed in chapter 3 to extract real frequency information.

We now turn to the case where inhomogeneities occur on a macroscopic scale. In this scenario the density of electrons is inhomogeneous on a more macroscopic scale. A fraction f_1 is in an insulating phase with the local concentration of the Mott insulating phase $n_{ins} = 1$ and a fraction $1 - f_1$ with the metallic concentration n_{met}. The total density is given by $n = f_1 n_{ins} + (1 - f_1) n_{met}$ and the measured Green function by

$$\bar{G} = f_1 G_{n_{ins}} + (1 - f_1) G_{n_{met}} \tag{5.3}$$

$G_{n_{ins}}$ and $G_{n_{met}}$ can again be calculated using the mean field theory now in the respective homogeneous phases. To explore this scenario we took $n_{met} = .1$ (which corresponds to a chemical potential $\mu = -.78$) and varied the density n by varying the volume fraction f_1 in equation (5.3). The spectral function in these two scenarios for $n = .2$ are shown in figure 5.4 a and b. To model the finite experimental resolution of photoemission spectra, we introduced a finite broadening ($\eta = 0.04D$). The theoretically expected photoemission and inverse photoemission spectra are plotted in figure 5.5. For the unoccupied spectral function, we have incorporated a further broadening (Gaussian with full width at half maximum of $0.64D$) to account for the poorer resolution in this technique. In both cases the spectra have two features, a Hubbard band centered around $\epsilon_A - \mu$ and a coherent part or less correlated part centered around ϵ_B. Figure 5.6 displays the doping dependence of the spectral function for both scenarios,

[1] We consider a *fully frustrated* Bethe lattice. Compare with the discussion in appendix B.

a)

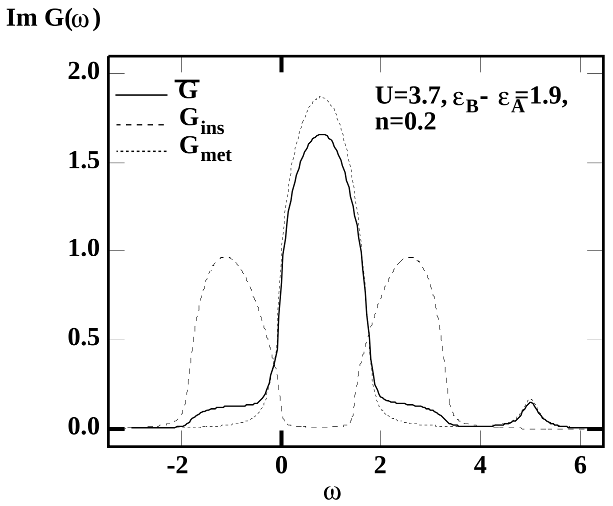

b)

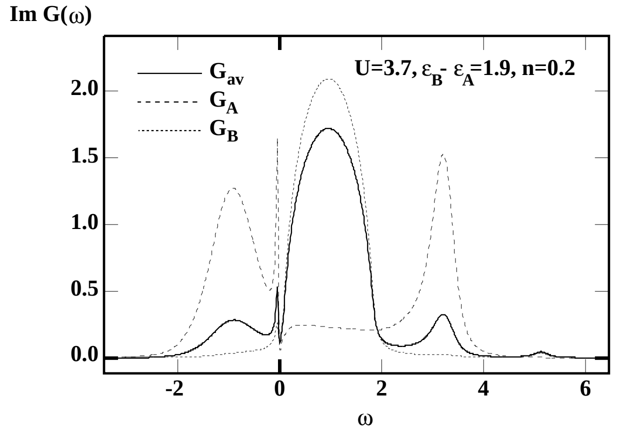

Figure 5.4: Spectral functions of the disordered Hubbard model for density n=.2, U=3.7 in the case of (a) macroscopically and (b) microscopically inhomogeneous disorder. The energy scale is given in units of D $(= 1.25 \text{ eV})$.

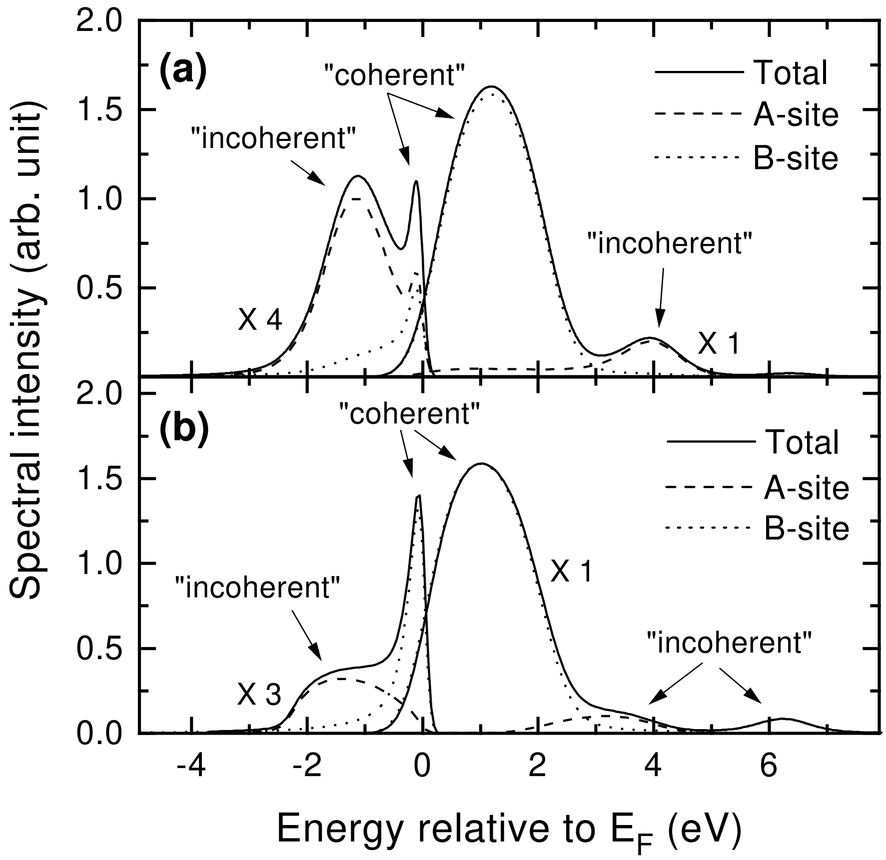

Figure 5.5: Theoretical spectra of the disordered Hubbard model for density $n = .2$, $U = 3.7$, and $\epsilon_b - \epsilon_a = 1.9$ in the case of (a) microscopic and (b) macroscopic inhomogeneities. The dashed and dotted curves indicate the partial contributions from the A and B sites. The energy scale is given in units of D $(= 1.25$ eV). The occupied parts of the spectral functions are expanded for clarity, as shown in the figures.

microscopically inhomogeneous disorder (left column) and phase separation (right column). The corresponding theoretical photoemission and inverse photoemission spectra for the case of microscopically inhomogeneous disorder are given in figure 5.7. As can be seen from the plots the feature around $\epsilon_A - \mu$ increases with increasing filling.

To illustrate the different maxima appearing in the density of states it is useful to perform the calculation in the atomic limit.

Let us first consider the case of microscopically inhomogeneous systems. In the atomic limit the Green functions of the Anderson impurity model have the form [36, 44]

$$G_a(\omega) = \frac{1-n_a}{\omega-\epsilon_a+\mu} + \frac{n_a}{\omega-\epsilon_a-U+\mu} \tag{5.4}$$

$$G_b(\omega) = \frac{1-n_b}{\omega-\epsilon_b+\mu} + \frac{n_b}{\omega-\epsilon_b-U+\mu} \tag{5.5}$$

Here n_a and n_b are the occupation numbers per spin. Since A is a rather deep level ($\epsilon_b - \epsilon_a = 1.9$), we can assume that each lattice site A is singly occupied, i. e. $n_a = \frac{1}{2}$. In order to allow for finite doping, the chemical potential μ has to be chosen such that G_b has a pol at zero frequency, i. e. $\mu = \epsilon_b$ (Here we assume that the doping is small enough so that there are no double occupancies). Thus (5.4) and (5.5) become

$$G_a(\omega) = \frac{1/2}{\omega-\epsilon_a+\epsilon_b} + \frac{1/2}{\omega-\epsilon_a+\epsilon_b} \tag{5.6}$$

$$G_b(\omega) = \frac{1-n_b}{\omega} + \frac{n_b}{\omega-U} \tag{5.7}$$

The particle number n_b follows from the condition

$$(1-x) = x\,n_a + (1-x)\,n_b = \frac{x}{2} + (1-x)\,n_b \tag{5.8}$$

which yields

$$n_b = \frac{x}{2(1-x)} \tag{5.9}$$

Since the lower pol of G_b has the weight $1-n_b$, we have the condition $n_b \le 1-n_b$, i. e. $n_b \le \frac{1}{2}$ or $x \le \frac{1}{2}$. The latter is consistent with our assumption that there are no double occupancies.

From (5.6), (5.7), and (5.9) we obtain the averaged Green function

$$\begin{aligned} G_{av}(\omega) &:= x\,G_a(\omega) + (1-x)\,G_b(\omega) \\ &= \frac{x/2}{\omega-\epsilon_a+\epsilon_b} + \frac{x/2}{\omega-\epsilon_a+\epsilon_b-U} + \frac{1-\frac{3}{2}x}{\omega} + \frac{x/2}{\omega-U} \end{aligned} \tag{5.10}$$

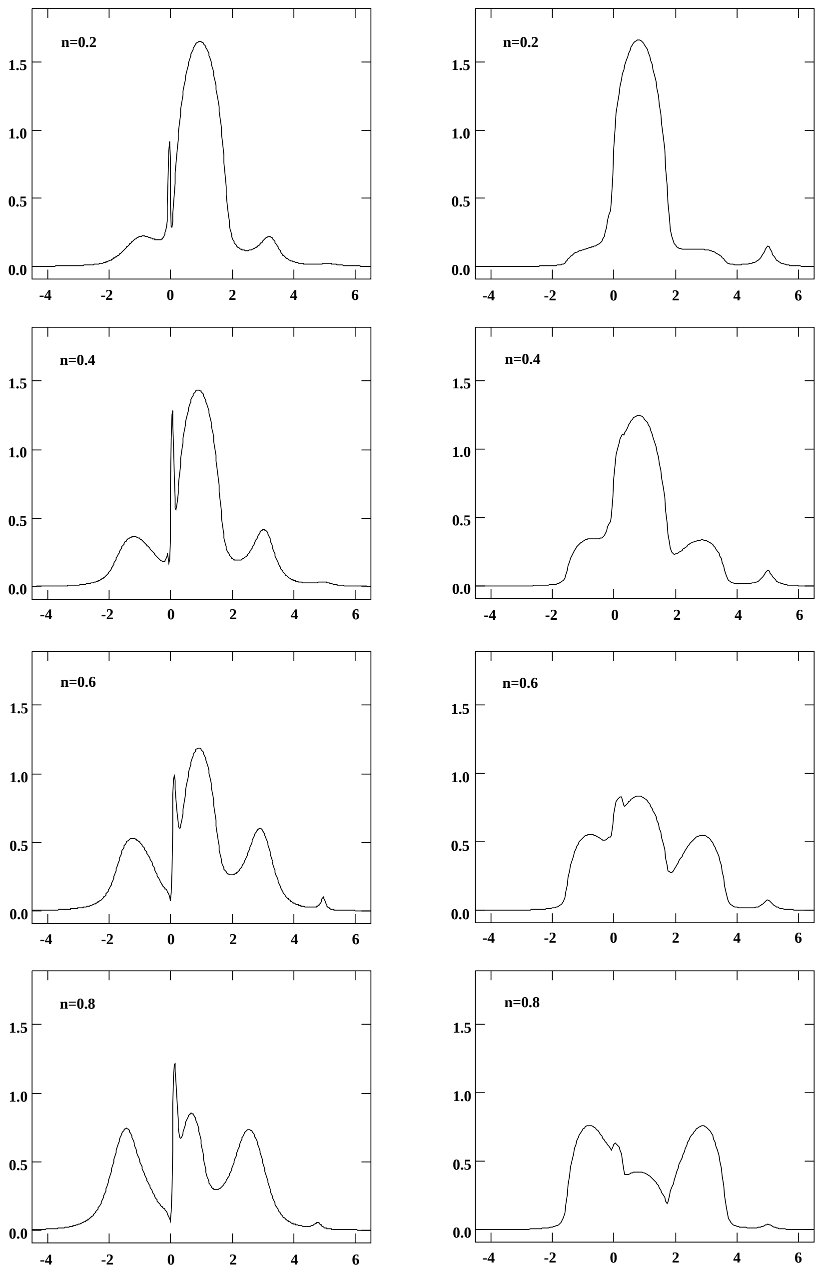

Figure 5.6: Spectral functions of the disordered Hubbard model for $U = 3.7$, $\epsilon_b - \epsilon_a = 1.9$, and increasing filling n; left column: homogeneous disorder, right column: inhomogeneous disorder

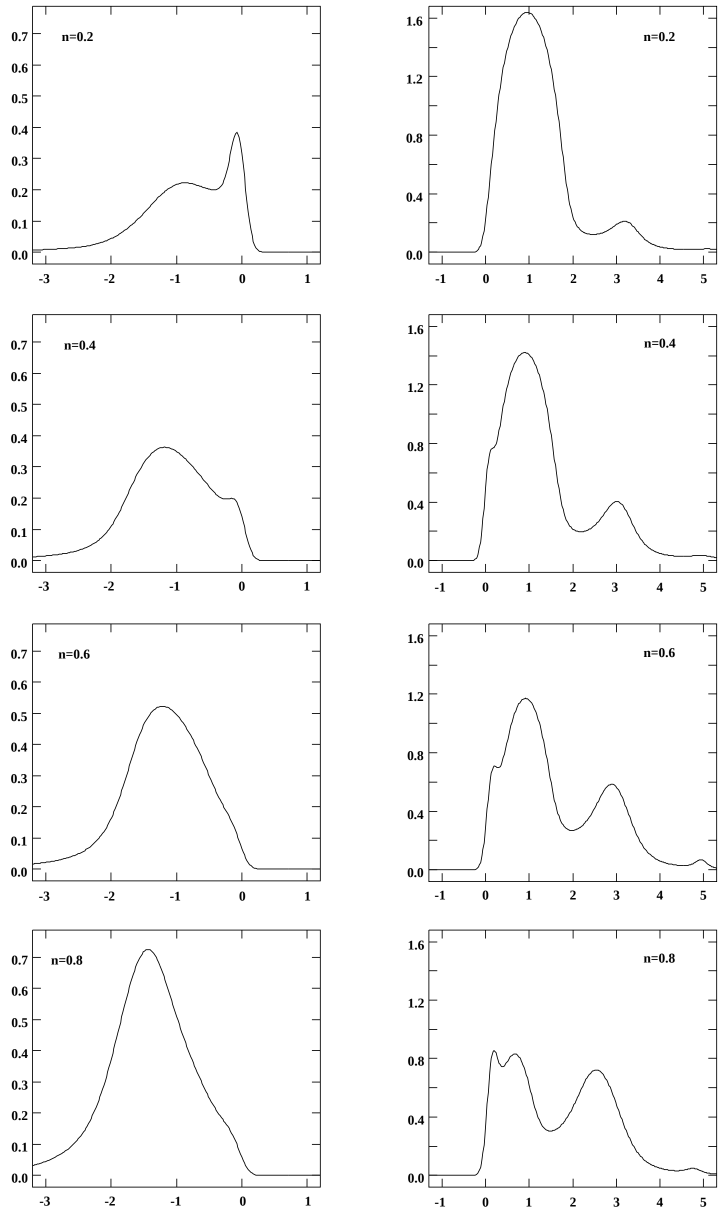

Figure 5.7: Theoretical spectra for the case of microscopically inhomogeneous disorder, $U = 3.7$, $\epsilon_b - \epsilon_a = 1.9$, and increasing filling n; left column: photoemission, right column: inverse photoemission

Here, we have four poles: The first one is at negative frequencies ($\omega_{p_1} = \epsilon_a - \epsilon_b = -1.9$), the second ($\omega_{p_2} = \epsilon_a - \epsilon_b + U = 1.8$) and the fourth ($\omega_{p_2} = U = 3.7$) at large positive frequencies and the third ($\omega_{p_3} = 0$) at zero frequency. The photoemission spectrum has therefore two maxima, one at $\omega_{p_1} = -1.9$ and one at zero frequency.

If the hybridization becomes finite one has to take into account three effects: First of all the δ peaks broaden. Secondly, μ becomes finite (negative) so that the peaks are shifted by $\approx |\mu|$ in positive direction. Finally, we expect the appearance of a resonance peak at zero frequency. Thus, we obtain for the averaged Green function a structure with five peaks as shown in figure 5.4b.

The case of phase separation is treated assuming that there is an insulating phase with total particle density $n_{ins} = 1$, i. e.

$$G_{ins}(\omega) = \frac{1/2}{\omega - \epsilon_a + \epsilon_b} + \frac{1/2}{\omega - \epsilon_a + \epsilon_b - U} \tag{5.11}$$

as well as a "metallic" phase with total particle density $n_{ins} = 0.1$ (density per spin=0.05), i. e.

$$G_{met}(\omega) = \frac{0.95}{\omega} + \frac{0.05}{\omega - U} \tag{5.12}$$

Here we used again $\mu = \epsilon_b$.

The averaged Green function follows from

$$\bar{G} = f_1 G_{ins} + (1 - f_1) G_{met} \tag{5.13}$$

where the weight f_1 is obtained from from $f_1\, n_{met} + (1 - f_1)\, n_{ins} = x$ which gives

$$f_1 = \frac{x - n_{met}}{n_{ins} - n_{met}} = \frac{x - 0.1}{0.9} \tag{5.14}$$

Relations (5.11) to (5.14) yield the average Green function

$$\begin{aligned} \bar{G} \;=\; & \frac{10\,(x-0.1)}{18}\frac{1}{\omega - \epsilon_a + \epsilon_b} + \frac{10\,(x-0.1)}{18}\frac{1}{\omega - \epsilon_a + \epsilon_b - U} \\ & + \frac{19\,(1-x)}{18}\frac{1}{\omega} + \frac{(1-x)}{18}\frac{1}{\omega - U} \end{aligned} \tag{5.15}$$

Note that the position of the poles is the same as for microscopically inhomogeneous disorder (see (5.10)). Only the weights are somewhat different. Again, the poles will be broadened and shifted once the hybridization is finite, explaining the four maxima in

$\bar{G}(\omega)$ in figure 5.4a. Notice that the main qualitative difference between both scenarios is the absence of the resonance peak at zero frequency.

The theoretical results presented in figure 5.5 a and b (as well as in 5.7) are in very good agreement with the experimental spectra (figures 5.1 and 5.2); this is more striking so, when we keep in mind that we expect the real system to be somewhere in between the two limiting cases theoretically considered here. For example, the calculation correctly predicts the existence of an intense incoherent feature at about 1.3 eV arising from the local Green function for site A with a band-like coherent feature near E_F due to the local Green function for site B. This is in perfect agreement with the experimentally observed features in the photoemission spectra of $\mathrm{SrTiO}_{3-\delta}$ (figure 5.1) and $\mathrm{La}_x\mathrm{Sr}_{1-x}\mathrm{TiO}_3$ [53]. Moreover, it is clear from the calculated results that unoccupied parts of the spectral function will be entirely dominated by coherent band-like features arising from the site B as observed in figure 5.2. Here we once again draw attention to the fact that these results are in sharp contrast to those expected on the basis of Hubbard and similar homogeneous models (see figure 5.3). While in the past there have been some attempts to deal with with substoichiometric correlated systems [99], effects of disorder inevitably present in such systems have not been addressed so far.

5.4 Mass enhancement and linear coefficient of the specific heat

Above, we showed that the concept of disorder can sucessfully explain the photoemission spectra of transition metal oxides. We studied two scenarios considering inhomogeneities on a either macroscopic or microscopic scale. Both approaches were able to describe the measurements and we assume that the real situation is somewhere in between.

In this section we address experimental measurements of the electronic specific heat. Measurements by Tokura *et al.* [28] show that γ, the linear coefficient of the specific heat, in $La_xSr_{1-x}TiO_3$ is strongly enhanced from its non interacting value γ_0 as the Mott transition is approached for $x \to 1$. The ratio $\frac{\gamma}{\gamma_0}$ is determined by the effective mass $m^\star$ or the quasiparticle residue Z: $\frac{\gamma}{\gamma_0} = \frac{m^\star}{m} = Z^{-1}$.

In the case of microscopic inhomogeneities this ratio has to be determined as average over the A and B sites:

$$\begin{aligned} \frac{\gamma}{\gamma_0} &= x\,\frac{m_A^\star}{m} + (1-x)\,\frac{m_B^\star}{m} \\ &= \frac{x}{Z_A} + \frac{1-x}{Z_B} \end{aligned} \tag{5.16}$$

The numerical result obtained by the IPT scheme for $U = 3.7$ and $\epsilon_B - \epsilon_A = 1.9$ is shown in figure 5.8 (full line). The main contribution comes from the A sites where the electrons are almost localized. Compared to the homogeneous Hubbard model with the same U we find a strong mass enhancement. This can be explained as follows: The number of A sites is equal to the number of particles. If $\epsilon_B - \epsilon_A$ is much larger than the kinetic energy, i. e. if the A sites are sufficiently low in energy, then the electrons will tend to localize on the A sites so that the effective particle density on these sites is almost one (and not x) resulting in a huge enhancement of the effective mass.

In the case of phase separation, on the other hand, we only get a contribution to $\frac{\gamma}{\gamma_0}$ from the metallic phase. Since $Z_{metallic} \approx 1$ we have

$$\frac{\gamma}{\gamma_0} \approx (1-x) \tag{5.17}$$

which decreases linearly in x.

In figure 5.8 we compare both scenarios (macroscopic and microscopic inhomogeneities) with the experimental data for $La_xSr_{1-x}TiO_3$ published in reference [28]. Notice that none of the limiting cases can describe the situation alone. The results are however consistent with the expectation that the real situation is somewhere in between the two scenarios. Under this assumption one could use the experimental data to determine the degree of inhomogeneity. However, it seems that the simple homogeneous Hubbard model can describe the $\frac{\gamma}{\gamma_0}$ ratio somewhat better than the disorder approach.

5.5 Summary

To summarize, high-energy spectroscopic data of compounds with a configuration close to $3d^0$ conclusively establish the need to go beyond the standard theories to describe spectral functions in doped transition metal compounds. Thus, we presented a new

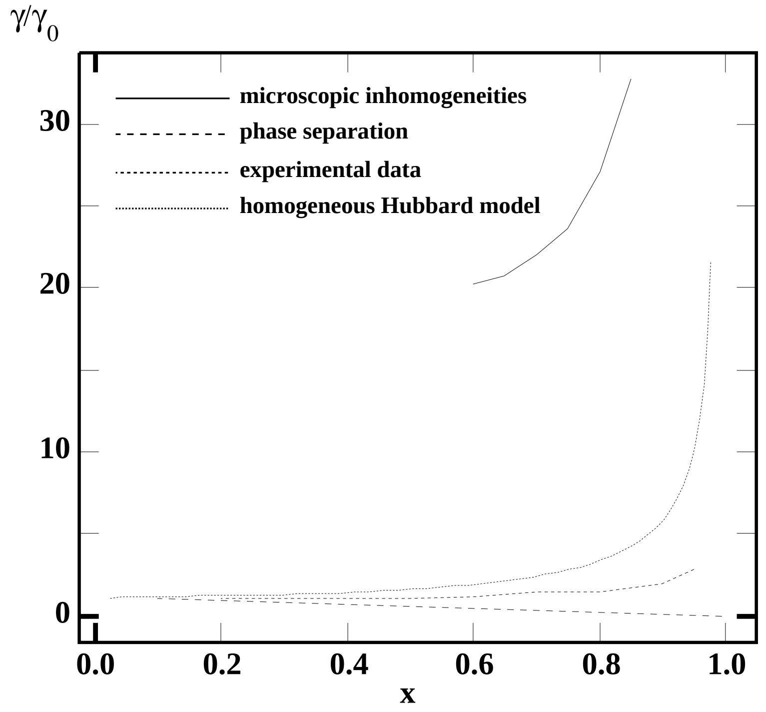

Figure 5.8: Comparision of the γ/γ_0 ratio: microscopic inhomogeneities (full line) and phase separation (long-dashed line) for $U = 3.7$ and $\epsilon_B - \epsilon_A = 1.9$ compared to the experimental data for $La_xSr_{1-x}TiO_3$ (short-dashed line). Also shown are the data of the homogeneous Hubbard model for $U = 3.7$ (dotted line)

theoretical approach for the evolution of the spectral function of correlated electron systems as a function of doping where the inhomogeneity of the medium is essential.

We considered two cases, in one the inhomogeneity is present only on a microscopic scale while in the other the system was assumed to be macroscopically inhomogeneous. Both models give similar angle integrated spectra which therefore cannot determine the length scale over which the system is inhomogeneous. The spectra of the inhomogeneous models, however are qualitatively different from that of a homogeneous system, conclusively establishing the need to go beyond the standard theories to describe spectral functions in a class of doped transition metal compounds.

With respect to the mass enhancement which is experimentally observed as the Mott transition is approached with increasing particle number, both disorder scenarios yield quite different results. In the case of microscopic disorder, the effective mass is extremely large indicating a tendency of the particles to localize on the A sites. The opposite, i. e. no drastic enhancement of $m^{\star}$ is observed when phase separation is considered. The experimental data are somewhere in between, which is consistent with the assumption that the real situation is between the two limiting disorder scenarios considered. Nevertheless, one has to admit that the aspect of the mass enhancement can better be described by the simple homogeneous Hubbard model. The theoretical description introduced in this chapter should thereby be viewed merely as a concept concerning the surface (photoemission measurements) rather than the bulk features (specific heat).

We conclude with a remark concerning the model of microscopically inhomogeneous disorder introduced in this chapter. For the description of the experiment we treated it within a special parameter range away from half filling. However, from a theoretical point of view already the particle hole symmetric case is of interest as it combines a band and a Mott insulator. There are some analytic results available which might serve as a further check for our perturbation scheme. Some remarks on this topic can be found in appendix D.

Chapter 6

Generalization to Multiband Models

6.1 Introduction

So far, almost all studies exploring the large d limit of correlated fermion systems have been concerned with single band models like the Hubbard model. This restriction has been necessary since there is no numerical tool available which is powerful enough to deal with the multiband case. However, real materials in nature contain several bands. Thus making the large d limit applicable to such systems requires a method which is able to treat models involving more than one band.

In this chapter we will show how our perturbation scheme can be extended to this case provided the particle density is less than one. The derivation is illustrated for the two band Hubbard model

$$\begin{aligned} H &= -t \sum_{<ij>,m\sigma} c^{+}_{im\sigma}\, c_{jm\sigma} + \frac{U_1}{2} \sum_{i,m\sigma} n_{im\sigma} n_{im\bar{\sigma}} \\ &\quad + \frac{U_2}{2} \sum_{i,m\sigma} n_{im\sigma} n_{i\bar{m}\bar{\sigma}} + \frac{U_3}{2} \sum_{i,m\sigma} n_{im\sigma} n_{i\bar{m}\sigma} \end{aligned} \tag{6.1}$$

where $m = 1, 2$ ($\sigma = \pm 1$) denotes the band (spin) index. A bar over m or σ means the complementary value, i. e. $\bar{m} = 2$ if $m = 1$ and $\bar{m} = 1$ if $m = 2$ ($\bar{\sigma} = -1$ if $\sigma = 1$ and $\bar{\sigma} = 1$ if $\sigma = -1$).

We introduced three interaction parameters U_i. U_1 describes the on site interaction between two particles in the same band but with opposite spin. U_2 relates to a pair of particles with opposite band and spin index. U_3 finally concerns the case of equal spin but opposite band index. U_3 is by an intraatomic exchange energy J smaller than U_2, i. e. $U_3 = U_2 - J$. Rotational symmetry requires $U_2 = U_1 - 2J$ [63].

The parameter J, which has no analogue in the one band model, originates in Hund's rule. It has a profound influence on the phase diagram. A detailed calculation of the competition between the different possible phases is however very difficult and will not be undertaken here. The behavior of the system can be analyzed in the limit of strong correlations, by deriving the effective Hamiltonian, which for half filling is given by:

$$\begin{aligned} H_{eff} &= -\frac{J_1}{2}\sum_{\langle ij\rangle,m\sigma} \vec{S}_i^{(m\sigma,m\bar{\sigma})}\vec{S}_j^{(m\sigma,m\bar{\sigma})} - \frac{J_2}{2}\sum_{\langle ij\rangle,m\sigma} \vec{S}_i^{(m\sigma,\bar{m}\bar{\sigma})}\vec{S}_j^{(m\sigma,\bar{m}\bar{\sigma})} \\ & -\frac{J_3}{2}\sum_{\langle ij\rangle,m\sigma} \vec{S}_i^{(m\sigma,\bar{m}\sigma)}\vec{S}_j^{(m\sigma,\bar{m}\sigma)} + \text{ const.} \end{aligned} \tag{6.2}$$

where we introduced generalized spin operators $\vec{S}_i^{(m\sigma,m'\sigma')}$ which are defined by

$$\begin{aligned} S_{i,x}^{(m\sigma,m'\sigma')} &:= \frac{1}{2}\left(c_{m\sigma}^{+}c_{m'\sigma'} + c_{m'\sigma'}^{+}c_{m\sigma}\right) \\ S_{i,y}^{(m\sigma,m'\sigma')} &:= -\frac{i}{2}\left(c_{m\sigma}^{+}c_{m'\sigma'} - c_{m'\sigma'}^{+}c_{m\sigma}\right) \quad \text{and} \\ S_{i,z}^{(m\sigma,m'\sigma')} &:= \frac{1}{2}\left(n_{m\sigma} - n_{m'\sigma'}\right) \end{aligned} \tag{6.3}$$

The exchange constants are given by $J_i = \frac{4t^2}{U_i}$. Notice that for finite intraatomic exchange J, the exchange constant J_3 is largest, so that the ground state is ferromagnetic. The difference in energy per spin with a Neel state is given by the energy scale $\frac{t^2 J}{U^2}$, which can be rather small since J tends to be much smaller than U.

Nevertheless, to understand the low temperature ordering transition and the observed transition from the antiferromagnetic phase to the paramagnetic phase in the $Y_{1-x}La_xTiO_3$ system requires the introduction of oxygen orbitals. As shown in appendix B, magnetism is suppressed in these systems. Therefore, it is reasonable to restrict our study again to the *frustrated* model. In particular, we will study the influence of orbital degeneracy on the properties of the Hubbard model.

Recently, some aspects of the two band model have also been investigated with the slave boson approximation [94] and with the quantum Monte Carlo method [95].

In section 6.2 we derive the perturbation scheme for the impurity model corresponding to 6.1. Afterwards (section 6.3) the validity of the approximation is checked with an exactly solvable toy model. Then the lattice problem (6.1) is solved by iteration (section 6.4). The results are compared with the one band Hubbard model. In section 6.5 we discuss briefly the breakdown of the scheme at fillings larger than one particle

λ	$E_\lambda^{(m\sigma)}$	$P_\lambda^{(m\sigma)}$
1	0	$\langle(1-n_{m\bar{\sigma}})\,(1-n_{\bar{m}\sigma})\,(1-n_{\bar{m}\bar{\sigma}})\rangle$
2	U_3	$\langle(1-n_{m\bar{\sigma}})\,n_{\bar{m}\sigma}\,(1-n_{\bar{m}\bar{\sigma}})\rangle$
3	U_2	$\langle(1-n_{m\bar{\sigma}})\,(1-n_{\bar{m}\sigma})\,n_{\bar{m}\bar{\sigma}}\rangle$
4	U_3	$\langle n_{m\bar{\sigma}}\,(1-n_{\bar{m}\sigma})\,(1-n_{\bar{m}\bar{\sigma}})\rangle$
5	U_2+U_3	$\langle(1-n_{m\bar{\sigma}})\,n_{\bar{m}\sigma}\,n_{\bar{m}\bar{\sigma}}\rangle$
6	U_1+U_3	$\langle n_{m\bar{\sigma}}\,n_{\bar{m}\sigma}\,(1-n_{\bar{m}\bar{\sigma}})\rangle$
7	U_1+U_2	$\langle n_{m\bar{\sigma}}\,(1-n_{\bar{m}\sigma})\,n_{\bar{m}\bar{\sigma}}\rangle$
8	$U_1+U_2+U_3$	$\langle n_{m\bar{\sigma}}\,n_{\bar{m}\sigma}\,n_{\bar{m}\bar{\sigma}}\rangle$

Table 6.1: Position $E_\lambda^{(m\sigma)}$ and weights $P_\lambda^{(m\sigma)}$ of the impurity Green function's poles in the atomic limit

per lattice site. Afterwards, an extension to larger fillings is discussed (section 6.6). Finally, the optical conductivity of the two band Hubbard model is compared with experimental data on $La_{1-x}Ti_xTiO_3$ and $La_{2-x}Sr_xCuO_4$ (section 6.4). In section 6.8 we conclude with a summary.

6.2 Impurity problem with two bands

The impurity problem related to the (frustrated) lattice model (6.1) is given by

$$\begin{aligned} H_{imp} &= \epsilon_f \sum_{m\sigma} f^+_{m\sigma} f_{m\sigma} + \sum_{k,m\sigma} \epsilon_k c^+_{km\sigma} c_{km\sigma} + \sum_{k,m\sigma} V_k \left(c^+_{km\sigma} f_{m\sigma} + f^+_{m\sigma} c_{km\sigma} \right) \\ &+ \frac{U_1}{2} \sum_{m\sigma} n^{(f)}_{m\sigma} n^{(f)}_{m\bar{\sigma}} + \frac{U_2}{2} \sum_{m\sigma} n^{(f)}_{m\sigma} n^{(f)}_{\bar{m}\bar{\sigma}} + \frac{U_3}{2} \sum_{m\sigma} n^{(f)}_{m\sigma} n^{(f)}_{\bar{m}\sigma} \end{aligned} \tag{6.4}$$

We assume that the hybridization function $\Delta(\omega) = \sum_k \frac{V_k^2}{\omega - \epsilon_k - i\eta}$ is given. As in the single band case, we will construct an interpolating self energy which is exact in different limits, namely the atomic limit ($V_k \to 0$), the weak coupling limit ($U \to 0$) as well as the low and high frequency limits.

Let us first consider the atomic limit. In the most general case the impurity Green function $G^{(m\sigma)}_{f,atomic}(\omega)$ has eight poles E_λ with weights P_λ:

$$G^{(m\sigma)}_{f,atomic}(\omega) = \sum_{\lambda=1}^{8} \frac{P_\lambda^{(m\sigma)}}{\omega - \epsilon_f - E_\lambda^{(m\sigma)}} \tag{6.5}$$

The poles $E_\lambda^{(m\sigma)}$ and their weights are shown in table 6.1.

For the frustrated lattice the quantities are independent of the combined band and spin index $m\sigma$:

$$E_\lambda := E_\lambda^{(m\sigma)} \quad \text{and} \quad P_\lambda := P_\lambda^{(m\sigma)} \tag{6.6}$$

so that

$$G_{f,atomic} := G_{f,atomic}^{(m\sigma)} \tag{6.7}$$

In many real substances, like e. g. $La_xSr_{1-x}TiO_3$, one is dealing with relatively large interactions and a filling which is less than one electron per lattice site. In this case one might neglect the higher order excitations E_5 to E_8 since their weights will be small. However, at this point we include all poles to keep the scheme as general as possible. A simplified version of the scheme will be derived later.

The relation between the Green function $G_{f,atomic}$ and the corresponding self energy Σ_{atomic},

$$G_{f,atomic}(\omega) = \frac{1}{\omega - \epsilon_f - \Sigma_{atomic}(\omega)} \quad , \tag{6.8}$$

implies that $\Sigma_{atomic}(\omega)$ has seven poles.

In the following we will make use of the fact that a general self energy $\Sigma(\omega)$ can be expanded into a continuous fraction [34]:

$$\Sigma(\omega) = (U_1 + U_2 + U_3)n + \cfrac{\alpha_2\alpha_3}{\omega + \alpha_3 + \alpha_4 - \cfrac{\alpha_4\alpha_5}{\omega + \alpha_5 + \alpha_6 - \cfrac{\alpha_6\alpha_7}{\ddots}}} \tag{6.9}$$

Each parameter α_i depends on the spectral moments $\mu_1, \ \ldots, \ \mu_{i-1}$ where $\mu_i := \frac{1}{\pi}\int_{-\infty}^{+\infty} d\omega\, \omega^i\, \mathrm{Im}G(\omega)$. The first expressions are

$$\begin{aligned}
\alpha_1 &= 1 \\
\alpha_2 &= -\mu_1 \\
\alpha_3 &= -\frac{\mu_2 - \mu_1^2}{\mu_1} \\
\alpha_4 &= -\frac{\mu_1\mu_3 - \mu_2^2}{\mu_1(\mu_2 - \mu_1^2)} \\
\alpha_5 &= -\frac{\mu_1\mu_2\mu_4 - \mu_1^3\mu_4 - \mu_1\mu_2^3 - \mu_1\mu_3^2 + 2\mu_1^2\mu_2\mu_3}{(\mu_1\mu_3 - \mu_2^2)(\mu_2 - \mu_1^2)} \\
&\vdots
\end{aligned} \tag{6.10}$$

An efficient algorithm to calculate the α_i to arbitrary order can be found in ref [34][1]. In the atomic limit, expansion (6.9) truncates at the appropriate depth so that there are exactly seven poles:

$$\Sigma_{atomic}(\omega) = (U_1 + U_2 + U_3)n + \cfrac{\alpha_2\alpha_3}{\omega + \alpha_3 + \alpha_4 - \cfrac{\alpha_4\alpha_5}{\omega+\alpha_5+\alpha_6 - \cfrac{\alpha_6\alpha_7}{\ddots \over \omega+\alpha_{15}+\alpha_{16}}}} \tag{6.11}$$

Here, the α_i are calculated for $V = 0$ where

$$\begin{aligned} \mu_k &= \left\langle (\epsilon_f + U_1\, n_{m\bar\sigma} + U_2\, n_{\bar m\bar\sigma} + U_3\, n_{\bar m\sigma})^k \right\rangle \\ &= \sum_j \begin{pmatrix} k \\ j \end{pmatrix} \epsilon_f^k\, T_{k-j} \end{aligned} \tag{6.12}$$

with

$$\begin{aligned} T_l &:= \left\langle (U_1\, n_{m\bar\sigma} + U_2\, n_{\bar m\bar\sigma} + U_3\, n_{\bar m\sigma})^l \right\rangle \\ &= \sum_{i=0}^{l}\sum_{j=0}^{i} \begin{pmatrix} l \\ i \end{pmatrix} \begin{pmatrix} i \\ j \end{pmatrix} U_1^j\, U_2^{i-j}\, U_3^{l-i}\, \langle n_{m\bar\sigma}^j n_{\bar m\bar\sigma}^{i-j} n_{\bar m\sigma}^{l-i} \rangle \end{aligned} \tag{6.13}$$

For a frustrated two band model, the correlation functions in the last equation can be expressed by five independent expectation values:

$$\langle n_{m\bar\sigma}^i n_{\bar m\bar\sigma}^j n_{\bar m\sigma}^k \rangle = \begin{cases} \langle nnn \rangle := \langle n_{m\bar\sigma} n_{\bar m\bar\sigma} n_{\bar m\sigma} \rangle & \text{if } i \geq 1,\ j \geq 1 \text{ and } k \geq 1 \\ \langle nn \rangle_3 := \langle n_{m\bar\sigma} n_{\bar m\bar\sigma} \rangle & \text{if } i \geq 1,\ j \geq 1 \text{ and } k = 0 \\ \langle nn \rangle_2 := \langle n_{m\bar\sigma} n_{\bar m\sigma} \rangle & \text{if } i \geq 1,\ j = 0 \text{ and } k \geq 1 \\ \langle nn \rangle_1 := \langle n_{\bar m\bar\sigma} n_{\bar m\sigma} \rangle & \text{if } i = 0,\ j \geq 1 \text{ and } k \geq 1 \\ \langle n \rangle := \langle n_{m\sigma} \rangle & \text{otherwise} \end{cases} \tag{6.14}$$

The expansion (6.11) is the starting point for the construction of the interpolating self energy $\Sigma_{int}(\omega)$. It has to be connected to the small U limit. For this purpose we consider the second order self energy contribution

$$\begin{aligned} \tilde\Sigma_0^{(2)}(\omega) &= \left(U_1^2 + U_2^2 + U_3^2\right) \int_{-\infty}^{E_F=0} d\epsilon_1 \int_{E_F=0}^{\infty} d\epsilon_2 d\epsilon_3 \frac{\rho^{(0)}(\epsilon_1)\rho^{(0)}(\epsilon_2)\rho^{(0)}(\epsilon_3)}{\omega + \epsilon_1 - \epsilon_2 - \epsilon_3 - i\eta} \\ &+ \left(U_1^2 + U_2^2 + U_3^2\right) \int_{E_F=0}^{\infty} d\epsilon_1 \int_{-\infty}^{E_F=0} d\epsilon_2 d\epsilon_3 \frac{\rho^{(0)}(\epsilon_1)\rho^{(0)}(\epsilon_2)\rho^{(0)}(\epsilon_3)}{\omega + \epsilon_1 - \epsilon_2 - \epsilon_3 - i\eta} \end{aligned} \tag{6.15}$$

---

[1] Be aware of a different sign convention for the moments.

with $\rho^{(0)}(\omega) = \frac{1}{\pi}\mathrm{Im}G_0(\omega)$. As in the single band case the (advanced) Green function $G_0(\omega)$ is defined by

$$G_0(\omega) = \frac{1}{\omega + \tilde{\mu}_0 - \Delta(\omega)} \tag{6.16}$$

where $\tilde{\mu}_0$ will be fixed later. The atomic limit of (6.15) takes the simple form

$$\tilde{\Sigma}^{(2)}_{0,atomic}(\omega) = \frac{\gamma_0}{\omega + \tilde{\mu}_0 - i\eta} \tag{6.17}$$

where $\gamma_0 := (U_1^2 + U_2^2 + U_3^2)\, n_0(1 - n_0)$ with $n_0 = \frac{1}{\pi}\int_{-\infty}^{0} \mathrm{Im}G_0(\omega)$. Thus, multiplying each numerator and denominator in the chain fraction (6.11) by $\frac{1}{\omega+\tilde{\mu}_0-i\eta}$ allows to express $\Sigma_{atomic}(\omega)$ in terms of the building block $\tilde{\Sigma}^{(2)}_{0,atomic}(\omega)$:

$$\Sigma_{atomic}(\omega) = (U_1 + U_2 + U_3)n + \cfrac{A_0\, \tilde{\Sigma}^{(2)}_{0,atomic}(\omega)}{1 + B_1 \tilde{\Sigma}^{(2)}_{0,atomic}(\omega) + \cfrac{C_1 \left(\tilde{\Sigma}^{(2)}_{0,atomic}(\omega)\right)^2}{1 + B_2 \tilde{\Sigma}^{(2)}_{0,atomic}(\omega) + \cfrac{C_2 \left(\tilde{\Sigma}^{(2)}_{0,atomic}(\omega)\right)^2}{\cfrac{\ddots}{1 + B_7 \tilde{\Sigma}^{(2)}_{0,atomic}(\omega)}}}} \tag{6.18}$$

where

$$\begin{aligned}
A_0 &= \frac{\alpha_2\alpha_3}{\gamma_0} = \frac{\mu_2 - \mu_1^2}{\gamma_0} \\
&= \frac{1}{\gamma_0}\{\left(U_1^2 + U_2^2 + U_3^2\right)\, n(1-n) + 2\,U_1 U_2\, \left(\langle nn\rangle_3 - n^2\right) \\
&\quad + 2\,U_1 U_3\, \left(\langle nn\rangle_2 - n^2\right) + 2\,U_2 U_3\, \left(\langle nn\rangle_1 - n^2\right)\} \\
B_i &= \frac{\alpha_{2i+1} + \alpha_{2i+2} - \tilde{\mu}_0}{\gamma_0} \\
C_i &= -\frac{\alpha_{2i+2}\alpha_{2i+3}}{\gamma_0^2}
\end{aligned} \tag{6.19}$$

Assuming that (6.18) holds not only in the atomic limit but for all V yields finally the interpolating self energy

$$\Sigma_{int}(\omega) = (U_1 + U_2 + U_3)n + \cfrac{A_0\, \tilde{\Sigma}^{(2)}_0(\omega)}{1 + B_1 \tilde{\Sigma}^{(2)}_0(\omega) + \cfrac{C_1 \left(\tilde{\Sigma}^{(2)}_0(\omega)\right)^2}{1 + B_2 \tilde{\Sigma}^{(2)}_0(\omega) + \cfrac{C_2 \left(\tilde{\Sigma}^{(2)}_0(\omega)\right)^2}{\cfrac{\ddots}{1 + B_7 \tilde{\Sigma}^{(2)}_0(\omega)}}}} \tag{6.20}$$

Here, the coefficients A_0, B_i and C_i are evaluated using equation (6.12) for the moments. In general this relation is valid only in the atomic limit. But it can be verified by evaluating a commutator formula [35] that for the first two moments (μ_1 and μ_2) this relation yields the exact results for all V. Taking into account that the high frequency behavior of the exact self energy is given by $\Sigma(\omega) = (U_1 + U_2 + U_3)n + \frac{\mu_2-\mu_1^2}{\omega+\ldots}$, we conclude that $\Sigma_{int}(\omega)$ has the correct large ω limit.[2]

The proper low frequency limit is ensured by imposing the Friedel sum rule (3.14) as criterion for fixing $\tilde{\mu}_0$. Furthermore, the atomic limit is correct by construction, and the interpolating self energy is also exact to order U^2. The latter follows from $A_0 = 1 + O(U)$, $B_1U^2 = O(U)$, and $C_1U^4 = O(U^2)$. The first two of these relations are analogous to the single band case, and the third can be verified by some straightforward (but tedious) algebra.

Thereby, we have reached our goal of constructing an interpolating self energy which becomes exact in various limits. However, we do not have a closed set of equations yet since the expressions contain four correlation functions which have to be determined in some way: $\langle nn\rangle_1$, $\langle nn\rangle_2$, $\langle nn\rangle_3$, and $\langle nnn\rangle$. For $J = 0$ the first three terms are equal and one could try to determine their value from the equations of motion for the Green function which yields $\langle nn\rangle_i = \frac{1}{3\pi}\int_{-\infty}^{0} \mathrm{Im}\,(G(\omega)\Sigma(\omega))$. Unfortunately, the numerical accuracy with which the integral can be determined is of the same order of magnitude as the correlation function itself ($\approx 10^{-3}$) so that this approach cannot be useful for the numerical implementation. Therefore, we proceed differently using the alloy analogy [61, 62, 63] (or, respectively, the coherent potential approximation [64]) to determine the correlation functions.

In this approximation the motion of an $(m\sigma)$ f-electron is approximately described by the Hamiltonian:

$$H_{imp,CPA}^{(m\sigma)} = (\epsilon_f + E)f_{m\sigma}^+ f_{m\sigma} + \sum_k \epsilon_k c_{km\sigma}^+ c_{km\sigma} + \sum_k V_k \left(c_{km\sigma}^+ f_{m\sigma} + f_{m\sigma}^+ c_{km\sigma}\right) \quad (6.21)$$

The impurity site energy E takes the values E_λ with the probabilities P_λ shown in table 6.1. For a frustrated two band model the P_λ can be expressed entirely in terms of five independent expectation values which already appeared in (6.14):

$$P_1 = 1 - 3\langle n\rangle + \langle nn\rangle_1 + \langle nn\rangle_2 + \langle nn\rangle_3 - \langle nnn\rangle$$

[2] We used that for large frequencies $\tilde{\Sigma}_0^{(2)}(\omega) = \frac{\gamma_0}{\omega+\ldots}$

$$
\begin{aligned}
P_2 &= \langle n\rangle - \langle nn\rangle_1 - \langle nn\rangle_2 + \langle nnn\rangle \\
P_3 &= \langle n\rangle - \langle nn\rangle_1 - \langle nn\rangle_3 + \langle nnn\rangle \\
P_4 &= \langle n\rangle - \langle nn\rangle_2 - \langle nn\rangle_3 + \langle nnn\rangle \\
P_5 &= \langle nn\rangle_1 - \langle nnn\rangle \\
P_6 &= \langle nn\rangle_2 - \langle nnn\rangle \\
P_7 &= \langle nn\rangle_3 - \langle nnn\rangle \\
P_8 &= \langle nnn\rangle
\end{aligned} \tag{6.22}
$$

The coherent potential approximation [64] yields an average Green function

$$
G_{f,CPA}(\omega) = \sum_{\lambda=1}^{8} P_\lambda G_\lambda = \sum_{\lambda=1}^{8} \frac{P_\lambda}{\omega + \mu + \delta\mu - E_\lambda - \Delta(\omega)} \tag{6.23}
$$

where $G_\lambda(\omega) := \frac{1}{\omega+\mu+\delta\mu-E_\lambda-\Delta(\omega)}$. Here, we introduced an additional shift $\delta\mu$ for the chemical potential. It is chosen such that $G_{f,CPA}$ yields the exact particle number $n = \langle n\rangle$:

$$
\langle n\rangle_{CPA} = \langle n\rangle \tag{6.24}
$$

Let n_λ be the formal particle number determined from G_λ:

$$
n_\lambda = \frac{1}{\pi}\int_{-\infty}^{0} d\omega\, \mathrm{Im} G_\lambda(\omega) \tag{6.25}
$$

To obtain a closed set of equations, one can express $\langle n\rangle$, $\langle nn\rangle_i$ $(i = 1\ldots3)$ and $\langle nnn\rangle$ by P_λ and n_λ, e. g.

$$
\langle n\rangle_{CPA} = \sum_\lambda P_\lambda n_\lambda \tag{6.26}
$$

Moreover, $\langle nn\rangle_{1,CPA} = \langle n_{\bar m\bar\sigma} n_{\bar m\sigma}\rangle_{CPA}$ is the number of $(\bar m\bar\sigma)$ electrons on sites having a $(m\bar\sigma)$ electron (or the number of $(m\bar\sigma)$ electrons on sites having a $(\bar m\bar\sigma)$ electron): [3]

$$
\langle nn\rangle_{1,CPA} = P_4 n_4 + P_6 n_6 + P_7 n_7 + P_8 n_8 \tag{6.27}
$$

Analogously, one has

$$
\langle nn\rangle_{2,CPA} = P_3 n_3 + P_5 n_5 + P_7 n_7 + P_8 n_8 \tag{6.28}
$$

[3] For a more detailed derivation see ref [63].

and

$$\langle nn \rangle_{3,CPA} = P_2 n_2 + P_5 n_5 + P_6 n_6 + P_8 n_8 \tag{6.29}$$

The three particle correlation function $\langle nnn \rangle = \langle n_{m\bar{\sigma}} n_{\bar{m}\bar{\sigma}} n_{\bar{m}\sigma} \rangle$ is the number of $(m\bar{\sigma})$ electrons on sites having both, an $(\bar{m}\sigma)$ and an $(m\bar{\sigma})$ electron plus two similar terms divided by three:

$$\langle nnn \rangle_{CPA} = \frac{1}{3} \left(P_5 n_5 + P_6 n_6 + P_7 n_7 \right) + P_8 n_8 \tag{6.30}$$

Replacing P_λ in equations (6.26) to (6.30) by the expressions (6.22) yields a linear set of equations for $\langle n \rangle_{CPA}$, $\langle nn \rangle_{i,CPA}$ $(i = 1 \ldots 3)$ and $\langle nnn \rangle_{CPA}$. As stated above $\delta\mu$ is chosen such that $\langle n \rangle_{CPA}$ equals the real particle number n determined from G_f. The correlation functions $\langle nn \rangle_{i,CPA}$ and $\langle nnn \rangle_{CPA}$ are used for the perturbation scheme (equation (6.14)).

The use of the alloy analogy for determining the correlation functions is justified because this approximation yields the exact results in various limits. This is obvious in the atomic limit $(V \to 0)$. But it is also true for $U = 0$ where the correlation functions factorize, and for large doping where the system gets dilute so that correlations become negligible small. For the interpolating self energy the use of CPA implies that the large frequency limit is only approximately correct.

The numerical implementation can be realized as in the single band case. A solution of the impurity model is completely determined by a pair $(n, \tilde{\mu}_0)$ which can be obtained by searching the zeros of two functions $f_1(n, \tilde{\mu}_0) := n - \frac{1}{\pi} \int_{-\infty}^{0} d\omega \, \mathrm{Im} G_f[n, \tilde{\mu}_0](\omega)$ and $f_2(n, \tilde{\mu}_0) := n - n_{Friedel}[n, \tilde{\mu}_0]$ using Broyden's method [43].

Since the scheme presented here is a pure generalization of the method introduced earlier for the single band model we expect that the remarks in chapter 3 about the validity of the approximation also apply to the multiband case. A more detailed study of the accuracy of the scheme will be presented in the next section. We will see that the scheme gives reasonable results only for fillings less than one particle per lattice site.

In this case, the expression for the interpolating self energy can be simplified by neglecting higher order excitations. If in particular $J = 0$, only the poles at $-\epsilon_f$ and $-\epsilon_f + U$ of the atomic Green function have a considerable weight. It is then reasonable to truncate the continuous fraction in the interpolating self energy such that the self energy has only one pole in the atomic limit. However, this procedure has to be done with care in order to obtain a well defined large U limit. We proceed as follows: First we note that for vanishing J the expansion (6.20) truncates at the third level:

$$\Sigma_{int}(\omega) = 3Un + \cfrac{A_0\,\tilde{\Sigma}_0^{(2)}(\omega)}{1 + B_1\tilde{\Sigma}_0^{(2)}(\omega) + \cfrac{C_1\left(\tilde{\Sigma}_0^{(2)}(\omega)\right)^2}{1+B_2\tilde{\Sigma}_0^{(2)}(\omega)+\cfrac{C_2\left(\tilde{\Sigma}_0^{(2)}(\omega)\right)^2}{1+B_3\tilde{\Sigma}_0^{(2)}(\omega)}}} \tag{6.31}$$

This expression can even be truncated at the second level since triple occupancies are extremely unlikely for $n_{tot} < 1$:

$$\Sigma_{int}(\omega) \approx 3Un + \cfrac{A_0\,\tilde{\Sigma}_0^{(2)}(\omega)}{1 + B_1\tilde{\Sigma}_0^{(2)}(\omega) + \cfrac{C_1\left(\tilde{\Sigma}_0^{(2)}(\omega)\right)^2}{1+B_2\tilde{\Sigma}_0^{(2)}(\omega)}} \tag{6.32}$$

For large U, one can show that C_1,B_1, and B_2 behave as $C_1 \sim 1/U^2$,$B_2 \sim 1/U$, and $B_2 \sim 1/U$. Therefore (6.32) can be rewritten in the form:[4]

$$\Sigma_{int}(\omega) \approx 3Un + \frac{A_0\,\tilde{\Sigma}_0^{(2)}(\omega)}{\left(1-\frac{C_1}{B_2^2}\right) + \left(B_1 + \frac{C_1}{B_2}\right)\tilde{\Sigma}_0^{(2)}(\omega) + O(\frac{1}{U})} \tag{6.33}$$

Neglecting the terms of order $\frac{1}{U}$ in the denominator, we arrive at an expression which has a form similar to in the one band model. By construction the self energy (6.33) has the right atomic limit only for $U = \infty$. In this limit the simplified expression agrees with that of the original scheme. If used for the treatment of the multiband Hubbard model, (6.33) agrees well with the full scheme.

The large U limit of the multiband scheme can be derived from (6.33):

$$\Sigma_{int}(\omega) = 3Un + \frac{A_0}{B_1+\frac{C_1}{B_2}}\left(1 - \frac{1-\frac{C_1}{B_2^2}}{B_1+\frac{C_1}{B_2}}\frac{1}{\tilde{\Sigma}_0^{(2)}(\omega)}\right) \tag{6.34}$$

To leading order in U, one has

$$\frac{A_0}{B_1+\frac{C_1}{B_2}} = -\epsilon_f - 3Un \; + \; O(U^0) \tag{6.35}$$

so that Hartree shift in (6.34) cancels and one is left with a finite limit.

[4]Notice that $\tilde{\Sigma}_0^{(2)}(\omega)$ has a factor 3 compared to the single band model.

The generalization of the general scheme 6.20 to more than two bands is straightforward. The main difference is that the number of independent expectation values for the correlation functions in equation (6.14) becomes larger than in the two band case. Nevertheless, these quantities can still be obtained without much numerical effort within the coherent potential approximation.

6.3 Benchmark against an exactly solvable toy model

As we did for the single band case we will again establish the validity of our approximation scheme by testing it against an exactly solvable toy model. For this purpose we choose the straightforward generalization of (3.53) to the two band case:

$$H_{imp} = \epsilon_f \sum_{m\sigma} f^+_{m\sigma} f_{m\sigma} \; + \; \sum_{m\sigma} V \left(c^+_{m\sigma} f_{m\sigma} + f^+_{m\sigma} c_{m\sigma} \right) \; + \; U \sum_{m} f^+_{m\downarrow} f_{m\downarrow} \, f^+_{m\uparrow} f_{m\uparrow} \tag{6.36}$$

For given parameters V, U, and ϵ_f, this model can be diagonalized exactly. Numerical results are shown in figure 6.1 where we plotted the evolution of the spectral function with decreasing ϵ_f, i. e. increasing filling. For $\epsilon_f > -\frac{U}{2}$ the results are similar to the one band model except for the relation of the weight in the Hubbard bands.

A new regime occurs for $\epsilon \leq -\frac{U}{2} = -2$ where the total filling becomes larger than one. Half filling ($n_{tot} = 2$) is reached for $\epsilon_f = -\frac{3}{2}U = -6$.

These results have to be contrasted with those obtained by the interpolating perturbation scheme (figure 6.2). As can be seen by comparing figures 6.1 and 6.2, there is a reasonable agreement as song as ϵ_f is larger than $\approx -\frac{U}{2}$. This regime corresponds to fillings less than one. For larger particle densities however clear deviations are visible. Both, the exact solution and the interpolating perturbation scheme, form a resonance at zero frequency as the particle density approaches one from below. If n_{tot} is increased further the resonance broadens considerably in the exact solution while it remains narrow in the perturbation scheme. This issue is illustrated in figure 6.3, where we display the exact spectral function together with the approximation for $U = 4$, $V = 0.25$, and $\epsilon_f = -U$. The two low energy peaks making up the resonance in approximation scheme (figure 6.3 b) are separated by a distance which scales with $\frac{V^2}{U}$. The two small frequency poles in the exact solution (figure 6.3 a), in contrast, are separated by the energy scale

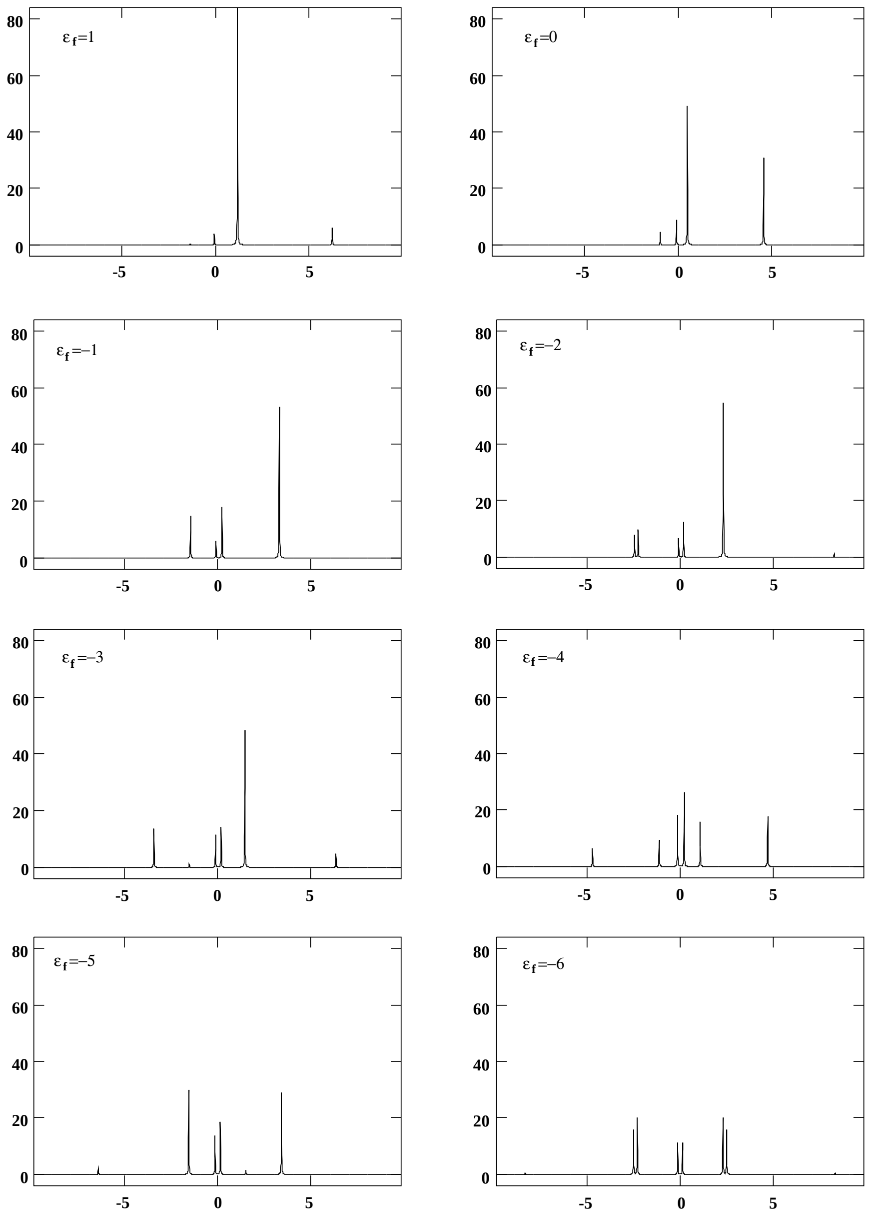

Figure 6.1: *Exact solution* of the two band toy model: Evolution of the spectral function with increasing filling (decreasing ϵ_f) for $U = 4$ and $V = 0.25$. The poles were broadened by a finite $\eta = 0.01$ to make them visible.

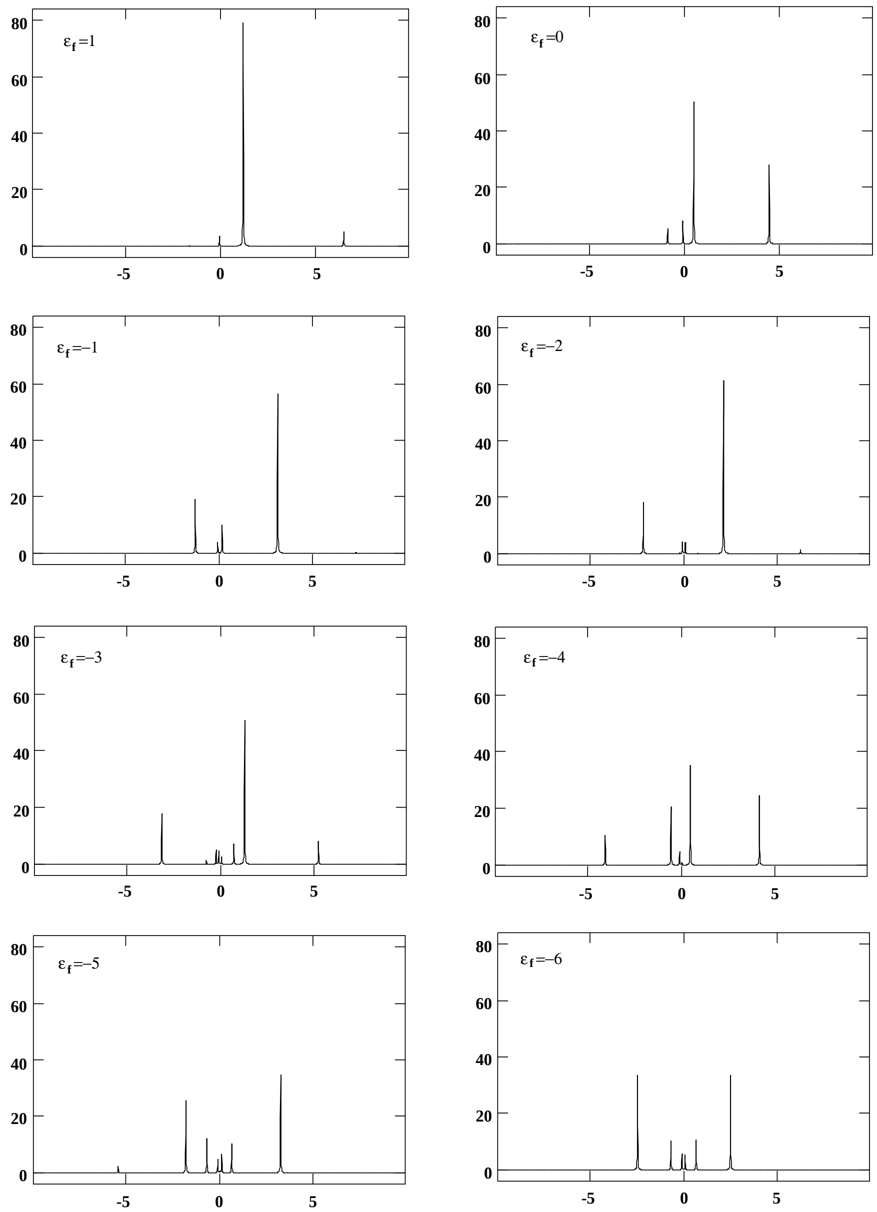

Figure 6.2: *Interpolating perturbation scheme* for the two band toy model: Evolution of the spectral function with increasing filling (decreasing ϵ_f) for $U = 4$ and $V = 0.25$. The poles were broadened by a finite $\eta = 0.01$ to make them visible.

$U = 4$, $V = 0.5$, increasing filling $n_{tot} < 1$

	n_{tot}	p_1	p_2	p_3	p_4	w_1	w_2	w_3	w_4
$\epsilon_f = 1$									
pt	0.336	-2.11458	-0.144112	1.55164	6.71225	0.0084	0.0776	0.7886	0.1161
ed	0.338	-2.02753	-0.144975	1.53806	6.72270	0.0077	0.0769	0.7942	0.1205
$\epsilon_f = 0$									
pt	0.630	-1.66030	-0.180415	0.947587	4.90022	0.0485	0.1107	0.5410	0.2920
ed	0.621	-1.88377	-0.185952	0.976742	5.21793	0.0387	0.1164	0.5832	0.2588
$\epsilon_f = -1$									
pt	0.899	-1.87355	-0.186093	0.564661	3.50806	0.1126	0.1056	0.2740	0.4854
ed	0.880	-2.28945	-0.205648	0.679350	4.01462	0.0888	0.1312	0.3958	0.3749

Table 6.2: Perturbation scheme vs exact diagonalization for $U = 4$, $V = 0.5$, and increasing filling $n_{tot} < 1$.

V. The appearance of the resonance in the solution of the perturbation scheme for larger fillings is therefore clearly an artifact of the method and limits its applicability to particle densities less than one. We will discuss the failure of the scheme for $n_{tot} > 1$ in more detail in section 6.5.

To obtain a more quantitative comparison, we listed in tables 6.2 - 6.4 the position of the poles and the corresponding weights in the regime $n_{tot} < 1$. Only those poles with a non negligible weight were considered. We find in all cases a reasonable agreement between the perturbation scheme and the exact solution. Table 6.2 contains the data for $U = 4$, $V = 0.5$ and increasing filling (i. e. decreasing ϵ_f). We see that the accuracy of the perturbation scheme becomes somewhat worse as $n_{tot} = 1$ is approached. Notice that this trend is the opposite what is observed in the single band case. In tables 6.3 and 6.4 the behavior with increasing U and decreasing V respectively is studied for fixed ϵ_f. There is no clear trend visible because the decrease in the particle number obviously compensates for the decline of the accuracy in the limits $U \to \infty$ and $V \to 0$ respectively.

We conclude that the perturbation scheme for the multiband case is reliable as long as the total particle density is less than one. For larger particle densities the method produces an unphysical narrow resonance peak in the density of states.

6.4 Solution of the lattice problem

We now address the solution of the two band Hubbard model (6.1). The iterative procedure is analogous to the single band case. Starting with a guess for the Green

a)

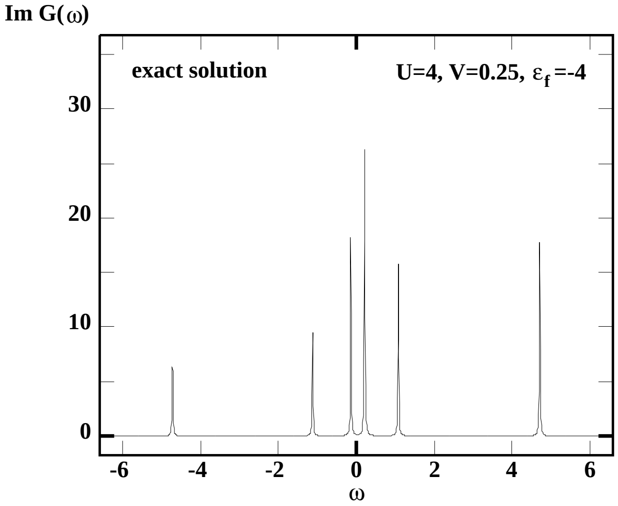

b)

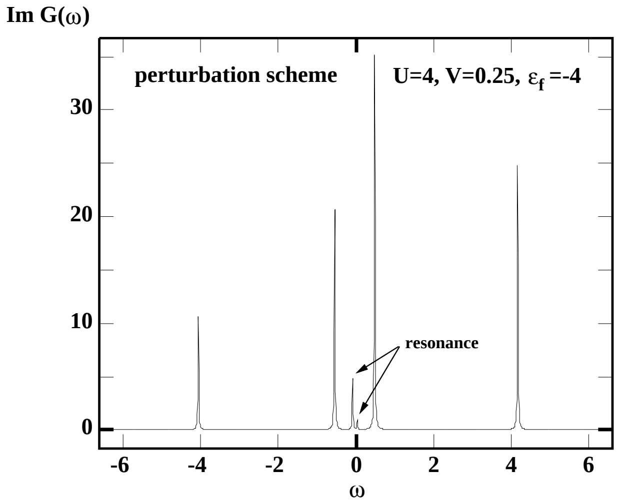

Figure 6.3: Two band toy model for $U = 4$, $V = 0.25$, and $\epsilon_f = -4$: a) The exact solution has no resonance peak. b) The interpolating perturbation scheme however has a resonance at zero frequency.

$V = 0.5$, $\epsilon_f = 0$, increasing U

	n_{tot}	p_1	p_2	p_3	p_4	w_1	w_2	w_3	w_4
$U = 2$									
pt	0.749	-1.60561	-0.21890	0.90310	2.94506	0.0306	0.1556	0.5875	0.2111
ed	0.749	-1.83697	-0.22190	0.93075	3.37062	0.0275	0.1597	0.6355	0.1722
$U = 4$									
pt	0.630	-1.66030	-0.18042	0.94759	4.90022	0.0485	0.1107	0.5410	0.2920
ed	0.621	-1.8838	-0.18595	0.97674	5.21793	0.0387	0.1165	0.5832	0.2588
$U = 8$									
pt	0.569	-1.73468	-0.15418	0.98535	8.90550	0.0607	0.0832	0.5155	0.3348
ed	0.556	-1.88561	-0.16247	0.99338	9.11723	0.0484	0.0906	0.5448	0.3152

Table 6.3: Perturbation scheme vs exact diagonalization for $\epsilon_f = 0$, $V = 0.5$, and increasing U

$U = 4$, $\epsilon_f = 0$, increasing V

	n_{tot}	p_1	p_2	p_3	p_4	w_1	w_2	w_3	w_4
$V = 0.1$									
pt	0.531	-0.36661	-2.6992E-02	0.20511	4.18857	0.0716	0.0714	0.4918	0.3597
ed	0.520	-0.37533	-2.9205E-02	0.19977	4.20976	0.0563	0.0738	0.5185	0.3512
$V = 0.5$									
pt	0.630	-1.66030	-0.18042	0.94759	4.90022	0.0485	0.1107	0.5410	0.2920
ed	0.621	-1.88377	-0.18595	0.97674	5.21793	0.0387	0.1165	0.5832	0.2588
$V = 1$									
pt	0.749	-3.19276	-0.436864	1.80546	5.87137	0.0312	0.1545	0.5866	0.2116
ed	0.749	-3.67393	-0.44379	1.86152	6.74124	0.0275	0.1597	0.6355	0.1722
$V = 2$									
pt	0.951	-6.26538	-1.07222	3.33261	8.24989	0.0155	0.2171	0.6404	0.0991
ed	0.954	-6.85594	-1.07719	3.37701	10.1182	0.0179	0.2205	0.6702	0.0870

Table 6.4: Perturbation scheme vs exact diagonalization for $\epsilon_f = 0$, $U = 4$, and increasing V

function $G(\omega)$ one determines the corresponding bath $\Delta(\omega)$ from the self consistency condition, which for the Bethe lattice is given by $\Delta(\omega) = t^2\, G(\omega)$. Afterwards the corresponding impurity model with $\epsilon_f = -\mu$ is solved as described in the previous section. This yields a new Green function $G_f(\omega) = G(\omega)$ so that the iteration loop is closed.

Here again it is most accurate to perform the calculation first on the imaginary axis to determine $\tilde{\mu}_0$ and the parameters A_0, B_i and C_i which enter the interpolating self energy according to (6.20) or (6.33). Then their values can be used as input for the code on the real axis.

The results obtained for the Hamiltonian (6.1) are particle hole symmetric around $\mu = \frac{1}{2}(U_1 + U_2 + U_3)$. This can be seen by repeating the arguments known for the single band Hubbard model [71]: A gauge transformation in the Wannier representation $\phi_{i,m\sigma} \rightarrow \phi_{i,m\sigma} \exp(i\alpha_i)$ with $\alpha_i - \alpha_j = \pi$ for next neighbor sites i and j yields for the partition function

$$Z_\mu(t) = \mathrm{Tr} e^{-\beta(H-\mu N)} = Z_\mu(-t) \tag{6.37}$$

Now, performing a particle-hole exchange, $c_{im\sigma} \rightarrow c^+_{im-\sigma}$, one finds that $H(t) - \mu N$ is transformed into $H(-t) - (U_1 + U_2 + U_3 - \mu)N + (U_1 + U_2 + U_3 - 2\mu)2L$, where N is the total number of particles and L the number of lattice sites. Using (6.37) we conclude

$$Z_\mu(t) = e^{-\beta(U_1+U_2+U_3-2\mu)2L}\; Z_{U_1+U_2+U_3-\mu}(t) \tag{6.38}$$

The partial derivative $\frac{\partial}{\partial \mu}$ of the logarithm of this equation yields

$$-\langle N_{tot} \rangle = \frac{1}{\beta} \frac{\partial}{\partial(U_1 + U_2 + U_3 - \mu)} \log Z_{U_1+U_2+U_3-\mu}(t) - 4L \tag{6.39}$$

where $N_{tot} = \sum_{im\sigma} n_{im\sigma}$ is the total particle number. Half filling, i. e. $\langle N_{tot} \rangle = 2L$, implies[5] $\mu = U_1 + U_2 + U_3 - \mu = \mu$ or

$$\mu = \frac{1}{2} \left(U_1 + U_2 + U_3 \right) \quad \text{(half filling)} \tag{6.40}$$

Taking the particle hole symmetry into account, we can restrict our discussion to fillings between zero and two or chemical potentials up to $\mu = \frac{1}{2}(U_1 + U_2 + U_3)$.

First we study the "pure" two band Hubbard model where $J = 0$. Afterwards, the effects of different U_i, i. e. finite J are explored.

6.4.1 Vanishing J

In the case $J = 0$, all U_i in (6.1) are equal and the model simplifies to

$$H = -t \sum_{\langle ij \rangle, (m,\sigma)} c^+_{im\sigma} c_{im\sigma} + \frac{1}{2} U \sum_{i,(m,\sigma) \neq (m',\sigma')} n_{im\sigma} \, n_{im'\sigma'} \tag{6.41}$$

This Hamiltonian has a $SU(4)$ symmetry which corresponds to the $SU(2)$ symmetry of the single band case.

If U is large enough, we expect a Mott transition to occur for all integer fillings, i. e. for $n_{tot} = 1$, $n_{tot} = 2$, and $n_{tot} = 3$. As can be seen from the n vs μ plot (figure 6.4) these transitions occur for $U = 4$ around $\mu = 2$, $\mu = 6$, and $\mu = 10$. Notice that the scheme yields only reliable low energy features for $n_{tot} \leq 1$ (or $n_{tot} \geq 3$). But we obtain reasonable data for $n_{tot}(\mu)$ also in the regime $1 < n_{tot} < 2$ because this function is mainly determined by the atomic limit. In comparison with the single band model, the slope of the n vs μ plots is somewhat steeper for the case of two bands (figure 6.5). Thus the compressibility $\kappa = \frac{1}{n^2} \frac{\partial n}{\partial \mu}$ is increased as a result of orbital degeneracy.

As in the single band model the Mott insulator is obtained by fixing $\tilde{\mu}_0$ by $\tilde{\mu}_0 = \mathrm{Re}\Delta(0)$. Plots of the corresponding density of states at $U = 4$, $n_{tot} = 1$ and $\mu = 2$

[5] Strictly speaking this conclusion can only be drawn for the metal but not for the Mott insulator, where there is no one to one correspondence between the particle number and the chemical potential. However, in any case $\mu = \frac{1}{2} \left(U_1 + U_2 + U_3 \right)$ implies half filling.

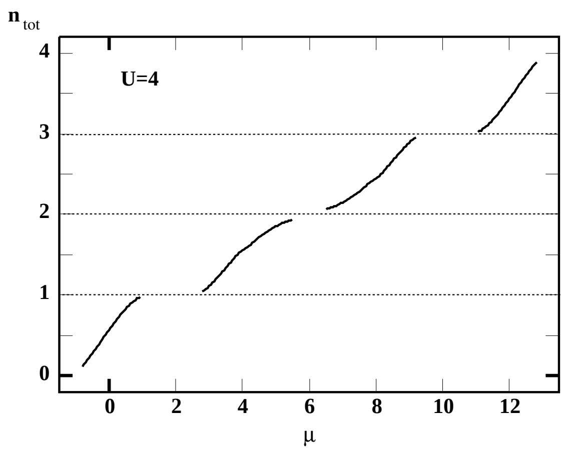

Figure 6.4: Total particle density $n_{tot} := \sum_{m\sigma} n_{m\sigma}$ as a function of the chemical potential μ for $U = 4$ and $J = 0$.

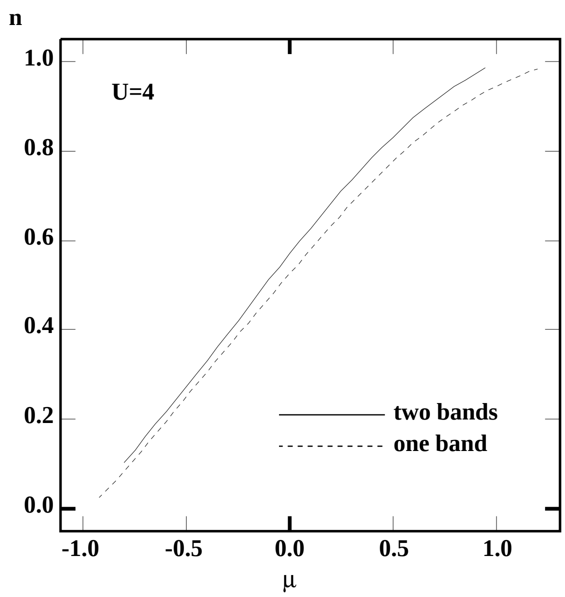

Figure 6.5: Comparison of the n vs μ plots for the two band and the single band model ($U = 4,\ J = 0$).

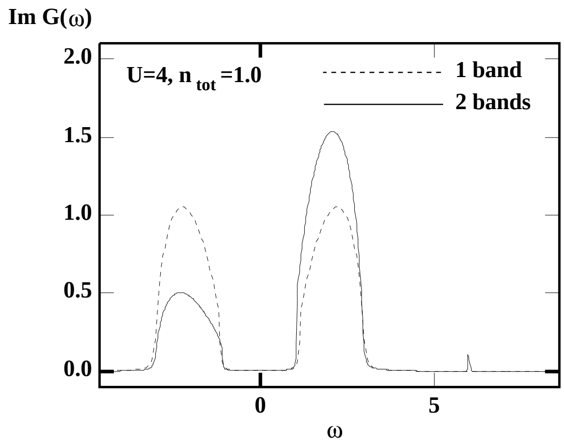

Figure 6.6: Density of states of the Mott insulator at $U = 4$, $J = 0$, and $\mu = 2$ for the one band model (dashed line) and the two band model (full line).

are shown in figure 6.6. For comparison the data of the single band model were also included. In both cases there are two broad Hubbard bands around $-\mu$ and $-\mu + U$. The main difference is the weights of these bands, which in the two band problem are given by $\frac{1}{4}$ and $\approx \frac{3}{4}$ respectively (in contrast to $\frac{1}{2}$ for each band in the single band case). In addition, the density of states of the two band model shows a tiny feature around $\omega \approx -\mu + 2U$. It stems from higher order excitations, which are not possible in the single band model and does not appear if the simplified scheme (6.33) is used. In principle, there has two be another pole around $U \approx \mu + 3U$. But its weight is negligible small so that it cannot be seen in the numerical solution. The density of states for two different values of μ are shown in figure 6.7. Obviously, the relation $G(\omega, \mu) = G(\omega + \mu)$, which is characteristic for a Mott insulator, is not fulfilled. However, the scheme approximates the shift of the Hubbard bands as the chemical potential is varied. The basic features of the Mott insulator can already be obtained within CPA, as is shown in figure 6.8.

Figure 6.9 illustrates how states are created inside the gap upon doping. The evolution of the density of states of the metallic two band Hubbard model with increasing particle density $n_{tot} < 1$ is plotted in figure 6.10. The main difference between the two and the single band case is again the increased weight of the upper Hubbard band (figure 6.9) , which for the two band model approaches $\frac{3}{4}$ (in contrast to one half) for $n_{tot} \to 1$. Like in the insulating state, we observe in the two band model a small peak at

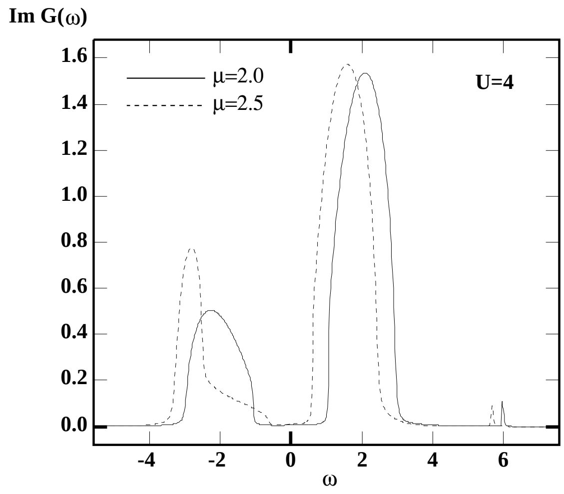

Figure 6.7: Density of states of the Mott insulator at $U = 4$, $J = 0$, and $n_{tot} = 1$ for $\mu = 2$ (full line) as well as $\mu = 2.5$ (dashed line).

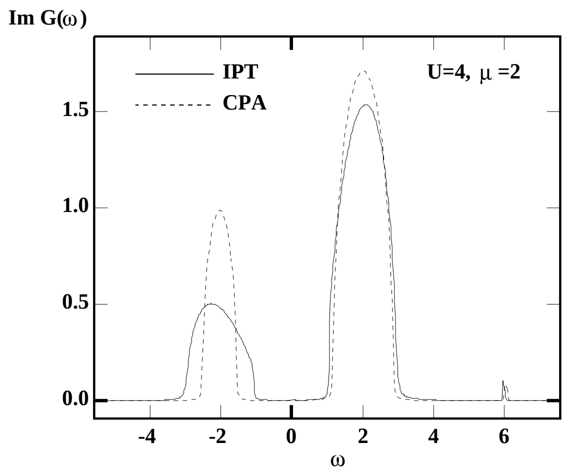

Figure 6.8: IPT compared with CPA: Spectral function of the Mott insulator at $U = 4$, $J = 0$, and $\mu = 2$.

a)

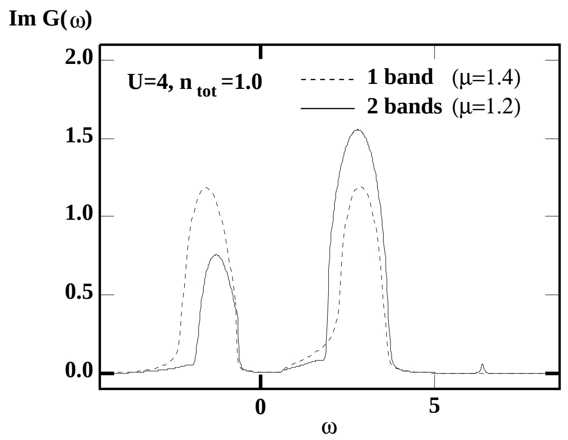

b)

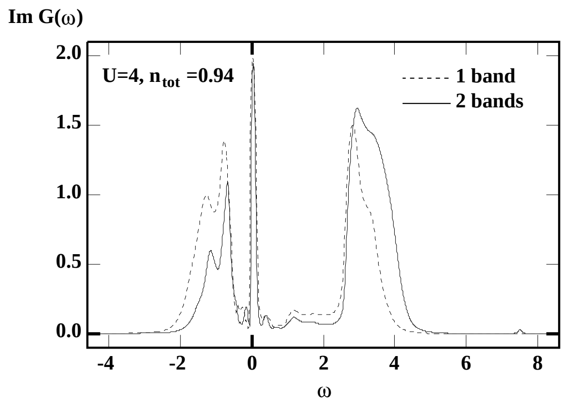

Figure 6.9: Comparison of the spectral functions in the one and the two band model for $U = 4$ (an $J = 0$): a) Mott insulator ($n_{tot} = 1$). b) metallic state for small doping ($n_{tot} = 0.94$). The chemical potential for the Mott insulator in figure a) is chosen such that the difference $\mu_{1band} - \mu_{2band}$ is the same as for the metal plotted in figure b.

$\omega \approx -\mu + 2U$. The weight of this peak is approximately given by $\langle n_{m\sigma} n_{m'\sigma'} \rangle$. Therefore it decreases as the filling is reduced.

Except for these points, the results of the two band model resemble the single band case. We find again a quasiparticle peak which broadens with increasing doping (i. e. decreasing particle number). Near $n_{tot} = 1$ this peak is well separated from the lower Hubbard band. Notice that the distance between both is almost the same like for the one band model (see figure 6.9 b).

Figure 6.11 contains the optical conductivity $\sigma(\omega)$ corresponding to the plots of figure 6.9. The data were calculated from formula (4.1) with an additional factor 2

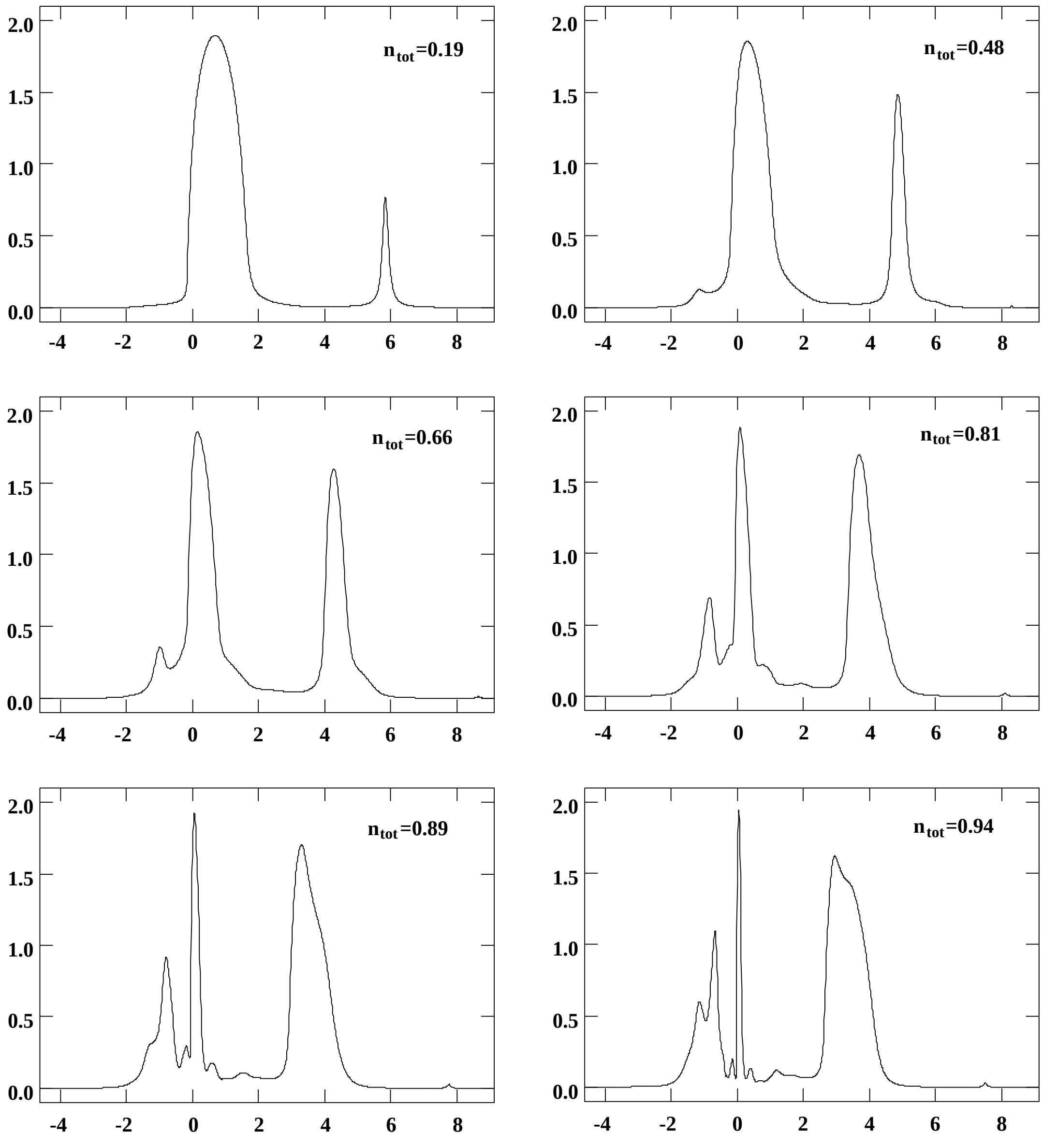

Figure 6.10: Evolution of the spectral functions with increasing particle number n_{tot} for the two band model ($U = 4$, $J = 0$).

taking the orbital degeneracy into account:

$$\sigma(\omega) = 2\sigma_o \frac{D^2}{\omega} \int_{-\infty}^{+\infty} d\epsilon\, \rho_o(\epsilon) \int_{-\infty}^{+\infty} \frac{d\omega'}{2\pi} A_\epsilon(\omega')\, A_\epsilon(\omega'+\omega)(n_f(\omega') - n_f(\omega'+\omega)) \;, \quad (6.42)$$

where $\sigma_o = \frac{e^2 a^2}{4\nu\hbar}$ and $A_{\epsilon_k}(\omega) = -2\,\mathrm{Im}\, G_k(\omega) = -2\,\mathrm{Im} \frac{1}{\omega+\mu-\epsilon_k-\Sigma_{int}(\omega)}$.

For the insulator (figure 6.11 a) we find a single maximum around $\omega = U$. The optical conductivity of the metal at small doping (figure 6.11 b), in contrast, is more complicated. Like in the one band case there are three main maxima P_1, P_2, and P_3. P_1 stems from excitations from the lower Hubbard band to the resonance peak, P_2 represents excitations from the resonance peak to the upper Hubbard band, and P_3 corresponds to excitations from the lower to the upper Hubbard band. This peak is split into two maxima due to the satellite peaks in the lower Hubbard band. The smaller feature between the Drude peak and P_1 is due to the satellite peaks which appear in the spectral function next to the resonance. In the two band model these satellite peaks are quite pronounced. Notice that P_1 has almost the same weight in the one and the two band model because the factor 2 for the orbital degeneracy compensates for the fact that the weight of the lower Hubbard band is reduced by approximately $\frac{1}{2}$.

The evolution of the optical conductivity with increasing filling is displayed in figure 6.12. The data shown correspond to the spectral functions of figure 6.10. For the dilute system $\sigma(\omega)$ does not have much structure. It increases for $\omega \to 0$ and has a small maximum at high frequencies corresponding to excitations into the upper Hubbard band. As the filling is increased, the resonance peak develops in the density of states. This results in the formation of the associated peaks P_1 and P_2, indicating excitations between the resonance and the Hubbard bands. At the same time weight in the upper Hubbard band increases.

As the filling is reduced from $n_{tot} \approx 1$ the resonance peak in the spectral function merges with the lower band. The width of the peak 2Δ measures the quasiparticle residue $Z = 1/\left(1 - \frac{\partial \mathrm{Re}\Sigma(\omega)}{\partial\omega}|_{\omega=0}\right) \approx \Delta/D$, which in turn determines the effective mass $m^* = m/Z$. The quasiparticle residue as a function of the particle number n_{tot} is plotted in figure 6.13. The data were obtained from the imaginary axis with an effective temperature $T = 0.003$. For the very dilute system ($n_{tot} << 1$) Z is of the order one.

a)

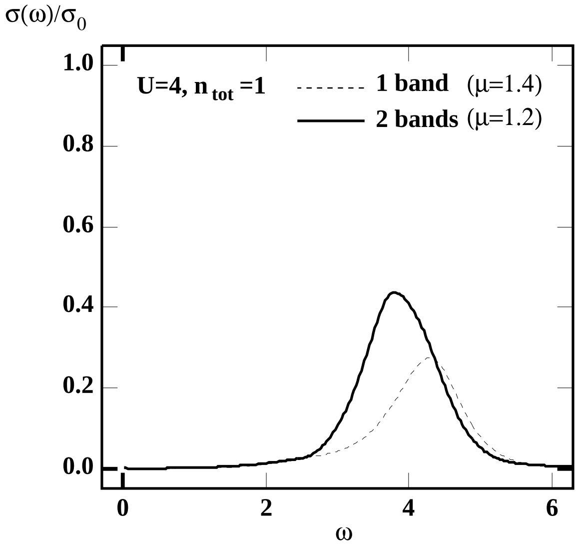

b)

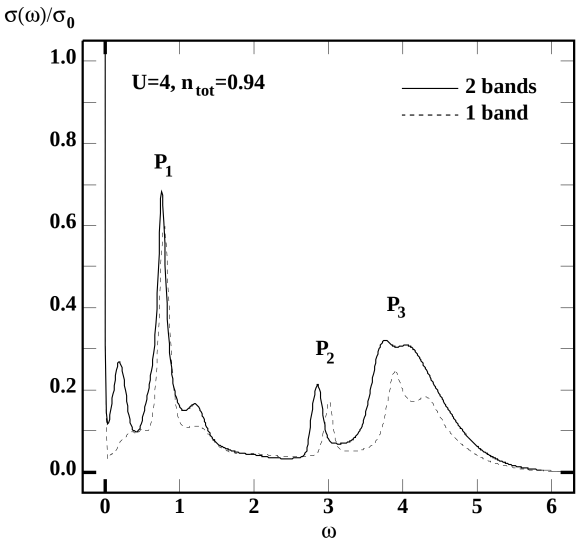

Figure 6.11: Comparison of the optical conductivity of the one and the two band model for $U = 4$ (and $J = 0$): a) Mott insulator ($n_{tot} = 1$) and b) metal at small doping ($n_{tot} = 0.94$).

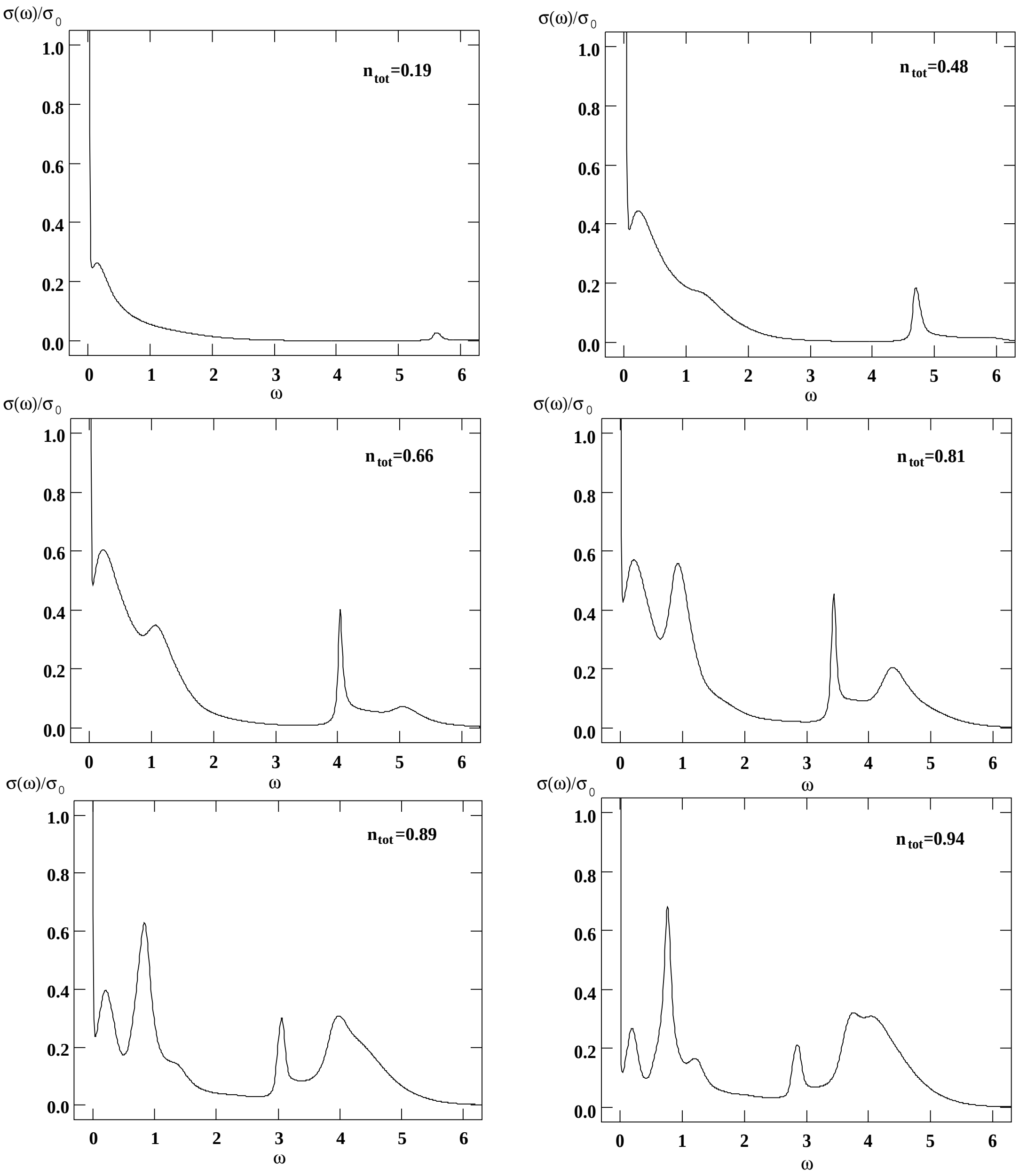

Figure 6.12: Evolution of the optical conductivity with increasing filling ($U = 4$, $J = 0$).

It decreases as the first Mott transition is approached from below. There is a large regime where the dependence of Z on n_{tot} is almost linear. These results for fillings less than one should be compared with the single band model. As can be seen from figures 6.13 to 6.15 the effective mass is slightly *enhanced* by orbital degeneracy. This seems to be a surprising result as one might expect that the system becomes more metallic as the number of bands is increased. In the dilute limit where correlations are weak the effect can be understood by comparing the interaction energy per particle. For the two band model this quantity is given by $6\,U(\frac{n_{tot}}{4})^2/n_{tot} = \frac{3}{8}\,Un_{tot}$ because there are six pairs of interacting orbitals $(m\sigma)$ and the particle density per orbital $(m\sigma)$ is $\frac{n_{tot}}{4}$. This has to be contrasted with the result for the single band case: $U(\frac{n_{tot}}{2})^2/n_{tot} = \frac{1}{4}\,Un_{tot}$. Thus the two band model has per particle a higher interaction energy compared to the single band case so that the effective mass is enhanced. This argument also holds for more than two bands: For l_b orbitals the number of pairs $(m\sigma, m'\sigma')$ is given by $\frac{2l_b(2l_b-1)}{2}$ while $n_{tot}/2l_b$ is the particle density per orbital. For negligible correlations we thus obtain $\frac{2l_b(2l_b-1)}{2}\left(\frac{n_{tot}}{2l_b}\right)^2/n_{tot} = \frac{2l_b-1}{4l_b}\,U\,n_{tot}$ as interaction energy per particle. This expression increases slightly with increasing orbital degeneracy l_b.

As a function of U, the quasiparticle residue decreases from its noninteracting value $Z(U = 0) = 1$ and approaches at finite doping a finite value for large interactions (figure 6.14). For integer filling ($n_{tot} = 1$), on the other hand, Z goes to zero at a critical value U_{c_2} (figure 6.15). The critical U_{c_2} for the instability of the metallic solution is approximately 2.9 which is slightly smaller than in the single band case ($U_{c_2} \approx 3.3$) and in agreement with the observation that the two band model is somewhat less metallic than the single band model with the same U.

The nature of the Mott transition remained a controversial issue for some time and was finally resolved by the application of the projective self consistent method. We have extended these considerations to the degenerate case and shown that the nature of the Mott transition is not qualitatively changed by orbital degeneracy. That is, at zero temperature there is a region in the chemical potential and interaction plane where a metallic and an insulating solution coexist. Simple approximations within this scheme explain the differences in the critical U_c and in the size of the band gaps that

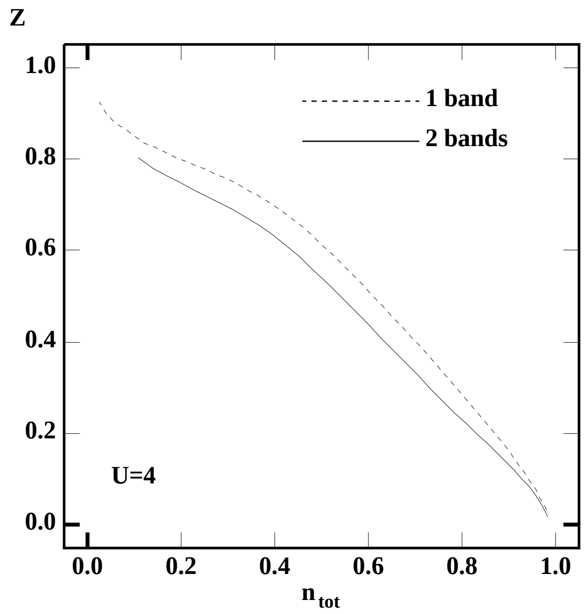

Figure 6.13: Quasiparticle residue $Z = \frac{m}{m^*}$ as a function of the total particle number n_{tot} for $U = 4$ and $J = 0$. The full line corresponds to the two band model while the dashed line marks the single band case. The data were obtained from the imaginary axis with an effective temperature $T = 0.003$.

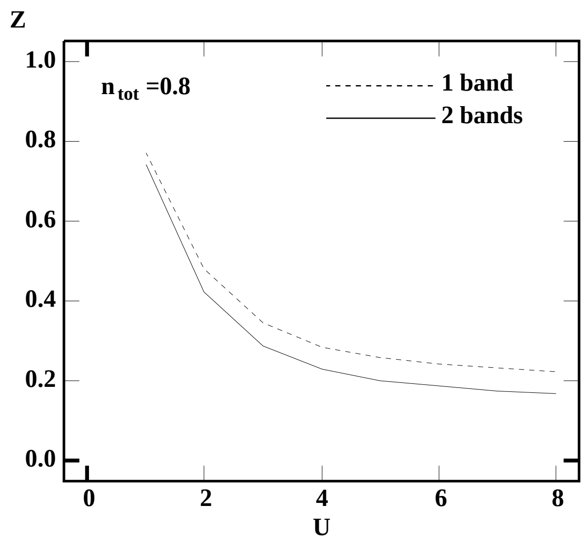

Figure 6.14: Quasiparticle residue $Z = \frac{m}{m^*}$ as a function of U for $n_{tot} = 0.8$ and $J = 0$. The full line corresponds to the two band model while the dashed line marks the single band case. The data were obtained from the imaginary axis with an effective temperature $T = 0.003$.

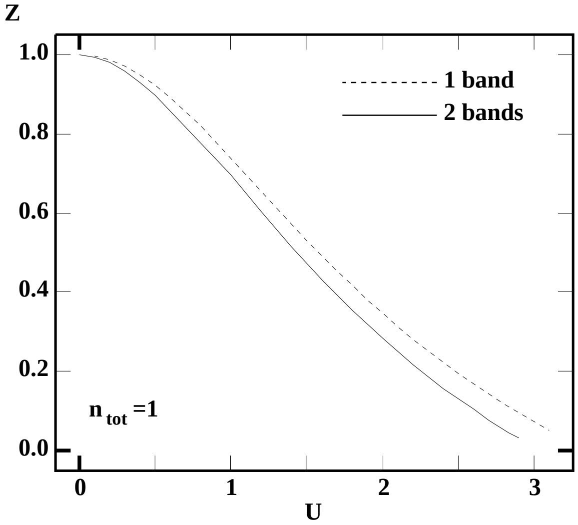

Figure 6.15: Quasiparticle residue $Z = \frac{m}{m^*}$ as a function of U for $n_{tot} = 1.0$ and $J = 0$. The full line corresponds to the two band model while the dashed line marks the single band case. The data were obtained from the imaginary axis with an effective temperature $T = 0.005$.

we observed in IPT and which have also been found in QMC calculations.

In the projective self consistent scheme one separates the set $\{k\}$ of "bath" electrons into sets $H \subset \{k\}$ and $L \subset \{k\}$ with corresponding couplings $\{\epsilon_k^H, V_k^H\}$ and $\{\epsilon_k^L, V_k^L\}$ describing the high and low energy features. Then one projects out the high energy degrees of freedom to obtain an effective self consistent problem for the spectral density, involving the low energy variables only.

The weight of the quasiparticle resonance is $w = \sum_{k \in L} \left(V_k^L\right)^2$. For notational clarity we also affix an L to ϵ_k and $c_{k\alpha}$ for $k \in L$. The quantity w is the small parameter in a singular perturbation theory.

To construct the exact conditions for the Mott transition we separate the impurity Hamiltonian into three parts as

$$\mathcal{H}_{AM} = \mathcal{H}_a + \mathcal{H}_b + \mathcal{H}_m \tag{6.43}$$

The high energy ("atomic"-like) part $\mathcal{H}_a$ is given by

$$\begin{aligned} \mathcal{H}_a &= \frac{U}{2} \sum_{(m\sigma)\neq(m'\sigma')} n_{m\sigma} n_{m'\sigma'} + \sum_{\alpha,k\in H} V_k^H (f_\alpha^+ c_{k\sigma}^H + h.c.) \\ &\quad + \sum_{\alpha,k\in H} \epsilon_k^H \left(c_{k\alpha}^H\right)^+ c_{k\alpha}^H - \mu N \end{aligned} \tag{6.44}$$

$\mathcal{H}_a$ is the Hamiltonian of the Mott insulator with proper occupancy. It has d degenerate ground states carrying a representation of $SU(N)$ ($d = 2l_b$ for $n_{tot} = 1$ and $d = l_b(2l_b - 1)$ for $n_{tot} = 2$; $N = 2l_b$). We label the ground states as $|l>_a$ and define Hubbard operators $X_{ll'} = |l>_a \, _a<l'|$ acting on this low energy impurity doublet.

The low energy spectrum of the impurity Hamiltonian consists of this degenerate manifold combined with excitations of the low energy bath electrons described by the Hamiltonian

$$\mathcal{H}_b = \sum_{\alpha, k \in L} {\epsilon_k}^L ({c^L}_{k\alpha})^\dagger {c^L}_{k\alpha} \tag{6.45}$$

These low energy states are mixed with the high energy excitations of $\mathcal{H}_a$ by

$$\mathcal{H}_m = \sum_{\alpha, k \in L} V_k^L (f_\alpha^+ c_{k\alpha}^L + hc) = \mathcal{V}^{LH} + \mathcal{V}^{HL} \tag{6.46}$$

since $f_\alpha^\dagger$ or f_α acting on $|l>_a$ create particle or hole states with energies increased by at least the particle or hole gap. It is convenient to define normalized operators of the local low energy bath electrons at the impurity site,

$$c_\alpha := \frac{1}{\sqrt{w}} \sum_{k \in L} V_k^L c_{k\alpha}^L \tag{6.47}$$

The total Hamiltonian is then of the form $\mathcal{H}_{AM} = \begin{pmatrix} \mathcal{H}_b & \mathcal{V}^{LH} \\ \mathcal{V}^{HL} & \mathcal{H}_a \end{pmatrix}$. Applying a canonical transformation, one obtains an effective Hamiltonian which is block diagonal and does not mix low and high energy states: $\mathcal{H}_{eff} := e^S \mathcal{H}_{AM} e^{-S} = \begin{pmatrix} \mathcal{H}_{\text{eff}}^L & 0 \\ 0 & \mathcal{H}_{\text{eff}}^H \end{pmatrix}$. Here, the effective Hamiltonian $\mathcal{H}_{\text{eff}}^L$ is defined on the low energy Hilbert space $\{|l>_a\} \otimes \{k \in L\}$. Analogously, the operators f_α are transformed into $F_\alpha := e^S f_\alpha e^{-S} = \begin{pmatrix} F_\alpha^{LL} & F_\alpha^{LH} \\ F_\alpha^{HL} & F_\alpha^{HH} \end{pmatrix}$. In particular, we obtain $F_\alpha^{LL} = \sqrt{w} X_{ll'} J_{ll'}^{\mu\alpha} c_\mu$ where

$$J_{ll'}^{\mu\alpha} \quad := \quad \langle l | f_\mu^+ \frac{1}{H - E_{gs}} f_\alpha | l' \rangle - \langle l | f_\alpha^+ \frac{1}{H - E_{gs}} f_\mu | l' \rangle \tag{6.48}$$

and summation over repeated indices is assumed

The indices μ, μ', and α in (6.48) denote the $2l_b$ spin orbital combinations $(m\sigma)$. The same is true for all other indices as far as $n_{tot} = 1$ is concerned. If $n_{tot} = 2$ and $l_b = 2$, however, the indices l, l', p, and p' should be thought of as double indices, e.g. $l = (l_1, l_2)$, describing one of six possible pairs $(m\sigma, m'\sigma')$, which denote the quantum numbers of the ground state.

If $n_{tot} = 1$ ($l_b = 1$ or $l_b = 2$), the $J_{ll'}^{\mu\alpha}$ are of the form $J_{ll'}^{\mu\alpha} = a_1\, \delta_{ll'}\delta_{\mu\alpha} + b_1\, \delta_{l'\alpha}\delta_{l\mu}$, while for $n_{tot} = 2$ ($l_b = 2$) one has $J_{ll'}^{\mu\alpha} = a_2\, \delta_{l_1 l_1'}\delta_{l_2 l_2'}\delta_{\mu\alpha} - b_2\, \epsilon^{\rho\alpha l_1 l_2}\epsilon^{\rho\mu l_1' l_2'}$.

The low energy part of the self consistency condition becomes $t^2 G^{LL}(\omega) = \sum_{k\in L} \frac{\left(V_k^L\right)^2}{\omega - \epsilon_k^L}$, where $G^{LL}(t-t') = \left\langle T F_\alpha^{LL}(t) \left(F_\alpha^{LL}(t')\right)^+ \right\rangle_{\mathcal{H}_{\text{eff}}^L}$.

In addition, one can write the effective low energy Hamiltonian as

$$\mathcal{H}_{\text{eff}}^L = \mathcal{H}_b + J_s O_s + J_p O_p + \text{const} \tag{6.49}$$

where O_s and O_p are the $SU(N)$ ($N = 2l_b$) generalizations of the spin spin interaction and the potential scattering between the impurity states and the low energy part of the bath of conduction electrons, respectively. For $n_{tot} = 1$ and $SU(N = 2l_b)$, O_s has the form

$$O_s = \left(X_{\mu\mu'} c_\mu c_{\mu'}^+ - \frac{1}{N} X_{\mu\mu} c_{\mu'} c_{\mu'}^+ \right) \tag{6.50}$$

which for $l_b = 1$ (i. e. $N = 2$) can be written as $O_s = 4\,\vec{S} c_\sigma^+ \vec{\sigma}_{\sigma\sigma'} c_{\sigma'}$. For $l_b = 2$ and $n_{tot} = 2$, O_s is given by

$$O_s = \left(\frac{1}{2} X_{pp} c_\mu c_\mu^+ - \epsilon^{\rho\mu p_1' p_2'} \epsilon^{\rho\mu' p_1 p_2} X_{pp'}\, c_\mu c_{\mu'}^+ \right) \tag{6.51}$$

The potential scattering is described by

$$O_p = X_{\mu'\mu'} c_\mu^+ c_\mu \tag{6.52}$$

In equations (6.50) to (6.52) as well as below summation over repeated indices is assumed.

The condition for the destruction of the metallic solution follows from the self consistency condition and is given by $t^2 \left\langle \{ \left(F_\alpha^{LL}\right)^+, F_\alpha^{LL} \} \right\rangle = \sum_{k\in L} \left(V_k^L\right)^2$. Evaluating this expression we obtain:

$$\begin{aligned} 1 \;&=\; \frac{t^2}{2l_b} \left\langle X_{pp'} c_\mu c_{\mu'}^+ \right\rangle \left\{ J_{pl'}^{\mu\alpha} \left(J_{p'l'}^{\mu'\alpha}\right)^\star - J_{lp'}^{\mu\alpha} \left(J_{lp}^{\mu'\alpha}\right)^\star \right\} \\ &\quad + \frac{t^2}{2l_b d} \sum_{ll'\mu\alpha} |J_{ll'}^{\mu\alpha}|^2 \end{aligned} \tag{6.53}$$

It assumes a very simple form in specific cases: For $n_{tot} = 1$ and $l_b = 1$

$$\frac{1}{t^2} = (\frac{3}{4} - \langle O_s \rangle)\, J_s^2 + {J_p}^2 \tag{6.54}$$

with $J_s = b_1$ and $J_p = a_1 + \frac{b_1}{2}$, for $n_{tot} = 1$ and $l_b = 2$

$$\frac{1}{t^2} = (\frac{15}{16} - \langle O_s \rangle)\, J_s^2 + {J_p}^2 \tag{6.55}$$

with $J_s = b_1$ and $J_p = a_1 + b_1/4$, and for $n_{tot} = 2$ and $l_b = 2$

$$\frac{1}{t^2} = \left(\frac{5}{4} - \langle O_s \rangle\right)\, J_s^2 + J_p^2 \tag{6.56}$$

with $J_s = b_2$ and $J_p = a_2 - \frac{b_2}{2}$. Here $\langle \ldots \rangle$ indicates the expectation value with respect to the effective low energy Hamiltonian $\mathcal{H}^L_{\text{eff}}$.

An expression for the parameters a_i and b_i (and therefore J_s and J_p) can be obtained by an expansion in the hybridization. It turns out that the main differences between the transitions at $n_{tot} = 1$ and $n_{tot} = 2$ appear to leading order in this expansion. To illustrate this point let us evaluate $J^{\mu\alpha}_{ll'}$ for the single band model at $n_{tot} = 1$ and for the two band model at $n_{tot} = 1$ as well as $n_{tot} = 2$ (and $J = 0$). We obtain for $n_{tot} = 1$ ($l_b = 1$ or $l_b = 2$) $a_1 = \frac{1}{\mu - U}$ and $b_1 = \frac{1}{\mu} + \frac{1}{U-\mu}$. For $n_{tot} = 2$ and $l_b = 2$, in contrast, one has $a_2 = \frac{1}{\mu - U}$ and $b_2 = \frac{1}{\mu - U} + \frac{1}{2U-\mu}$. These results can be used to estimate U_{c1}, the critical value of the interaction when the insulator ceases to exist, as well as the regime of the stability of the insulating solution in the $\mu - U$ plane. As discussed in reference [16] these quantities are obtained by noticing that for small perturbations $\langle X_{pp'} c_\mu c^+_{\mu'} \rangle \approx \langle X_{pp'} \rangle\ \langle c_\mu c^+_{\mu'} \rangle$. The resulting conditions can be used to determine for given value U the size g_1 of the regime where the insulating solution is stable ("insulating gap"). Around particle hole symmetry, i. e. for $n_{tot} = l_b$ this quantity is given by $g_1 = 2\Delta\mu_c$, where an analytic expression can be obtained for $\Delta\mu_{c_1}$:

$$\Delta\mu^2_{c_1} = \left(\frac{U}{2}\right)^2 + \frac{t^2}{2}\left(1 - \sqrt{1 + 2\,(l_b + 1)\left(\frac{U}{t}\right)^2}\right) \tag{6.57}$$

We see that the insulating gap in the two band model at $n_{tot} = 2$ is smaller than that of the one band model at $n_{tot} = 1$. In addition, it can be shown by evaluating the equations numerically that the gap for $l_b = 2$ and $n_{tot} = 2$ is also smaller than that

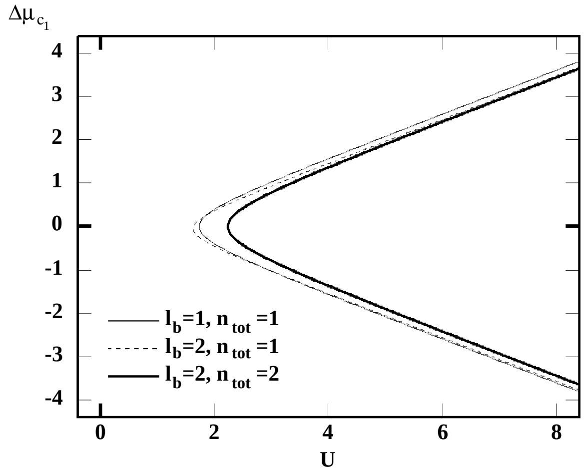

Figure 6.16: Stability of the insulating solution: $\Delta\mu_{c_1}$ as a function of U for a different number of bands l_b and fillings $n_{tot} = 1$ or 2. For $n_{tot} = 1$, $\Delta\mu_{c_1} := \mu_{c_1} - \frac{1}{2}U$ while for $n_{tot} = 2$, $\Delta\mu_{c_1} := \mu_{c_1} - \frac{3}{2}U$.

for $l_b = 2$ and $n_{tot} = 1$. A plot of the critical μ_{c_1} as a function of U is shown in figure 6.16. When comparing the insulating gaps for $n_{tot} = 1$, we find that the values are very similar for $l_b = 1$ and $l_b = 2$.

For the critical interaction at which the insulating gap closes we obtain $U_{c_1}(l_b = 2, n_{tot} = 1) = 1.63 < U_{c_1}(l_b = 1, n_{tot} = 1) = \sqrt{3} < U_{c_1}(l_b = 2, n_{tot} = 2) = \sqrt{5}$.

Notice that $U_{c_1}(l_b = 2, n_{tot} = 1) = 1.63$ is only slightly below $U_{c_1}(l_b = 1, n_{tot} = 1) \approx 1.73$.

There is a second gap g_2 which indicates the instability of the metallic solution. For clarity, let us call this quantity "metallic gap". It is this gap which appears in the n vs μ plot (figure 6.4). A numerical evaluation of this case requires an assumption about the expectation values $\langle O_s \rangle$. Experience with the one band case has shown that these expectation values are in the intermediate coupling range and about one half of their values in the strong coupling (sc) limit: $< O_s >_{sc} = -\frac{3}{2}$ for $n_{tot} = 1$ and $l_b = 1$, $< O_s >_{sc} = -5/4$ for $n_{tot} = 1$ and $l_b = 1$, as well as $< O_s >_{sc} = -5$ for $n_{tot} = 2$ and $l_b = 2$. To estimate g_2 as well as the critical value U_{c_2} at which the metallic solution breaks down, we assume therefore $< O_s > = \frac{1}{2} < O_s >_{sc}$. This yields $U_{c_2} = 2.4$ for $l_b = 1$ and $n_{tot} = 1$, $U_{c_2} = 2.5$ for $l_b = 2$ and $n_{tot} = 1$, and $U_{c_2} = 3.9$ for $l_b = 2$ and $n_{tot} = 2$. Notice, that the values for $n_{tot} = 1$ are again very similar. Within the

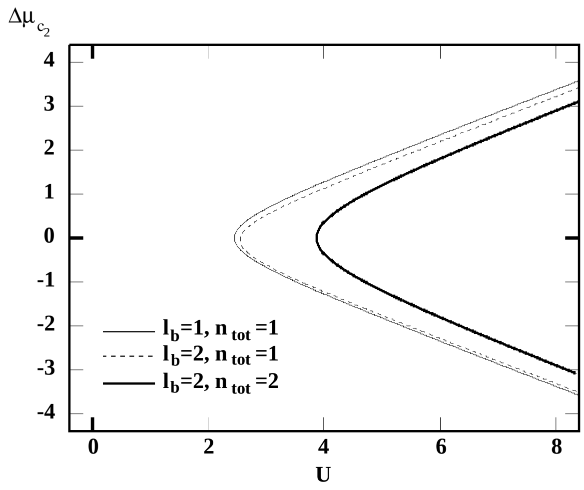

Figure 6.17: Stability of the metallic solution: $\Delta\mu_{c_2}$ as a function of U for a different number of bands l_b and fillings $n_{tot} = 1$ or 2. For $n_{tot} = 1$, $\Delta\mu_{c_2} := \mu_{c_2} - \frac{1}{2}U$ while for $n_{tot} = 2$, $\Delta\mu_{c_2} := \mu_{c_2} - \frac{3}{2}U$.

accuracy of our rough estimates it is not possible to decide which value is smaller in the exact solution. The critical interaction for $l_b = 2$ and $n_{tot} = 2$, in contrast, is clearly larger than for $n_{tot} = 1$. The region in the $\mu - U$ plane where the metallic solution is stable is indicated in figure 6.17, where we plotted $\Delta\mu_{c_2}$ as a function of U. For $n_{tot} = 1$, this quantitiy is defined by $\Delta\mu_{c_2} := \mu_{c_2} - \frac{1}{2}U$ while for $n_{tot} = 2$, $\Delta\mu_{c_2} := \mu_{c_2} - \frac{3}{2}U$. Obviously, also the size of the metallic gap g_2 depends only weakly on orbital degeneracy. For $U = 4$ and $n_{tot} = 1$ we obtain, for example, $g_2 = 2.6$ for $l_b = 1$ and $g_2 = 2.4$ for $l_b = 2$. On the other hand, in the two band model this gap is found to be smaller at $n_{tot} = 2$ than at $n_{tot} = 1$ ($g_2 = 0.7$ for $l_b = 2$, $n_{tot} = 2$, and $U = 4$).

All the qualitative results obtained for U_{c_i} and g_i are in agreement with IPT.

6.4.2 Finite J

Once the intraatomic exchange J is finite, one is dealing with three different interaction constants: $U_1 = U$, $U_2 = U - 2J$ and $U_3 = U - 3J$. The evolution of the spectral density as a function of J is displayed in figure 6.18. As long as J is not too large the main effect is a broadening of the upper Hubbard band. As can be seen from the plots for $J = 0.4$ and $J = 0.6$, the band actually splits into three peaks located around U_1, U_2, and U_3, where the maxima at U_2 and U_3 are hardly separated. Once J becomes so large that $U_3 = U - 3J$ approaches a metallic (i. e. small) value, the overall shape of the density of states changes.

The splitting of the upper Hubbard band can also be seen in the evolution of the spectral density as a function of n_{tot}. This is shown in figure 6.19 for $U = 4$ and $J = 0.5$. Of course, there is also a splitting in the higher order excitations which now occur around $\omega \approx U_1 + U_2$, $\omega \approx U_2 + U_3$, and $\omega \approx U_1 + U_3$. But these peaks are almost invisible due to their small weight.

6.5 Failure of the scheme for $n_{tot} > 1$

In this section we discuss how the iterative perturbation scheme fails to work at fillings larger than one.

When doping the Mott insulator at $n_{tot} = 1$ with particles, we expect in the exact solution a picture similar to that of hole doping: A quasiparticle peak should appear which broadens and merges with the Hubbard band as the filling is increased [95, 94]. In particular, the resonance peak should be broad once it has moved to the middle of the Hubbard band (i. e. $\mu = U$ or $n_{tot} = 1.5$). The only difference compared to the regime with $n_{tot} < 1$ is that with increasing doping spectral weight is transfered to a new Hubbard band appearing around $\omega = -\mu + 2U$. Therefore, one has to consider three (in contrast to two) poles for the Green function in the atomic limit.

Since the physics for fillings larger than one is the same as for $n_{tot} < 1$ or that of the one band model, a reasonable perturbation scheme should describe the Mott transition with the same mechanism as discussed in section 3.7: That is, the Luttinger theorem fixes a value for the self energy $\Sigma_{int}(0)$, which in turn determines a dependence for $\tilde{\Sigma}_0^{(2)}(0) = U^2 S_0$ on the chemical potential μ. For small doping S_0 is essentially a function of $\tilde{\mu}_0$ and the parameter c_1 originating from the high frequency features of the Green function. Since c_1 is almost constant, $\tilde{\mu}_0$ has to adjust as the chemical potential is varied. This forces the resonance with width $\Gamma = \alpha(\tilde{\mu}_0 - c_0)$ to broaden as the doping is increased.

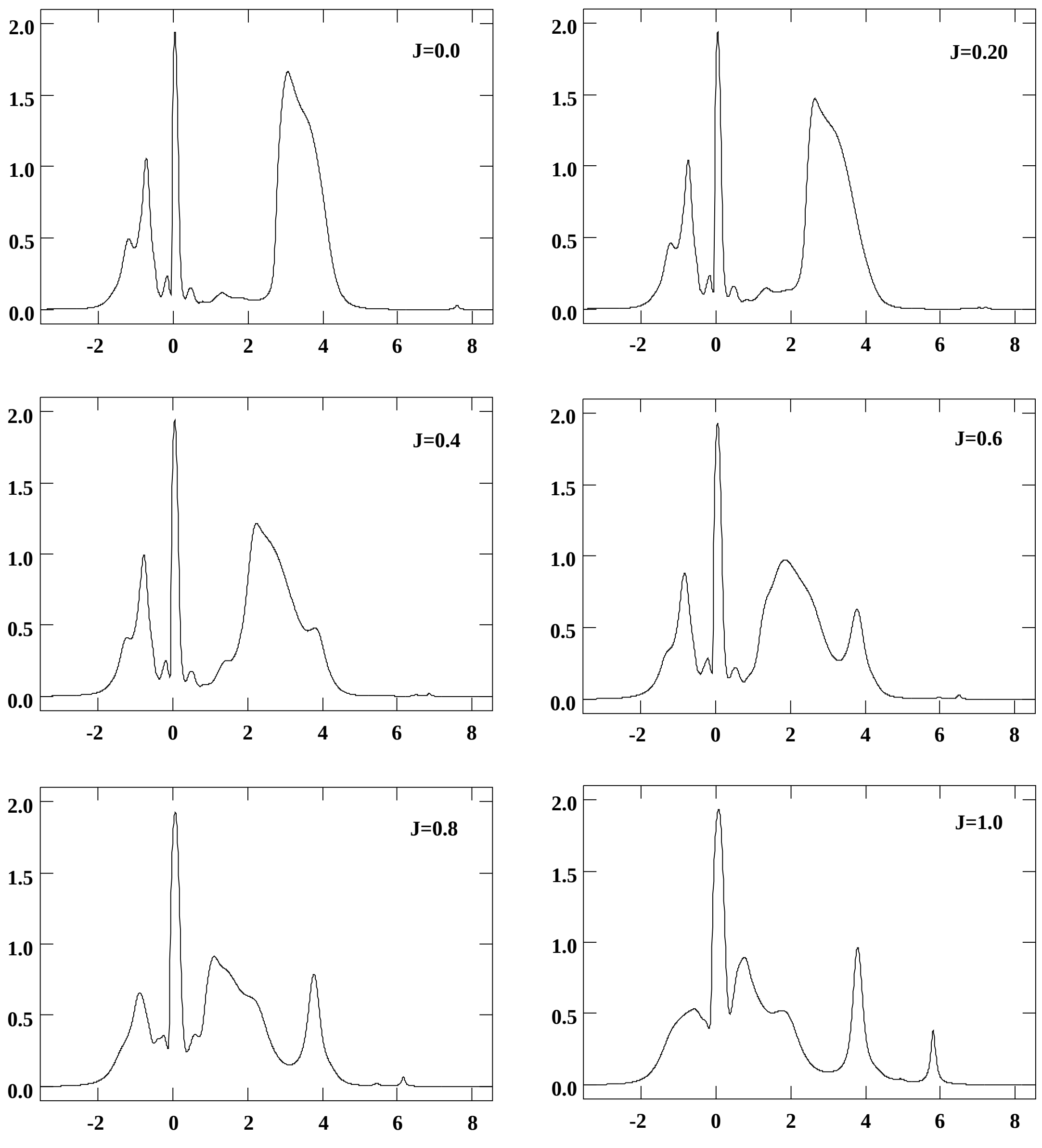

Figure 6.18: Evolution of the spectral function for $U = 4$ and $\mu = 0.75$ with increasing J.

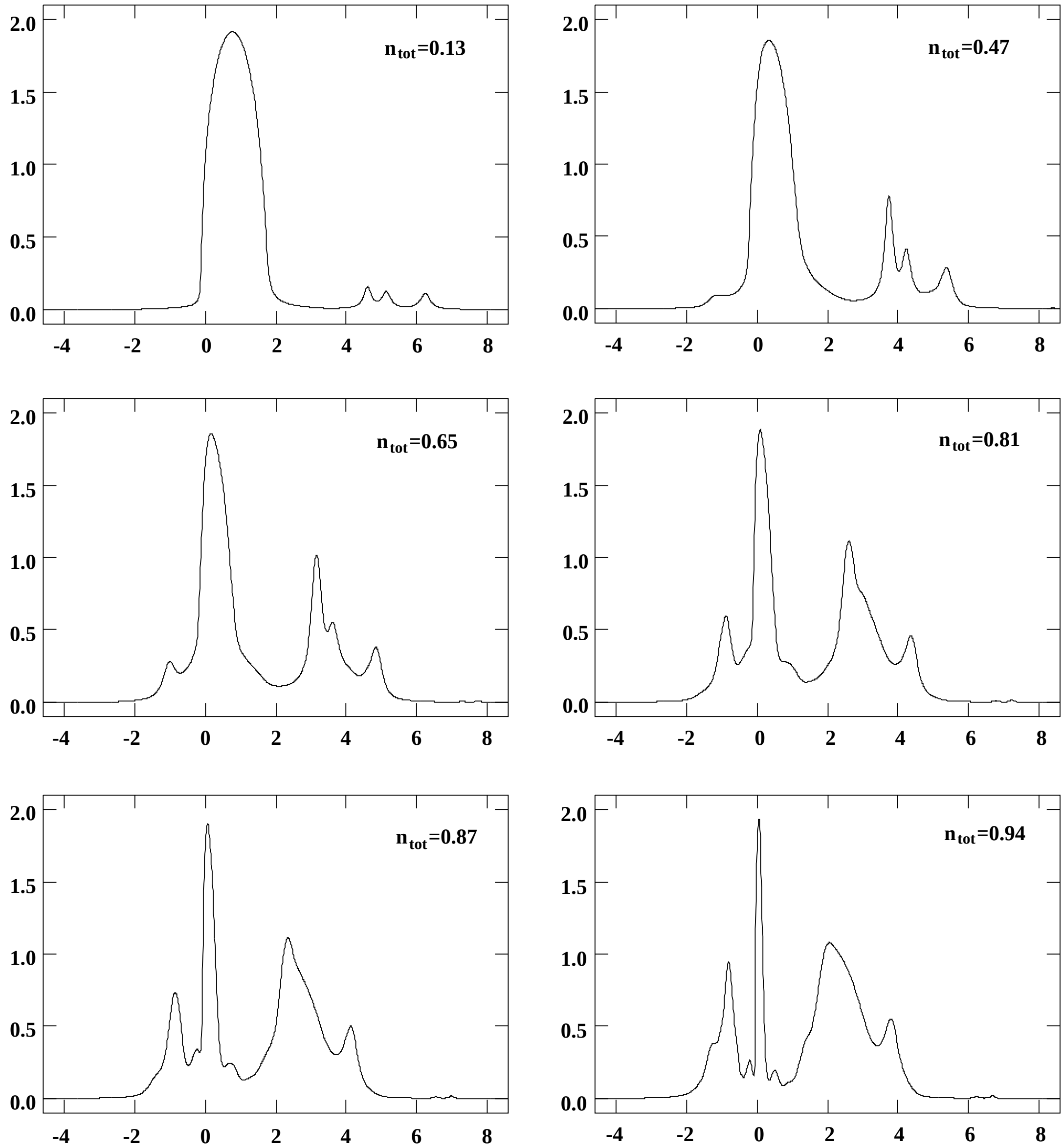

Figure 6.19: Evolution of the spectral function for $U = 4$ and $J = 0.5$ with increasing particle density n_{tot}.

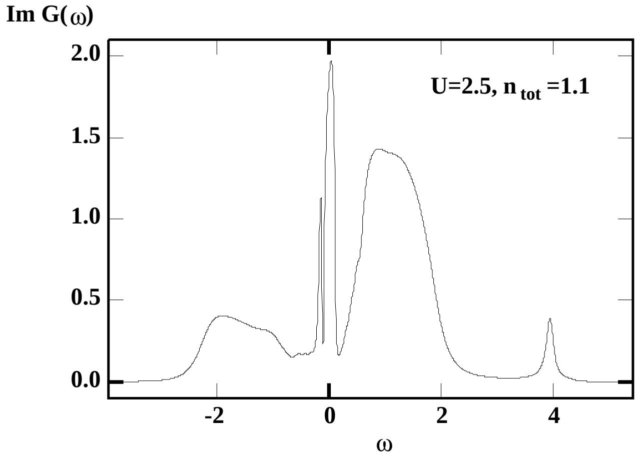

Figure 6.20: Failure of the scheme for $n_{tot} > 1$: The plot displays the double pole structure for $n_{tot} = 1.1$ and $U = 2.5$.

Unfortunately, our scheme behaves differently for $n_{tot} > 1$. For small particle doping it produces a double peak structure instead of a single resonance (see figure 6.20). More precisely, we find a small peak next to the resonance, which allows to satisfy the Luttinger theorem while retaining a narrow resonance peak for all fillings between one and two. At the same time the quantity $\tilde{\mu}_0$ (or $\tilde{\mu}_0 - c_0$) remains small and almost constant.

As will become clear in the next section, these problems are caused by the tail in the continuous fraction of the self energy. This correction does not only insure the right *large* frequency behavior but it also destroys the low energy features.

In particular, the coefficients appearing in the formula for the atomic limit (6.9) acquire a rather nonmonotonic μ dependence once they are evaluated with the correlation functions for *finite* V. The minimal scheme for fillings between one and two has to contain three poles for the atomic limit of the Green function and thus two poles for the self energy:

$$\Sigma(\omega) = 3Un + \frac{Q_1}{\omega + Q_2 + \frac{Q_3}{\omega + Q_4}} \tag{6.58}$$

where $Q_1 = \alpha_1\alpha_2$, $Q_2 = \alpha_3 + \alpha_4$, $Q_3 = \alpha_4\alpha_5$, and $Q_4 = \alpha_5 + \alpha_6$. In figure (6.21) we evaluated these coefficients in CPA. It is apparent that Q_3 and Q_4 vary significantly in the second regime. In particular, there is a point where Q_4 vanishes. Here drastic effects on the low frequency behavior of the self energy are to be expected.

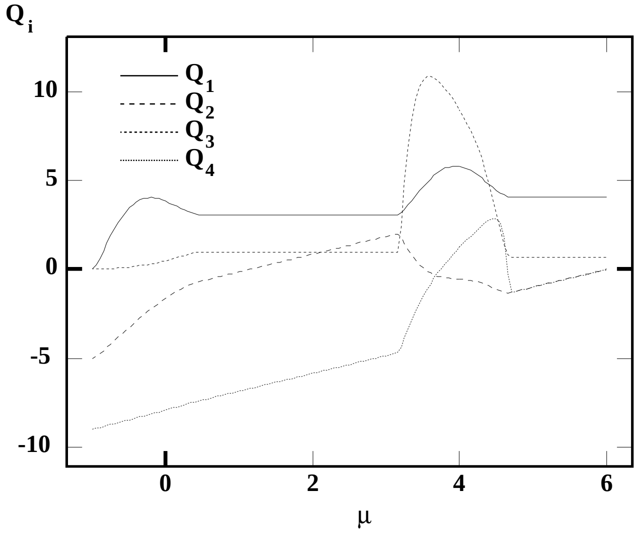

Figure 6.21: Dependence of the coefficients Q_i on the chemical potential for $U = 4$. The data were obtained by CPA.

A more promising approach should clearly separate the different energy scales of the problem. For this purpose however, it seems more reasonable to base an approximation scheme on the the Green function rather than the self energy.

6.6 An extension to fillings larger than one

The artifacts concerning the low frequency behavior can be avoided if the atomic limit used as skeleton for the interpolating self energy expression is expressed in terms of single poles instead of a continuous fraction.

From CPA we know that for fillings between one and two only three poles of the atomic limit of the Green function have a considerable weight. Therefore two poles are required for the atomic limit of the self energy:

$$\Sigma(\omega) = 3Un + \frac{\alpha_2\alpha_3}{\omega + \alpha_3 + \alpha_4 - \frac{\alpha_4\alpha_5}{\omega+\alpha_5+\alpha_6}} \tag{6.59}$$

This expression can be transformed into

$$\Sigma(\omega) = 3Un + \frac{G_1}{\omega - \epsilon_1} + \frac{G_2}{\omega - \epsilon_2} \tag{6.60}$$

where $\epsilon_1 := -\frac{p}{2} - \sqrt{\frac{p^2}{4} - q}$ and $\epsilon_2 := -\frac{p}{2} + \sqrt{\frac{p^2}{4} - q}$ with $p := \alpha_3 + \alpha_4 + \alpha_5 + \alpha_6$ and $q := (\alpha_3 + \alpha_4)(\alpha_5 + \alpha_6) - \alpha_4\alpha_5$. Moreover, the weights G_i are given by $G_1 = \frac{\alpha_2\alpha_3}{\epsilon_1-\epsilon_2}(\epsilon_1 + \alpha_5 + \alpha_6)$ and $G_2 = \frac{\alpha_2\alpha_3}{\epsilon_2-\epsilon_1}(\epsilon_2 + \alpha_5 + \alpha_6)$.

a)

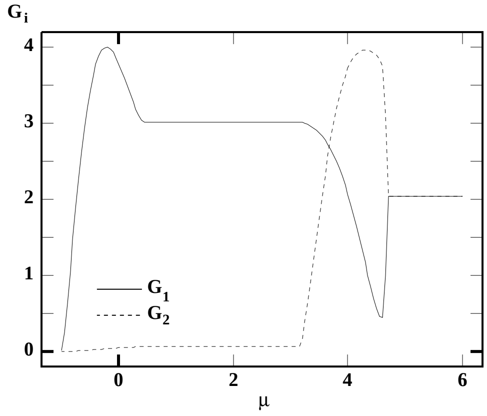

b)

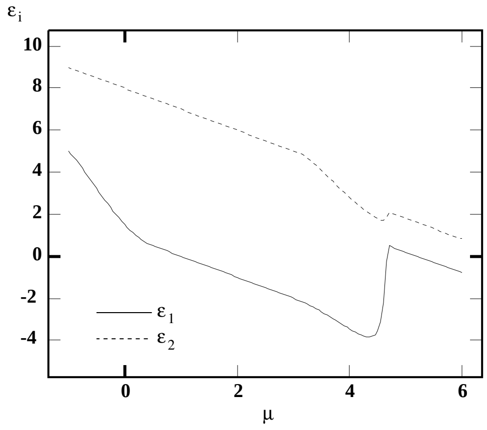

Figure 6.22: Dependence of the coefficients g_i and ϵ_i on the chemical potential. The data were obtained from CPA for $U = 4$.

The parameters G_i and ϵ_i depend again on the particle number as well as the correlation functions $\langle nn \rangle$. In figure 6.22 we evaluated these quantities as a function of μ using CPA (for finite t). For small fillings we have $G_1 >> G_2$.

To construct an interpolating self energy expression, we thus replace the first pole in (6.60) by the building block $\tilde{\Sigma}_0^{(2)}(\omega)$:

$$\Sigma_{int,2}(\omega) = 3Un + \frac{\frac{G_1}{\gamma_0}\tilde{\Sigma}_0^{(2)}(\omega)}{1 - \frac{\epsilon_1 + \tilde{\mu}_0}{\gamma_0}\tilde{\Sigma}_0^{(2)}(\omega)} + \frac{G_2}{\omega - \epsilon_2} \tag{6.61}$$

The parameter $\tilde{\mu}_0$ is again fixed by the Luttinger theorem. Then $\Sigma_{int,2}(\omega)$ has the correct limits for small and large frequencies as well as for $t \to 0$ (or $V \to 0$). However, (6.61) is *not* exact to order U^2.

Numerical results for $U = 4$ obtained by this approach are shown in figure 6.23.

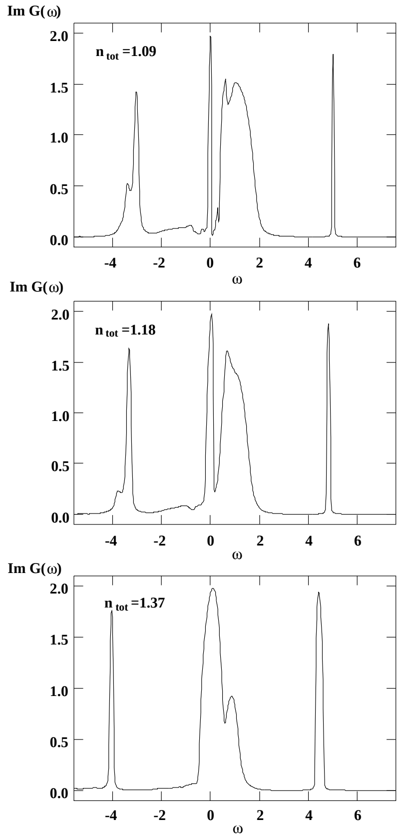

Figure 6.23: Evolution of the spectral function as obtained from the modified scheme for $U = 4$ and $n_{tot} > 1$.

In contrast to the previous scheme we obtain a single resonance peak which broadens with increasing filling (see $Z(n_{tot})$ in figure 6.24). But the scheme breaks down once G_2 becomes larger than G_1, i. e. at $n_{tot} \approx 1.37$ and $\mu \approx 3.7$ respectively. Therefore this approach can only be used for small particle doping.

As far as the original multiband scheme is concerned, these results confirm that the failure of this approach is due to the tail in the continuous fraction, which seriously effects the low frequency behavior.

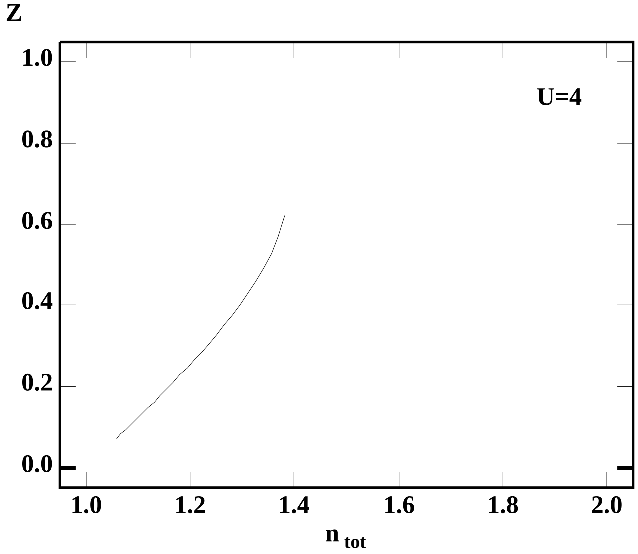

Figure 6.24: Quasiparticle residue as obtained from the modified scheme for $U = 4$ and $n_{tot} > 1$.

6.7 Comparison with experimental data

There is a class of transition metal oxides which shows a filling controlled Mott transition and has been studied experimentally by Tokura *et al.* [28, 29]. An example is $La_{1-x}Sr_xTiO_3$. For $x = 0$, we have $LaTiO_3$, which is a Mott insulator with a Ti $3d^1$ configuration. As x is increased to a finite value, the trivalent La is replaced by the divalent Sr resulting in an effective hole concentration x on the Ti sites. For $x = 1$, i. e. $SrTiO_3$, the d orbitals of Ti are completely empty so that one is left with a band insulator. Hole doping can also be achieved by adding additional oxygens. Since each oxygen accepts two electrons to achieve the O $2p^6$ configuration, we conclude that $LaTiO_{3+\delta/2}$ has hole concentration δ on the Ti sites. Consequently, $La_{1-x}Sr_xTiO_{3+\delta/2}$ has in average $x + \delta$ holes on each Ti site.

Although the perovskite structure of the material should be described by a more complicated Hamiltonian taking the overlap between the different titanium d and oxygen p orbitals into account (see appendix B), it is believed that the Hubbard model might provide a suitable effective Hamiltonian. Here, we will compare the results of the degenerate two band Hubbard model with the experimental data for the optical conductivity [30] shown in figure 6.25. Due to disorder, the experimental sample is

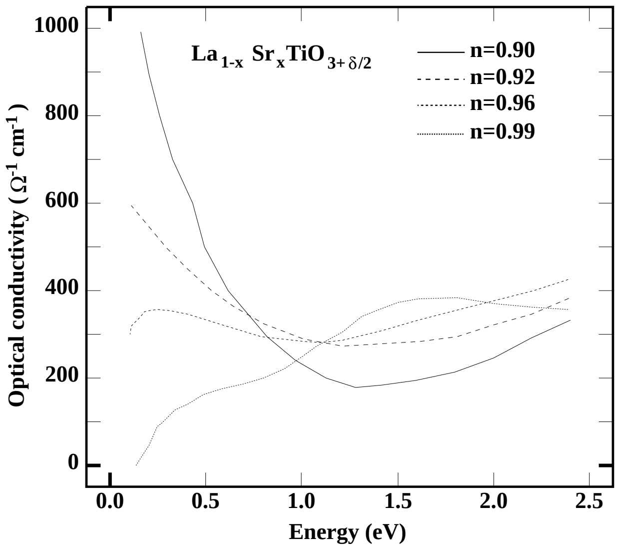

Figure 6.25: Experimental data for the optical conductivity of $La_{1-x}Sr_xTiO_{3+\delta/2}$

found to be insulating for small doping up to $x \approx 0.05$. Therefore only the data for $n_{tot} = 0.9$ and $n_{tot} = 0.92$ in figure 6.25 correspond to the metal. From bandstructure calculations [31] the bandwidth $W = 2D$ of the $La_{1-x}Sr_xTiO_3$ has been estimated to be about $2.5eV$, thus $D \approx 1.25eV$. Substituting La by Y, it is possible to vary the effective interaction U/D. This can be used to determine the critical value of U_c by extrapolating experimental data for the Mott insulator $La_zY_{1-z}TiO_3$. Okimoto *et al.* [31] find $U_c \approx 3.2D = 4eV$, which is reasonably close to the value we found for the two band Hubbard model, $U_{c,IPT} = 2.9D$. $La_{1-x}Sr_xTiO_3$ is only slightly above the Mott transition, $U = 1.02U_c$ [31]. For the theoretical data we choose $U = 3D$. Since the experiments are done at room temperature, which corresponds to $T \approx 0.02D$, we perform our calculations at this temperature. The algorithm for finite T calculations is described in the following chapter.[6] The main difference compared to the $T = 0$ result is that the satellite peaks which appear in the density of states next to the resonance are smeared out. In addition, we model the disorder present in the experimental sample by introducing a finite $\Gamma = 0.2D$ in the formula for the optical conductivity.

The data for the evolution of the conductivity obtained in this way are displayed in

[6] Since $T \approx 0.02D$ is lower than the Kondo temperature of the corresponding impurity model, we do not expect any problems with the application of the finite T code in this case.

figure 6.26. For small doping, we observe a large maximum around $\omega = U$, a peak at an intermediate energy range, and a Drude peak at zero frequency. Notice that in the experiment $U = 4eV$ so that the high energy feature related to the Hubbard bands is not shown in figure 6.25.

The most striking difference between the experimental data and the predictions of the two band model is the absence of the mid-infrared peak in the optical conductivity. From measurements of the specific heat coefficient γ it is known that in the experiment too there is a mass enhancement as the Mott transition is approached (see chapter 5). Therefore a quasiparticle peak should be present. An explanation could be that the distance between the resonance peak and the lower Hubbard band in nature is much smaller than predicted by our simple model. This is consistent with differences in the isobetic point ω_c. As shown in figure 6.27, there is a point ω_c where is the optical conductivity is almost independent of the doping. Our theory yields $\omega_c \approx 1.6D$, which is somewhat larger than the value determined by Tokura *et al.* [30], who obtained $\omega_c = 1.2eV \approx 1D$. Figure 6.27 shows that near the Mott transition with increasing hole doping there is a transfer of spectral weight from the high frequency regime $\omega > \omega_c$ to frequencies $\omega < \omega_c$.

This effect is measured by the doping dependence of an effective particle number defined as [30]

$$N_{eff} := \frac{2m_0\nu}{\pi e^2} \int_0^{\omega_c} \sigma(\omega) d\omega \tag{6.62}$$

Here, m_0 is the free electron mass and ν the volume per Ti atom. Choosing $a \approx 6A$ as lattice constant [111] we evaluated N_{eff} for the theoretical data and compare it in figure 6.28 with the experimental results [30]. For $n_{tot} > 0.5$ there is a good agreement, meaning that the model is able to describe the transfer of spectral weight. Deviations for small filling are an artifact of introducing a finite Γ into the optical conductivity. Katsufuji *et al.* [33] obtained similar plots for a whole series of substances $R_{1-x}Ca_xTiO_3$ with rare earth ions $R = La,\ Pr,\ Nd,\ Sm$, and Y. Fitting a linear behavior to the experimental data for small doping, they showed that the corresponding slope C increases drastically as U_c is approached: $C \sim 1/(U - U_c)$. To check this result we calculated N_{eff}/a^2 for $U = 2.5,\ 3$, and 4 (figure 6.29). In all three cases the

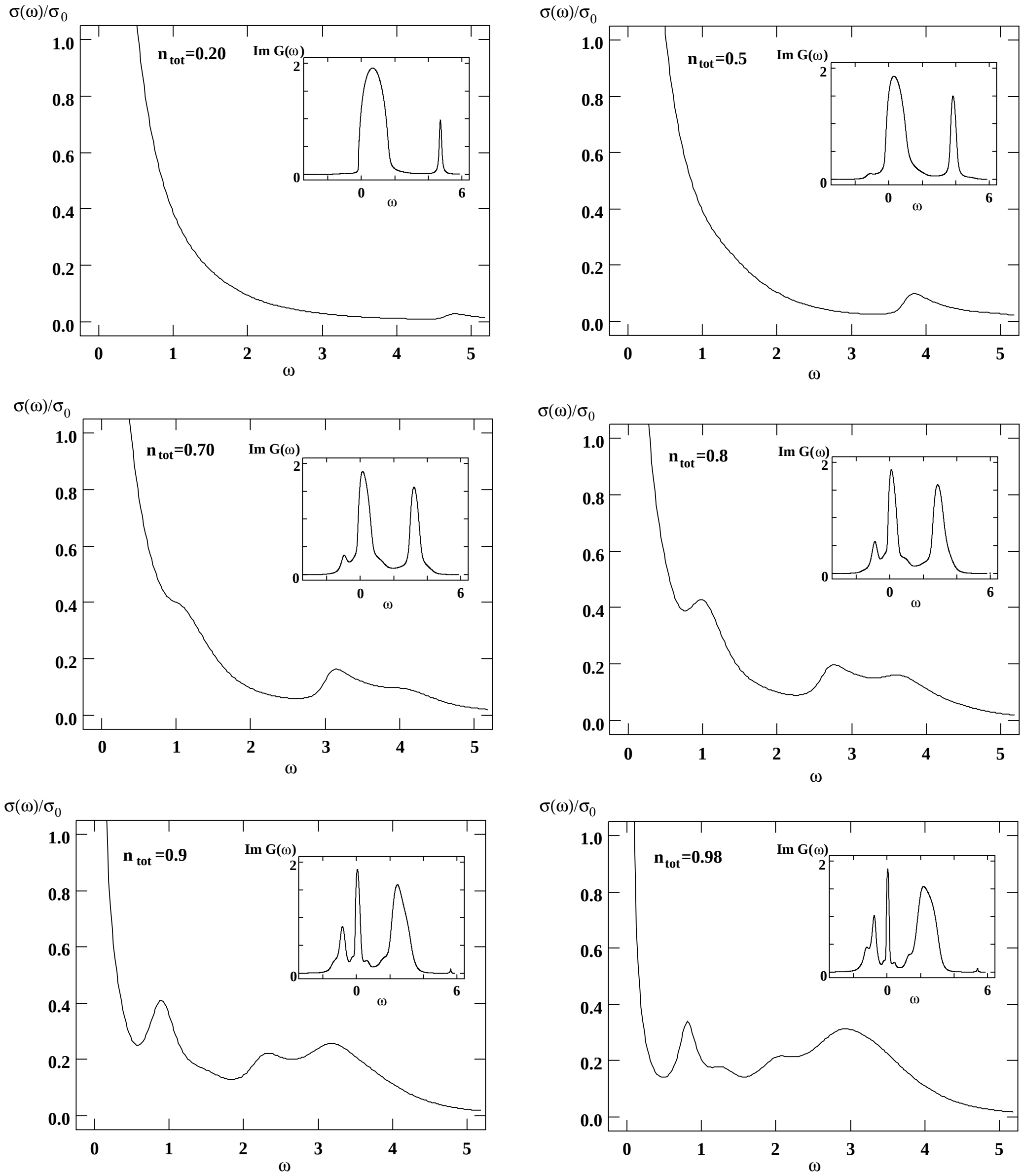

Figure 6.26: Evolution of the optical conductivity for $U = 3$ and $T = 0.02$. The insets show the corresponding spectral functions. A finite $\Gamma = 0.2$ has been introduced in the formula for $\sigma(\omega)$ to model the disorder present in the experimental sample.

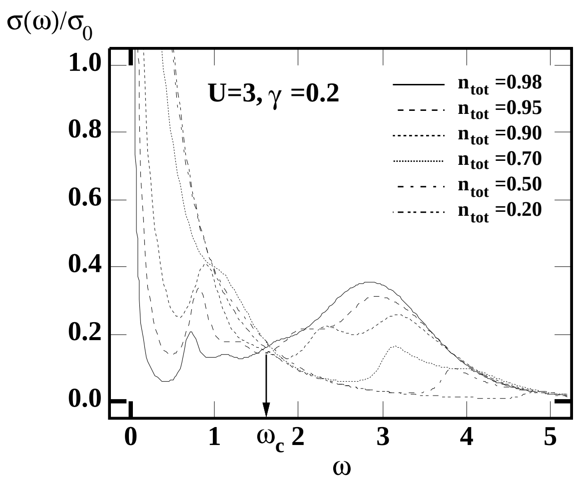

Figure 6.27: Optical conductivity for $U = 3$, $\gamma = 0.2$, $T = 0.02$, and different fillings. The isobetic point is indicated by ω_c

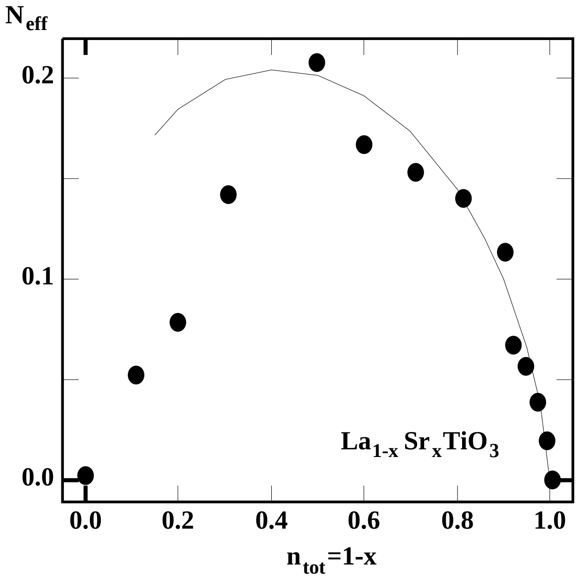

Figure 6.28: Effective electron number N_{eff} as a function of n_{tot}. The full line indicates theoretical results for $U = 3$, $T = 0.02$, and $\Gamma = 0.2$. Experimental data are represented by circles.

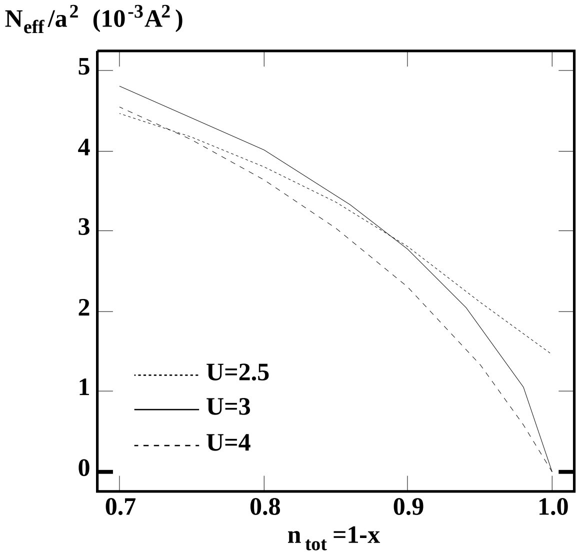

Figure 6.29: N_{eff}/a^2 for different U. The calculations were done at $T = 0.02$ with a finite $\Gamma = 0.2$.

curves are not really linear. The mean slope is enhanced near $U_c = 2.9$. However, comparing the data for $U = 4$ and $U = 3$, we see that the slope does change very much as U_c is approached. These findings are in agreement with Monte Carlo data for the two dimensional Hubbard model [113]. A possible explanation for the deviations between theory and experiment could be the presence of disorder in real materials. It is well known [29] that for small doping several members of the series $R_{1-x}Ca_xTiO_3$ are insulating, so that disorder effects should be taken into account more accurately.

We conclude with a remark on $La_{2-x}Sr_xCuO_4$, a high T_c superconductor with a two dimensional structure. The system differs from $La_{1-x}Sr_xTiO_3$ in that it varies between completely filled d orbitals (d^{10} for $x = 1$) and a d^9 configuration (for $x = 0$). Using the particle hole symmetry of our model Hamiltonian, we expect that our model should also be applicable to this case. However, due to the twodimensional structure, there is only one d orbital which is lowest in energy, so that one is dealing with the single band model. Experimental data [112] for this class of materials are shown in figure 6.30. In contrast to $La_{1-x}Sr_xTiO_3$ the experimental data show a clear mid-infrared peak (indicated by arrows). With increasing hole doping this resonance peak moves towards the Drude peak. Our theoretical results however suggest, that the position of the mid-infrared peak in the optical conductivity shifts slightly to *higher* frequencies

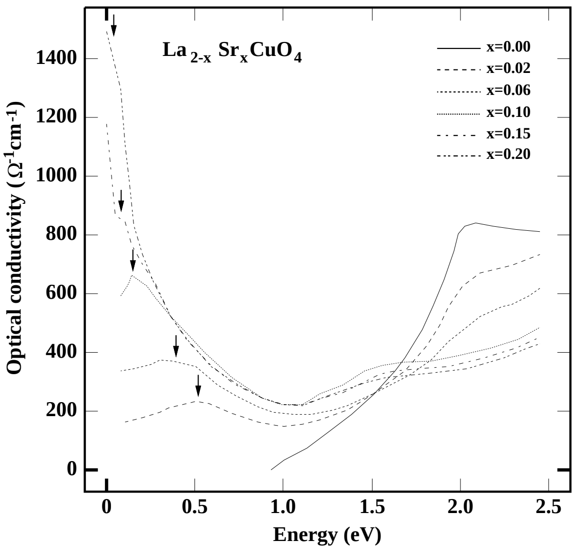

Figure 6.30: Experimental data for the optical conductivity in $La_{2-x}Sr_xCuO_4$. The mid-infrared peak is indicated by arrows.

(see figure 6.27) while the gap between this and the Drude peak is gradually filled up with spectral weight.

The maximum around $\omega = 2eV$ in the experimental data corresponds to a charge transfer excitation between the $O\ 2p$ and $Cu\ 3d$ orbitals in the CuO_2 plane [112] making it impossible to resolve the Hubbard band. Assuming $U = 3.5$, we compare in figure 6.31 the effective electron number of the experiment with the results for the single band Hubbard model. The lattice constant in the theoretical data was fitted such that there is an agreement for small doping (yielding $a = 11A$). Obviously, the theory does not yield a good description for this material.

6.8 Discussion and Conclusions

We showed how the IPT scheme can be generalized for the treatment of multiband models with fillings less than (or close to) one.

Following the spirit of chapter 3 a self energy is constructed which is correct in different limits. The resulting expression depends on correlation functions which are evaluated within the coherent potential approximation. As in the single band case, the numerical solution requires only little computation time so that the algorithm is

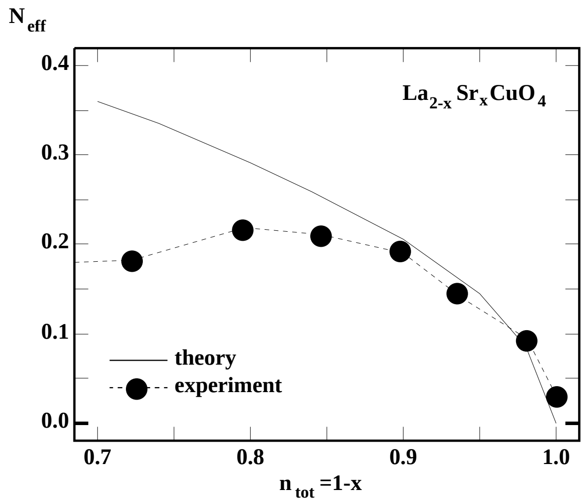

Figure 6.31: Filling dependence of N_{eff} for $La_{2-x}Sr_xCuO_4$: experimental data (closed circles) and results of the single band Hubbard model with $U = 3.5$, $T = 0.02$, $\Gamma = 0.2$, and lattice constant $a = 11A$.

extremely efficient.

For simplicity, the scheme was illustrated for the two band Hubbard model. But the it is also applicable to other multiband problems, so that a method is provided which allows to treat realistic models needed for the description of real materials.

The benchmark against an exactly solvable toy model showed that the scheme is valid only for particle densities less than one. This problem occurs, since the approach does not clearly separate the important energy scales. By correcting for the right high energy poles the low energy features are distroyed. With respect to substances like $La_xSr_{1-x}TiO_3$ the condition $n_{tot} < 1$ is fulfilled. However, it should be mentioned that there are also systems in nature with $n_{tot} > 1$ (e. g. $La_{1-x}Ca_xVO_3$ [75]). They cannot be treated by this approach. We discussed a possible way to obtain a scheme for fillings larger than one. But this attempt is limited to small (particle) doping and not exact to order U^2 for small U.

To explore the effects of orbital degeneracy, we studied the frustrated two band Hubbard model and compared the results with the single band problem. In general, differences appear only in the high energy features while the low energy properties remain unchanged. As expected the calculations lead to a Mott transition at all integer fillings provided the interaction is large enough.

The spectral functions show the same qualitative features: A resonance peak, which at small doping is well separated from the lower Hubbard band and merges into this band as the (hole) doping is increased. The weights of the Hubbard bands change however significantly if orbital degeneracy is introduced. A finite J at fillings less than one yields a broadening and splitting respectively of the upper Hubbard band.

We find that in the two band case the compressibility is slightly enhanced and the effective mass a bit decreased compared to the single band problem with the same interaction U. The critical values U_{c_i} for the instability of the metallic or the insulating solution at $n_{tot} = 1$ are slightly lower than in the one band case. The fact that these values depend only weakly on orbital degeneracy can be understood within the projective self consistent method, which also predicts that the critical U_{c2} at $n_{tot} = 2$ is smaller than at $n_{tot} = 1$. In addition, we saw that at the $n_{tot} = 1$ transition the size of the gap is also almost independent of the number of bands, while the gap for $l_b = 2$ and $n_{tot} = 2$ is considerably smaller.

Our results explain why the simple single band Hubbard model can successfully describe several experiments on multiband systems qualitatively [5]. On the other hand it is clear that a more detailed description will require more complicated models, which have to be solved by iterative perturbation theory.

To make contact with experiments, we calculated the optical conductivity of the two band Hubbard model and compared the results with experimental data on $La_{1-x}Ti_xTiO_3$ and $La_{2-x}Sr_xCuO_4$. As far as $La_{1-x}Ti_xTiO_3$ is concerned, we find that the theory correctly describes the transfer of spectral weight as a function of doping. However, our calculations predict the presence of a clear mid-infrared peak in the optical conductivity, which is not seen in these materials. Such a peak is found in $La_{2-x}Sr_xCuO_4$, but it does not show the right behavior as a function of doping. Presumably, these differences are due to the simplicity of the model considered thus confirming the need of exploring more refined models.

Chapter 7

Extension to Finite Temperatures

So far our perturbation scheme has only been formulated for zero temperature. Various applications treated in previous chapters proof that the method is very powerful in this case. However, being interested in the application of the large d limit to experiments one would like to have an approach which is applicable at finite temperatures too. In this chapter we will therefore look for a suitable generalization.

The Luttinger theorem and the Friedel sum rule respectively are only valid at zero temperature so that one is missing an important ingredient for fixing the low frequency limit of the interpolating self energy. Instead one has to make an additional assumption to obtain a closed set of equations.

In the context of the single impurity Anderson model, two possibilities have been studied: Horvatic et al. require the bare Green function G_0 to be the Hartree Fock approximation of the Anderson Hamiltonian [73]. Martin-Rodero et al., in contrast, assume that the particle numbers determined from G and G_0 are equal ($n = n_0$) [37]. Since both approaches do not capture the correct low frequency behavior at zero temperature we will proceed differently fixing $\tilde{\mu}_0(n)$ at its zero temperature value. The advantage of this procedure is that we recover the $T = 0$ results for $T \to 0$. This approximation describes the decay of the resonance peak as a function of temperature. However, we obtain some unphysical results if more sensitive quantities like the scattering rate are considered. The deficiencies of the scheme can be traced back to an incorrect transfer of spectral weight as the resonance peak decays with increasing temperature. This is a general problem of the IPT scheme which is already present at particle hole symmetry.

7.1 The scheme at finite temperatures

For simplicity, the equations are formulated for the one band Hubbard model on a Bethe lattice.

First, we determine $\tilde{\mu}_0(n; T = 0)$ using the zero temperature scheme. As an approximation we then require that this relation also holds at finite temperatures (i. e. $\tilde{\mu}_0(n; T) = \tilde{\mu}_0(n; T = 0)$).

For fixed particle number n (and therefore fixed parameter $\tilde{\mu}_0 = \tilde{\mu}_0(n, T = 0)$), the iterative algorithm looks as follows: Starting with a guess for the advanced Green function G and the chemical potential μ we obtain G_0 from

$$G_0^{-1}(\omega) = \omega - i\eta + \tilde{\mu}_0 - t^2\, G(\omega) \tag{7.1}$$

Afterwards the fictitious particle number n_0 is computed from G_0. Now, following the equations A.14 to A.19, we compute the second order contribution to the self energy $\tilde{\Sigma}_0^{(2)}$. The result is used to determine the interpolating self energy:

$$\tilde{\Sigma}_{int}(\omega) = Un + \frac{\frac{n\,(1-n)}{n_0\,(1-n_0)}\, \tilde{\Sigma}_0^{(2)}(\omega)}{1 - \frac{(1-n)\,U-\mu+\tilde{\mu}_0}{n_0\,(1-n_0)\,U^2}\, \tilde{\Sigma}_0^{(2)}(\omega)} \tag{7.2}$$

which in turn allows to obtain a new chemical potential μ from the condition:

$$n = \frac{1}{\pi} \int_{-\infty}^{+\infty} d\omega \quad \mathrm{Im} \frac{1}{G_0^{-1}(\omega) - \tilde{\mu}_0 + \mu - Un - \tilde{\Sigma}_{int}(\omega)} \tag{7.3}$$

Finally, the new Green function is given by

$$G^{-1}(\omega) = G_0^{-1}(\omega) - \tilde{\mu}_0 + \mu - Un - \tilde{\Sigma}_{int}(\omega) \tag{7.4}$$

The iteration loop is closed by returning to (7.1).

The interpolating expression for the self energy (7.2) was derived in chapter 3. At finite temperature it is still correct in the weak coupling, the atomic, and the high frequency limit. More precisely, it is exact to order U^2 for small U and to zeroth order in V for $V \to 0$. The low frequency behavior, however, which is determined by the choice of $\tilde{\mu}_0$ is not implemented correctly for $T \neq 0$. Consequently, the numerical results of our scheme show clear deviations for small ω when compared with data from exact diagonalization. Some examples on the imaginary axis are shown in figure 7.1. The agreement between both methods becomes worse with decreasing doping and increasing temperature.

Figure 7.2 displays the corresponding plots on the real axis. The important features of the density of states like the two Hubbard bands and the resonance peak are reproduced at least qualitatively.

Figures 7.3 and 7.4 provide the evolution of the spectral function with increasing temperature for $U = 2$ and $\delta = 0.17$ as well as $U = 4$ and $\delta = 0.07$. In both cases the resonance peak decays so that one is left with two Hubbard bands. Unfortunately we observe that at high temperatures the spectral function for $U = 4$ develops an additional maximum around $\omega = 0.7$. This feature, which does not occur in other methods like exact diagonalization or quantum Monte Carlo, indicates a general problem of the IPT scheme: IPT does not describe the transfer spectral weight as a function of temperature correctly. This will be shown in the next section.

7.2 Transfer of spectral weight - benchmark against an exactly solvable toy model

In order to study the IPT scheme at finite temperatures we compare it again with the exact solution of the toy model which we already explored in section 3.5:

$$H_{imp} = \epsilon_f \sum_\sigma f_\sigma^+ f_\sigma \; + \; \sum_\sigma V \left(c_\sigma^+ f_\sigma + f_\sigma^+ c_\sigma \right) \; + \; U f_\downarrow^+ f_\downarrow \, f_\uparrow^+ f_\uparrow \tag{7.5}$$

Similar like at zero temperature the model can be diagonalized exactly yielding the eigenstates $|n\rangle$ with energies E_n. Then the Green function is determined by[1]

$$G_{f\sigma}(\omega) = \frac{1}{Z} \sum_{n,m} \left(e^{-\beta E_n} + e^{-\beta E_m} \right) \frac{|\langle m|f_\sigma|n\rangle|^2}{\omega + (E_m - E_n) - i\eta} \tag{7.6}$$

The diagonalization can always be performed numerically. In addition, analytic results can be obtained for $U = \infty$. In this case the Green function at low temperatures

[1] $Z := \sum_n e^{-\beta E_n}$

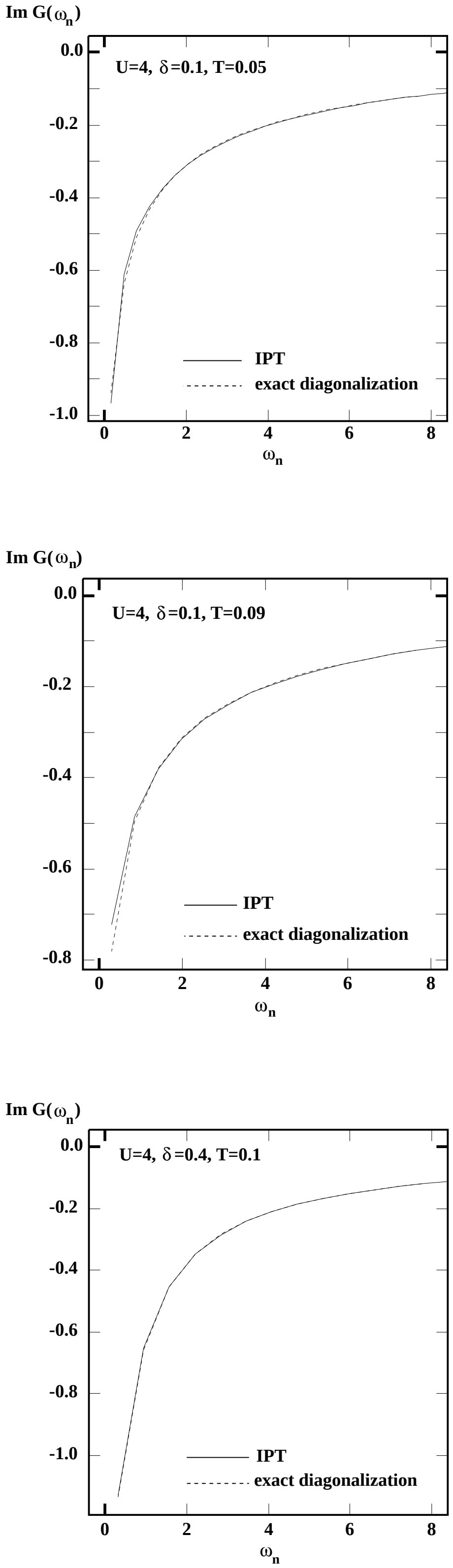

Figure 7.1: Imaginary axis: IPT (full line) versus exact diagonalization (dashed line).

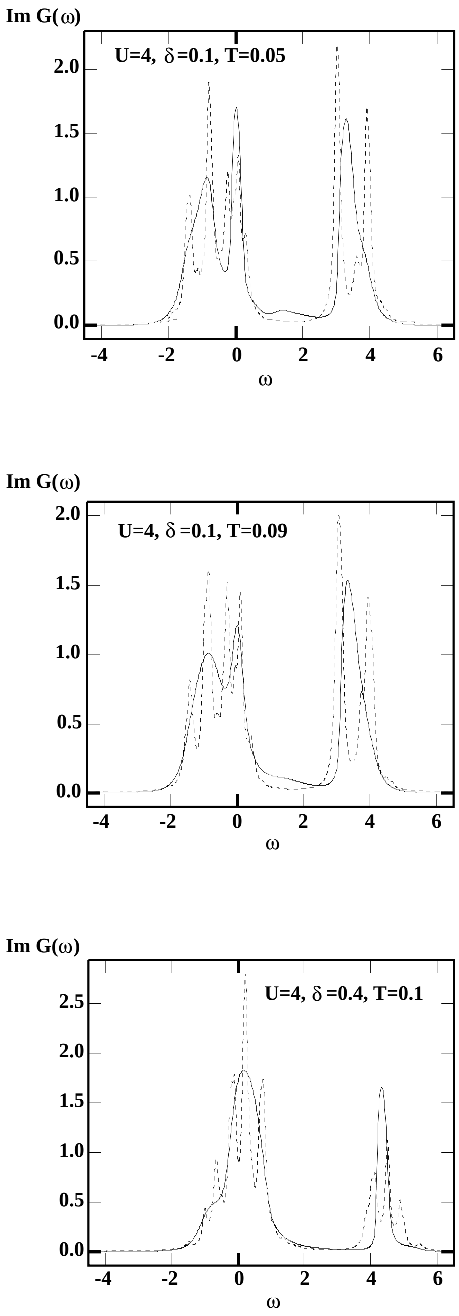

Figure 7.2: Real axis: IPT (full line) versus exact diagonalization (dashed line).

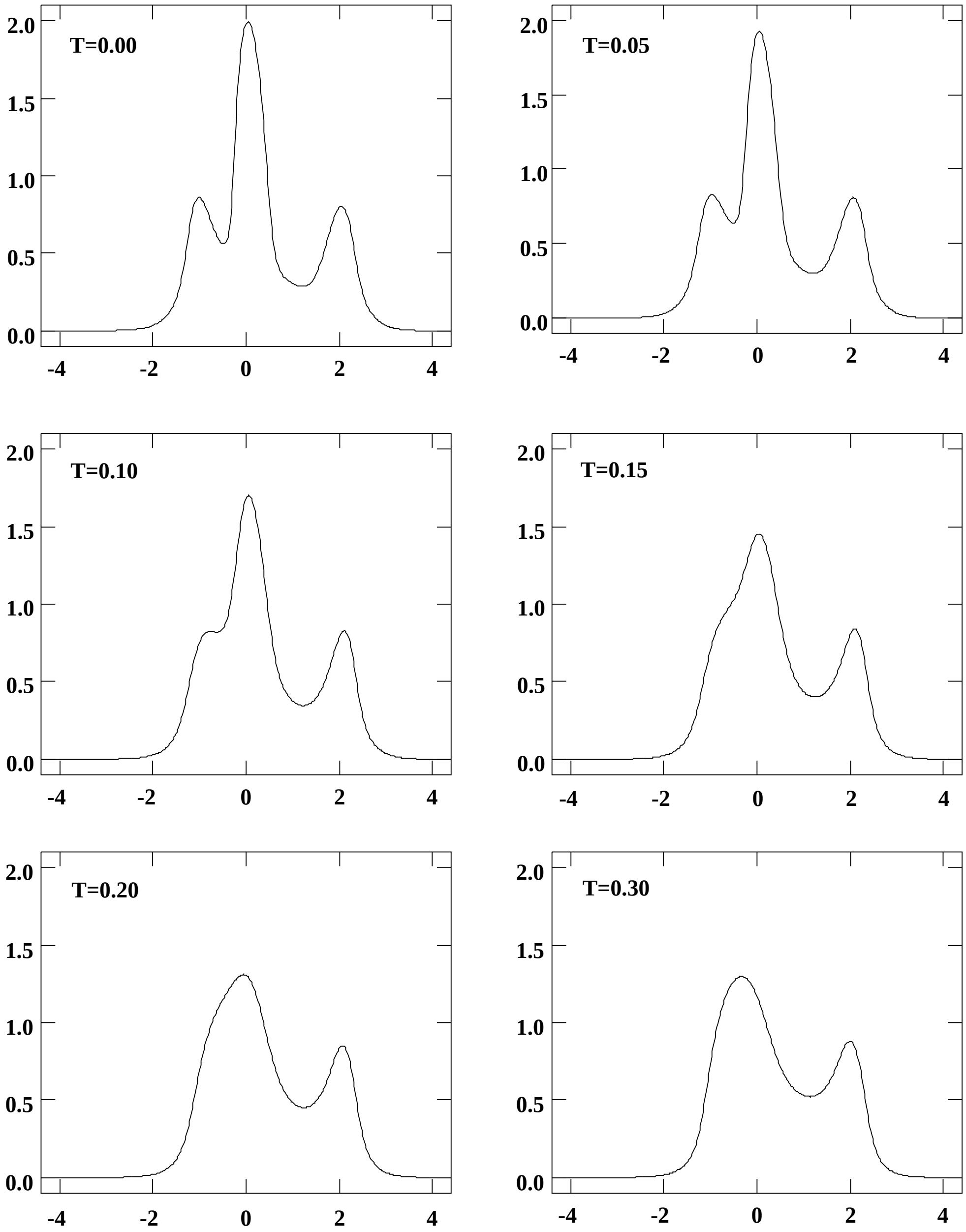

Figure 7.3: Temperature dependence of the spectral function for $U = 2$ and $\delta = 0.17$.

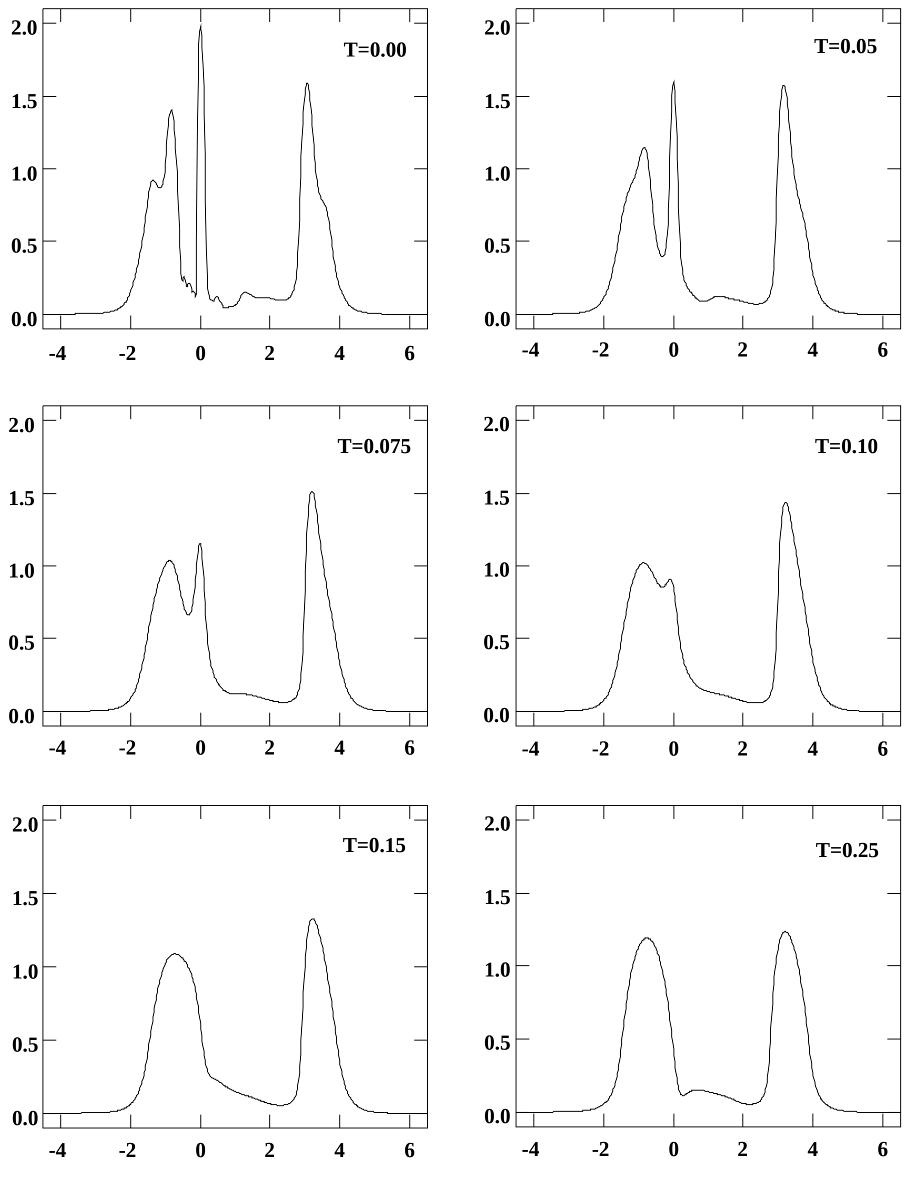

Figure 7.4: Temperature dependence of the spectral function for $U = 4$ and $\delta = 0.07$.

(i. e. $T << \left|\frac{V^2}{\epsilon_f}\right|$) is given by

$$G_f(\omega) = \frac{\frac{1}{2}\left(1 - 3\frac{V^2}{\epsilon_f^2}\right)}{\omega - \epsilon_f - 3\frac{V^2}{\epsilon_f} - i\eta} + \frac{\frac{1}{2}\frac{V^2}{\epsilon_f^2}}{\omega - \frac{V^2}{\epsilon_f} - i\eta} + \frac{2\frac{V^2}{\epsilon_f^2}}{\omega + 2\frac{V^2}{\epsilon_f} - i\eta} \tag{7.7}$$

Here, we assumed $\frac{V}{\epsilon_f} << 1$ and expanded the weights and poles of the Green function up to quadratic order.[2]

The first term in (7.7) represents the lower Hubbard band which is located around ϵ_f and has a weight of almost $\frac{1}{2}$. The other two poles represent the low frequency feature near $\omega = 0$. Their weight is of order $\frac{V^2}{\epsilon_f^2}$. The corresponding spectral function for large U is plotted in figure 7.5.

This picture changes as the temperature is increased. In the temperature regime $\left|\frac{V^2}{\epsilon_f}\right| << T << |\epsilon_f|$ the Green function for $U = \infty$ and $\left|\frac{V}{\epsilon_f}\right| << 1$ is given by

$$\begin{aligned} G_f(\omega) \quad &= \quad \frac{1}{8}\left(\frac{\frac{1}{2}\left(1 - 3\frac{V^2}{\epsilon_f^2}\right)}{\omega - \epsilon_f - 3\frac{V^2}{\epsilon_f} - i\eta} + \frac{\frac{V^2}{\epsilon_f^2}}{\omega - \frac{V^2}{\epsilon_f} - i\eta} + \frac{4\frac{V^2}{\epsilon_f^2}}{\omega + 2\frac{V^2}{\epsilon_f} - i\eta}\right. \\ &\quad \left. + \frac{\frac{5}{2} - 3\frac{V^2}{\epsilon_f^2}}{\omega - \epsilon_f - \frac{V^2}{\epsilon_f} - i\eta} + \frac{1 - 8\frac{V^2}{\epsilon_f^2}}{\omega - \epsilon_f - 2\frac{V^2}{\epsilon_f} - i\eta} + \frac{3\frac{V^2}{\epsilon_f^2}}{\omega + \frac{V^2}{\epsilon_f} - i\eta}\right) \end{aligned} \tag{7.8}$$

I. e. there are six poles (see figure 7.6). Three of them are located around $\omega = \epsilon_f$ and represent the lower Hubbard band. At finite temperature it is "broadened" and slightly shifted in positive ω-direction. The remaining three poles put some spectral weight at low frequencies. The total sum of this spectral weight at small energies is given by $\frac{V^2}{\epsilon_f^2}$, which is smaller than at zero temperature ($\frac{5}{2}\frac{V^2}{\epsilon_f^2}$). The difference ($\frac{3}{2}\frac{V^2}{\epsilon_f^2}$) is transferred to the Hubbard bands.

These results have to be contrasted with the IPT scheme at finite temperatures. In figure 7.7 the evolution of the spectral density in IPT as a function of temperature is shown. At $T = 0$ there is a good agreement with the exact solution. However, as the temperature increases the spectral weight of the resonance is transfered mainly to an intermediate frequency range into two new peaks P_1 and P_2 but almost not to the Hubbard bands. This failure of the IPT scheme is *not* related to our choice for $\tilde{\mu}_0$ but

[2]Notice that for $\omega = 0$ the expression for $G_f(\omega)$ is only exact to zeroth order in V. Thus (7.7) is consistent with $G_f(0) = 0$.

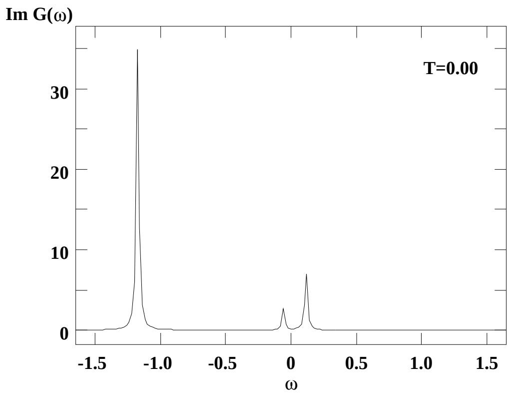

Figure 7.5: Spectral function of the toy model at $T = 0$: exact diagonalization for $U = 30$, $\epsilon_f = -1$ and $V = 0.25$. The upper Hubbard band is not shown. The δ- peaks were broadened by a finite $\eta = 0.01$ to make them visible.)

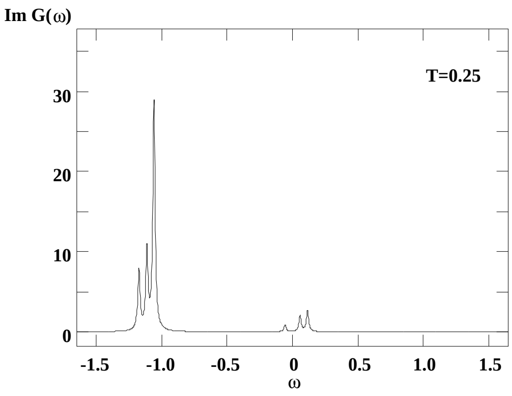

Figure 7.6: Spectral function of the toy model at $T = 0.25$: exact diagonalization for $U = 30$, $\epsilon_f = -1$ and $V = 0.25$. The upper Hubbard band is not shown. The δ-peaks were broadened by a finite $\eta = 0.01$ to make them visible.

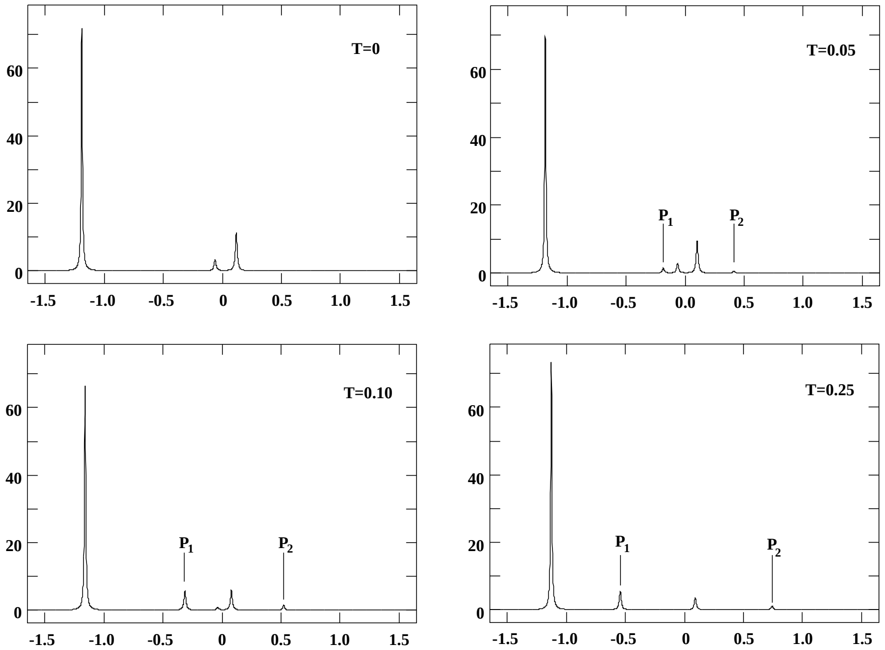

Figure 7.7: Evolution of the spectral function with increasing temperature according to IPT: The spectral weight of the resonance is transfered into two new peaks P_1 and P_2. The data correspond to $U = 30$, $\epsilon_f = -1$, and $V = 0.25$. A finite η was used to broaden the poles. (The upper Hubbard band is not shown.)

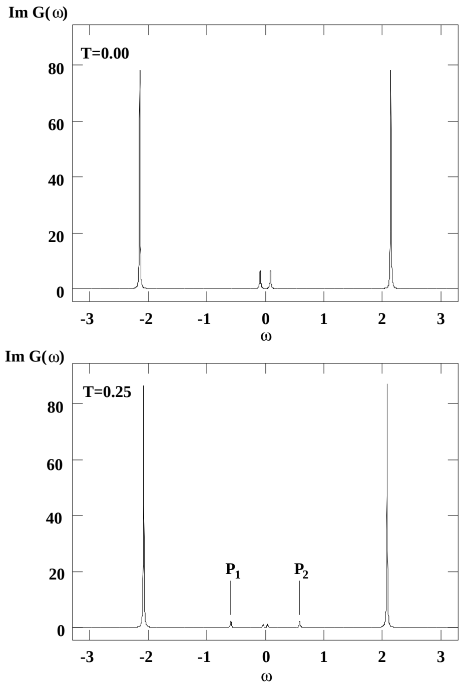

Figure 7.8: IPT: Spectral function for the particle hole symmetric case ($U = 4$, $\epsilon_f = -2$, and $V = 0.25$) at $T = 0$ and $T = 0.25$.

a genuine failure of IPT in general. Actually, the effect is already present at particle hole symmetry (i. e. in ordinary IPT), which is illustrated in figure 7.8. For the data displayed ($U = 4$, $\epsilon_f = -2$, $V = 0.25$) more than 50 % of the transfer of spectral weight goes to additional poles P_1 and P_2 at an intermediate energy range. This is again in contrast to the exact solution where the weight is exclusively transferred to the Hubbard bands (see figure 7.9).

The existence P_1 and P_2 in the IPT scheme for finite temperatures can easily be understood: For the particle hole symmetric case (i. e. $\epsilon_f = -\frac{U}{2}$) the self energy for the toy model is given by

$$\begin{aligned} \Sigma(\omega) &= \frac{U}{2} + \tilde{\Sigma}(\omega) \\ &= \frac{U}{2} + \frac{1}{2}U^2 \frac{(n_f(-V))^3\,\omega}{\omega^2 - 9V^2 - i\eta} + \frac{3}{4}U^2 \frac{n_f(V)n_f(-V)\,\omega}{\omega^2 - V^2 - i\eta} \end{aligned} \tag{7.9}$$

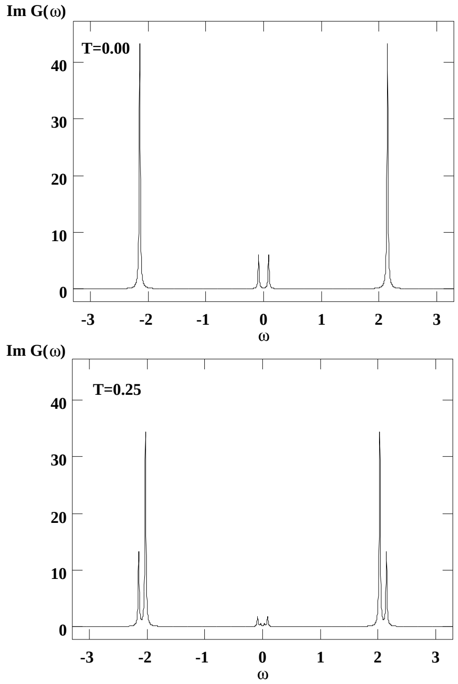

Figure 7.9: Exact diagonalization: Spectral function for the particle hole symmetric case ($U = 4$, $\epsilon_f = -2$, and $V = 0.25$) at $T = 0$ and $T = 0.25$.

This implies for the Green function[3]

$$G_f(\omega) = \frac{1}{\omega - \frac{1}{2}U^2 \frac{\left(n_f(-V)\right)^3 \omega}{\omega^2 - 9V^2} - \frac{3}{4}U^2 \frac{n_f(V) n_f(-V)\omega}{\omega^2 - V^2} - \frac{V^2}{\omega} - i\eta} \tag{7.10}$$

which for $T << V$ simplifies to:

$$G_f(\omega) = \frac{1}{\omega - \frac{1}{2}U^2 \frac{\left(n_f(-V)\right)^3 \omega}{\omega^2 - 9V^2} - \frac{V^2}{\omega} - i\eta} \tag{7.11}$$

Here, $G_f^{-1}(\omega)$ has three poles at $\omega = 0$ and $\omega = \pm 3V$. These are the zeros of $G_f(\omega)$. Between two (neighbor) zeros there has to be exactly one pole of $G_f(\omega)$. At zero temperature, we know from the comparison with exact diagonalization that two of the corresponding poles are at an energy scale $\frac{V^2}{\epsilon_f} \sim \frac{V^2}{U}$ near $\omega = 0$ while the other two represent the Hubbard bands around $\pm\frac{U}{2}$.

If the temperature is increased so that it becomes comparable to V the full Green function 7.10 has to be taken into account. It has two additional zeros at $\pm V$. I. e. there

[3] $n_f(\epsilon) := \frac{1}{1+\exp(\epsilon/T)}$

have to be two additional poles P_1 and P_2, one of them between $-V$ and $-3V$ (P_1) and the other between V and $3V$ (P_2).[4] We thereby established that some spectral weight is transferred to an intermediate energy range of order V which is clearly separated from the resonance ($\frac{V^2}{\epsilon_f}$).

In the light of these results it should not be very surprising that the spectral function as obtained from the IPT scheme develops an unphysical maximum above the resonance peak (see figure 7.4). This feature plays the role of P_2 in the underlying impurity model.

7.3 Scattering rate and conductivity for the Hubbard model

In chapter 4 we calculated the optical conductivity at zero temperature. Apart from the Drude peak the plot displays three sharp maxima which can be attributed to transitions between the lower Hubbard band and the resonance peak, the resonance peak and the upper Hubbard band, as well as the two Hubbard bands (see figure 4.4). These structures, which are particularly pronounced at $T = 0$, are smeared quickly as the temperature is increased (figure 7.10). The resulting plots are in good qualitative agreement with quantum Monte Carlo data [72].

However, when looking at the dc-resistivity $\rho_{dc}(T)$ or the scattering rate $\mathrm{Im}\Sigma(\omega = 0, T)$ we find deviations from the results obtained by quantum Monte Carlo: Figure 7.11 shows the temperature dependence of the scattering rate. For low temperatures our scheme gives the usual T^2 behavior predicted by Fermi liquid theory: $\mathrm{Im}\Sigma(\omega = 0, T) \sim T^2$. This behavior breaks down at an energy scale T_0, above which the scattering rate is either constant (for large doping) or decreasing (for small doping). The decrease of the scattering rate at high temperatures and small doping is not seen in the Monte Carlo data and presumably a consequence of the incorrect transfer of spectral weight in the IPT scheme.

In agreement with quantum Monte Carlo data our dc-resistivity shows a linear regime above T_0 (see figure 7.12). According to our scheme the corresponding slope decreases with decreasing doping. But exactly the opposite effect is observed in quantum

[4] In figure 7.8 it can be verified that P_1 and P_2 are indeed located in this frequency range.

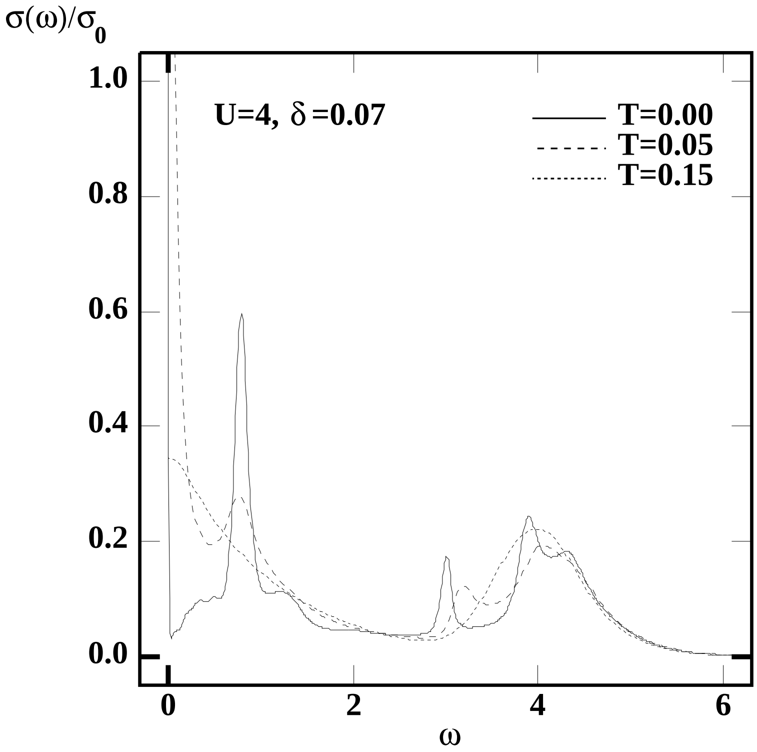

Figure 7.10: Temperature dependence of the optical conductivity for $U = 4$ and $\delta = 0.07$.

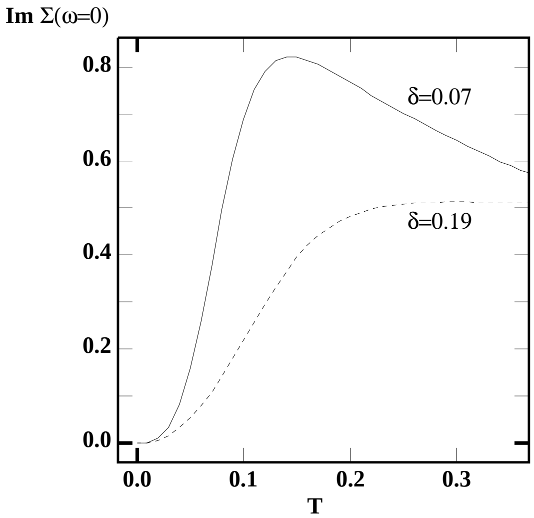

Figure 7.11: Temperature dependence of the scattering rate $\mathrm{Im}\Sigma(\omega = 0)$ for $U = 2.82$ and small and large doping.

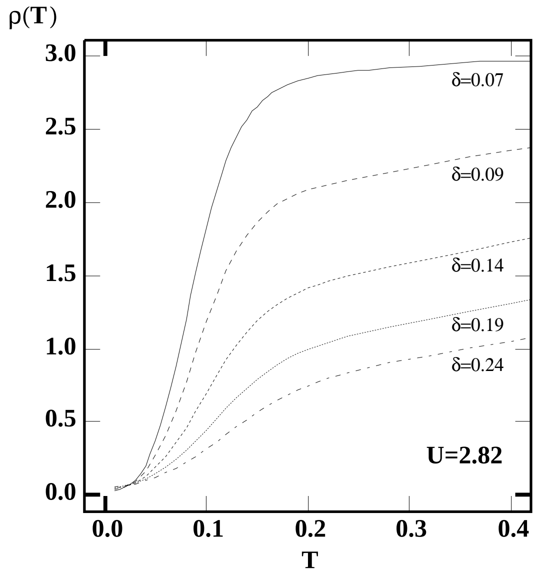

Figure 7.12: Temperature dependence of the dc-resistivity $\rho_{dc}(T)$. for $U = 2.82$ and various dopings.

Monte Carlo calculations [72]. The deviation is due to the unphysical behavior which we obtained for the scattering rate.

7.4 Discussion and conclusions

For the construction of our interpolating self energy at zero temperature the Luttinger theorem is crucial to fix the low frequency limit. With the exact solution of our toy model it can be verified that simple generalizations of the Friedel sum rule (or the Luttinger theorem) to finite temperatures, like e. g. claimed in reference [74] are incorrect. Since there is no equivalent at $T \neq 0$ one has to make an additional assumption in order to fix $\tilde{\mu}_0$. To recover our results for $T \to 0$ we fixed $\tilde{\mu}_0(n)$ at its zero frequency value. This approximation describes the decay of the resonance peak as well as the associated structures in the optical conductivity. However, the IPT scheme suffers from an incorrect transfer of spectral weight. In contrast to the exact solution, some of the spectral weight of the resonance peak is transferred to intermediate frequencies instead of the Hubbard bands. Away from particle hole symmetry this causes several unphysical features which become visible in sensitive quantities like the scattering rate and the dc-conductivity.

For our interpolating perturbation scheme, we learned in this chapter that the approach should mainly be viewed as a zero temperature tool. The application to finite temperatures is much less accurate and not very reliable.

Chapter 8

Density Fluctuations of Spinless Fermions in Infinite Dimensions

The preceding chapters were devoted to the development of a new perturbation scheme which allows to obtain an *approximate* solution for lattice models in infinite dimensions. The application to real systems is often quite successful. However, even if the *exact* solution of the large d limit was known one would still find that there are some artifacts of this limit which are absent in real, i. e. finite dimensional, systems. The most prominent examples perhaps are the k-independence of the self energy and the pinning of the density of states at zero frequency. It is therefore reasonable to ask whether it is possible to modify the large d limit itself so that it becomes somewhat more realistic. In this context, we explore in this chapter a new scaling for nearest neighbor interactions in infinite dimensions.

The procedure is studied for the spinless fermion model. Our scaling retains density fluctuations in infinite dimensions. This yields an additional interaction term. Its nature is investigated in the case of a homogeneous phase. Moreover, we explore the phase transition into a staggered phase at half filling.

8.1 Introduction

In the investigation of correlated Fermi systems, there has been some interest in the spinless fermion model (see e. g. [100, 101] and references therein). Its Hamiltonian contains a kinetic energy term combined with a nearest neighbor interaction:

$$H = -t \sum_{<ij>} c_i^+ c_j + U \sum_{<ij>} n_i n_j \tag{8.1}$$

In one dimension this model can be solved exactly by a Bethe ansatz solution [102, 103, 104]. In two and three dimensions it has been shown by renormalization group techniques that at zero temperature and half filling on an A-B lattice, there is a symmetry broken staggered phase for all positive values of the interaction [105]. The existence of such a phase can also be proofed at finite temperatures for sufficiently large U [106].

As far as the limit of infinite dimensions is concerned one has to choose a scaling for the model parameters t and U, such that the corresponding energies remain finite. In previous publications, this was done by taking $t = \tilde{t}/\sqrt{z}$ and $U = \tilde{U}/z$ (see e. g. [100, 101]), where z is the coordination number of the lattice. Using this scaling, Uhrig and Vlaming [107] showed that in general one observes for $z \to \infty$ a rich phase diagram containing phase separation, incommensurate states, a nonseggregated staggered phase, and an homogeneous phase. At half filling only the staggered phase and the homogeneous phase exist. Halverson et al. calculated $\frac{1}{d}$-corrections. They find that the transition temperature into the symmetry broken phase is reduced compared to the infinite dimensional case.

Here, we define the limit of infinite dimensions in a different way. The Hamiltonian (8.1) can be written as:

$$
\begin{aligned}
H &= -t \sum_{<ij>} c_i^{+} c_j + 2\,U \sum_{<ij>} < n_i > n_j - U \sum_{<ij>} < n_i >< n_j > \\
&\quad + U \sum_{<ij>} (n_i - < n_i >)(n_j - < n_j >) \qquad (8.2)
\end{aligned}
$$

I. e. the interaction splits into two contributions: a mean field like part and a term describing density fluctuations between nearest neighbor sites. With the scaling mentioned above the latter is of order $1/\sqrt{z}$. Thereby, it is not preserved in the limit $z \to \infty$. On the other hand, we expect fluctuations to play a role in finite dimensions. In fact the two contributions should compete at the phase transition. That is why we will consider a scaling which goes beyond the ordinary approach used so far by keeping the fluctuation term finite. More precisely, we scale U in two different ways, namely as U_1/z and $U_2/\sqrt{z}$ respectively:

$$
H = -\frac{t}{\sqrt{z}} \sum_{<ij>} c_i^{+} c_j + 2\,\frac{U_1}{z} \sum_{<ij>} < n_i > n_j - \frac{U_1}{z} \sum_{<ij>} < n_i >< n_j >
$$

$$+\frac{U_2}{\sqrt{z}}\sum_{<ij>}(n_i-<n_i>)(n_j-<n_j>) \tag{8.3}$$

Our aim is to investigate the influence of the fluctuation term and to show that this ansatz captures some of the finite dimensional physics.

In infinite dimensions a self energy should be called *non local* if its non local terms Σ_{ij} $(i \neq j)$ yield together a finite contribution in the perturbation expansion of the Green function, i. e. if $\Sigma_{ij} \sim z^{-|i-j|/2}$. With this definition the self energy diagrams of the Hamiltonian (8.3) turn out to be *local*, i. e. they collapse in (real) space $(i = j)$. Figure 8.1 shows examples for the resulting diagrams. Their shape resembles cacti.

For practical reasons we will again perform our calculations on a Bethe lattice setting $D = 2t = 1$.

The chapter is organized as follows: First we show how our approach can be mapped onto an impurity model (section 8.2). In section 8.3 we treat the case of an homogeneous phase. We begin with a canonical transformation (section 8.3.1). The resulting Hamiltonian can be used to define a mean field theory for the strong coupling limit, which serves for an investigation of the large U_2 behavior (section 8.3.2). In section 8.3.3 we present the results of a simplified non crossing approximation, while section 8.3.4 contains perturbation theory results. In section 8.4 we allow for symmetry breaking. Since we expect that the phase diagram away from half filling contains incommensurate phases [107], we restrict ourselves to the case of half filling. The investigation of the phase transition into a charge density wave allows to study the competition between the interaction contributions described by U_1 and U_2 respectively. We discuss our results in section 8.5.

8.2 Mapping onto a single impurity problem

In the following, we will derive the mapping onto a single impurity problem. For simplicity we formulate the equations for an homogeneous phase. It is a simple exercise to write down the corresponding equations for the case of symmetry breaking (half filling) as we will use them in section 8.4.

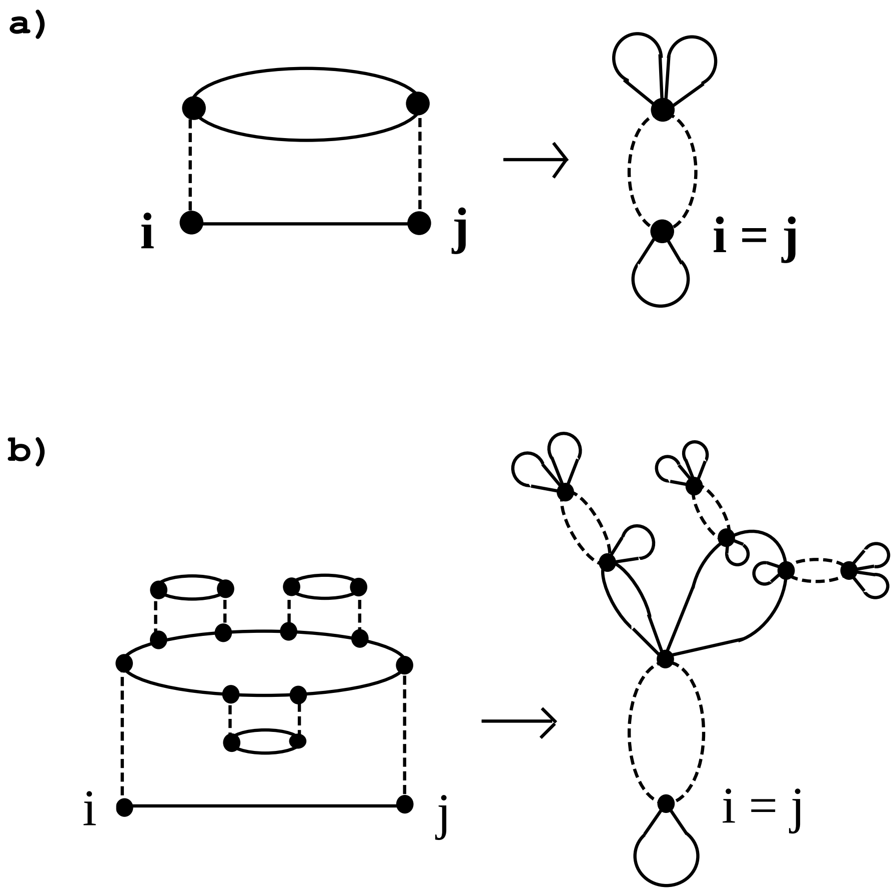

Figure 8.1: Examples for contributions to the self energy in infinite dimensions

Integrating out all but one lattice sites yields the following effective action:

$$S_{eff}(\psi,\psi^\star) = -\int_0^\beta d\tau \int_0^\beta d\tau' \Big(\psi^\star(\tau)\, G_o^{-1}(\tau-\tau')\, \psi(\tau') + (n(\tau) - < n >)\ \Pi_o^{-1}(\tau,\tau')\ (n(\tau') - < n >) \Big) \quad , \tag{8.4}$$

where[1]

$$G_o^{-1}(i\omega_n) := i\omega_n + \tilde{\mu} - t^2\, G(i\omega_n) \tag{8.5}$$

and

$$\Pi_o^{-1}(i\nu_n) := 2\, U_2^2\, \Pi(i\nu_n) \quad . \tag{8.6}$$

Here, $G(\tau-\tau') = - < \psi(\tau)\,\psi^\star(\tau') >$ is the full local Green function and $\Pi(\tau,\tau') =< (n(\tau) - < n >)\,(n(\tau') - < n >) >$ the full local density-density correlation function.

The impurity model which corresponds to (8.4) is given by an impurity (f) which is coupled to a bath of conduction electrons (a_k) as well as phonons (b_q):

$$H_{imp} = \sum_k \epsilon_k\, a_k^+ a_k + \sum_q \omega_q\, b_q^+ b_q + \sum_k V_k\, (a_k^+\, f + f^+\, a_k) + (f^+ f - < n >) \sum_q g_q\, (b_q + b_q^+) \tag{8.7}$$

This Hamiltonian has an action of the form (8.4) with

$$G_{o,imp}^{-1}(i\omega_n) = i\omega_n + \mu_f - \sum_k \frac{V_k^2}{i\omega_n - \epsilon_k} \tag{8.8}$$

and

$$\Pi_{o,imp}^{-1}(i\nu_n) = \sum_q \frac{g_q^2\, \omega_q}{\nu_n^2 + \omega_q^2} \quad . \tag{8.9}$$

The mapping requires that (8.5) and (8.8) as well as (8.6) and (8.9) are equal, which yields:

$$G(i\omega_n) = t^{-2} \sum_k \frac{V_k^2}{i\omega_n - \epsilon_k} \tag{8.10}$$

and

$$\Pi(i\nu_n) = \frac{1}{2}\, U_2^{-2} \sum_q \frac{g_q^2\, \omega_q}{\nu_n^2 + \omega_q^2} \quad . \tag{8.11}$$

(8.5) and (8.6) or respectively (8.10) and (8.11) provide the self consistency conditions necessary for the iterative solution of our problem. They will play an important role throughout the following parts of this chapter.

---

[1] $\tilde{\mu} := \mu - 2\langle n\rangle U_1$

8.3 Investigation of the homogeneous phase

In this section, we will consider only an homogeneous phase, i. e. we do not allow for symmetry breaking (even in the limit of large U_2). This has the advantage, that we are able to study the fluctuation term independently of the U_1-part of the interaction as the Hamiltonian reduces to

$$H = -\frac{t}{\sqrt{z}} \sum_{<ij>} c_i^+ c_j + \frac{U_2}{\sqrt{z}} \sum_{<ij>} (n_i - < n >)(n_j - < n >) \tag{8.12}$$

with a renormalized chemical potential $\tilde{\mu} := \mu - 2 < n > U_1$.

8.3.1 Canonical transformation

In order to treat the impurity model (8.7), we perform a canonical transformation [108] which eliminates the electron-phonon coupling term for all frequencies ω_q that are larger than a cutoff Λ: $\bar{H}_{imp} = e^S H_{imp} e^{-S}$, with $S = (f^+ f - < n >) \sum_{|\omega_q| > \Lambda} \frac{g_q}{\omega_q}(b_q^+ - b_q)$. This yields the following transformed impurity Hamiltonian

$$\begin{aligned} \bar{H}_{imp} &= \sum_k \epsilon_k \, a_k^+ a_k + \sum_q \omega_q b_q^+ b_q - (1 - 2 < n >) \sum_{|\omega_q| > \Lambda} \frac{g_q^2}{\omega_q} f^+ f \\ &- \sum_{|\omega_q| > \Lambda} \frac{g_q^2}{\omega_q} < n >^2 + \sum_k V_k \left(a_k^+ f X + X^+ f^+ a_k \right) \\ &+ \; (f^+ f - < n >) \sum_{|\omega_q| \le \Lambda} g_q \, (b_q^+ + b_q) \end{aligned} \tag{8.13}$$

where $X = \exp\left(-\sum_{|\omega_q| > \Lambda} \frac{g_q}{\omega_q} (b_q^+ - b_q)\right)$. We thereby separated the electron-phonon interaction into a strong coupling part incorporating fast phonons ($|\omega_q| > \Lambda$) and a weak coupling contribution referring to slow phonons ($|\omega_q| \le \Lambda$). At this point the cutoff Λ remains unspecified. We will assume a certain scaling behavior when treating a mean field theory for the strong coupling limit.

8.3.2 Mean field-theory for the strong coupling limit

We will now study the strong coupling part of the electron phonon interaction in (8.13). For large U_2 we define a mean field theory by replacing X by its expectation value

$$R := < X > = \exp\left(- \sum_{|\omega_q| > \Lambda} \frac{g_q^2}{\omega_q^2} \left(\frac{1}{2} + n(\omega_q) \right) \right) \quad . \tag{8.14}$$

The cutoff Λ assures that the sum in this expression remains finite. The physical picture is that only phonons whose energy is large enough are able to follow the electronic motion. Therefore Λ should scale with the effective bandwidth.

The corresponding mean field Hamiltonian reads

$$\begin{aligned}\bar{H}_{imp}^{MFT} &= \sum_k \epsilon_k\, a_k^+ a_k + \sum_q \omega_q b_q^+ b_q + (1 - 2 < n >) \sum_{|\omega_q|>\Lambda} \frac{g_q^2}{\omega_q^2} f^+ f \\ &+ \sum_k V_k R\, (a_k^+ f + f^+ a_k) - \sum_{|\omega_q|>\Lambda} \frac{g_q^2}{\omega_q} < n >^2 \qquad (8.15)\end{aligned}$$

which implies $G^{-1}(i\omega_n) = i\omega_n + \bar{\mu}_f - \sum_k \frac{V_k^2 R^2}{i\omega_n - \epsilon_k}$ with a renormalized chemical potential $\bar{\mu}_f$.

From $\Pi(\tau) = -G(\tau)G(-\tau)$ and the self consistency equations (8.10) and (8.11) we establish the connection between the model parameters of the impurity model and U_2 and t:

$$\omega_q = |\epsilon_{k_1} - \epsilon_{k_2}| \qquad (8.16)$$

and

$$g_q = 2\, U_2 \,\frac{V_{k_1} V_{k_2}}{t^2}\, \sqrt{|n(\epsilon_{k_1}) - n(\epsilon_{k_2})|} \qquad (8.17)$$

where $q = (k_1, k_2)$ with $k_1 < k_2$. Moreover, we have $G^{-1}(i\omega_n) = i\omega + \bar{\mu}_f - t^2 R^2 G(i\omega_n)$ which means that G can be interpretated as the Green function of a one dimensional chain with tridiagonal Hamiltonian

$$H - \bar{\mu}_f\, N = \begin{pmatrix} -\bar{\mu}_f & tR & & & \\ tR & -\bar{\mu}_f & tR & & \\ & tR & -\bar{\mu}_f & tR & \\ & & \ddots & \ddots & \ddots \end{pmatrix} \qquad (8.18)$$

This implies the following scaling behavior for ϵ_k and $\bar{\mu}_f$:

$$\begin{aligned}\epsilon_k &= tR\, \tilde{\epsilon}_k \\ \bar{\mu}_f &= tR\, \tilde{\bar{\mu}}_f \\ V_k &= tR\, \tilde{V}_k \qquad (8.19)\end{aligned}$$

where $\tilde{\epsilon}_k$, $\tilde{\tilde{\mu}}_f$ and $\tilde{V}_k$ are independent of R. We then obtain from (8.16) and (8.17) at zero temperature: $\omega_q = tR\,\tilde{\omega}_q$ and $g_q = U_2R^2\,\tilde{g}_q$. This means

$$R = \exp(-\frac{1}{2}\frac{U_2^2}{t^2}\,R^2 \sum_{|\omega_q|>\Lambda} \frac{\tilde{g}_q^2}{\tilde{\omega}_q^2}) \quad . \tag{8.20}$$

As mentioned above, Λ should scale with the effective bandwidth i. e. $\Lambda = tR\tilde{\Lambda}$. By diagonalizing (8.18) one can show that the sum in (8.20) depends logarithmically on $\tilde{\Lambda}$:

$$\sum_{|\omega_q|>\Lambda} \frac{\tilde{g}_q^2}{\tilde{\omega}_q^2} = \alpha_o\,(\alpha_1 - \ln\tilde{\Lambda}) \tag{8.21}$$

where α_o and α_1 are numerical constants ($\alpha_o > 0$ and $\alpha_1 > \ln\tilde{\Lambda}$). Together with (8.20) this yields

$$\ln R = -\gamma\,(\alpha_1 - \ln\tilde{\Lambda})R^2 \tag{8.22}$$

where $\gamma := \frac{\alpha_o}{2}\,(\frac{U_2}{t})^2$. The relation (8.22) is an equation for R, which can be solved graphically. For $\frac{U_2}{t} \to \infty$, we have $R \to 0$, which means that the effective bandwidth scales to zero: $t_{eff} = tR \to 0$. On the other hand, $g_q = U_2R^2\,\tilde{g}_q$ implies that the effective interaction scales with R^2: $U_{2,eff} = U_2R^2 \to 0$ and thereby $\frac{U_{2,eff}}{t_{eff}} \sim R \to 0$. These considerations indicate that the fluctuation part of the interaction does not localize the particles for large U_2.

8.3.3 A simplified non crossing approximation

In order to get a more concrete idea about the strong coupling term in (8.13) we now sum up a certain class of diagrams for the Green function. The diagrams under consideration are those where each phonon line ends at the same fermion line at which it started. For an example see figure 8.2.

Since the phonon lines do not cross each other we will call this treatment *a modified non crossing approximation.* If $D_q(\tau)$ is the (free) phonon propagator ($D_q^{-1}(i\nu_n) = i\nu_n - \omega_q$), $G_{f,o}(\tau)$ the local bare f-electron Green function and $G_{a_k,o}(\tau)$ the free conduction electron Green function ($G_{a_k,o}^{-1}(i\omega_n) = i\omega_n - \epsilon_k$) then the full f-electron Green function $G_f(i\omega_n)$ is determined by the following equations

$$D(\tau) \;\; := \;\; \exp(\frac{1}{2}\sum_q \frac{g_q^2}{\omega_q^2}\,(D_q(\tau) + D_q(-\tau))$$

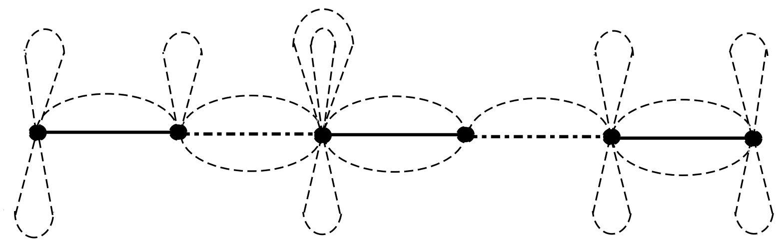

Figure 8.2: Example for the diagrams considered in the modified non crossing approximation (Full line: $G_{f,0}$, dashed-dotted line: G_{a_k} and dashed line: D_q)

$$
\begin{aligned}
\bar{G}_{f,o}(\tau) &:= D(\tau)/D(0)\, G_{f,o}(\tau) \\
\bar{G}_{a_k,o}(\tau) &= D(\tau)\; G_{a_k,o}(\tau) \\
G_f(i\omega_n) &= \frac{1}{\bar{G}^{-1}_{f,o}(i\omega_n)\; -\; \sum_k V_k^2\, \bar{G}_{a_k,o}(i\omega_n)}
\end{aligned}
\tag{8.23}
$$

Solving the full self consistent problem requires an approximation for the polarisation propagator $\Pi(\tau-\tau') = <(n(\tau) - <n>)\,(n(\tau') - <n>)>$. In this section we choose $\Pi(\tau-\tau') = -G(\tau)\,G(-\tau)$, which becomes exact in the mean field theory treated above and has the advantage that ω_q and g_q are related to ϵ_k and V_k in a simple way (see (8.16) and (8.17)).

The self consistent procedure looks as follows: We start with a guess for a finite number of values ϵ_k and V_k. Then we calculate ω_q and g_q by (8.16) and (8.17). Afterwards, equation (8.23) determines G_f to which new parameters ϵ_k and V_k are fitted according to the self consistency condition (8.10).

The lower cutoff Λ for the phonon frequencies is considered automatically by treating only a finite number of poles ϵ_k. We belief that this procedure like the standard non crossing approximation (NCA) yields reasonable results at high temperatures.

When evaluating the density of states in this way, the resolution with a fixed number of poles is the better the more the curve is centered around zero frequency, i. e. the smaller U_2 is. In figure 8.3 we chose $U_2 = 1$ as well as $T = 0.3$, $T = 0.6$ and $T = 0.9$ respectively (half filling, 25 poles). A broadening $\eta = 0.05$ was introduced to plot the poles. At lower temperatures, we see a strong peak at zero frequency implying that there is a maximum at this point. This peak decays as the temperature is increased. In addition, the plots suggest that there is some structure at finite frequencies (see next paragraph). The small peaks appearing at high frequencies indicate, that the tails of the density of states contain a finite weight.

8.3.4 Weak coupling approach: iterative perturbation theory

The self consistency problem with the impurity model (8.7) can easily be treated in iterative perturbation theory. One starts with a guess for G_o and Π_o^{-1}. The self energy

a)

b)

c)

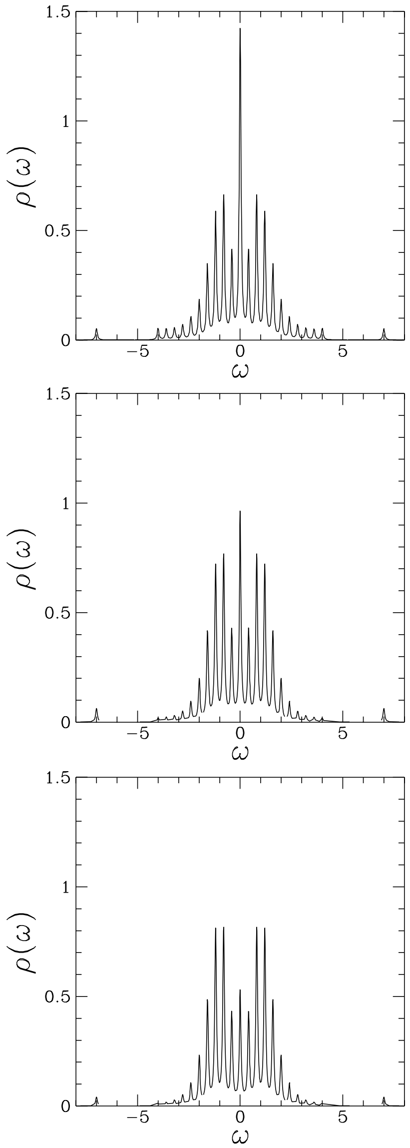

Figure 8.3: Modified non crossing approximation: poles indicating the density of states $\rho(\omega)$ for $U_2 = 1$ at $T = 0.3$ (figure 2a), $T = 0.6$ (figure 2b) and $T = 1.0$ (figure 2c). A broadening $\eta = 0.05$ was introduced to plot the poles.

is then determined by the diagram shown in figure (8.4):

$$\Sigma(\tau) = 2\, G_o(\tau)\, \Pi_o^{-1}(\tau) \tag{8.24}$$

which gives for the full Green function

$$G(i\omega_n) = \frac{1}{G_o^{-1}(i\omega_n) - \Sigma(i\omega_n)} \tag{8.25}$$

For the evaluation of the phonon propagator we choose the RPA-approximation:

$$\Pi(i\nu_n) = \frac{1}{\Pi_{loop}^{-1}(i\nu_n) - \Pi_o^{-1}(i\nu_n)} \tag{8.26}$$

with $\Pi_{loop}(\tau) = -G(\tau)\, G(-\tau)$. The relations (8.5) and (8.6) close the self consistency by yielding a new G_o and Π_o^{-1}.

We performed our numerical calculations using the Keldysh formalism (see appendix A), which has the advantage of using the real time and real frequency dependent quantities, so that no analytic continuation is necessary. Figure 8.5 shows the results at half filling for $U_2 = 1$ and different values of T. At zero temperature, there is a strong peak, which - compared to our modified non crossing approximation - decreases quickly as the temperature is increased. The existence of this peak can be explained by the pinning of the density of states for $T = 0$ at zero frequency (see figure 8.6), which is caused by the k-independence of the self energy and characteristic for the limit of infinite dimensions [42]. As the zero frequency peak decays, there is an intermediate temperature regime, where maxima appear at a finite frequency (figure 8.5). They correspond to the structure observed with the modified non crossing approximation. With increasing U_2 the width of the resonance peak is decreased. However, we do not find an insulating solution of the self consistency equations for large U_2. A localization of the particles would correspond to a divergence of the zero frequency value of the density-density correlation function (i. e. $\mathrm{Re}\Pi(\omega = 0)$). This quantity is plotted in figure 8.7. $\mathrm{Re}\Pi(\omega = 0)$ increases for small U_2, reaches its maximum around $U_2 \approx 0.6$, and decreases for large U_2.

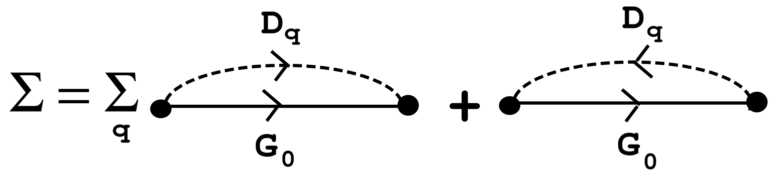

Figure 8.4: Perturbation theory: diagram for the self energy $\Sigma(\omega)$.

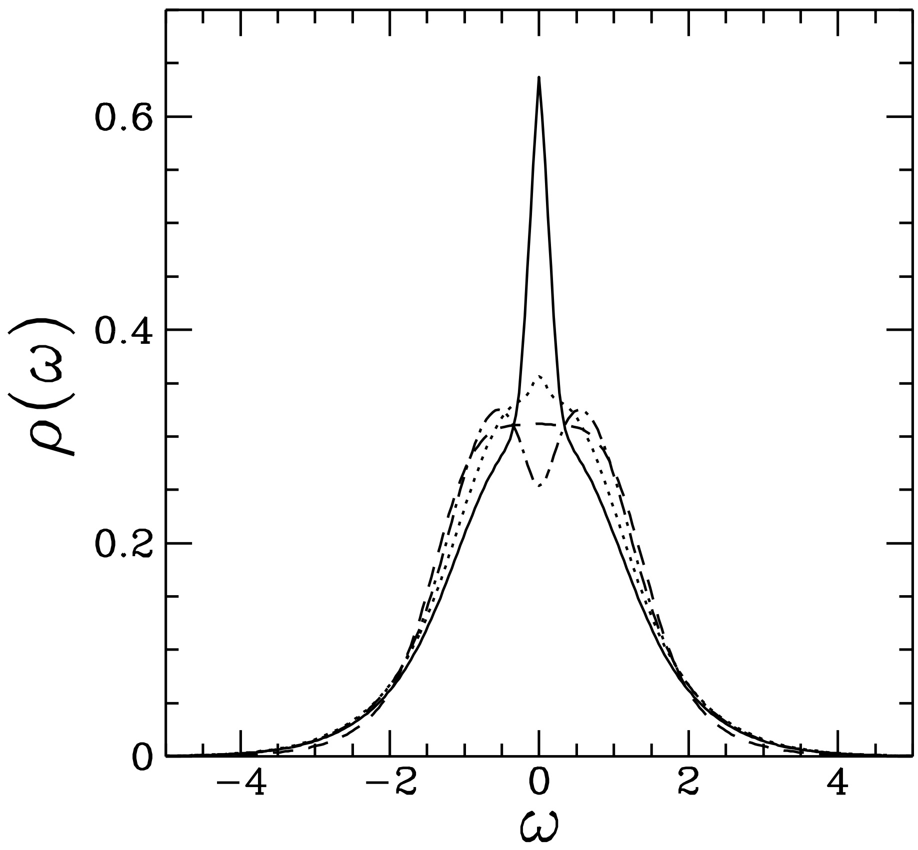

Figure 8.5: IPT: density of states $\rho(\omega)$ for $U_2 = 1$ at $T = 0$ (full line), $T = 0.07$ (dotted line), $T = 0.3$ (dashed-dotted line) and $T = 1.0$ (dashed line)

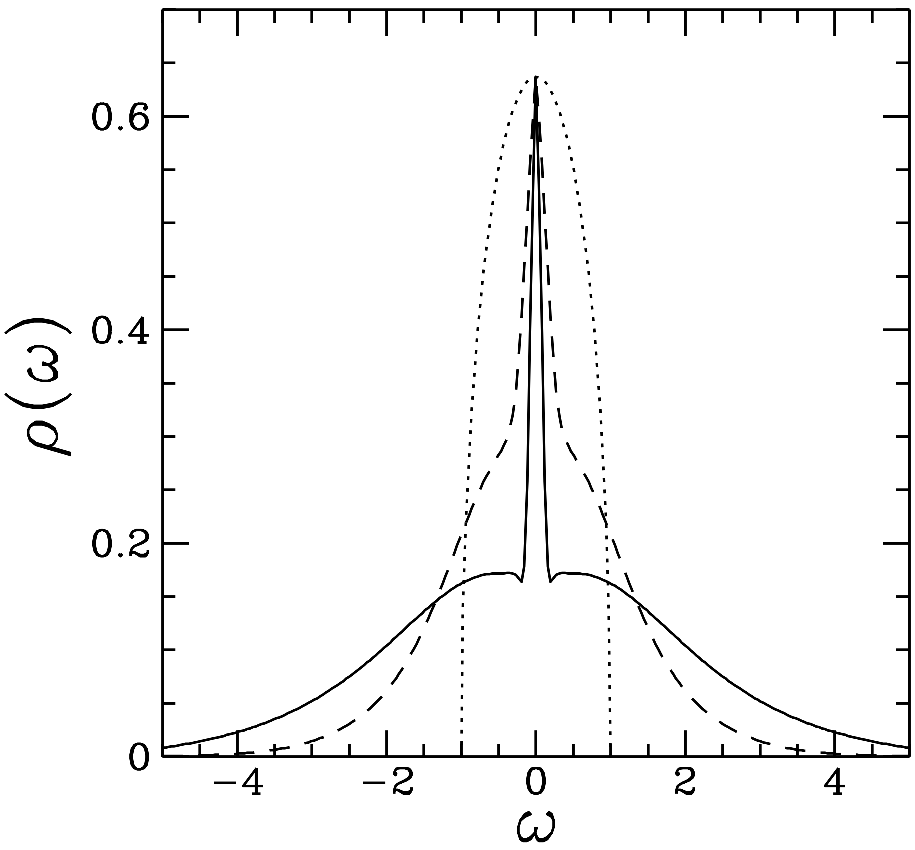

Figure 8.6: Pinning of the density of states at zero frequency (IPT). The plot shows $\rho(\omega)$ at $T = 0$ for $U_2 = 0$ (dotted line), $U_2 = 1$ (dashed line), and $U_2 = 2$ (full line)

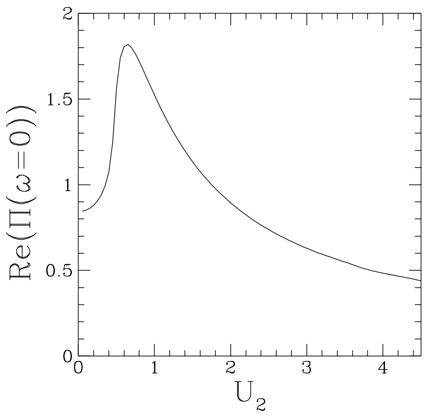

Figure 8.7: ReΠ($\omega = 0$) as a function of U_2 (T=0, IPT).

8.4 The phase transition at half filling

So far we did not allow for symmetry breaking. But, as outlined in the introduction, we expect at half filling a phase transition into a charge density wave as the temperature is lowered or the interaction is increased. In this case the full Hamiltonian (8.3) has to be taken into account. Our scaling ($U = U_1/z$ and $U = U_2/\sqrt{z}$) implies a relationship between U_1 and U_2:

$$\frac{U_2}{U_1} = \frac{1}{\sqrt{z}} \tag{8.27}$$

I. e. the influence of the fluctuation term increases with decreasing coordination number. Being interested in finite dimensional physics we choose the coordination number of a three dimensional simple cubic lattice for our numerical evaluation, i. e. $U_2/U_1 = 1/\sqrt{6}$.

It is straightforward to rederive the equations of section 8.2 taking two sublattices A and B into account. One basically has to solve two impurity problems like (8.7) which are coupled by the following self consistency conditions

$$G^{-1}_{o,A}(i\omega_n) = i\omega_n - U_1\,(<n>_B - <n>_A) - t^2\,G_B(i\omega_n) \tag{8.28}$$

$$G^{-1}_{o,B}(i\omega_n) = i\omega_n - U_1\,(<n>_A - <n>_B) - t^2\,G_A(i\omega_n) \tag{8.29}$$

$$\Pi^{-1}_{o,A}(i\nu_n) = 2\,U_2^2\,\Pi_B(i\nu_n) \tag{8.30}$$

$$\Pi^{-1}_{o,B}(i\nu_n) \quad = \quad 2\,U_2^2\,\Pi_A(i\nu_n) \tag{8.31}$$

Starting with initial guesses for $G_{o,A}$, $G_{o,B}$, $\Pi^{-1}_{o,A}$ and $\Pi^{-1}_{o,B}$, one can obtain the full Green functions G_A and G_B as well as the correlation functions Π_A and Π_B by applying equations (8.24) to (8.26) to each sublattice separately. We perform these steps in real time and frequency (again using the Keldysh formalism). The particle number on each sublattice ($< n >_A$ and $< n >_B$) can be determined from the corresponding advanced Green function, e. g. $< n >_A = \int_{-\infty}^{+\infty} \frac{1}{\pi}\mathrm{Im}G_A^{(adv)}(\omega)/(1+\exp(\omega/T))d\omega$. The iteration is closed by the analytic continuation of the self consistency conditions (8.28) to (8.31).

Since at half filling the spectral functions on both sublattices are related by $\rho_A(\omega) = \rho_B(-\omega)$, we plot only one of them. Moreover, we can label the sublattices such that $< n >_A \geq < n >_B$.

Figure 8.8 shows how the gap forms as the temperature is decreased. In figure 8.9, $\rho_A(\omega)$ is plotted at $T = 0.3$ and $U_1 = 1.0$. The dotted line represents the density of states without including density fluctuations ($U_2 = 0$). In this case, we have two sharp bands with a singularity at the upper edge of the lower band. These features are not expected to be present in finite dimensions [96]. They disappear for finite U_2 (full line in figure 8.9), while a narrow satellite band forms at negative frequencies.

Moreover, it is interesting to study the temperature dependence of the order parameter $\Delta(T) := < n >_A - < n >_B$ (figure 8.10). The transition temperature T_c is decreased considerably by density fluctuations.

All our findings are in good agreement with [96]. Therefore, our approach to the limit of infinite dimensions indeed captures some of the finite dimensional physics.

8.5 Discussion and critical remarks

We introduced a new scaling for the spinless fermion model which allows to investigate density fluctuations in infinite dimensions. While the traditional treatment retains only the mean field contribution of the interaction we also keep the fluctuation part.

The nature of this term was first studied by investigating the homogeneous phase. A simple mean field theory indicated that for large U_2 the effective interaction scales

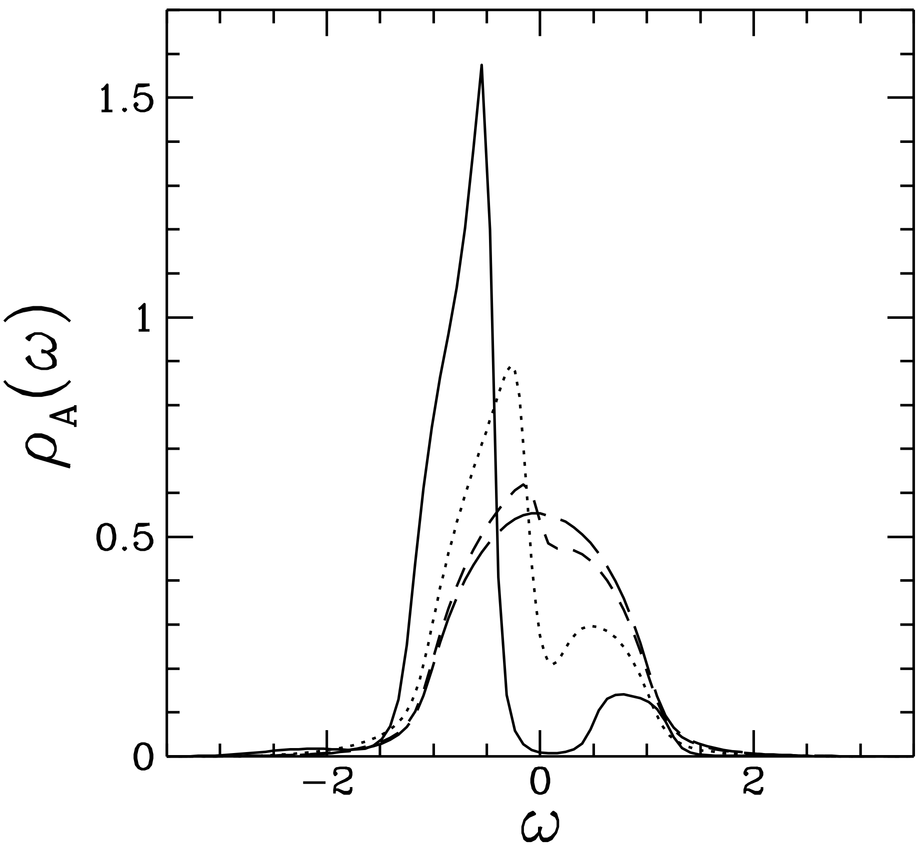

Figure 8.8: Gap formation in the density of states: $\rho_A(\omega)$ for $U_1 = 1$ at $T = 0.33$ (full line), $T = 0.364$ (dotted line), $T = 0.365$ (short-dashed line) and $T = 0.367$ (long-dashed line)

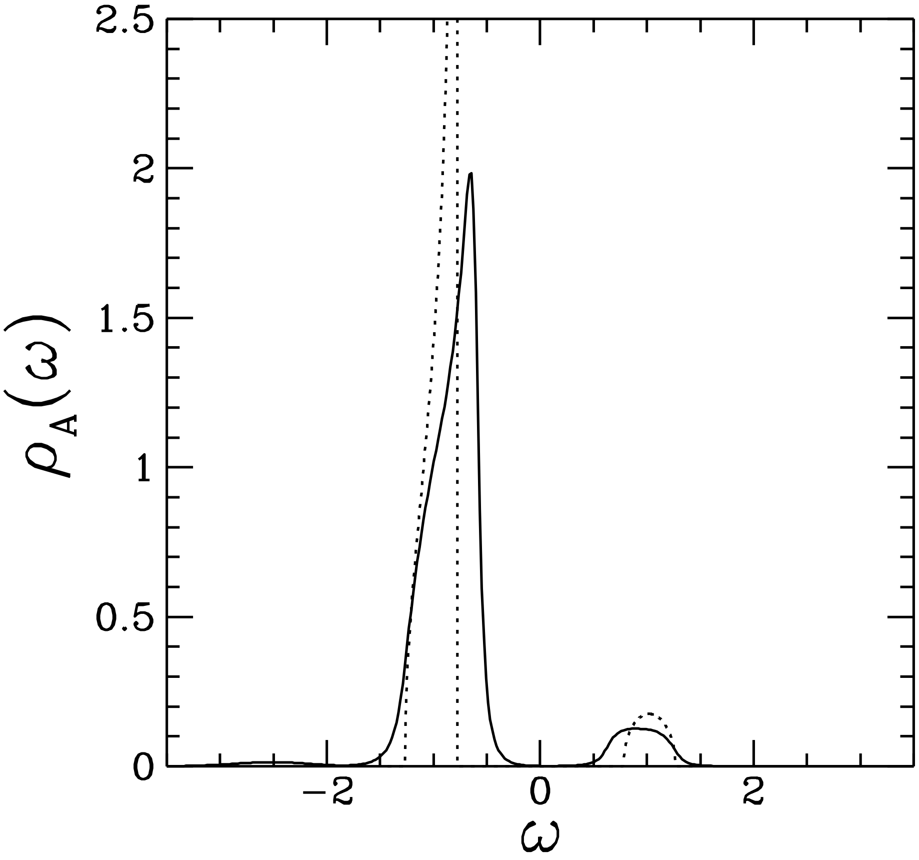

Figure 8.9: Density of states on the A-sublattice for $U_1 = 1$ and $T = 0.3$: $U_2 = 0$ (dotted line) vs. $U_2 = 6^{-\frac{1}{2}}$. Note the satellite band in the frequency range from -3 to -2.

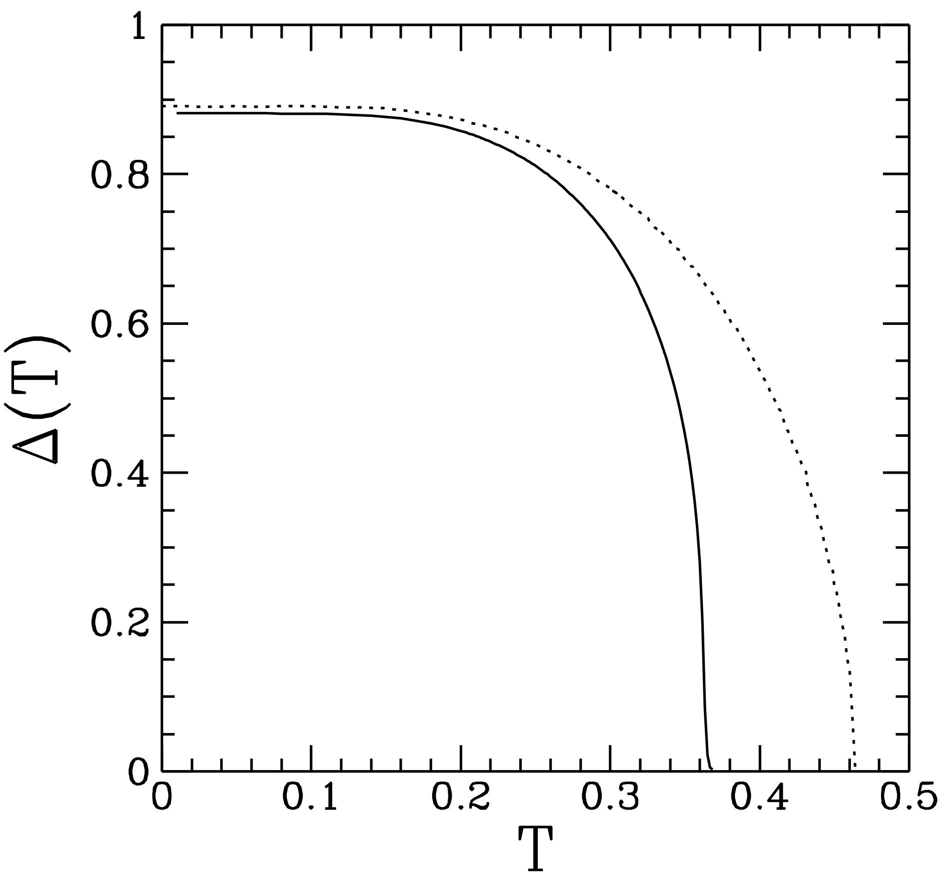

Figure 8.10: Temperature dependence of the order parameter $\Delta(T) = < n >_A - < n >_B$ for $U_1 = 1$ and $U_2 = 6^{-\frac{1}{2}}$ (full line) as well as $U_2 = 0$ (dotted line)

faster to zero than the effective bandwidth, so that we do not expect a localizing effect of this additional term. The density of states was calculated in two different ways. First by applying a modified non crossing approximation and then by iterative perturbation theory. In both cases, we find at low temperatures a large peak at zero frequency. The existence of this peak was explained by the pinning of the density of states, which is a typical artifact of the limit of large dimensions. Both approximations are different in that the peak decays much faster in perturbation theory as the temperature is increased. This can be explained by the the different approximations used for the treatment of the polarisation propagator.

In both approaches, the modified non crossing approximation and the IPT, we did not find a Mott transition as a function of U_2. At this point we should add some critical remarks. From the Hubbard model is is known that for IPT to produce a Mott transition the scheme has to be constructed such that it is exact in the atomic limit [42, 6]. Here, we used the RPA approximation to evaluate the density density correlation function (see equation (8.26)). Therefore, the approach applied here is *not* correct for $V_k \to 0$.

As far as the modified non crossing approximation is concerned it has to be emphasized that its validity is restricted to sufficiently high temperatures.

At the phase transition, density fluctuations compete with the mean field part of the interaction. The transition temperature is reduced considerably by density fluctuations. Moreover, they produce a more realistic spectral function. In fact, we found a lot of features which are also present in $\frac{1}{d}$-corrections to the traditional scaling. This should not be very astonishing because our scaling for the fluctuation term can be interpretated as a partial inclusion of $\frac{1}{d}$-corrections. Thereby, our approach goes beyond the traditional treatment by incorporating some of the finite dimensional physics.

We illustrated our approach for the spinless fermion model. But obviously it is much more general because it can also be applied to other lattice models with nearest neighbor interaction (e. g. a generalized Hubbard model).

Chapter 9

Summary, Conclusions, and Outlook

In this thesis we introduced a new iterative perturbation scheme for the study of the large d limit of correlated electron systems. The scheme makes use of an interpolating self energy which is correct in various limits. The approach can be applied to the doped metal as well as the Mott insulator. It is applicable not only to single band models but also to the multiband case provided that the filling is less than (or close to) one. The results are most accurate at zero temperature.

In **chapter 1** we motivated the need for an efficient algorithm for solving the impurity problem once more refined lattice models are considered.

Then a short summary on the limit of infinite dimensions was given in **chapter 2** establishing the notation for the succeeding parts.

Chapter 3 should be considered as the core of the present work. Here, the perturbation scheme was derived for the single band case by constructing an interpolating self energy, which is exact for small and large frequencies as well as for the weak coupling and the atomic limit. We introduced a new parameter $\tilde{\mu}_0$, which, in contrast to previous schemes [37, 38, 39], is fixed by imposing the Friedel sum rule or the Luttinger theorem, respectively. This is important to obtain a good agreement with the exact diagonalization results on the imaginary axis and to capture the Mott transition occurring in the lattice model. We checked the accuracy of the scheme for both, the impurity model as well as the lattice problem. In the former case, we performed a benchmark against an exactly solvable toy model. We obtained overall a reasonable agreement where the accuracy tends to become somewhat worse for large U and small V. This can be explained by the fact that the Green functions obtained by the scheme are exact to order U^2 in the small U limit but, away from particle hole symmetry, only to zeroth order in

V if the atomic limit is considered. For the lattice model, we compared our results on the imaginary axis with those obtained with the exact diagonalization method. There is an excellent agreement for $\mathrm{Im}G(i\omega)$. Deviations in $\mathrm{Re}G(i\omega)$ can be explained by the different critical U_c in IPT and exact diagonalization.

It is a remarkable result that the approach has a well defined large U limit. We studied in detail how the Mott transition occurs in the infinite U Hubbard model as a function of the chemical potential. To obtain the Mott insulator, the parameter $\tilde{\mu}_0$ has to be fixed by $\tilde{\mu}_0 = \mathrm{Re}\Delta(0)$. The scheme approximates the shift of the Hubbard bands with varying chemical potential.

A first application was treated in **chapter 4**, where we explored some aspects of the single band Hubbard model at zero temperature. Although many results had been known for this problem from other methods before, it was useful to apply our scheme as it yields results on the real axis with a much higher resolution than the exact diagonalization. We explored the evolution of the density of states as a function of doping. The plots show a resonance peak the width of which scales to zero as the Mott transition is approached. The most striking feature of the density of states is the finite shift of the resonance from the insulating band edge as the doping goes to zero. It had been shown before that this is an exact analytic result for infinitesimal doping [18]. This feature had not appeared in earlier studies of the Hubbard model in large dimensions using Monte Carlo techniques [17] and is also not easily seen in exact diagonalization algorithms [15]. Our perturbation scheme allowed for the first time to calculate the optical conductivity of the doped Hubbard model at zero temperature. Particularly characteristic is the appearance of a strong peak at an intermediate frequency range. Most of our calculations were done for the Bethe lattice. We showed however how more realistic lattices can be treated within our approach. In particular, we determined the evolution of the spectral functions for the two dimensional case, where the bare lattice density of states has a logarithmic singularity. The results suggest that correlations enhance the effects caused by a van Hove singularity.

In **chapter 5** we demonstrated that our perturbation scheme is a useful tool to describe real materials with more refined models. We established a new paradigm for the description of spectral functions of transition metal oxides. In contrast to general belief the homogeneous Hubbard model cannot explain the spectra obtained from photoemission and inverse photoemission experiments. A theoretical description can however be given if inhomogeneities at some length scale are taken into account. We calculated the resulting spectral densities in the two limiting cases of microscopic and macroscopic (i. e. phase separation) disorder. This concept yields a good description as far as surface properties are concerned. However it does not apply to the features measured in the bulk material, e. g. the specific heat.

Since real materials contain several bands we showed in **chapter 6** how the scheme can be generalized for the treatment of multiband models. The calculations were illustrated for a frustrated two band Hubbard model but can be generalized immediately to an arbitrary number of bands. We tested the scheme again against an exactly solvable toy model and found a good agreement for fillings less than one. For occupations between one and two particles per lattice site a new regime occurs which has no counterpart in the single band Hubbard model. Here our scheme fails to yield the right low energy physics. Instead it produces for all fillings under consideration a sharp unphysical resonance. This failure originates from the fact that small and high energy scales are not clearly separated in the continuous fraction used for the interpolating self energy. We proposed a modified scheme which is constructed from the atomic limit written as a sum of single poles. While this approach yields reasonable results for small particle doping, it is not exact to order U^2 and breaks down for larger doping ($n_{tot} >\approx 1.37$ for $U = 4$).

Nevertheless, our interpolating perturbation scheme allows to treat multiband models relevant for substances like $La_{1-x}Sr_xTiO_3$. We studied in detail the influence of orbital degeneracy on the low and high energy physics of the Hubbard model. In general the low energy features are not much altered by introducing the multiband picture. This explains why already the simple single band Hubbard model is able to describe several aspects of doped transition metal oxides. The high energy features, in contrast, do depend on orbital degeneracy. Most characteristically, are the differences in the weights of the Hubbard bands. For the two band model at $n_{tot} = 1$ these weights are $\frac{1}{4}$

and $\approx \frac{3}{4}$ respectively in contrast to $\frac{1}{2}$ for each band in the single band case. In addition, for the frustrated system with a finite intraatomic exchange J the upper Hubbard band is split into three maxima.

In agreement with estimates obtained from the projective self consistent method, the IPT scheme yields for $n_{tot} = 1$ critical values U_i for the breakdown of the insulating ($i = 1$) and metallic ($i = 2$) solution which depend only weakly on orbital degeneracy. On the other hand the U_i for $n_{tot} = 2$ in the two band model are larger than for $n_{tot} = 1$. The metallic and insulating gaps for $n_{tot} = 1$ are almost independent of the number of bands. For the two band model we find that these gaps are considerably smaller at $n_{tot} = 2$ than at $n_{tot} = 1$.

We studied in detail the optical conductivity of the two band Hubbard model and compared the results with measurements on $La_{1-x}Sr_xTiO_3$ [28, 29] and $La_{2-x}Sr_xCuO_4$ [112]. Like in the one band model, the theoretical data display a sharp peak at intermediate frequencies, which is related to transitions between the lower Hubbard band an the resonance. No such peak can be observed in the experimental data of $La_{1-x}Sr_xTiO_3$. Although a resonance is visible in $La_{2-x}Sr_xCuO_4$, its position does not have the right doping dependence. One can on the other hand evaluate the transfer of spectral weight from high to low frequencies with increasing doping. This quantity is measured by an effective electron number N_{eff}. For $La_{1-x}Sr_xTiO_3$ we find remarkably even a quantitative agreement between the experimental and theoretical data. The agreement is worse for $La_{2-x}Sr_xCuO_4$, which has a twodimensional structure. While experimental data suggest that the slope of the N_{eff} vs n_{tot} plot is strongly enhanced as U_c is approached from above, the Hubbard model displays a much weaker dependence on U.

Chapter 7 discusses a generalization of the scheme to finite temperatures. Since the Luttinger theorem is only valid at zero temperature, one has to make an additional assumption to fix the parameter $\tilde{\mu}_0$. We proceeded by choosing the zero temperature results for the function $\tilde{\mu}_0(n)$. The scheme describes the decay of the resonance as a function of temperature at least qualitatively. However, there are some unphysical features, which stem from an incorrect transfer of spectral weight. Making again use of the exactly solvable toy model, we showed that the IPT scheme transfers with increasing temperature some spectral weight from the resonance to an intermediate frequency range determined by the energy scale V while the exact solution adds this weight completely to the high energy states of the Hubbard bands. This problem is a genuine feature of iterative perturbation theory and already present at half filling. However, its consequences are more disturbing away from particle hole symmetry where the basic trends are not restored by the symmetry properties and larger U are considered. We conclude that our approach should mainly be viewed as a zero temperature scheme. The application to finite temperatures is less accurate and should be done with care.

Chapter 8 is independent from the preceding parts. Here, we discussed a new scaling for the next neighbor interactions. The idea is illustrated for the spinless fermion model. The traditional scaling eliminates density fluctuations between next neighbor sites. We retain these contributions by scaling the interaction parameter in two different ways. We first studied the influence of this term for a frustrated lattice. Within the approximations employed, a mean field theory for the strong coupling limit, a simplified non crossing approximation, and iterative perturbation theory, we did not find a Mott transition. Once one allows for magnetic symmetry breaking, the phase transition into a staggered phase can be explored. The density of states thus obtained is somewhat more realistic than the result of the traditional scaling because the inclusion of density fluctuations can be interpreted as the partial summation of $\frac{1}{d}$ corrections.

In **appendix A** we showed how iterative perturbation theory can be implemented on the real axis using the Keldysh formalism. Some results for the half filled Hubbard model at finite temperatures were also presented.

Appendix B studied the magnetic exchange in $LaTiO_3$. Taking into account the oxygen orbitals, it was established that the material is rather frustrated. This justifies the use of the *frustrated* Hubbard model as an effective Hamiltonian for the description of such systems.

In **appendix C** we discussed briefly that our approach to construct an interpolating self energy is mainly restricted to infinite dimensions and cannot easily be transferred to the finite dimensional case.

Finally, **appendix D** was devoted to the half filled Hubbard model with binary site randomness. As an additional check of our method, we confirmed some previously obtained analytic results [88].

Although the approximation scheme introduced in this thesis proved quite successful in many cases, it remains an unresolved problem how to treat multiband models at arbitrary fillings larger than one. From the discussion of the multiband scheme it became apparent that a separation of the different energy scales is important. This, however, cannot be achieved within IPT. A more promising approach would reduce the Hamiltonian of the original model by projecting out contributions from high energies. The basic task is then to find an approximation scheme for solving the effective Hamiltonian obtained in this way.

In spite of these restrictions, our perturbation scheme provides an important tool for numerous applications as might be illustrated by the fact that other groups have already started using it since the first results were published. Examples are a study of the interplay of interaction and disorder [114] and a publication dealing with the Hall coefficient in the doped Mott insulator [115]. Particularly interesting is the work of Anisimov [116] who is combining our multiband scheme with bandstructure calculations. We anticipate further progress in the description of real materials along these lines.

Appendix A

Keldysh Version of Iterative Perturbation Theory at Half Filling

A.1 Introduction

So far finite temperature calculations with the ordinary IPT scheme have mostly been done using the Matsubara frequency dependent Green functions [20]. It turns out that on the imaginary axis convergence is achieved quickly. However, in order to obtain the density of states one has to continue the numerical values of $G(i\omega_n)$ to the real axis which requires more sophisticated tools (e. g. the maximum entropy method) [7].

Here we will describe how iterative perturbation theory (at half filling) can be formulated in real frequency space using the *Keldysh formalism*. Thus, an elegant way of computing the density of states at finite temperatures is provided.

After deriving the formalism (section A.2) we present some finite temperature results for the half filled Hubbard model (section A.3). Section A.4 contains a comparison with exact diagonalization.

A.2 Formalism

The *Keldysh formalism* [49] is a generalization of the standard $T = 0$ diagram technique to finite temperatures. It uses four different Green functions (G^{--}, G^{++}, G^{+-} and G^{-+}) which for fermions are defined as follows:

$$\begin{aligned} iG^{--}(x_1,t_1;x_2,t_2) &:= \langle T\psi(x_1,t_1)\psi^+(x_2,t_2)\rangle \\ &= \theta(t_1-t_2)\langle\psi(x_1,t_1)\psi^+(x_2,t_2)\rangle - \\ &\quad\ \theta(t_2-t_1)\langle\psi^+(x_2,t_2)\psi(x_1,t_1)\rangle \qquad \text{(A.1)} \\ iG^{++}(x_1,t_1;x_2,t_2) &:= \langle\tilde{T}\psi(x_1,t_1)\psi^+(x_2,t_2)\rangle \end{aligned}$$

$$
\begin{aligned}
&= \theta(t_2 - t_1)\langle\psi^+(x_1,t_1)\psi(x_2,t_2)\rangle - \\
&\quad \theta(t_1 - t_2)\langle\psi(x_2,t_2)\psi^+(x_1,t_1)\rangle \qquad \text{(A.2)}
\end{aligned}
$$

$$
iG^{+-}(x_1,t_1;x_2,t_2) := \langle\psi(x_1,t_1)\psi^+(x_2,t_2)\rangle \qquad \text{(A.3)}
$$

$$
iG^{+-}(x_1,t_1;x_2,t_2) := \langle\psi^+(x_2,t_2)\psi(x_1,t_1)\rangle \qquad \text{(A.4)}
$$

It is easy to verify that

$$
G^{--} + G^{++} = G^{-+} + G^{+-} \quad ; \qquad \text{(A.5)}
$$

i. e. only three of these four functions are independent of each other. The advanced Green function can be obtained from

$$
\begin{aligned}
iG^{(adv)}(x_1,t_1;x_2,t_2) &:= -\theta(t_2 - t_1)\langle\psi(x_1,t_1)\psi^+(x_2,t_2) + \psi^+(x_1,t_1)\psi(x_2,t_2)\rangle \\
&= G^{--} - G^{+-} \\
&= G^{-+} - G^{++} \quad . \qquad \text{(A.6)}
\end{aligned}
$$

A similar relation holds for $G^{(ret)}$.

For noninteracting fermions the Fourier transforms of (A.1) to (A.4) are given by

$$
\begin{aligned}
G^{(0)^{-+}}(\omega,p) &= 2\pi i\; n_p\, \delta(\omega - \epsilon_p + \mu) \qquad \text{(A.7)} \\
G^{(0)^{+-}}(\omega,p) &= -2\pi i\; (1 - n_p)\; \delta(\omega - \epsilon_p + \mu) \qquad \text{(A.8)} \\
G^{(0)^{--}}(\omega,p) &= \frac{1 - n_p}{\omega - \epsilon_p + \mu + i0^+} + \frac{n_p}{\omega - \epsilon_p + \mu - i0^+} \qquad \text{(A.9)} \\
G^{(0)^{++}}(\omega,p) &= -\left(G^{(0)^{--}}(\omega,p)\right)^* \qquad \text{(A.10)}
\end{aligned}
$$

where n_p denotes the Fermi factor.

In the corresponding diagram technique each vertex has a $+$ or $-$ sign so that there are four contributions to the self energy: Σ^{++}, Σ^{--}, Σ^{-+} and Σ^{+-}. Again only three of them are independent since

$$
\Sigma^{++} + \Sigma^{--} = -\left(\Sigma^{+-} + \Sigma^{-+}\right) \quad . \qquad \text{(A.11)}
$$

The advanced self energy can be obtained by

$$
\Sigma^{(adv)} = \Sigma^{--} + \Sigma^{+-} \quad . \qquad \text{(A.12)}
$$

Within this framework iterative perturbation theory can be performed in the following way:

We start with a guess for the advanced Green function $G^{(adv)}(\omega)$. Then $G_0^{adv}(\omega)$ is determined by:

$$\left(G_0^{(adv)}\right)^{-1}(\omega) = \omega - i\eta - t^2\, G^{(adv)}(\omega) \tag{A.13}$$

Let $A(\omega)$ be the spectral weight of $G_0^{(adv)}$:

$$A(\omega) = \frac{1}{\pi}\,\mathrm{Im}\, G_0^{(adv)}(\omega) \tag{A.14}$$

It is convenient to introduce functions $A(t)$ and $\tilde{A}(t)$ as Fourier transforms of $A(\omega)$ and $\tilde{A}(\omega) := A(\omega)\, n_f(\omega)$:[1]

$$\begin{aligned} A(t) &= \int_{-\infty}^{+\infty} \frac{d\omega}{2\pi}\, A(\omega) e^{-i\omega t} && \text{(A.15)} \\ \tilde{A}(t) &= \int_{-\infty}^{+\infty} \frac{d\omega}{2\pi}\, \tilde{A}(\omega) e^{-i\omega t} && \text{(A.16)} \end{aligned}$$

Now, using $G^{\sigma\sigma} = \int d\epsilon_p\, G^{(0)^{\sigma\sigma}}(\omega, \epsilon_p)\, A(\epsilon_p)$, and (A.7) to (A.10), we can express all four Green functions in terms of $A(t)$ and $\tilde{A}(t)$:

$$\begin{aligned} G_0^{--}(t) &= 2\pi i \left(-\theta(t)\left(A(t) - \tilde{A}(t)\right) + \theta(-t)\tilde{A}(t)\right) \\ G_0^{++}(t) &= \left(-G_0^{--}(-t)\right)^{\star} \\ G_0^{-+}(t) &= 2\pi i\, \tilde{A}(t) \\ G_0^{+-}(t) &= -2\pi i \left(A(t) - \tilde{A}(t)\right) && \text{(A.17)} \end{aligned}$$

These Green functions are necessary to evaluate the second order self energy diagrams for Σ^{--} and Σ^{+-} (see figure A.1):

$$\begin{aligned} \Sigma^{--}(t) &= U^2 \left(G_0^{--}(t)\right)^2 G_0^{--}(-t) \\ \Sigma^{+-}(t) &= -U^2 \left(G_0^{+-}(t)\right)^2 G_0^{-+}(-t) && \text{(A.18)} \end{aligned}$$

Now equations (A.6) and (A.12) allow us to change back to the advanced functions:

$$\begin{aligned} G_0^{(adv)}(t) &= G_0^{--}(t) - G_0^{+-}(t) \\ \Sigma^{(adv)}(t) &= \Sigma^{--}(t) + \Sigma^{+-}(t) && \text{(A.19)} \end{aligned}$$

---

[1]By n_f we denote the Fermi factor $n_f(\omega) = \frac{1}{\exp(\omega/T)-1}$.

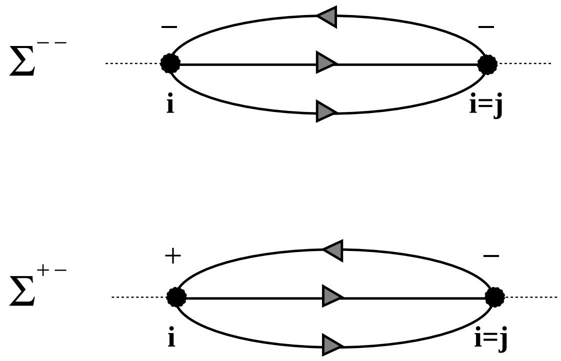

Figure A.1: Second order diagrams for Σ^{--} and Σ^{+-}

The new (full) Green function $G^{(adv)}$ is finally given by

$$\left(G^{(adv)}(\omega)\right)^{-1} = \left(G_0^{(adv)}(\omega)\right)^{-1} - \Sigma^{(adv)}(\omega) \quad . \tag{A.20}$$

Returning to equation (A.13) closes the iteration.

The numerical implementation requires Fourier transforms between time and frequency space. These can be realized by using fast Fourier transforms [50].

We formulated the equations for the Hubbard model. The corresponding results will be presented in the next section. But this procedure can also be applied to the large d limit of other lattice models. In most cases only slight modifications are necessary.

A.3 Results for the Hubbard model

During recent years the phase diagram of the Hubbard model has been studied intensively [20, 7, 25, 46, 47]. For a fully frustrated lattice there is no magnetic ordering at low temperatures. Thus one expects the existence of a metallic phase for small interactions and an insulator in the strong coupling limit. The nature of the transition between both phases at intermediate values of U has been the focus of several publications [8, 13, 21, 27]. One of the simplest approaches to the half filled case is the use of iterative perturbation theory [20]. At temperatures below $T_c \approx 0.5$[2] one observes a coexistence regime where there is a metallic as well as an insulating solution. The former

[2] D=2t=1

exists up to $U_{c_2}(T)$ while the latter extends down to $U_{c_1}(T) < U_{c_2}(T)$. At zero temperature these critical values can be determined analytically yielding $U_{c_1}(T=0) \approx 2.6$ and $U_{c_2}(T=0) \approx 3.3$. The lines $U_{c_1}(T)$ and $U_{c_2(T)}$ merge at T_c such that there is a crossover from a metal to a paramagnetic insulator for $T > T_c$.

Since previous calculations (iterative perturbation theory [20], quantum Monte Carlo studies [25, 46, 47]) were done using the Matsubara frequency formalism they did not directly yield the density of states. Instead it was necessary to apply the maximum entropy method to the Matsubara frequency dependent results.

However, the procedure developed in the last section provides an elegant way to obtain the density of states $\rho(\omega)$.

In figure A.2 we show how this quantity behaves at the crossover as U is increased for fixed T. For temperatures near T_c the quasiparticle peak decays quickly as the crossover is passed (figure A.2a). At higher temperatures a quasiparticle peak exists only for small U. With increasing interaction the weight at zero frequency decreases continuously thus indicating the change from a metal to a semiconductor (figure A.2b).

Figure A.3 shows the lines with $\rho(\omega=0) = const$ in the $U-T$-plane. They are nearly vertical. Only near the critical point T_c, there is a slight deformation which can be understood by the presence of the quasiparticle peak in the metallic phase (figure A.2a). This behavior has an interesting consequence for the resistivity. As shown in figure A.4, there is a crossover form a metal ($\frac{\partial\rho}{\partial T} > 0$) to a semiconductor ($\frac{\partial\rho}{\partial T} < 0$). This result is in good agreement with experimental measurements in $(V_{1-x}Cr_x)_2O_3$ systems where $x \approx 0.006 - 0.0015$ (see [48, 19]).

The high temperature phase diagram for the Hubbard model (see figure A.5) displays three different regions. For small interactions, the system is metallic. As U is increased, a gap develops in the density of states. This yields a crossover into the semiconductor. The gap increases, and at some point the pure insulator is reached.

As mentioned above, there might be two solutions below T_c. This is the case if $U_{c_1}(T) < U < U_{c_2}(T)$. Only the phase with the lower free energy is physically realized. As was pointed out by Rozenberg et al. [20] the energy difference between the metal and the insulator is quite small. Using iterative perturbation theory, they obtained a

a)

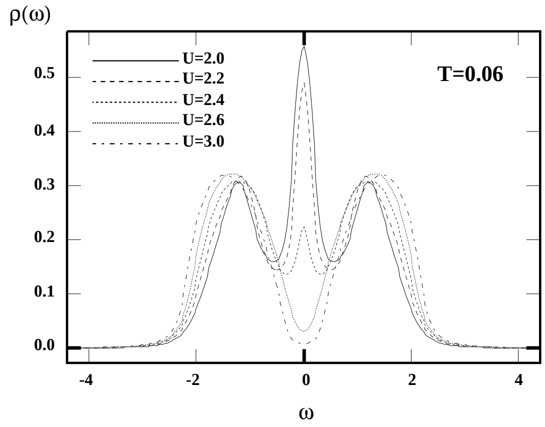

b)

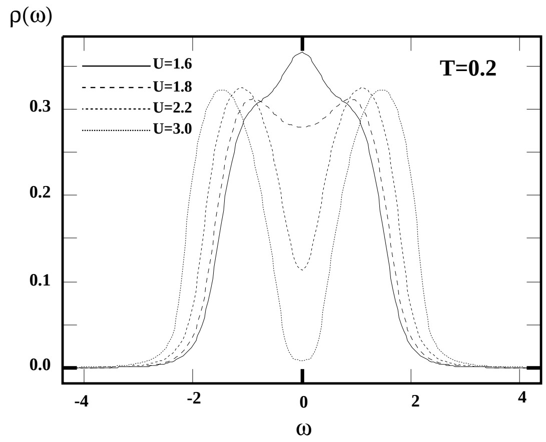

Figure A.2: Crossover in the density of states at $T = 0.06$ and $T = 0.2$

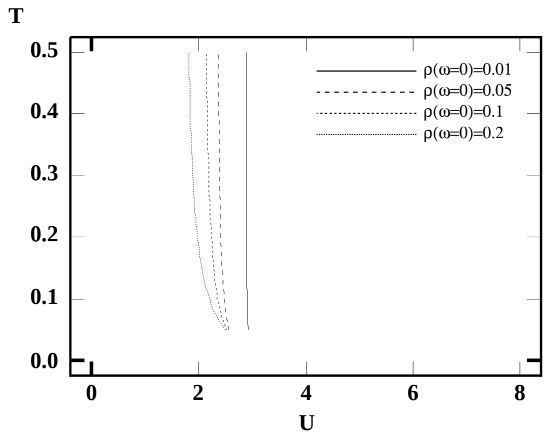

Figure A.3: Spectral weight at zero frequency: The plot shows lines with $\rho(\omega = 0) = const.$

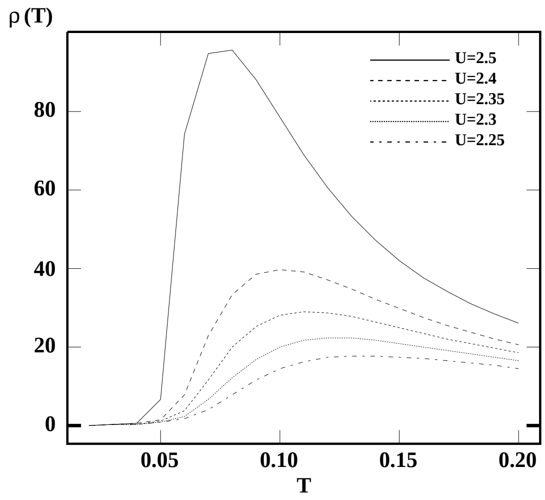

Figure A.4: Temperature dependence of the resistivity for different U

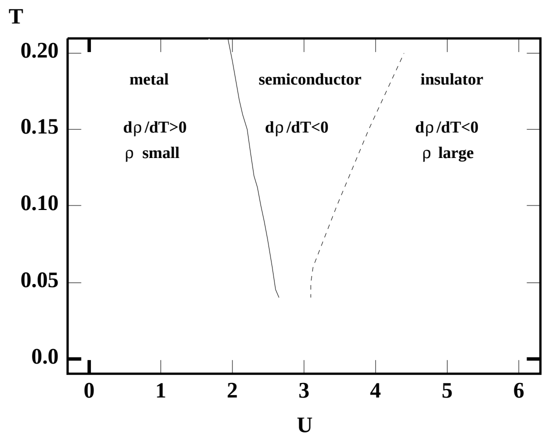

Figure A.5: High temperature phase diagram of the half filled Hubbard model

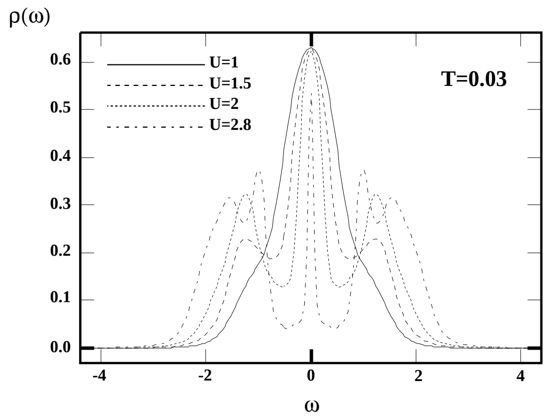

Figure A.6: Metallic solution at $T = 0.03$ and for different values of U.

first order (Mott) transition for all temperatures $0 < T < T_m$. At zero temperature the phase transition is of second order [45].

We do not want to study the Mott transition here but only present a few plots showing the evolution of $\rho(\omega)$. Figure A.6 contains the metallic density of states at $T = 0.03$ for different values of U. With increasing interaction the Hubbard bands form at approximately $\pm\frac{U}{2}$. In addition we keep a clear resonance peak at zero frequency which in contrast to the situation above T_m decreases only slowly. However, its width gets smaller as U_{c_2} is approached.

Coming from the insulating region, we can observe how the gap is reduced with decreasing interaction (figure A.7). Due to finite temperature the gap is not sharp. In particular for smaller interactions ($U < 3$) some finite weight is built up at zero frequency as the bands move together. In order to study the U-dependence of the gap, we extrapolated the density of states assuming a square root behavior at the inner band edges (see figure A.8). The gap defined in this way is plotted in figure A.9 as a function of U . For large interaction we have $\Delta \sim U - 2D$. The behavior for small U, however, is clearly influenced by the finite temperature.

For $T = 0.03$ the regime where both, the insulating and the metallic solution, coexist extends from $U_{c_1} \approx 2.6$ to $U_{c_2} \approx 2.8$. Figure A.10 compares both solutions in this regime.

With regard to the metallic phase, it is finally interesting to study the temperature

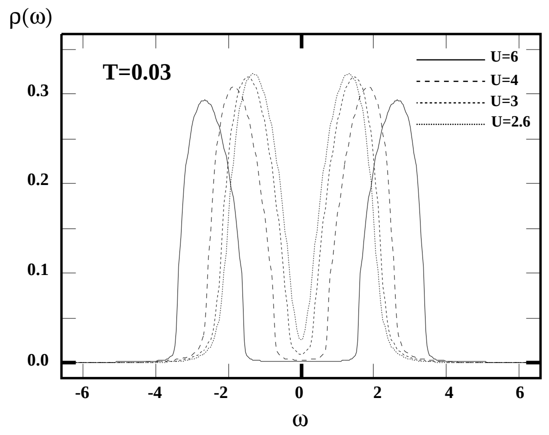

Figure A.7: Insulating solution at $T = 0.03$ and for different values of U.

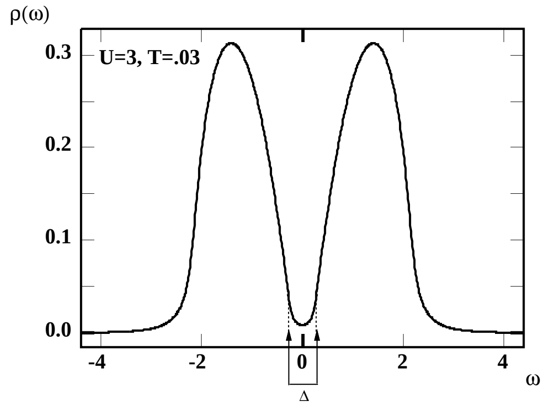

Figure A.8: Determination of the gap at finite temperature.

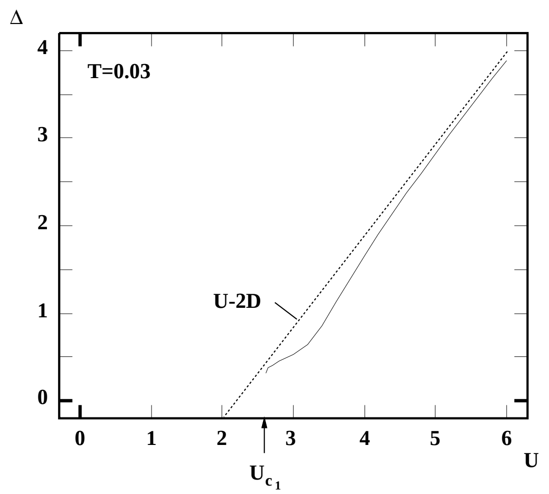

Figure A.9: Gap as a function of U determined from the data at T=0.03

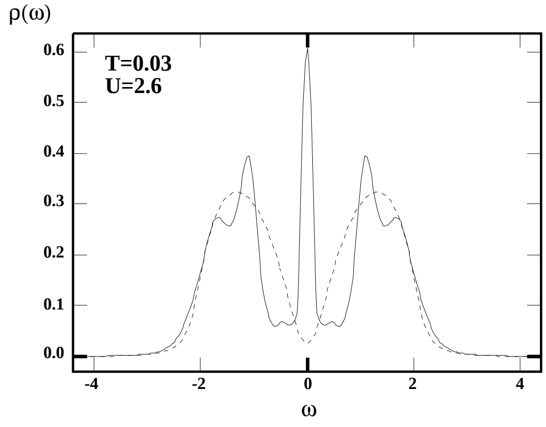

Figure A.10: Coexistence of two solutions at $T = 0.03$ and $U = 2.6$.

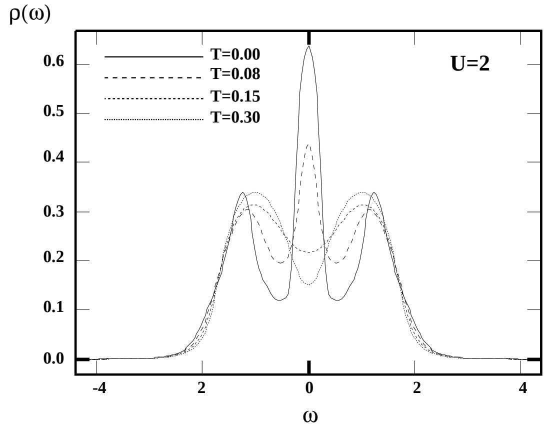

Figure A.11: Temperature dependence of the density of states for $U = 2.0$

dependence of the resonance peak. In figure A.11 we plotted the density of states for $U = 2$ and various temperatures. The quasiparticle peak is thermally destroyed above the coherence temperature T_{coh} (see figure A.12). Note that for $T > T_{coh}$ the zero frequency weight of the density of states is nearly temperature independent. This holds for all values of U and explains that the lines with constant spectral weight $\rho(\omega = 0)$ in figure A.3 are nearly vertical.

All the plots above were obtained with relatively low numerical effort. In conclusion, we have seen in that the Keldysh version of iterative perturbation theory is a quite useful tool to compute the density of states at finite temperatures.

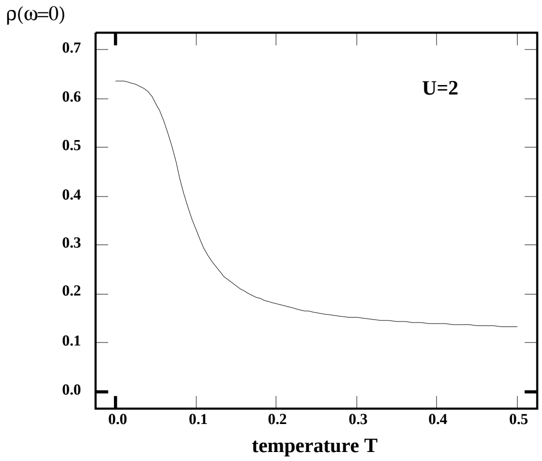

Figure A.12: Decay of the quasiparticle peak: Density of states at zero frequency as a function of temperature for $U = 2$.

A.4 Comparison with exact diagonalization

So far we have seen that the formalism developed at the beginning of this chapter provides an efficient way of performing iterative perturbation theory at finite temperatures. Now, we want to go one step further and check the quality of iterative perturbation theory as an approximation scheme for the particle hole symmetric case. As mentioned above it becomes exact not only in the weak but also in the strong coupling limit. Therefore the region of intermediate interaction strength is of particular interest. Recently exact diagonalization techniques have been developed which allow to study this parameter range [21].

In figures A.13 to A.16 we compare our results (full line) with those of an exact diagonalization code. The latter treats only a finite number of poles. For the plots of $G(\omega)$ and $\Sigma(\omega)$ we introduced a broadening $\eta = 0.075$. The positive values of $\Sigma(\omega)$ in figure A.15 are an artifact of the analytic continuation in the exact diagonalization code and should not be taken seriously. We see that the basic structures of $G(\omega)$ and $\Sigma(\omega)$ agree for both methods.

On the imaginary axis there is an excellent agreement. Deviations are visible only at low temperatures and intermediate interactions (e. g. $U = 2$, $T = 0.03$).

However, when a more detailed study is performed on the real axis it can be seen that the IPT scheme does not have the correct transfer of spectral weight with increasing temperature. This aspect is addressed in chapter 7. The consequences at half filling are minor since the particle hole symmetry restores the main physical results at least qualitatively. Morevover, the interactions which are relevant for a metallic phase are not very large.

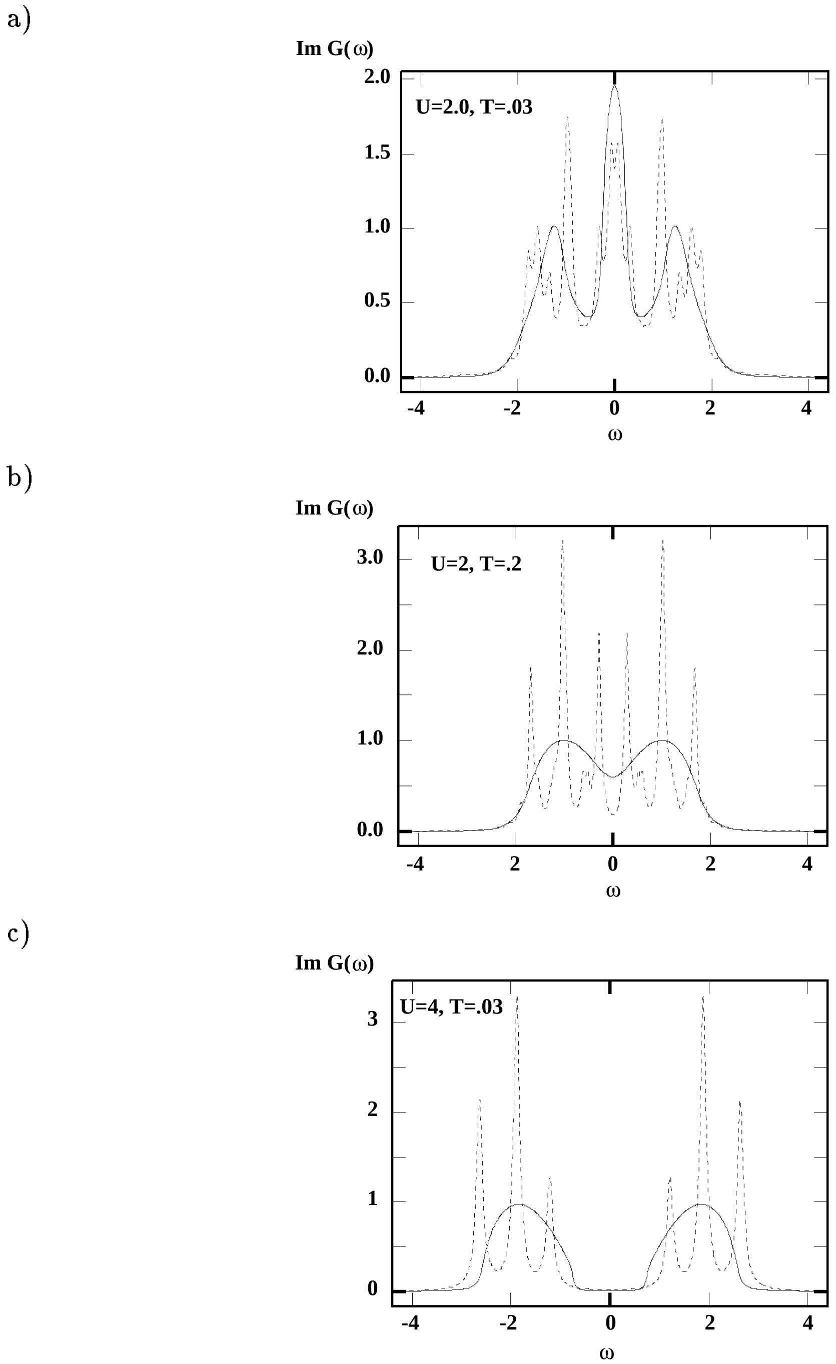

Figure A.13: Comparison between iterative perturbation theory (full line) and exact diagonalization (dashed line): Im$G(\omega)$

a)

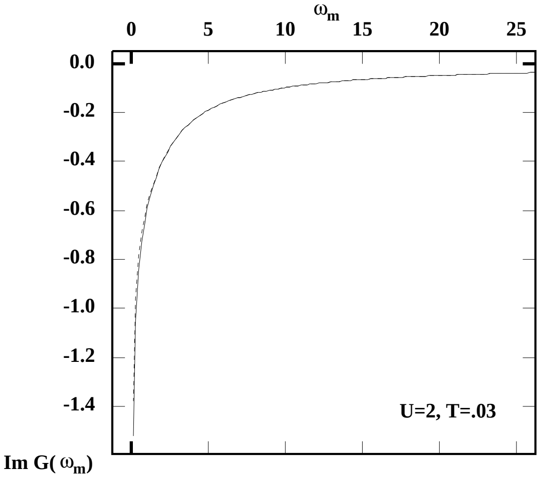

b)

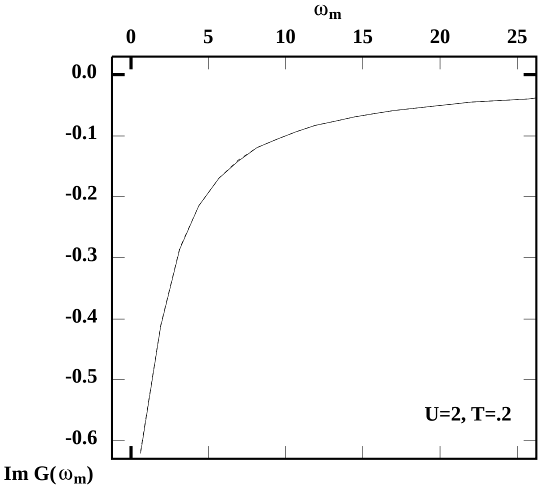

c)

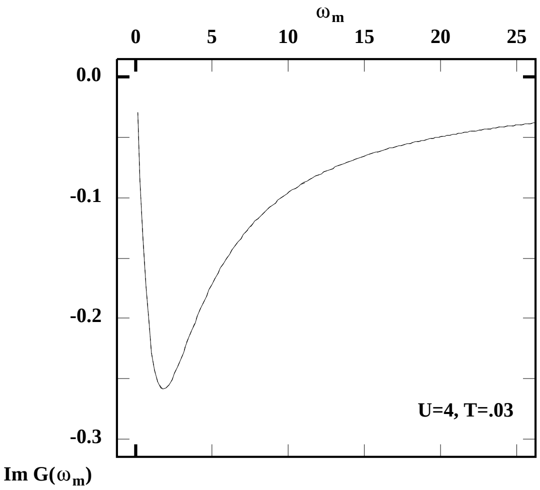

Figure A.14: Comparison between iterative perturbation theory (full line) and exact diagonalization (dashed line): Im$G(\omega_n)$

a)

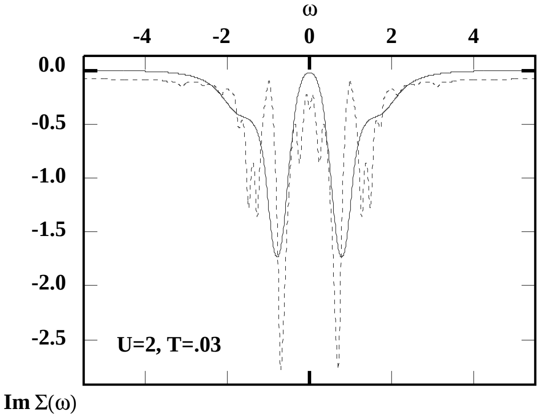

b)

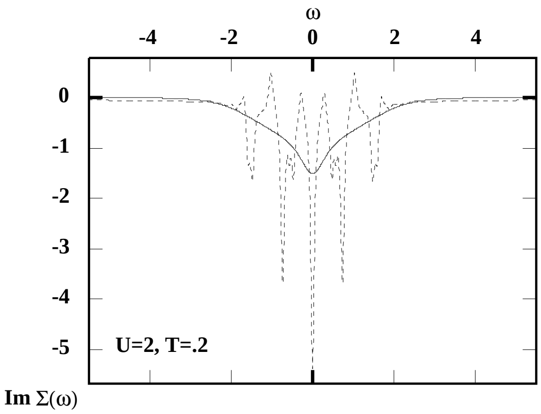

c)

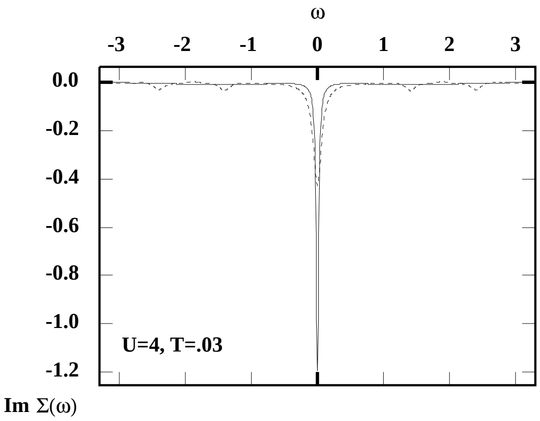

Figure A.15: Comparison between iterative perturbation theory (full line) and exact diagonalization (dashed line): $\mathrm{Im}\Sigma(\omega)$

a)

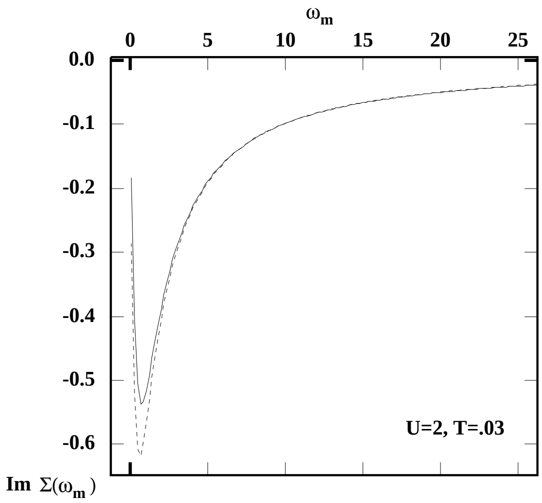

b)

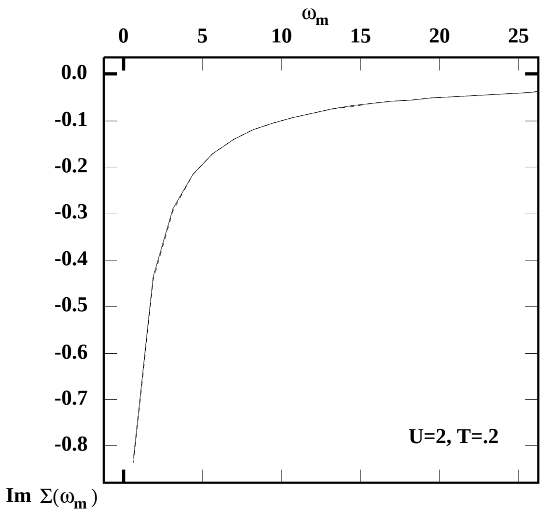

c)

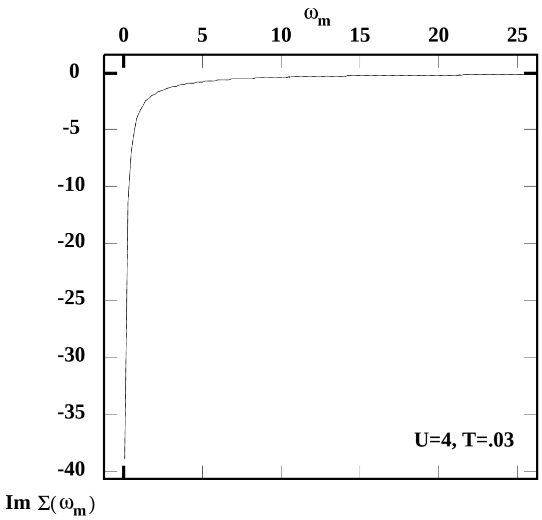

Figure A.16: Comparison between iterative perturbation theory (full line) and exact diagonalization (dashed line): $\mathrm{Im}\Sigma(\omega_n)$

Appendix B

Magnetic Superexchange in $LaTiO_3$

B.1 Introduction

Treatments of correlated Fermi systems are often restricted to one band models like the Hubbard model. This yields simplifications which allow to apply methods which otherwise would be too complicated (e. g exact diagonalization). It is believed that the one band model can be thought of as an effective Hamiltonian for the more sophisticated system. Obviously, it is important to know under which conditions this assumption is correct and where it might fail.

In this appendix, we will treat the magnetic superexchange in a multiband model constructed to describe the Mott Insulator $LaTiO_3$. The single band Hubbard model might serve as an effective Hamiltonian. However, the substance shows a transition into an antiferromagnetic ground state at a transition temperature which is much lower than predicted by the Hubbard model or than that found in quasi two dimensional cuprates, the corresponding single band materials. Thus, we expect that multiband effects play an important role in the case of $LaTiO_3$.

We address this question by constructing an appropriate Hamiltonian. Eliminating the oxygen sites, we obtain an effective model from which we draw conclusions on the magnetic properties.

The basic finding will be, that the antiferromagnetism originating from *intraband* coupling is strongly suppressed by *interband* processes. There is a large temperature range where the system is frustrated. Here a single band Hamiltonian can yield a reasonable description only if it is applied to a fully frustrated lattice.

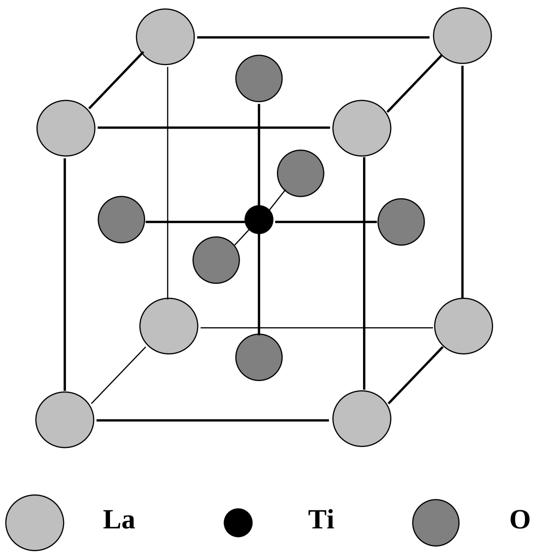

Figure B.1: Perovskite structure for $LaTiO_3$ (without distortion)

B.2 Derivation of the model Hamiltonian

It is useful to start with some remarks on $LaTiO_3$ [76]. Experiments show that this material is barely metallic or semiconducting. There is an antiferromagnetic phase transition at a temperature between 125 and 149 K [77, 78, 79, 80]. As mentioned in the introduction, this temperature is considerably lower than in quasi two dimensional cuprates (1300 K) [84].

$LaTiO_3$ has an orthorombically distorted perovskite structure [81]. When constructing our model Hamiltonian we neglect the distortion assuming an ideal perovskite structure (figure B.1).

The formal valances of the constituents are La^{3+}, O^{2-} and Ti^{3+}, where the latter has the electronic configuration $3d^1$. Thus, there is exactly one d electron per Ti site so that a Mott insulator occurs. All p orbitals in O^{2-} are occupied ($2s^2 2p^6$) and La^{3+} has a closed shell.

For the description of the electronic properties, only the Ti and O sites are important as La^{3+} has a closed shell. In particular, we have to consider the O $2p$ and the Ti $3d$ orbitals. Due to cubic symmetry the five 3d bands are split into two degenerate upper bands (x^2-y^2, $3x^2-y^2$) and three degenerate orbitals (xy, xz, yz). Only the latter have to be taken into account since they are lower in energy. The site dependent energies of the oxygens ($\epsilon_d - \Delta$) are considerably smaller than those of the Ti sites (ϵ_d). Following these remarks, we can write down the terms containing the local energy levels on O and Ti sites:

$$H_{site} = \epsilon_d \sum_{i,\sigma,m} d^+_{im\sigma} d_{im\sigma} + (\epsilon_d - \Delta) \sum_{i,\sigma,l,\delta} p^+_{i+\delta,l,\sigma} p_{i+\delta,l\sigma} \tag{B.1}$$

Here, i labels the position of the Ti sites. The index δ is half a unit vector ($\delta \in \{\frac{1}{2}e_x, \frac{1}{2}e_y, \frac{1}{2}e_z\}$) so that $i + \delta$ marks the position of the oxygens. Moreover, m and l are band indexes: $m \in \{xy, xz, yz\}$ and $l \in \{x, y, z\}$.

The kinetic term is characterized by that charge is carried only between orbitals parallel to the xy-, the xz-, or the yz-plane. This can be seen as follows: Let us consider a Ti at site i and the neighboring O at site $i + \frac{1}{2}e_x$ (see figure B.2). There are only two pairs of orbitals which overlap: the Ti $3d_{xy}$ with the O $2p_y$ (shown in figure B.2) and the Ti $3d_{xz}$ with the O $2p_z$ (xz plane). This results in

$$t_{pd} \left(d^+_{i,xy,\sigma}\ p_{i+\frac{1}{2}e_x,y,\sigma} + h.c. + d^+_{i,xz,\sigma}\, p_{i+\frac{1}{2}e_x,z,\sigma} + h.c. \right) \tag{B.2}$$

Taking into account all next neighbor pairs, we obtain the kinetic energy:

$$\begin{aligned} H_{kin} = t_{pd} \sum_{i,\sigma;\gamma\in\{-1,1\}} \quad & (d^+_{i,xy,\sigma}\ p_{i+\frac{\gamma}{2}e_x,y,\sigma} + h.c. + d^+_{i,xy,\sigma}\ p_{i+\frac{\gamma}{2}e_y,x,\sigma} + h.c. + \\ & d^+_{i,xz,\sigma}\ p_{i+\frac{\gamma}{2}e_x,z,\sigma} + h.c. + d^+_{i,xz,\sigma}\ p_{i+\frac{\gamma}{2}e_z,x,\sigma} + h.c. + \\ & d^+_{i,yz,\sigma}\ p_{i+\frac{\gamma}{2}e_y,z,\sigma} + h.c. + d^+_{i,yz,\sigma}\ p_{i+\frac{\gamma}{2}e_z,y,\sigma} + h.c.) \end{aligned} \tag{B.3}$$

Finally, we have to introduce interactions:

$$H_{int} \quad = \quad U_1 \sum_{i,m} n_{im\uparrow} n_{im\downarrow} + U_2 \sum_{i,m\neq m'} n_{im\uparrow} n_{im'\downarrow} + U_3 \sum_{i,m\neq m',\sigma} n_{im\sigma} n_{im'\sigma} \tag{B.4}$$

Here, U_1 is the on site interaction at a Ti site between electrons in the same band and opposite spins. Analogously, U_2 (U_3) couples electrons in different bands and with opposite (parallel) spins. The parameter U_3 is by an intraatomic exchange energy J smaller than U_2 ($U_3 = U_2 - J, J > 0$). Moreover, rotational symmetry requires $U_1 - U_2 = 2J$. For simplification, we neglected the on site interaction on oxygen sites

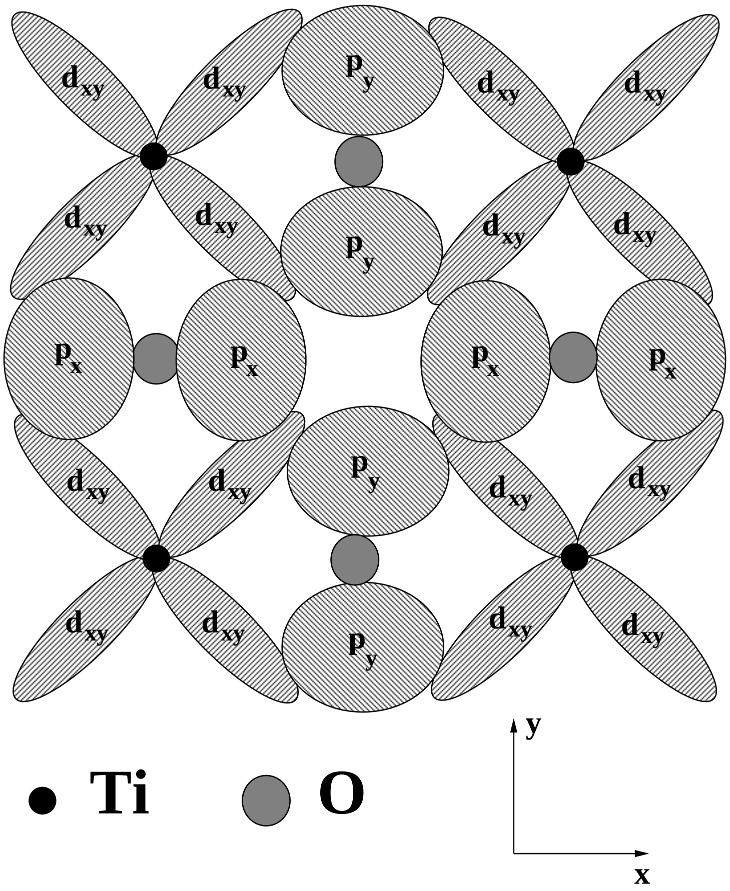

Figure B.2: Overlap of orbitals in the xy plane.

as well as next neighbor interactions. The sums over the spin and band indices are to be understood such that each tupel $(m\sigma, m'\sigma')$ or $(l\sigma, l'\sigma')$ is included only once.

The complete Hamiltonian is the sum of (B.1), (B.3) and (B.4):

$$H = H_{site} + H_{kin} + H_{int} \tag{B.5}$$

In the case of $LaTiO_3$ it has to be considered for large interactions, large Δ and a filling characterized by one electron per Ti site and fully occupied p orbitals on the oxygen sites. In this case, the d-electrons will be localized at the Ti sites. Both, p and d electrons are involved in virtual processes lowering the total energy.

B.3 Effective Hamiltonian

As we want to examine the magnetic exchange between electrons on neighboring Ti sites, we eliminate the oxygen sites. In principle, this could be done by a canonical transformation [82]. But here it is much more convenient to obtain the effective Hamiltonian by using perturbation theory up to fourth order in the O-Ti hopping t_{pd} [83].

To simplify the notations let us first introduce a definition. For each pair of next neighbor sites i and j, two of the three d orbitals (xy, xz, yz) have an overlap with one of the p orbitals of the oxygen between i and j while the third one has not. If e. g. $(\vec{r}_i - \vec{r}_j) \parallel \vec{e}_x$ then d_{xy} overlaps with p_z and d_{xz} with p_z. But no charge can be carried from d_{yz} in x direction. We thus define

$$L(i,j) := \{m | m = (\alpha\beta) \quad \text{and} \quad (\vec{r}_i - \vec{r}_j) \parallel \vec{e}_\alpha \quad \text{or} \quad (\vec{r}_i - \vec{r}_j) \parallel \vec{e}_\beta ; \alpha, \beta \in \{x, y, z\}\}.$$

Figure B.3 shows a possible virtual process between two Ti neighbors with electron configuration $m\sigma$ and $m'\sigma$ respectively where $m \in L(i,j)$ and $m' \notin L(i,j)$. The corresponding contribution to the Hamiltonian is given by

$$-\frac{t_{pd}^4}{(\Delta + U_3)^2(2\Delta + U_3 + U_1)} n_{m\sigma} n_{m'\sigma} \tag{B.6}$$

Altogether there are several hundreds of such processes which have to be evaluated. This task can only be done by computer. The resulting Hamiltonian has the following

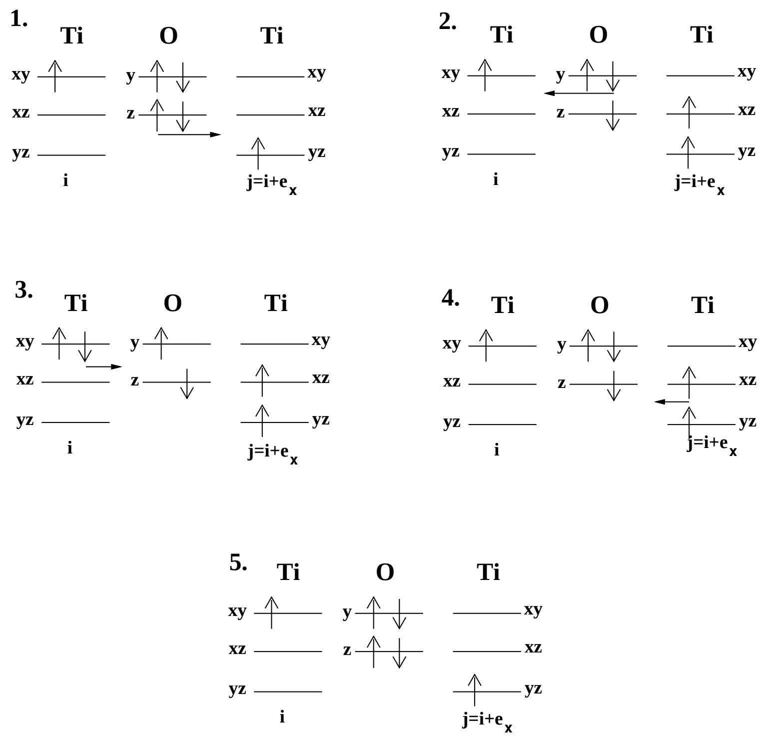

Figure B.3: Example for a sequence of virtual processes contributing in fourth order perturbation theory. The position of the orbitals does not indicate energy levels.

form:

$$H_{eff} = H_{mag} + H_{band} + H_{fluc} \tag{B.7}$$

where

$$\begin{aligned} H_{mag} &= J_1 \sum_{\langle ij\rangle, m\in L(i,j)} S_i^m \, S_j^m + J_2 \sum_{\langle ij\rangle; m,m'\in L(i,j); m\neq m'} S_i^m S_j^{m'} \\ &+ J_3 \sum_{\langle ij\rangle; m\in L(i,j), m'\notin L(i,j)} \left(S_i^m S_j^{m'} + S_i^{m'} S_j^m\right) + J_4 \sum_{\langle ij\rangle; m,m'\notin L(i,j)} S_i^m S_j^{m'} \end{aligned} \tag{B.8}$$

$$\begin{aligned} H_{band} &= B_1 \sum_{\langle ij\rangle, m\in L(i,j)} n_{im} \, n_{jm} + B_2 \sum_{\langle ij\rangle; m,m'\in L(i,j); m\neq m'} n_{im} n_{jm'} \\ &+ B_3 \sum_{\langle ij\rangle; m\in L(i,j), m'\notin L(i,j)} \left(n_{im} n_{jm'} + n_{im'} n_{jm}\right) + B_4 \sum_{\langle ij\rangle; m,m'\notin L(i,j)} n_{im} n_{jm'} \end{aligned} \tag{B.9}$$

$$\begin{aligned} H_{fluc} &= J_{sf} \sum_{\langle ij\rangle, m\in L(i,j)} \vec{S}_i^{\perp m} \vec{S}_j^{\perp m} \\ &+ J_{sf/bf} \sum_{\langle ij\rangle; m,m'\in L(i,j); m\neq m'; \sigma} \frac{1}{2} d^+_{im'-\sigma} d^+_{jm\sigma} d_{jm'-\sigma} d_{im\sigma} \end{aligned}$$

$$+J_{bf} \sum_{\langle ij\rangle;m,m'\in L(i,j);m\neq m';\sigma} \frac{1}{2}\left(d^{+}_{im'\sigma} d^{+}_{jm\sigma} d_{jm'\sigma} d_{im\sigma}\right) \tag{B.10}$$

Here, $n_{im} = \sum_\sigma n_{im\sigma}$ and $\vec{S}_i^{\perp m} := \vec{S}_i^m - (\vec{S}_i^m)_z \vec{e}_z$.

The parameters J_i and B_i $(i = 1\ldots4)$ as well as J_{sf}, J_{bf} and $J_{sf/bf}$ are known explicitly as a function of t_{pd}, Δ, U_1, U_2 and U_3. However, the expressions are rather long, so that we do not give them here. Each is made up of a sum of terms of the order $t_{pd}^4/(U_i,\Delta)^3$ where (U_i,Δ) denotes the U_i or Δ or a linear combination of them, e.g. $U_1 + U_2 + 2\Delta$, $U_1 + \Delta$ or U_1 etc. In the remaining part of this chapter, we will evaluate the parameters numerically for $U_1 = 4eV$, $\Delta = 6eV$, $t_{pd} = 0.5eV$ and variable intraatomic exchange J.[1]

The term H_{mag} describes the magnetic ordering. Intraband coupling (J_1, J_4) yields an antiferromagnetic contribution while interband coupling (J_2 and J_3) is ferromagnetic:

$$J_1 > 0\ ,\ J_2 < 0\ ,\ J_3 < 0 \ \text{ and }\ J_4 > 0 \tag{B.11}$$

As can be seen in figure B.4 $|J_4|$ is almost zero and considerably smaller than the other parameters. Moreover, J_1 depends only weakly on the intraatomic exchange, while the ferromagnetic contributions J_2 and J_3 increase strongly with increasing J. For small J the antiferromagnetic exchange described by J_1 is largest, while for large J the ferromagnetic coupling J_2 has the highest absolute value.

To judge about the magnetic properties of the ground state, one has also to take into account that not all configurations in the band index are energetically equally favorable. The corresponding information is contained in H_{band}. The latter is the analogous term to H_{mag} referring to the band index rather than the spin. As shown in figure B.5 H_{band} favors over a large range of J configurations $(im; jm')$ where the d orbitals m and m' are not linked via an oxygen (i. e. $m = m' \notin L(i,j)$). [2] A bond with $m = m' \in L(i,j)$ is highest in energy as far as the contribution H_{band} is concerned.

The third part of the effective Hamiltonian (B.8) is H_{fluct}. It describes spin flips (J_{sf}), band flips (J_{bf}) and simultaneous spin- and band-flips ($J_{sf/bf}$).

[1] Since $U_3 = U_1 - 3J > 0$, we have $J < \frac{U_1}{3}$; i. e. $J < 1.33eV$ for $U_1 = 4eV$.

[2] In the limit $J = 0$ and $U_1 = \Delta$ the parameters B_i can be estimated by the number of diagrams contributing. For $(m, m') \notin L(i,j)$ this number is maximal.

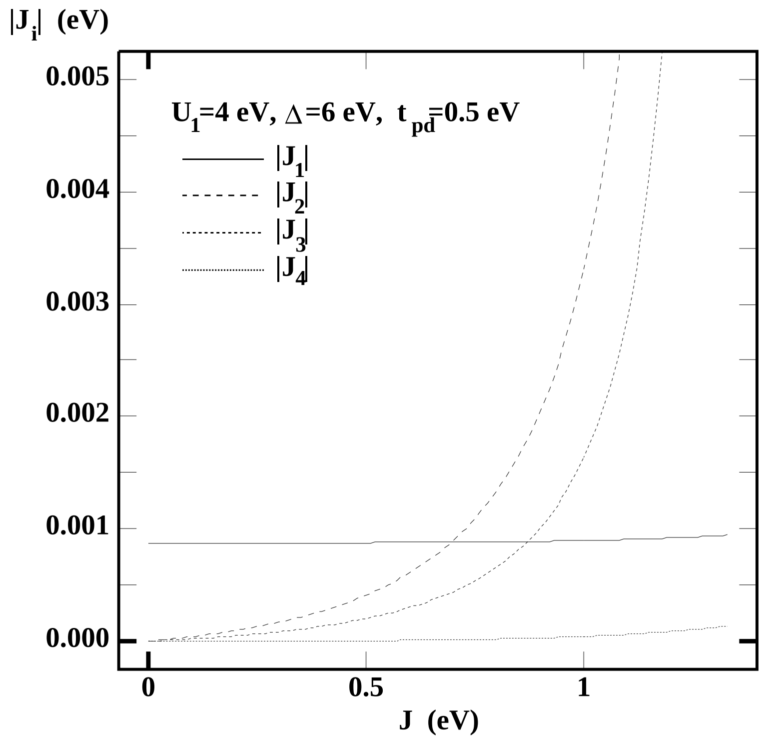

Figure B.4: Comparison of the J_i for $U_1 = 4eV$, $\Delta = 6eV$ and $t_{pd} = 0.5eV$ and a function of the intraatomic exchange J.

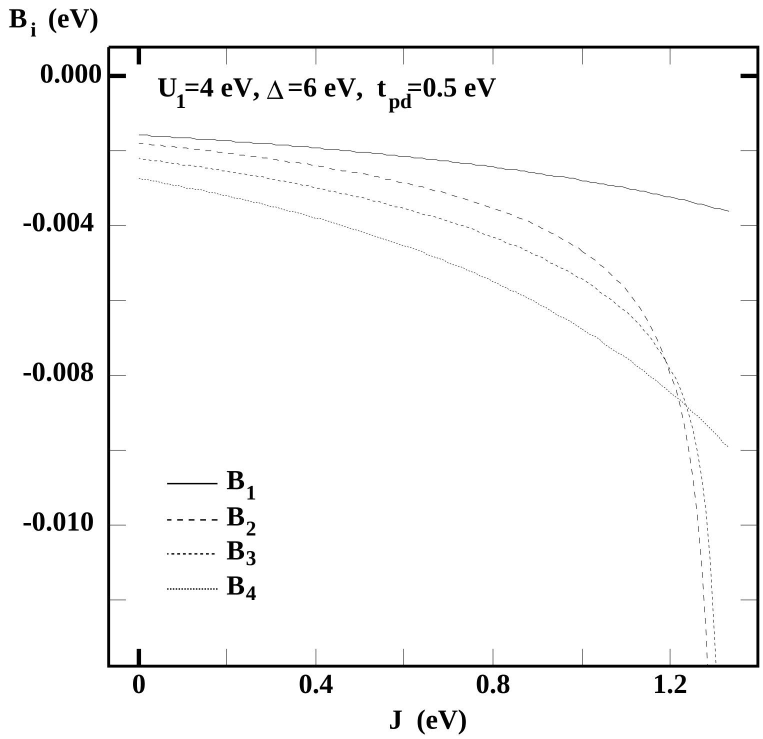

Figure B.5: Comparison of the B_i for $U_1 = 4eV$, $\Delta = 6eV$ and $t_{pd} = 0.5eV$ and a function of the intraatomic exchange J.

In the following we will compare the energy per bond for different configurations within mean field theory. In this approximation the fluctuation term is neglected:

$$H_{mean\ field} = H_{mag} + H_{band} \tag{B.12}$$

For a single next neighbor pair (i,j) there are eight independent types of configurations $(m\sigma, m'\sigma')$ whose energies have to be compared (figure B.6). As shown in figure B.7 over a large range of J again those bonds are favored where the d orbitals m and m' are not linked by an oxygen $((m = m') \notin L(i,j))$. The corresponding magnetic exchange constant J_4 is extremely small, so that these bonds are almost non magnetic. Only for extremely large J the ferromagnetic contributions become lowest in energy. But the antiferromagnetism related to J_1 (intraband coupling) is always suppressed (even for small J where $|J_1|$ is much larger than $|J_i|$ $(i = 2\ldots 4)$).

Above we argued with a certain set of parameters ($U_1 = 4eV$, $\Delta = 6eV$ and $t_{pd} = 0.5eV$). The qualitative results, however, are not very sensitive on the actual choice of the numerical values as long as the order of magnitude is correct.

We finally mention, that in the limit of extremely large Δ the energy gets minimal for ferromagnetic bonds (for all J, see figure B.8). In this case the ferromagnetism of a two band Hubbard model is recovered.

B.4 Discussion and conclusions

The aim of this appendix was to explore the influence of multiband effects on the magnetic superexchange in $LaTiO_3$. Experimentally the transition temperature into an antiferromagnetic ground state is found to be relatively small compared to the corresponding one band model.

We started our investigation by constructing a model Hamiltonian taking into account the electronic structure of $LaTiO_3$. In fourth order perturbation theory the oxygen sites can be eliminated. This yields an effective Hamiltonian (H_{eff}) containing Ising like terms (H_{mag}, H_{band}) as well as fluctuations in band and spin index (H_{fluc}). We compared the energy per bond for different configurations on the mean field level (neglecting H_{fluc}) and found that over a large range of the intraatomic exchange J an

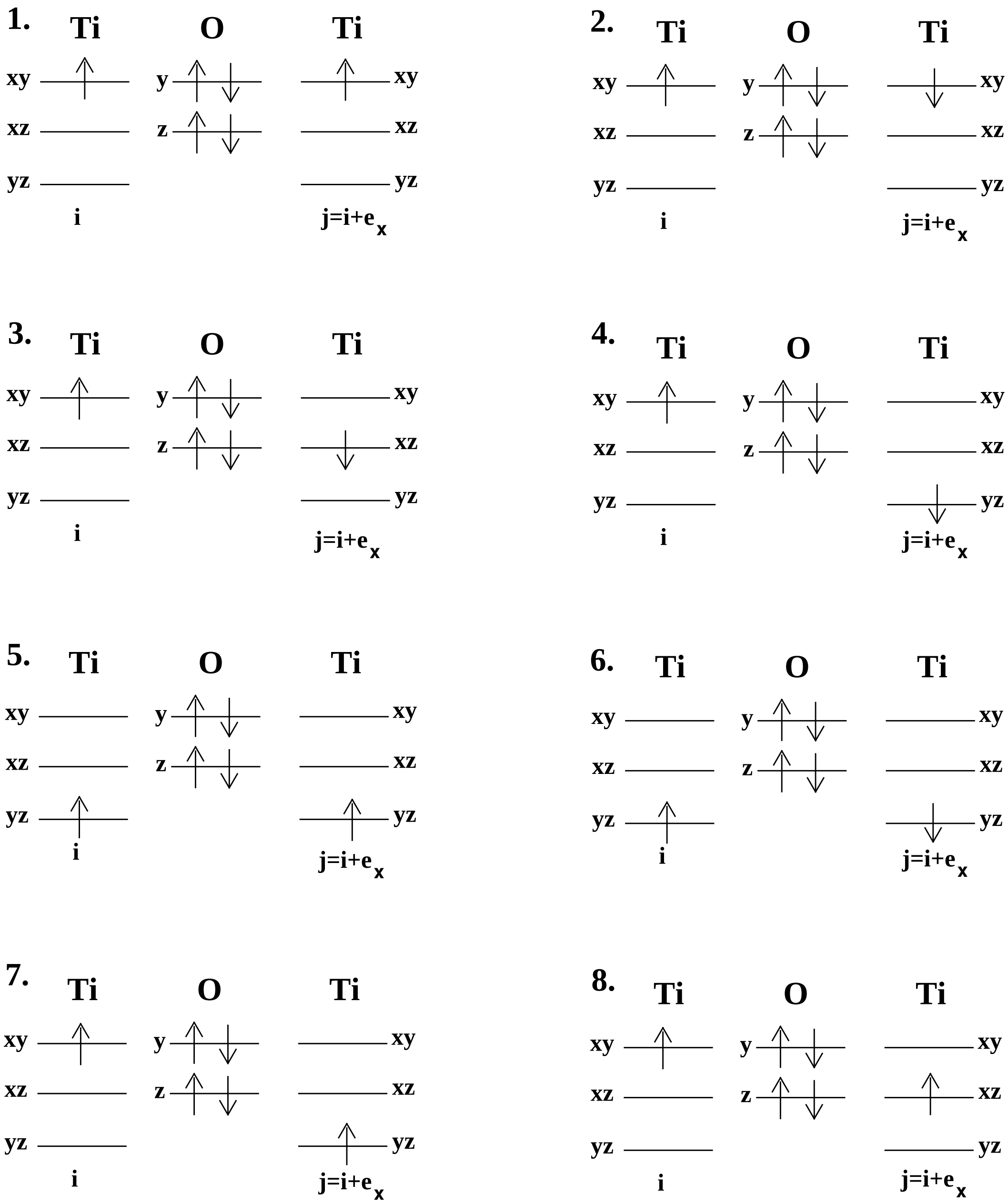

Figure B.6: Independent configurations yielding different energies.

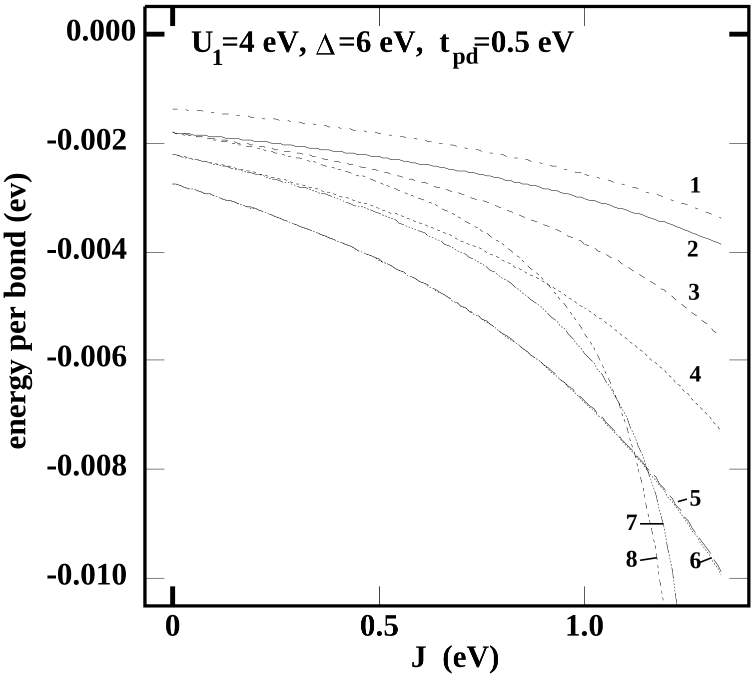

Figure B.7: Energy per bond for different configurations. (The configurations are shown in figure B.6).

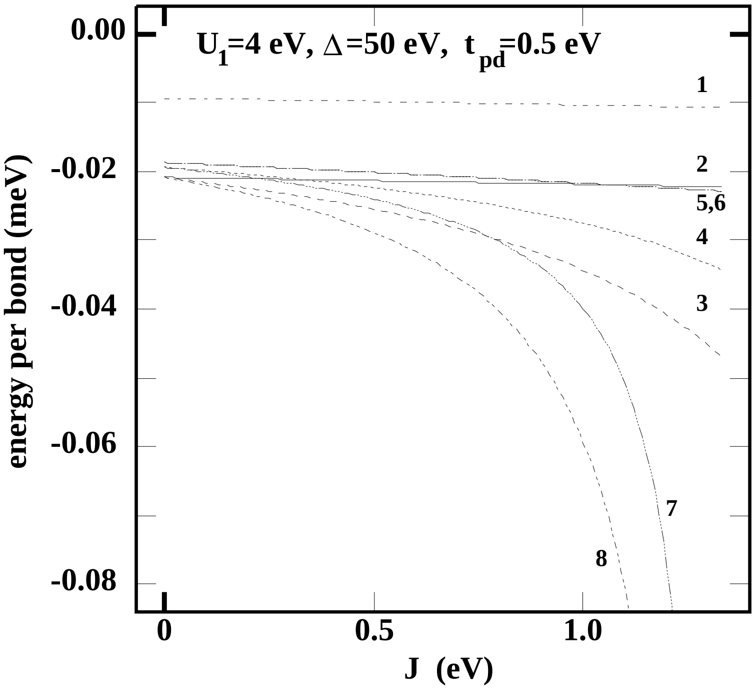

Figure B.8: Energy per bond for different configurations in the limit of extremely large Δ ($\Delta = 50$). (The configurations are shown in figure B.6).

almost non magnetic configuration, i. e. a configuration with a very small magnetic exchange constant, is lowest in energy. For extremely large J the ferromagnetic configurations are favored while the antiferromagnetic contributions related to J_1 have always higher energies.

So far, we only considered single bonds. To obtain the corresponding phase they have to be put into a three dimensional structure. This cannot be done by using only the type of bonds which has the lowest energy. Instead we expect a frustrated lattice with different configurations between next neighbor sites.

If on the other hand J gets so large that ferromagnetic bonds are energetically favored, one can think of a three dimensional ferromagnetic structure. In this context, it is interesting to notice that a ferromagnetic ground state is indeed found if La is replaced by Y [78, 85, 86]. Again the corresponding transition temperature is extremely small ($T_c \approx 30$ K).

For $LaTiO_3$, we conclude from our simple model that antiferromagnetism is strongly suppressed. In fact, our theoretical investigation suggests a frustrated lattice with preferably ferromagnetic and almost non magnetic bonds. To really describe the antiferromagnetic low temperature phase found in $LaTiO_3$ a more refined model is required. A more careful treatment would have to take into account fluctuations and the lattice distortion. Fluctuations will disturb any ordering so that they do not change our qualitative results. The distortion of the perovskite structure on the other hand will lift the degeneration of the three d orbitals considered. In this case every Ti site will have one d orbital which is lowest in energy. If this d orbital is the same for next neighbor sites an antiferromagnetic ground state (caused by J_1) might occur at low temperatures.

In any case, it is clear that magnetic ordering takes place only below a quite low transition temperature T_c. Above T_c the system is more or less frustrated. In this temperature regime the dynamical mean field theory has to be applied to a fully frustrated lattice to yield a reasonable description [87].

Appendix C

Interpolating Self Energy in Finite Dimensions

In chapter 3 we treated the limit of infinite dimensions or the impurity model, which can be viewed as the zero dimensional case. It is natural to ask whether our approach can also be used to construct an interpolating self energy in *finite* dimensions.

Let us consider the Hubbard model at dimension d on an arbitrary lattice with dispersion relation ϵ_k.[1] We start with a Green function

$$G_0(k,\omega) = \int_{-\infty}^{\infty} d\tilde{\epsilon} \frac{W_0(k,\tilde{\epsilon})}{\omega - \tilde{\epsilon} + \tilde{\mu}_0 - i\eta} \tag{C.1}$$

where the weight $W_0(k,\tilde{\epsilon})$ gets peaked in the atomic limit:

$$W_0(k,\tilde{\epsilon}) \to \delta(\tilde{\epsilon}) \text{ (atomic limit)} \tag{C.2}$$

G_0 is used to evaluate the second order contribution to the self energy (see figure C.1):

$$\begin{aligned}\tilde{\Sigma}_0^{(2)}(k,\omega) &= U^2 \int_{-\infty}^{0} d\tilde{\epsilon}_1 \int_{0}^{\infty} d\tilde{\epsilon}_2 d\tilde{\epsilon}_3 \, \frac{1}{N^2} \sum_{k_1,k_2} \frac{W_0(k_1+k,\tilde{\epsilon}_1)\; W_0(k_2,\tilde{\epsilon}_2)\; W_0(k_1+k_2,\tilde{\epsilon}_3)}{\omega + \tilde{\epsilon}_1 - \tilde{\epsilon}_2 - \tilde{\epsilon}_3 - i\eta} \\ &+ U^2 \int_{0}^{\infty} d\tilde{\epsilon}_1 \int_{-\infty}^{0} d\tilde{\epsilon}_2 d\tilde{\epsilon}_3 \, \frac{1}{N^2} \sum_{k_1,k_2} \frac{W_0(k_1+k,\tilde{\epsilon}_1)\; W_0(k_2,\tilde{\epsilon}_2)\; W_0(k_1+k_2,\tilde{\epsilon}_3)}{\omega + \tilde{\epsilon}_1 - \tilde{\epsilon}_2 - \tilde{\epsilon}_3 - i\eta}\end{aligned} \tag{C.3}$$

Using an ansatz similar to (3.5)

[1] For the d dimensional hyper cubic lattice we have e. g. $\epsilon_k = -2t\sum_{i=1}^{d}\cos(k_i)$.

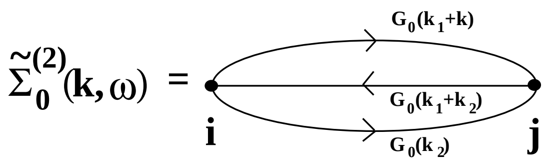

Figure C.1: Second order contribution to the self energy

$$\Sigma_{int}(k,\omega) = Un + \frac{A(k)\,\tilde{\Sigma}_0^{(2)}(k,\omega)}{1 - B\,\tilde{\Sigma}_0^{(2)}(k,\omega)} \tag{C.4}$$

an interpolating self energy can be constructed. we obtain the coefficient $A(k)$ from the high frequency behavior of $G(k,\omega)$, which is completely determined by the first two moments of the spectral weight. As before this yields for the exact self energy at high frequencies [35]

$$\Sigma(k,\omega) = \frac{U^2\,n(1-n)}{\omega + \ldots} \tag{C.5}$$

This has to be compared with the high ω behavior of (C.3):

$$\tilde{\Sigma}_0^{(2)}(k,\omega) = \frac{S_0(k,\omega)}{\omega + \ldots} \tag{C.6}$$

where

$$\begin{aligned} S_0(k,\omega) \;&=\; \int_{-\infty}^{0} d\tilde{\epsilon}_1 \int_0^{\infty} d\tilde{\epsilon}_2 d\tilde{\epsilon}_3\, \frac{1}{N^2} \sum_{k_1,k_2} W_0(k_1+k,\tilde{\epsilon}_1)\; W_0(k_2,\tilde{\epsilon}_2)\; W_0(k_1+k_2,\tilde{\epsilon}_3) \\ &+\; \int_0^{\infty} d\tilde{\epsilon}_1 \int_{-\infty}^{0} d\tilde{\epsilon}_2 d\tilde{\epsilon}_3\, \frac{1}{N^2} \sum_{k_1,k_2} W_0(k_1+k,\tilde{\epsilon}_1)\; W_0(k_2,\tilde{\epsilon}_2)\; W_0(k_1+k_2,\tilde{\epsilon}_3) \end{aligned} \tag{C.7}$$

Thus we obtain for $A(k)$

$$A(k) = \frac{n(1-n)}{S_0(k,\omega)} \tag{C.8}$$

In the atomic limit ($t \to 0$), we have $\tilde{\epsilon}_i \to 0$ (see C.2) so that $G_0(k,\omega) \to 1/(\omega + \tilde{\mu}_0 - i\eta)$. Therefore, the k dependence drops out and we are left with an impurity model yielding (see 3.11)

$$B = \frac{(1-n)\,U + \epsilon_f + \tilde{\mu}_0}{n_0(1-n_0)\,U^2} \tag{C.9}$$

Here, $n_0 = \frac{1}{\pi}\int_{-\infty}^{\infty} G_0(\omega)$ with $G_0(\omega) := \frac{1}{N}\sum_k G_0(k,\omega)$.

Once, the interpolating self energy is determined the full Green function follows from

$$G(k,\omega) = \int_{-\infty}^{+\infty} d\tilde{\epsilon} \frac{W(k,\tilde{\epsilon})}{\omega + \mu - \tilde{\epsilon} - \Sigma_{int}(\omega) - i\eta} \tag{C.10}$$

The weight $W(k,\tilde{\epsilon})$ contains the information of the specific lattice. Since in finite dimensions the exact full Green function is given by $G_{exact}(\omega) = 1/(\omega + \mu - \epsilon_k - \Sigma(\omega) - i\eta)$, we have

$$W(k,\tilde{\epsilon}) = \delta(\epsilon_k - \tilde{\epsilon}) \tag{C.11}$$

so that

$$G(k,\omega) = \frac{1}{\omega + \mu - \epsilon_k - \Sigma_{int}(\omega) - i\eta} \tag{C.12}$$

The parameter $\tilde{\mu}_0$ in G_0 is again fixed by imposing the Luttinger theorem: $\int_{-i\infty}^{+i\infty} d\omega\, G(\omega)\, \frac{\partial \Sigma_{int}(\omega)}{\partial \omega} = 0$.

The self consistency is closed by

$$\begin{aligned} G_0(\omega) &= \frac{1}{G^{-1}(\omega) + \Sigma(\omega) - \mu + \tilde{\mu}_0} \\ &= \frac{1}{\omega + \tilde{\mu}_0 - \epsilon_k - i\eta} \end{aligned} \tag{C.13}$$

which means

$$W_0(k,\tilde{\epsilon}) = \delta(\epsilon_k - \tilde{\epsilon}) \tag{C.14}$$

The iteration scheme then looks as follows: Starting with a guess for $\tilde{\mu}_0$ and n one obtains $G_0(k,\omega)$ from (C.13). This quantity is used to evaluate $\tilde{\Sigma}_0^{(2)}(k,\omega)$. Then, Σ_{int} is determined according to (C.4) and the full Green function follows from (C.12). Afterwards a new particle number is calculated by $n = \frac{1}{\pi}\int_{-\infty}^{0} \frac{1}{N}\sum_k G(k,\omega)$. A new $\tilde{\mu}_0$ follows from the Luttinger theorem and the next iteration step can be performed.

There are two issues which make such an interpolation scheme less attractive than for the case of the impurity model: First of all, the scheme is exact to order U^2 only for $k = 0$ because $\lim_{U\to 0} A(k) \neq 1$ for $k \neq 0$.[2] The other issue is of practical nature: The computational requirements of the procedure for finite dimensions are by several orders of magnitude higher than in $d = \infty$. This is not only due to the k sums in $\tilde{\Sigma}_0^{(2)}$ but also since the iteration has to be performed simultaneously for *all* k vectors. Therefore, we do not continue along these lines any further but restrict us in this thesis to the limit of infinite dimensions.

[2]For $k \neq 0$ the scheme is only exact to zeroth order in U.

Appendix D

Half Filled Hubbard Model with Binary Site Randomness

In chapter 5 we considered a Hubbard model with binary site randomness. The calculations were done away from half filling. But already the particle hole symmetric case is of interest since it reveals both, a Mott and a band insulator. There are some analytic results available for the half filled model. This allows us to perform an additional cross check of our iterative perturbation scheme.

Let us start by recapturing the most important equations. The model Hamiltonian is in general given by:

$$H = -\frac{t}{\sqrt{d}} \sum_{\langle ij\rangle,\sigma} a_{i\sigma}^{+}\, a_{j\sigma} + \sum_{i,\sigma} (\epsilon_i - \mu)\; n_{i\sigma} + U \sum_{i} n_{i\uparrow}\, n_{i\downarrow}. \tag{D.1}$$

It is assumed that there are two kinds of lattice sites a and b ϵ_a and ϵ_b respectively (i. e. $\epsilon_i \in \{\epsilon_a, \epsilon_b\}$). These lattice sites are distributed randomly so that an a-site appears with probability p_a and a b-site with probability $p_b = 1 - p_a$.

Let G_a (G_b) be the local Green function for an a (b) site. Due to the randomness of the problem, each electron hybridizes with an averaged bath[1]

$$\Delta(\omega) = t^2\; G_{av}(\omega) := t^2 \left(p_a\, G_a(\omega) + p_b\, G_b(\omega)\right) \tag{D.2}$$

Thus, we have the following relations for the a and the b sites

$$\begin{aligned} G_a(\omega) &= \frac{1}{\omega + \mu - \epsilon_a - \Sigma_a(\omega) - t^2\, G_{av}(\omega)} \\ G_b(\omega) &= \frac{1}{\omega + \mu - \epsilon_b - \Sigma_b(\omega) - t^2\, G_{av}(\omega)} \end{aligned} \tag{D.3}$$

To treat the problem iteratively, each step requires solving *two* impurity problems with site energies $\epsilon_f = \mu - \epsilon_a$ and $\epsilon_f = \mu - \epsilon_b$ respectively. This yields the Green functions G_a and G_b, which are averaged to obtain a new G_{av}.

---

[1] We assume a Bethe lattice.

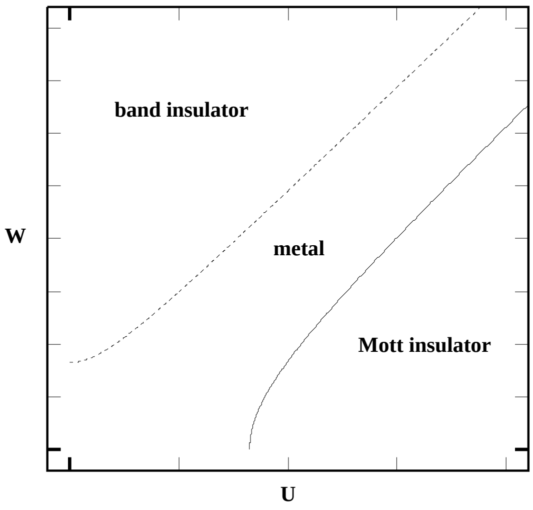

Figure D.1: Schematic phase diagram for the particle hole symmetric case.

The half filled case, which is given by $\epsilon_a = -\epsilon_b$ and $\mu = \frac{U}{2}$, [2] was studied by Dobrosavljevic and Koltiar [88]. They obtained some analytic results which can be used for testing our method. Two limits are clear: For vanishing interaction ($U = 0$), we get a transition from a metal to a band insulator as $W := \frac{1}{2}(\epsilon_b - \epsilon_a)$ is increased (starting from $W = 0$). If on the other hand $W = 0$, the problem reduces to a simple Hubbard model showing a Mott transition. The schematic phase diagram is sketched in figure D.1. There are two insulating regions (the Mott insulator and the band insulator) separated by a metallic phase. In figure D.2 we plotted the evolution of the spectral function $\mathrm{Im}G_{av}(\omega)$ for fixed $W = 0.8$ and increasing interaction U. The transition from a band insulator to a metal occurs at about $U = 0.7$. We find the Mott transition for $W = 0.8$ at $U = 3.9$ which is in excellent agreement with an analytic expression obtained by Dobrosavljevic and Kotliar [88] for the transition line:

$$U_c(W) = \frac{1}{2}\ U_c^0\ \left[1 + \sqrt{1 + (\frac{4W}{U_c^0})^2}\right] \tag{D.4}$$

For $U_0 \approx 3.3$, this yields $U_c(W = 0.8) \approx 3.9$ as observed.

Defining the self energy

$$\Sigma_{dis}(\omega) = \omega - t^2\ G_{av}(\omega) - \frac{1}{G_{av}(\omega)} \tag{D.5}$$

[2] Be aware of that only the averaged Green function is particle hole symmetric. The two single impurity models themselves are not.

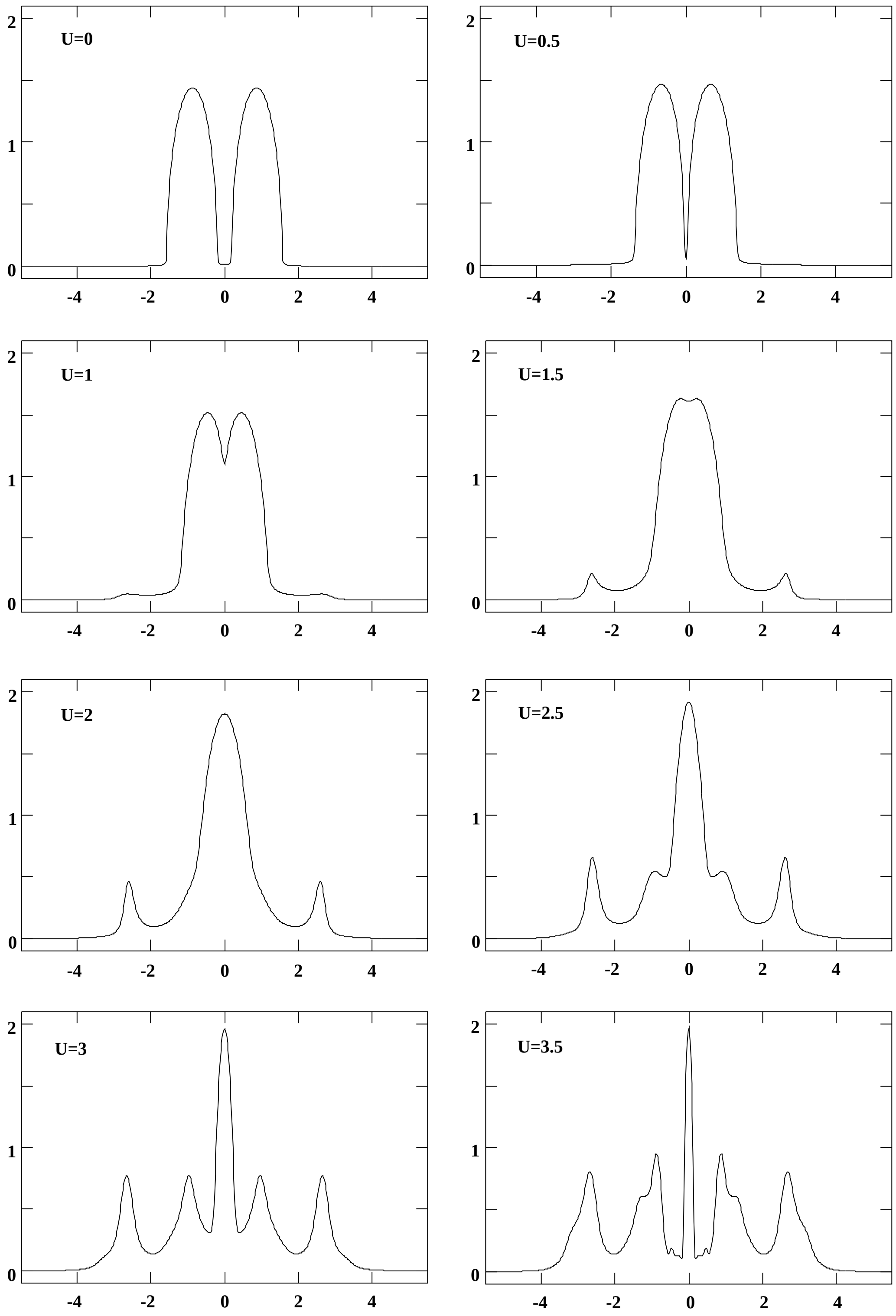

Figure D.2: Development of the spectral function for $W = 0.8$ and increasing U.

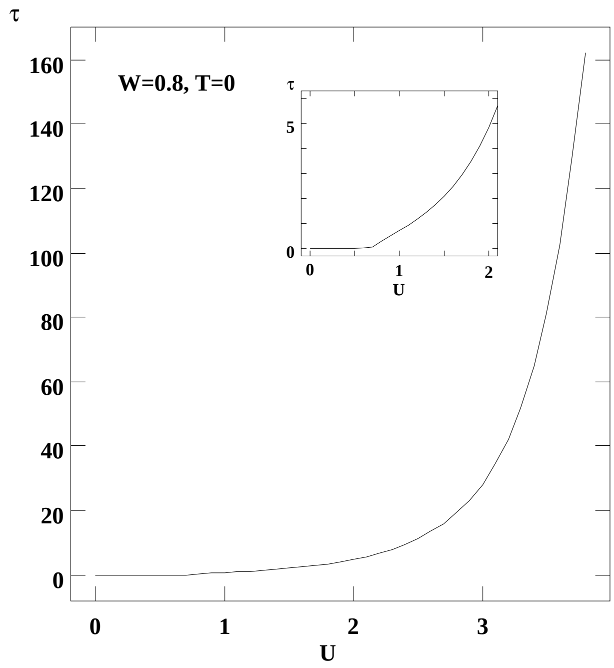

Figure D.3: Enhancement of the scattering time as the Mott transition is approached from below.

we can compute a scattering time $\tau = (2\ \mathrm{Im}\Sigma(\omega = 0))^{-1}$. It is a striking analytic result that the scattering time diverges as the Mott transition is approached from below. In agreement with this prediction, our iterative perturbation scheme shows a strong enhancement of τ near the transition (see figure D.3).

In conclusion, we have seen that our perturbation scheme is able to reproduce the most characteristic analytic results. This confirms that the method is also reliable for more complicated models.

References

[1] J. G. Bednorz and K. A. Mueller, *Z. Phys. B* **64**, 189 (1986)

[2] E. g.: P. A. Lee, T. M. Rice, J. W. Serene, L. J. Sham and J. W. Wilkins; *Com. on Cond. Mat. Physics* **XII**, 99 (1986)

[3] W. Metzner and D. Vollhardt, *Phys. Rev. Lett.* **62**, 324 (1989)

[4] C. J. Thompson, *Commun. Math Phys.* **36**, 255 (1974)

[5] H. Kajueter, G. Kotliar, and G. Moeller, accepted for publication in *Phys. Rev. B* (1996)

[6] A. Georges, G. Kotliar, *Phys. Rev. B* **45** 6479 (1992)

[7] M. Jarrell, *Phys. Rev. Lett.* **69**, 168 (1992)

[8] M. Rozenberg, X. Y. Zhang and G. Kotliar, *Phys. Rev. Lett.* **69**, 1236 (1992)

[9] M. C. Gutzwiller, *Phys. Rev. Lett.* **10**, 159 (1963)

[10] J. Hubbard, *Proc. Roy. Soc. (London)* **A276**, 238 (1964)

[11] J. Hubbard, *Proc. Roy. Soc. (London)* **A281**, 401 (1964)

[12] J. Kanamori, *Prog. Theor. Phys.* **30**, 275

[13] X. Y. Zhang, M. J. Rozenberg and G. Kotliar, *Phys. Rev. Lett.* **70**,1666 (1993)

[14] M. Caffarel and W. Krauth *Phys. Rev. Lett.* **72**, 1545 (1994), Q. Si, M. Rozenberg G. Kotliar and A. Ruckenstein, *Phys. Rev. Lett.* **72**, 2761 (1994)

[15] G. Moeller, Q. Si, G. Kotliar, M. Rozenberg and D. S. Fisher, *Phys. Rev. Lett.* **74**, 2082 (1995)

[16] D. Fisher, G. Kotliar, and G. Moeller, *Phys. Rev. B* **52**, 17112 (1995)

[17] M. Jarrell and T. Pruschke *Z. Phys. B* **90**, 187 (1993)

[18] D. Fisher, G. Kotliar and G. Moeller, to appear in *Phys. Rev. B*

[19] M. J. Rozenberg, G. Kotliar, H. Kajueter, G. A. Thomas, D. H. Rapkine, J. M. Honig, and P. Metcalf, *Phys. Rev. Lett.* **75**, 105 (1995)

[20] M. J. Rozenberg, G. Kotliar, and X. Y. Zhang, *Phys. Rev. B* **49**, 10181 (1994)

[21] Goetz Moeller, Ph. D. thesis, Rutgers University, NJ (1994)

[22] Gabriel Kotliar, preprint 1994

[23] A. C. Hewson, The Kondo Problem to Heavy Fermions, Cambridge University Press

[24] Marcelo Rozenberg, Ph. D. thesis, Rutgers University, NJ (1994)

[25] Th. Pruschke, D. L. Cox, and M. Jarrell *Phys. Rev. B* **47**, 3553 (1993)

[26] For a recent review see Antoine Georges, Gabriel Kotliar, Werner Krauth, and Marcelo Rozenberg, preprint (1995)

[27] A. Georges and W. Krauth, *Phys. Rev. Lett.* **69**, 1240 (1992)

[28] Y. Tokura, Y. Taguchi, Y. Okada , Y. Fujishima, and T. Arima, K. Kumagai and Y. Iye, *Phys. Rev. Lett.* **70**, 2126 (1993).

[29] Y. Okimoto, T. Katsufuji, and Y. Tokura, *Phys. Rev. B* **51**, 9581 (1995)

[30] Y. Tokura and T. Katsufuji, *Spectroscopy of Mott Insulators and Correlated Metals.*, ed. A. Fujimori and Y. Tokura, Springer

[31] Y.Okimoto, T. Katsufuji, Y. Okada, T. Arima, and Y. Tokura, *Phys. Rev. B* (1995)

[32] A. Asamitsu *et al.*, *Nature* **373**, 407 (1995)

[33] T. Katsufuji, Y. Okimoto, and Y. Tokura, *preprint* (1995)

[34] R. G. Gordon, *J. Math. Phys.* **9**, 655 (1968)

[35] W. Nolting and W. Borgiel, *Phys. Rev. B.* **39**, 6962 (1989)

[36] W. Brenig, K. Schönhammer, *Z. Phys.* **257**, 201 (1974)

[37] A. Martin-Rodero, F. Flores, M. Baldo and R. Pucci, *Sol. State Comm.* **44**, 911 (1982)

[38] D. M. Edwards and J. A. Hertz, *Physica B* **163**, 527 (1990)

[39] W. Wermbter and G. Czycholl, *J. Phys. Cond. Mat.* **7**, 7335 (1995)

[40] D. C. Langreth, *Phys. Rev.* **150**, 516 (1966)

[41] J. M. Luttinger, J. C. Ward, *Phys. Rev.* **118**, 1417 (1960)

[42] E. Müller-Hartmann, *Z. Phys. B.* **76**, 211 (1989)

[43] W. H. Press et al., *Numerical Recipes in Fortran*, 2nd edition, p. 382, Cambridge University Press

[44] B. Bell and A. Madhukar, *Phys. Rev. B* **14**, 4281 (1976)

[45] M. J. Rozenberg, G. Moeller, and G. Kotliar, *Modern Physics Letters B* **8**, 535 (1994)

[46] M. Jarrell, Th. Pruschke, *Z. Phys. B* **90**, 187 (1993)

[47] M. Jarrell, Th. Pruschke, *Phys. Rev. B* **49**, 1458 (1994)

[48] H. Kuwamoto, J. M. Honig, and J. Appel, *Phys. Rev. B* **22**, 2626 (1986)

[49] For an introduction see Landau-Lifshitz, volume 10

[50] William H. Press et. al., Numerical Recipes in Fortran, 2nd. edition, page 577, Cambridge University Press

[51] D. D. Sarma *et al.*, to be published

[52] A. Fujimori *et al.*, *Phys. Rev. Lett.* **69**, 1796 (1992); I. H. Inoue *et al.*, *Phys. Rev. Lett.* **74**, 2539 (1995)

[53] A. Fujimori *et al.*, *Phys. Rev. B* **46**, 9841 (1992)

[54] W. Gongo *et al.*, *J. Solid State Chem.* **90**, 320 (1991)

[55] D. D. Sarma *et al.*, *Phys. Rev. Lett.* (in press)

[56] S. R. Barman and D. D. Sarma, *Phys. Rev. B*, **51**, 4007 (1995)

[57] J. C. Fuggle *et al.*, *Phys. Rev. B* **27**, 7330 (1983); O. Gunnarsson *et al.*, *Phys. Rev. B* **28**, 7330 (1993).

[58] D. D. Sarma *et al.*,*Phys. Rev. Lett.* **57**, 2215 (1986).

[59] G. Treglia, F. Ducastelle and D. Spanjaard, *Phys. Rev. B* **21**, 3729 (1980); and *J. Physique* **41**, 281 (1980)

[60] See for example E. Dagotto *et al.*, *Phys. Rev. B* **45**, 10741 (1992)

[61] H. Fukuyama and H. Ehrenreich, *Phys. Rev. B* **7**, 3266 (1973)

[62] F. Brouers and D. Ducastelle, *J. Phys.* **36**, 851 (1975)

[63] C. Lacroix-Lyon-Caen and M. Cyrot, *Sol. State Comm.* **21**, 837 (1977)

[64] B. Velicky, S. Kirkpatrick, and H. Ehrenreich, *Phys. Rev.* **175**, 747 (1968)

[65] Abricosov, Gorkov and Dzyaloshinski, *Methods of quantum field theory in statistical physics*, page 167

[66] Th. Pruschke, D. L. Cox, and M. Jarrell, *Euro Phys. Lett.* **21**, 5 (1993)

[67] M. L. Horbach, H. Kajueter, *Phys. Rev. Lett.* **73**, 1309 (1994)

[68] M. L. Horbach, H. Kajueter, *Int. J. Mod. Phys. B* **9**, 1067 (1995)

[69] M. Jarrell, J. K. Frederics and Th. Pruschke, *(Preprint)*

[70] For an early review see G. Kotliar in: Strongly Correlated Electronic Materials, edited by K. S. Bedell, Z. Wang, D. Meltzer, A. Balatsky and E. Abrahams, Addison Wesley (1994)

[71] C. Castellani, C. Di Castro, D. Feinberg, and J. Ranninger, *Phys. Rev. Let.* **43**, 1957 (1979)

[72] Th. Pruschke, M. Jarrell, and J. K. Freericks, preprint 1995

[73] B. Horvatic, D. Sokcevic, and V. Zlatic, *Phys. Rev. B* **36**, 675 (1987)

[74] F. B. Anders, preprint (1995)

[75] H. C. Nguyen and J. B. Goodenough, *Phys. Rev. B* **52**, 8776 (1992)

[76] Y. Fujishima, Y. Tokura, T. Arima, and S.Uchida, *Phys, Rev. B* **46**, 11167 (1992)

[77] J. E. Greedan, J. Less-Common, *Met.* **111**, 335 (1985)

[78] D. A. MacLean and J. E. Greedan, *Inorg. Chem.* **20**, 1025 (1981)

[79] J. P. Goral, J. E. Greedan, and D. A. MacLean, *J. Solid State Chem.* **43**, 244 (1982)

[80] D. A. Crandles, T. Timusk, and J. E. Greedan, *Phys. Rev. B* **44**, 13250 (1991)

[81] D. A. McLean, Hok-Nam Ng, and J. E. Greedan, *J. Solid State Chem.* **30**, 35 (1979)

[82] J. R. Schrieffer and P. A. Wolff. *Phys. Rev.* **149**, 491 (1966)

[83] H. Eskes and John H. Jefferson *Phys. Rev. B* **48**, 9788 (1993)

[84] G. Kotliar, private communication

[85] J. D. Garrett, J. E. Greedan and S. A. MacLean, *Mat. Res. Bull.* **16**, 145 (1981)

[86] J. P. Goral, J. E. Greedan and D. A. MacLean, *J. Sol. Stat. Chem.* **43**, 244 (1982)

[87] D. D. Sharma, S. R. Barman, H. Kajueter and G. Kotliar, submitted to *Phys. Rev. Lett.* (1995), see also chapter 5

[88] V. Dobrosavljevic and G. Kotliar, notes

[89] R. Preuss, W. Hanke, and W. von der Linden, *Phys. Rev. Let.* **75**, 1344 (1995)

[90] G. Huelsenbeck and Frank Stephan, *Z. Phys. B* **94**, 281 (1994)

[91] A. Georges and W. Krauth, *Phys. Rev. B* **48**, 7167 (1993)

[92] A. Georges, G. Kotliar, and Q. Si, *Int. J. Mod. Phys. B* **6**, 705 (1992)

[93] M. Rozenberg, G. Kotliar, and H. Kajueter, submitted to *Phys. Rev. B* (1995)

[94] R. Fresnard and G. Kotliar, submitted to *Phys. Rev. Lett.* (1996)

[95] M. Rozenberg, preprint

[96] E. Halverson, G. S. Uhrig, G. Czycholl, *Z. Phys. B* **94**, 291 (1994)

[97] N. Furukawa and M. Imada, preprint 1991

[98] V. Emery, S. Kivelson, and H. Lin, *Phys. Rev. Lett.* **57**, 2215 (1986)

[99] J. Klima *et al.*, *J. Phys. F* **15**, 1307 (1985); F. Patthey *et al.*, *Europhys. Lett.* **2**, 883 (1986)

[100] R. Vlaming, G. S. Uhrig, D. Vollhardt, *J. Phys.* **C4**, 7773 (1992)

[101] G. S. Uhrig, R. Vlaming, D. Vollhardt, *J. Phys.* **C5**, 2561 (1993)

[102] R. J. Braxter, Exactly Solved Models in Statistical Mechanics, London: Academic Press

[103] C. N. Yang, C. P. Yang, *Phys. Rev.* **150**, 321 (1966); *Phys. Rev.* **150**, 327 (1966)

[104] J. des Cloizeaux, M. Gaudin, *J. Math. Phys.*, **7**, 1384 (1966); J. des Cloizeaux, *J. Math. Phys.*, **7**, 2136 (1966)

[105] R. Shankar, *Int. J. Mod. Phys.*, **B4**, 2371 (1990); *Physica*, **A177**, 530 (1991)

[106] P. Lemberger, N. Macris, *Lett. Math. Phys*, **28**, 295 (1993)

[107] G. S. Uhrig, R. Vlaming, *Phys. Rev. Lett.*, **71**, 271 (1993)

[108] Mahan, Many Particle Physics, 2nd edition, p. 286

[109] E. Dagotto, *Rev. Mod. Phys.* **66**, (1994)

[110] C. L. Kane, P. A. Lee, and N. Read, *Phys. Rev. B* **39**, 6880 (1989)

[111] D. A. McLean, Hok-Nam NG, and J. E. Greedan, *J. Sol. State Chem.* **30**, 35-44 (1979)

[112] S. Uchida *et al.*, *Phys. Rev. B* **43**, 7942 (1991)

[113] E. Dagotto, *et al.*, *Phys. Rev. B* **45**, 10741 (1992)

[114] V. Dobrosavljevic, private communication

[115] P. Majumdar and H. R. Krishnamurthy, COND-MAT/9512151, Dez. 1995

[116] V. Anisimov, private communication

Vita

Henrik Kajueter

1987	Graduated from Julius Stursberg Gymnasium (highschool), Neukirchen-Vluyn, Germany.
1987 - 1988	Mandatory military service, Wesendorf, Germany.
1988 - 1993	**Attended RWTH Aachen (University of Technology), Germany.** Majors: Physics and Mathematics. Scholar of the German National Scholarship Foundation (Studienstiftung des deutschen Volkes).
1990	Vordiplom in Physics and Mathematics.
1993	**Graduated as "Diplom-Physiker".** Diploma thesis: "Development of a Controlled Mean Field Theory for the BEG Model and Related Lattice Models" (under the direction of Prof. Dieter Vollhardt).
1993 - present	Participated in a **business administration program** for scientists and engineers at the Correspondence University Hagen, Germany.
1993 - present	**Graduate work in Physics, Rutgers University, New Brunswick, New Jersey.**
1993 - 1994	Fulbright scholar.
1994	**Master of Science** in Physics, Rutgers University.
1994 - present	Graduate assistant.
1996	**Ph.D. in Physics.**

Publications

1994	Comment on "Electronic Specific Heat of $YBa_2Cu_3O_{6+x}$ from 1.8 to 300 K". M. L. Horbach and H. Kajueter, *Phys. Rev. Lett.* **73**, 1309 (1994)
1995	Van Hove Singularity in High T_c Superconductors. M. L. Horbach and H. Kajueter, *Int. Jour. Mod. Phys. B* **9**, 1067 (1995)

1995	Optical Conductivity in Mott-Hubbard Systems. M. J. Rozenberg, G. Kotliar, H. Kajueter, G. A. Thomas, D. H. Rapkine, J. M. Honig, and P. Metcalf, *Phys. Rev. Lett.* **75**, 105 (1995)
1995	Spectral Functions of Correlated Electron Systems in the Local Impurity Self Consistent Approximation. H. Kajueter and G. Kotliar, *J. Phys. Chem. Solids* **56**, 1615 (1995)
1996	The Doped Mott Insulator: Results from Mean Field Theory. H. Kajueter, G. Kotliar, and G. Moeller, accepted for publication in *Phys. Rev. B* (1996)
1996	New Iterative Perturbation Scheme for Lattice Models with Arbitrary Filling. H. Kajueter and G. Kotliar, accepted for publication in *Phys. Rev. Lett.* (1996)
1996	Spectral Functions in Doped Transition Metal Oxides. D. D. Sharma, S. R. Barman, H. Kajueter, and G. Kotliar, submitted to *Phys. Rev. Lett.* (1996)
1996	Transfer of Spectral Weight in Spectroscopies of Correlated Electron Systems. M. Rozenberg, G. Kotliar, and H. Kajueter, submitted to *Phys. Rev. B* (1996)
1996	Effects of Orbital Degeneracy on the Mott Transition in Infinite Dimensions. H. Kajueter and G. Kotliar, in preparation